

INVESTIGATING THE POSSIBLE HALO STRUCTURE IN ^{22}Al AND ^{23}Al

By

Brooke Jayne Rickey

A DISSERTATION

Submitted to
Michigan State University
in partial fulfillment of the requirements
for the degree of

Physics—Doctor of Philosophy

2025

ABSTRACT

Nuclei with unique structures and phenomena, including largely enhanced nucleon distributions referred to as halo nuclei, occur along the driplines of the nuclear chart. To develop nuclear theory and unveil driving nuclear forces it is important to study and understand the unique dripline nuclei. Many neutron halo nuclei have been observed close to the neutron dripline for light-mass nuclei. Nuclei with a proton halo structure are much rarer due to the Coulomb barrier. Protons extending beyond the compact core of a nucleus see the charge of the protons in the core and must penetrate the Coulomb barrier. The first neutron halo studied and accepted as a halo nuclei is ^{11}Li . Known and suspected 1-neutron halos include ^{11}Be , ^{15}C , ^{19}C , and ^{23}O . Possible 2-neutron halos include ^6He , ^{14}Be , and ^{17}B . Though there are many neutron halos and candidates, no definite proton halo nucleus has been identified. Suspected proton halos include ^8B , ^{17}Ne , ^{27}S , ^{26}P , ^{22}Al , and ^{23}Al . It can be argued that due to the Coulomb barrier, it is impossible for any proton halos to exist. Of the possible proton halo nuclei ^{22}Al and ^{23}Al have many reasons supporting and denying the halo existence. An enhancement of the reaction cross section has been observed for ^{23}Al . The cross section measurement of ^{11}Li was essential in discovering its halo structure, making the cross section a good indicator of possible halo structure. However, the measured reaction cross section of ^{23}Al has a large uncertainty. Both nuclei have a small proton separation energy and a predicted increase in charge radius supporting a halo structure. However, their large spin makes the possibility of a halo structure unlikely. A large spin indicates the last nucleon occupies an orbital with large angular momentum. The larger angular momentum a nucleon carries, the larger the centrifugal barrier the nucleon needs to overcome to extend beyond the core. Contrasting conclusions regarding the halo structure in ^{22}Al and ^{23}Al demonstrates a need for a direct measurement of the proton distribution. To directly address the debated proton distribution, a laser spectroscopy experiment on ^{22}Al and ^{23}Al together with heavier Al isotopes ^{24}Al and ^{25}Al was performed at the BEam COoling LAsER spectroscopy (BECOLA) facility using the newly commissioned Resonant Ionization Spectroscopy Experiment (RISE)

instrument at the Facility for Rare Isotope Beams (FRIB). Through measurements of the hyperfine spectra of $^{22-25}\text{Al}$, the isotope shift between each isotope and stable ^{27}Al was measured. From the measured isotope shifts the differential mean square charge radii of the ground states of $^{22-25}\text{Al}$ were determined in addition to the isomeric state of ^{24}Al . Experimental results showed no largely enhanced proton distribution in ^{22}Al or ^{23}Al , ruling out the existence of a halo structure. Experimental results were compared with independently calculated theoretical results. Three theoretical methods were used to calculate the charge radius; Nuclear Lattice Effective Field Theory (NLEFT), Valence-Space In-Medium Similarity Renormalization Group (VS-IMSRG), and Skyrme Energy Density Functional (SKX-EDF). Both VS-IMSRG and SKX-EDF calculations predicted an increase in charge radius for ^{22}Al , while NLEFT predicted a decrease. NLEFT calculations most accurately reproduce experimental results for both the differential mean square charge radius and absolute charge radius results. SKX-EDF reproduces the overall trend of the experimental results well. VS-IMSRG calculations are the least accurate in reproducing experimental results. In addition to the differential mean square charge radius of each isotope, the magnetic dipole moment was determined in the experiment and compared with theoretical results. Three theoretical methods were used to obtain magnetic dipole moment results; NLEFT, VS-IMSRG, and Shell Model. NLEFT calculations are not as accurate reproducing the experimental magnetic dipole moment results as they are for the charge radius. Shell Model calculations reproduce the magnetic dipole moment experimental results within expected deviations, with the largest difference for ^{22}Al possibly due to deviation from well accepted effective g-factors in the region. IMSRG magnetic dipole moment results including a two body correction are the most accurate in reproducing the experimental results.

Copyright by
BROOKE JAYNE RICKEY
2025

Dedicated to my sister, Paige A. Rickey.

ACKNOWLEDGMENTS

This work is supported by NSF grant PHY-21-11185 and DOE award DE-SC0000661, DE-SC0021176, and DE-SC0021179 for the BECOLA/RISE collaboration.

TABLE OF CONTENTS

CHAPTER 1	BACKGROUND AND MOTIVATION	1
1.1	Extended Nucleon Distribution	1
1.2	Proton Halos	8
1.3	Arguments for Aluminum-22 and 23	13
1.4	Need for Charge Radius Measurement	20
CHAPTER 2	HYPERFINE INTERACTION	21
2.1	Hyperfine Interaction	21
2.2	Hyperfine Structure	22
2.3	Isotope Shift of Hyperfine Spectra	27
2.4	Charge Radii Studies by Laser Spectroscopy	34
CHAPTER 3	EXPERIMENT	39
3.1	Laser Spectroscopy Techniques	39
3.2	Laser Setup	48
3.3	Beamline Setup	62
CHAPTER 4	EXPERIMENTAL DATA	86
4.1	Hyperfine Spectra	86
4.2	Stable ^{27}Al Offline Transitions	87
4.3	Simulations	93
4.4	Online Run	100
CHAPTER 5	ANALYSIS	114
5.1	Fitting Function	114
5.2	Side Peak	115
5.3	Beam Energy Correction	118
5.4	Calibration Runs	124
5.5	Each Isotope Fit	130
5.6	Systematic Error Analysis	143
CHAPTER 6	RESULTS	147
6.1	Magnetic Dipole Moment Determination	147
6.2	Magnetic Dipole Moment Theory Results	148
6.3	Determining Charge Radii Trend	158
6.4	Charge Radii Theory Results	163
6.5	Structure of ^{22}Al and ^{23}Al	173
CHAPTER 7	CONCLUSION	174
BIBLIOGRAPHY	177
APPENDIX	OFFLINE TRANSITIONS	189
.1	Stable ^{27}Al Offline Transitions	189

CHAPTER 1

BACKGROUND AND MOTIVATION

1.1 Extended Nucleon Distribution

Moving towards the driplines of the nuclear chart, unique structures and phenomena occur. Understanding unique nuclei is important to unveil driving nuclear forces and develop nuclear theory. Among the unique structures, distribution beyond the compact core has been observed, including a largely enhanced nucleon distribution informally referred to as a halo phenomena [6]. An enhanced nucleon distribution is a unique structure that can occur in loosely bound nuclei. It is a nucleus with neutrons or protons extended far beyond the compact core which can lead to a "halo" around the core. Figure 1.1 shows a schematic of an extended nucleon distribution with a halo phenomena structure.

For a nucleus to be identified as exhibiting a halo structure a variety of characteristics need to present. Any number of characteristics found in a nucleus can indicate a possible halo structure. Halo candidates, potential nuclei with loosely bound nucleons extending beyond a compact core, can have identifying characteristics such as a large density distribution, large nuclear size relative to its core, narrow momentum distribution of the last nucleon, small separation energy, or an extended probability distribution. These characteristics can be seen in a very well known and good example of a halo nuclei studied, Lithium-11.

^{11}Li was first thought to have distribution beyond the compact core when studying the enlarged interaction cross section, indicating a large nuclear size relative to its core. The interaction cross sections for Li isotopes were measured through projectile-fragmentation at high energies [7]. The resulting interaction cross sections, σ_I , for the Lithium isotopic chain are shown in Figure 1.2. The interaction cross section was found by impinging a projectile, in this case Li isotopes, onto a target nucleus. The probability of the proton or neutron number changing for the projectile nucleus is the reaction cross section. The interaction cross section is defined in this work as the total reaction cross section, including the probability of any possible change in proton or neutron number. The interaction cross section is related to the

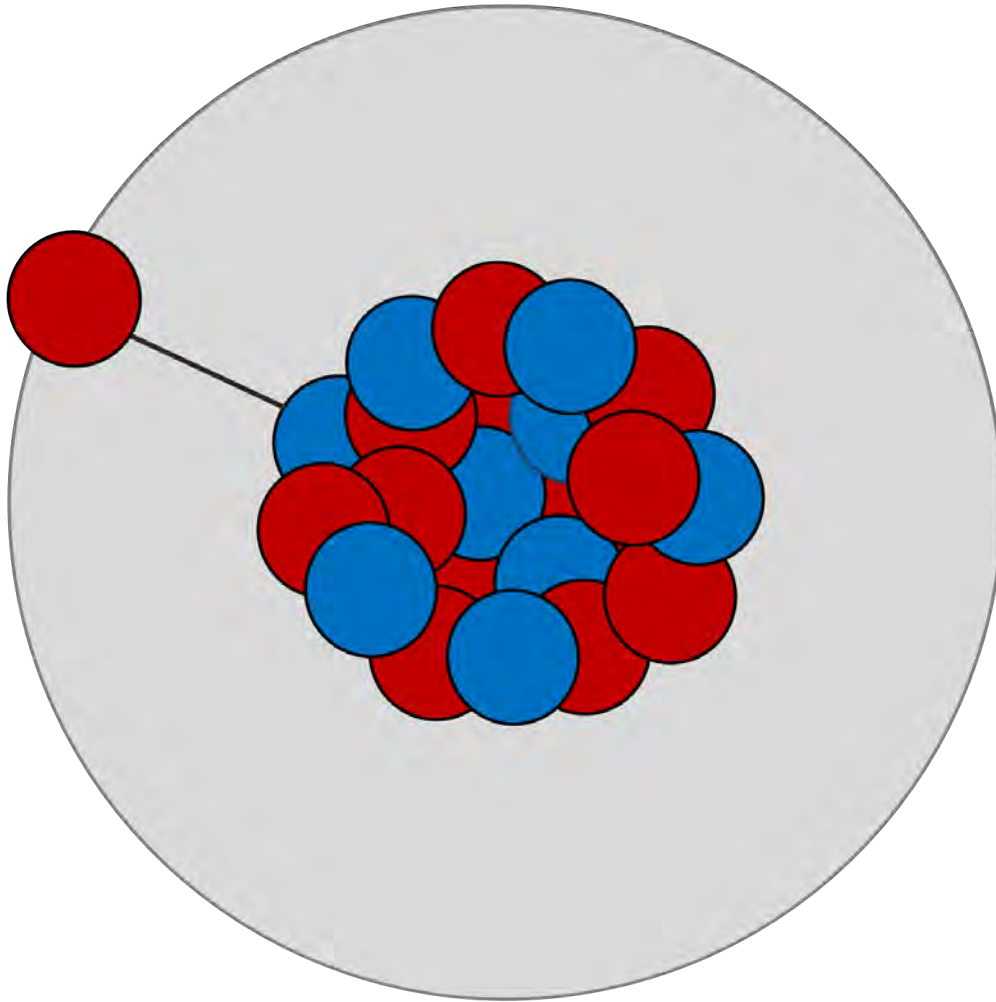


Figure 1.1 Halo schematic. A halo phenomena schematic is shown, blue circles represent neutrons, red circles indicate protons, and the grey circle indicates the proton distribution. The proton distribution is extended beyond the compact core due to the loosely bound proton. Similarly if the blue circles represent protons and red circles represents neutrons, then an extended neutron distribution is shown. This particular configuration is referred to as a halo phenomena.

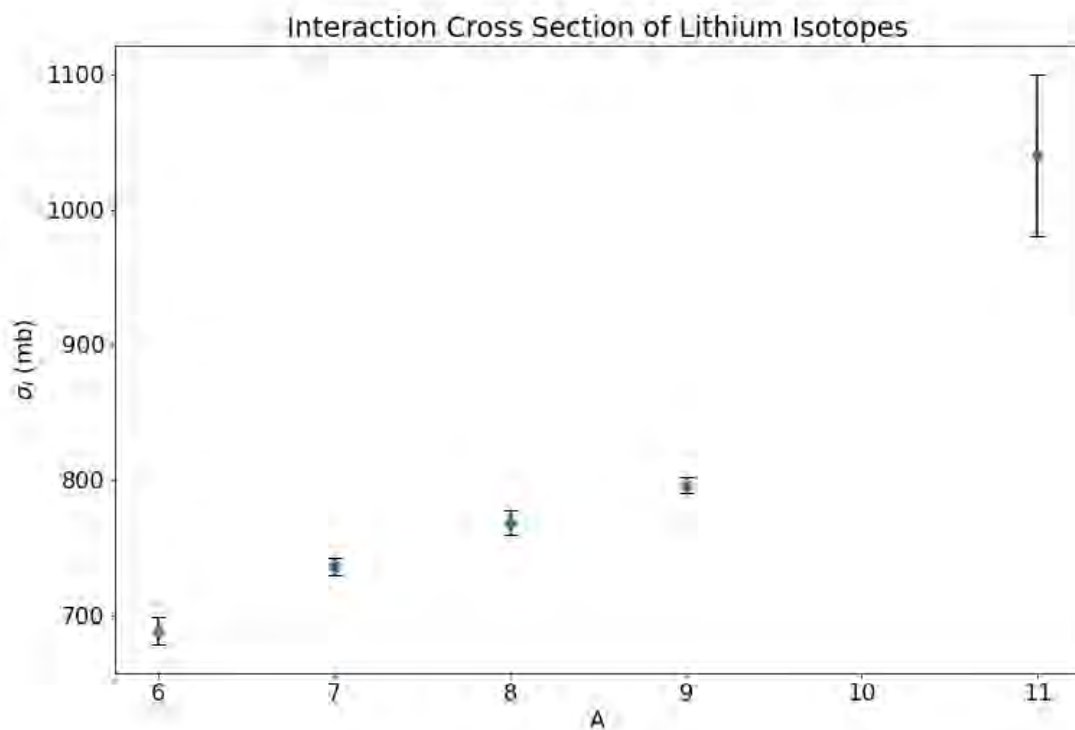


Figure 1.2 Cross section of Li isotopic chain. The interaction cross sections for the lithium isotopic chain are shown. The data plotted is taken and figure is reproduced from Reference [7]. A large increase can be seen moving towards ^{11}Li indicating a large nuclear size.

interaction radius of the projectile, $R_I(p)$, and target, $R_I(t)$, as shown in Equation 1.1.

$$\sigma_I = \pi[R_I(p) + R_I(t)]^2 \quad (1.1)$$

It is shown by the relation that for an isotopic chain of projectiles on the same target nucleus, an increase in interaction cross section shows an increase in interaction radius and overall size of the nucleus. The works result supported an enlarged nucleon distribution but indicated further studies on the nucleus were needed to understand the measured cross section. This motivated the charge radius to then be measured to determine ^{11}Li is a neutron halo with a ^9Li core and 2 neutrons extended beyond the compact core [8]. The charge radius is sensitive to charge distribution and is indirectly connected to the neutron distribution. Combining the charge radius with the cross section determines the relative distribution of the protons

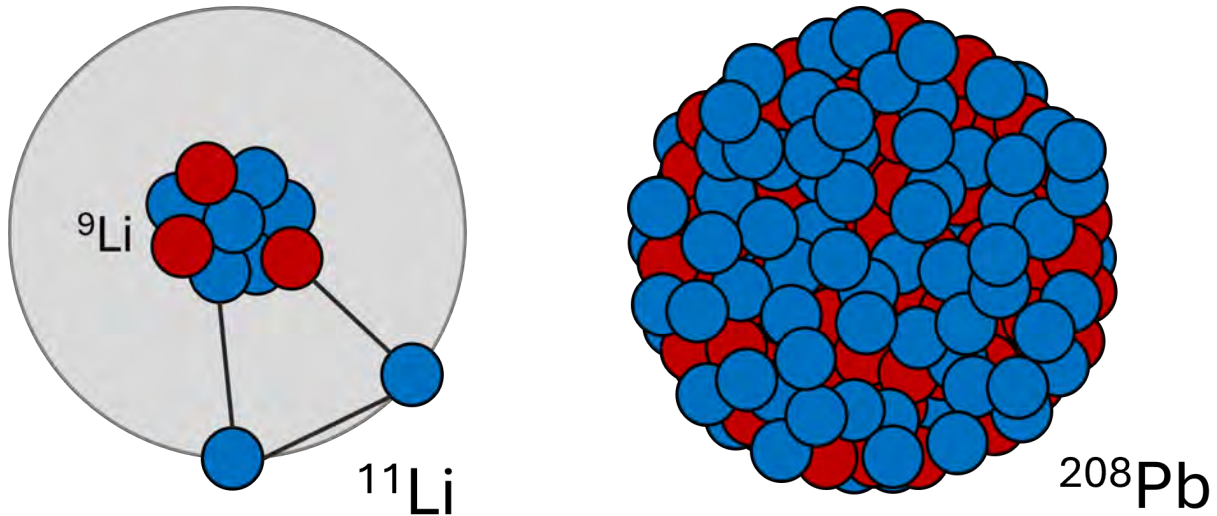


Figure 1.3 Schematic of ^{11}Li compared to ^{208}Pb . A schematic of ^{11}Li and ^{208}Pb are shown. Blue circles represent neutrons, red circles indicate protons, and the grey circle indicates the cross section of ^{11}Li . Note, the schematic is not drawn to scale. Two neutrons are extended beyond the compact core in ^{11}Li creating a cross section comparable to ^{208}Pb that has a compact structure.

and neutrons. Through study of the nuclei it is seen that ^{11}Li has a comparable size of its nucleon distribution to ^{208}Pb . A schematic of ^{11}Li compared to ^{208}Pb is shown in Figure 1.3. Both the cross section and charge radius of a nucleus can be measured to determine the size of a nucleus and the difference between the overall size relative to its core.

From measured interaction cross sections with several different targets, the density distribution can be obtained [9]. An extended density distribution with a long density "tail" can indicate a halo structure. A distribution displaying a tail has a very high density peak at the center of the nucleus and quickly decreases moving further from the center of the nucleus. This indicates a high density in a small area around $r = 0$, corresponding to the core of a nucleus, with an extended distribution of small density, corresponding to the one or two nucleons extended beyond the core. Figure 1.4 shows the density distribution for ^{11}Li .

To allow one or two nucleons to extend beyond the compact core, the nucleus must have a small separation energy, E_s . There is a direct connection between the separation energy and the density distribution. Equation 1.2 shows the relationship between the two characteristics

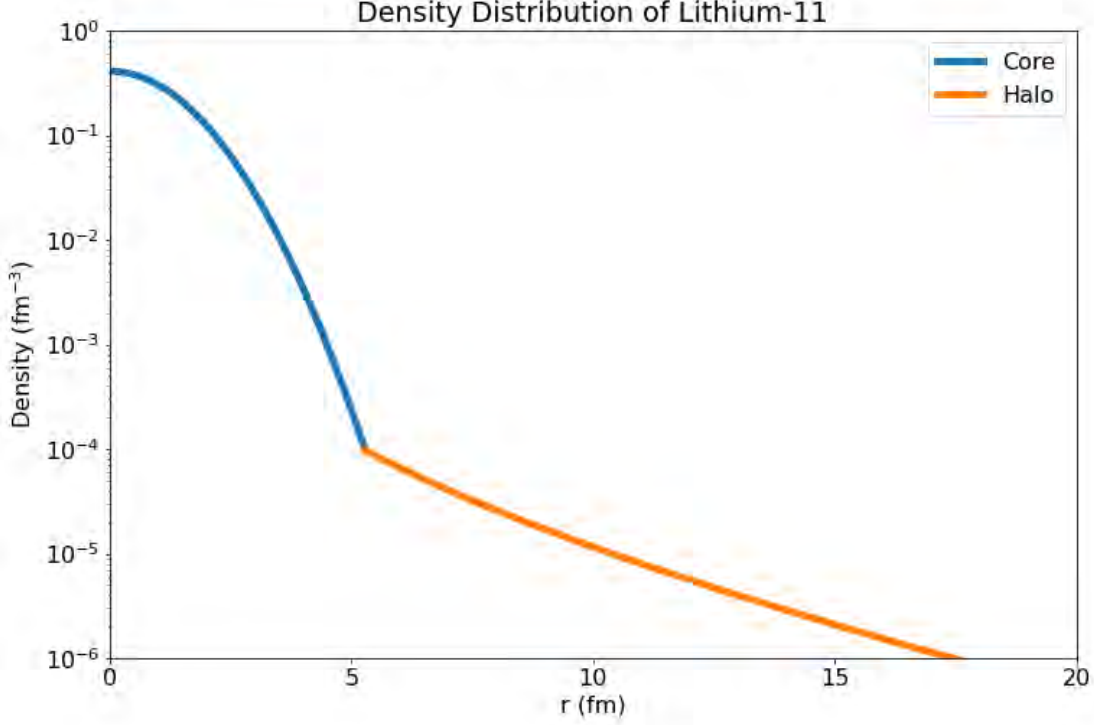


Figure 1.4 Density distribution of ^{11}Li . The density distribution of ^{11}Li is shown using matter density equations from Reference [9] and results from Reference [10]. The distribution is split into regions shown by two colors. The blue region represents the core of the nucleus with a Gaussian shape. The orange region represents the region beyond the compact core with a Yukawa-square tail. At a large distance from the core the extended tail distribution can be seen, which is a property of halo nuclei.

of halo nuclei where \hbar is the Plank constant, κ determines the slope of the energy tail, and μ is the effective mass [10].

$$(\hbar\kappa)^2 = 2\mu E_s \quad (1.2)$$

When the separation energy decreases, the slope of the energy tail decreases. The smaller the slope, the longer the tail takes to decay, broadening the density distribution.

The momentum distribution, $f(p)$, is directly related to the density distribution. Equation 1.3, where C is a constant and p_i is the Cartesian component of the momentum, shows the relationship between the momentum distribution and the slope of the energy tail [10].

$$f(p) = \frac{C}{p_i^2 + \kappa^2} \quad (1.3)$$

The opposite relation between the width and the slope is seen for momentum compared to density. For the momentum distribution the smaller the slope of the energy tail, the smaller the width of the distribution. This supports the reciprocal relation claim which states, when the distribution in coordinate space is wide, that in momentum space is narrow [10]. In Equation 1.3, if p_i increases then $f(p)$ decreases. Meaning an observed narrow momentum distribution of the last nucleon indicates an extended density distribution tail, supporting the existence of a halo structure. The transverse momentum distribution for ^{11}Li is shown in Figure 1.5. The momentum distributions of stable or close to stable nuclei can be hundreds of MeV/c. The ^{11}Li distribution is narrow, 20 MeV/c, indicating an extended tail in the density distribution.

Nucleons are able to tunnel out of the nuclear core into a region beyond the core volume due to the weak binding of the valence nucleons and the strong, short-range nuclear force. [11]. The strength and range of the force determines the height and thickness of the potential barrier. For a particle to tunnel through the barrier, the barrier must be a finite height and be relatively thin. The mean field of the core nucleons in the nucleus can be related to a square well potential. In a one dimension square well, states that have an eigen-energies slightly below the well's surface potential have a probability distribution with a tail that slowly decays and extends beyond the range of the well potential, depending on the state the tail can extend far beyond the range of the well. Comparing the square well to a halo nucleus, the valence nucleons have energies slightly below the core nucleus potential. The valence nucleons can have a probability density beyond the range of the core potential, extending the nucleon distribution.

Halo nuclei must overcome the centrifugal barrier. The centrifugal potential, U_{cf} , is proportional to the expression shown in Equation 1.4 [10].

$$U_{cf} \propto \frac{l(l+1)}{r^2} \quad (1.4)$$

The magnitude of the centrifugal barrier is directly dependent on the orbital angular momentum of the halo nucleon, l . This expression shows the most favorable case for halo formation,

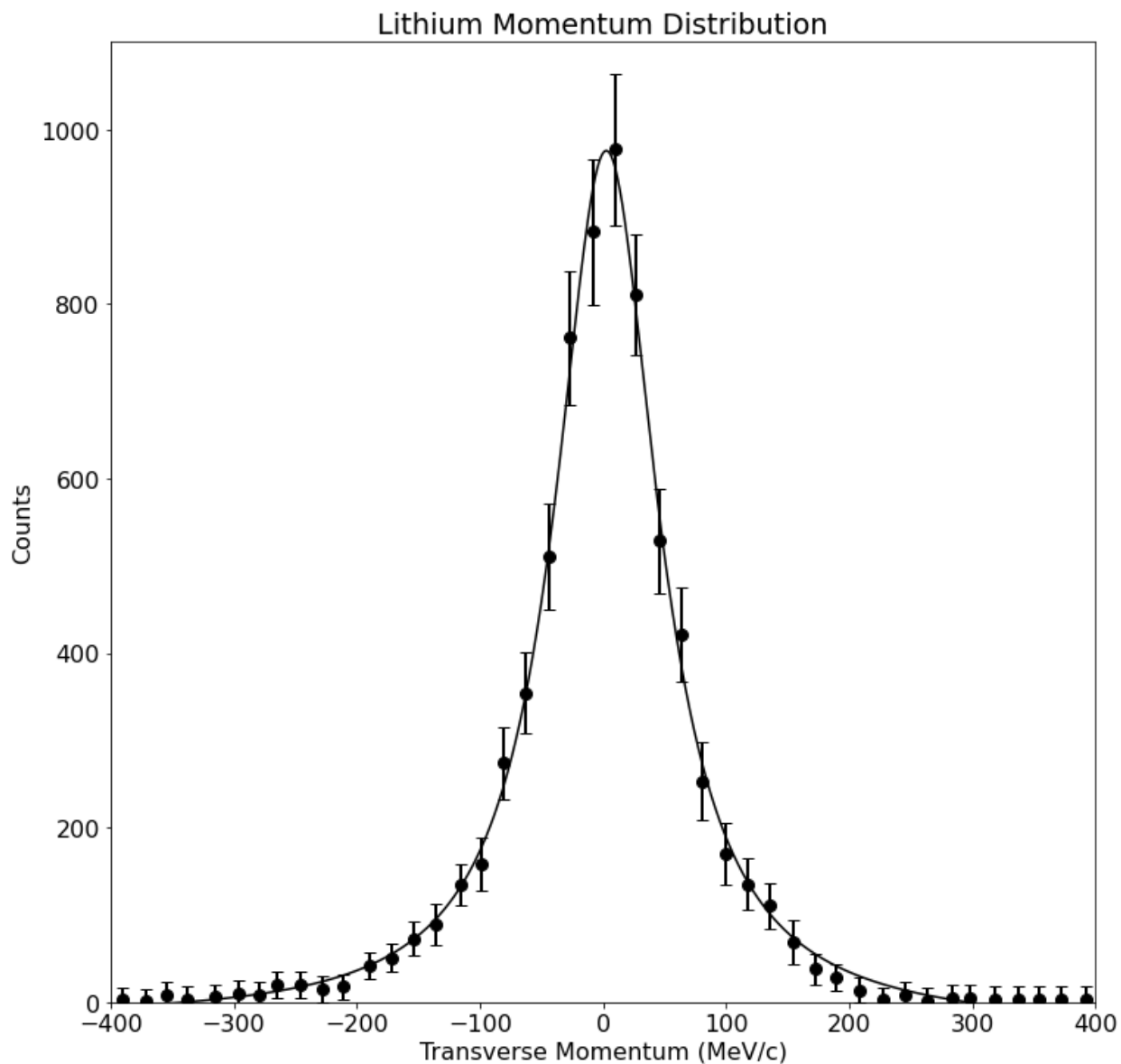


Figure 1.5 Momentum distribution of ^{11}Li . The transverse momentum distribution of ^{11}Li is shown. The ^{11}Li data is taken and figure reproduced from Reference [10]. The Li distribution was obtained from a ^9Li fragment from the reaction of ^{11}Li and a carbon target. The distribution shows a narrow peak compared to a momentum distribution of a stable or close to stable nuclei, which is a property of halo nuclei.

when the barrier is the lowest, is when the valence nucleon is in an s orbital, where $l = 0$. The higher orbital the valence nucleon is in, the larger potential barrier the nucleon must overcome to have an extended distribution. The centrifugal barrier with spin examples is discussed in the large spin sub-section of the arguments for Aluminum-22 and 23 section.

After the discovery of the ^{11}Li halo structure, more isotopes were considered to have similar structure and were consequently studied and measured. Searching along the neutron dripline known and suspected 1-neutron halos include ^{11}Be [12], ^{15}C [13], ^{19}C [14], and ^{23}O [15]. Possible 2-neutron halos include ^6He [16], ^{14}Be [17], and ^{17}B [18]. Candidates that could be either neutron halos or have a "skin" phenomena include ^{19}B [19] and ^{22}C [20]. A neutron skin phenomena is similar to a halo but is defined as a less extreme extended distribution, conceptually as protons and core neutrons in a tight core with the neutron distribution extending beyond the proton distribution. On the proton side, possible proton halos include ^8B , ^{17}Ne [21], ^{27}S [22], ^{26}P [22], ^{22}Al , and ^{23}Al . Figure 1.6 highlights the halo candidates across a selected light mass region of the nuclear chart. The nuclei listed here and in the figure are all nuclei with a halo structure known or suspected to exist in the ground state of the nucleus. Many more nuclei across the chart have suspected halo structure in their excited state such as ^{17}F [23] and ^{13}N [24]. This work will focus exclusively on the nuclear ground state. Visually it is seen there are many more neutron halos than proton halos. There are more nuclei accepted as neutron halos compared to the proton halo candidates due to debate over the feasibility of overcoming the coulomb barrier.

1.2 Proton Halos

Proton halos are an even rarer phenomena than a neutron halo due to the coulomb barrier. In addition, they are far from stability and have low production cross sections, making them hard to study. Figure 1.7 shows three different orbitals density distributions for both protons and neutrons. It can be seen that the proton distribution does not reach as far as the neutron distribution for the same orbital and separation energy. The Coulomb interaction at the core nucleons decreases the amplitude of the wave function for protons, limiting the

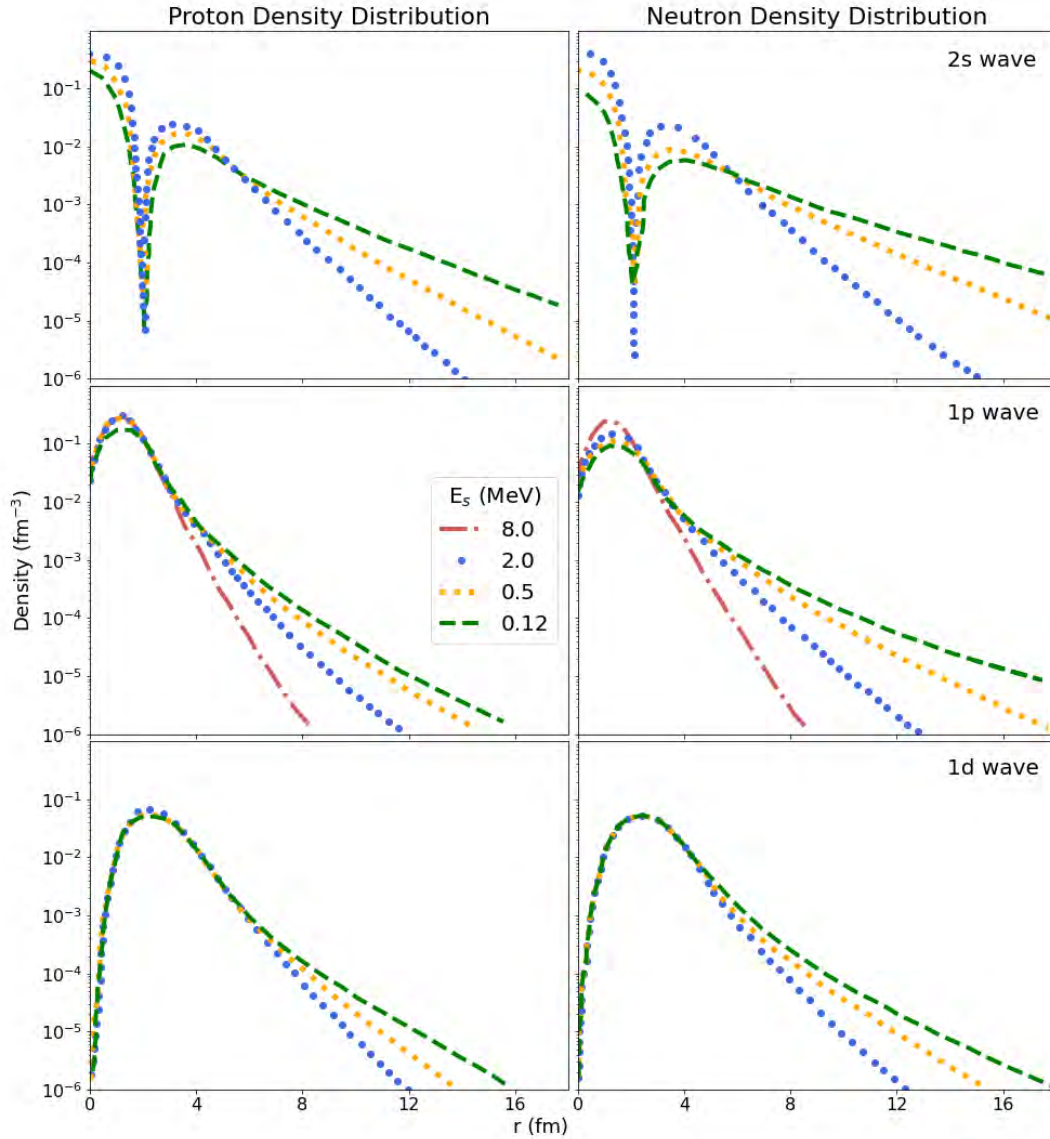


Figure 1.7 Proton and neutron density distributions for a variety of orbitals. The density distribution of a Woods-Saxon potential with $N=3$, $Z=4$ is shown from Reference [10]. The distributions show the effect of the Coulomb interaction and centrifugal potential. The proton density distributions are smaller than the neutron distributions due to the Coulomb interaction. The density distribution decreases for higher level orbitals due to the centrifugal barrier.

density distribution of protons compared to neutrons. Including the Coulomb potential in the wave function decreases the peak amplitude of the wave function and decreases the density distribution. The neutral charge of the neutron makes it favorable for halo formation. However, the Coulomb barrier could be overcome to create a proton halo in unique nuclei. As previously stated, the potential barrier must be both finite height and relatively thin for a particle to tunnel through. A repulsive barrier such as the Coulomb barrier is finite if it decreases slower than r^{-2} [1] where r is the distance from the center of the nucleus. Assuming a Gaussian charge distribution, a Gaussian nuclear potential can be used to represent the Coulomb potential, U_c , of the valence proton for a two body system [1]. U_c is shown in Equation 1.5 where $Z_h e$ is the charge of the proton outside of the core nucleons and $Z_c e$ is the charge of the core nucleons.

$$U_c = Z_h Z_c e^2 \frac{1}{r} \quad (1.5)$$

Since the potential decreases slower than r^{-2} , the potential has a finite size. The thickness of the barrier varies with the depth of the potential and the separation energy [25]. The barrier can be thin enough to allow for tunneling given a unique combination of potential depth and small separation energy. An example of a situation where the proton distribution overcomes the Coulomb barrier is in ${}^8\text{B}$ [26]. The proton and neutron density distributions were obtained and it was found that the radius of the protons overcomes the Coulomb barrier when compared to the neutron distribution.

The first proton halo candidate studied was ${}^8\text{B}$. The ground-state spectroscopic quadrupole moment was measured using modified β -NMR and found it was a factor of two times greater than previous theoretical predictions [26]. The quadrupole moment gives insight to the radial and angular distributions of the valence protons. An unexpectedly large quadrupole moment indicates deviation from the predicted spatial distribution, possibly an enhanced nucleon distribution. The same work also studied the density distributions for both the protons and neutrons, and found the proton distribution is more extended, overcoming both the Coulomb and centrifugal barriers [26]. Both of these factors strongly support a proton

halo structure and helped to motivate more studies. The reaction and breakup cross sections at multiple energy and momentum distributions were obtained for ${}^8\text{B}$ [27] [28]. From these measurements the proton density distribution and the proton, neutron, and matter radii were determined. All results support the proton halo structure and it was later argued that ${}^8\text{B}$ does have a proton halo structure and should be accepted as a halo nuclei. An extended proton distribution cannot extend to the same extent as an extended neutron distribution due to the Coulomb potential decreasing the amplitude of the wave-function. This less extended distribution can be used as an argument that no proton halos can exist and that they are not as big as neutron halos. Theory work has shown that ${}^8\text{B}$ can have features such as a large quadrupole moment without displaying a halo structure [29]. The argument for ${}^8\text{B}$ will be strengthened by a direct measurement of the charge radius [30]. The ${}^8\text{B}$ charge radius is a model-independent observable that directly addresses the proton distribution.

With a proton halo structure highly supported, although there are opposing opinions, in ${}^8\text{B}$ an effort was started to identify other isotopes that have a proton halo structure. ${}^{17}\text{Ne}$ is supported to be a two proton halo with some disputing arguments [31]. ${}^{17}\text{Ne}$ is referred to as a "second tier" or "modest" proton halo, meaning the halo phenomena is very small compared to other halo nuclei [32]. With a smaller proton distribution for a suspected halo candidate there are arguments that it is not extended enough to be a halo nuclei. The decision to accept ${}^{17}\text{Ne}$ as a halo nuclei or not is dependent on the definition an individual or journal is using to define the unique halo phenomena. Moving along the proton dripline, ${}^{22}\text{Al}$ and ${}^{23}\text{Al}$ lie on the proton dripline and their ground states have been thought to display proton-halo or skin phenomena. ${}^{26,27}\text{P}$ and ${}^{27}\text{S}$ are considered optimal cases for proton halo structure in theoretical models due to their low nucleon separation energy and valance nucleons occupying low l orbitals [33], however experimental data needs to be collected to support these models. Pushing to higher mass, even for nuclei where an extended proton distribution would not be expected, a variety of nuclei can be found that have theory arguments for halo phenomena. One example is ${}^{31}\text{Cl}$ studied with relativistic

mean-field theory [34]. However, these higher mass candidates need more studies to make a definitive statement on the extent of their proton distribution. Looking at Equation 1.2, if the mass of the system increases, the slope of the density tail increases, reducing the density distribution. Looking at Equation 1.5, the higher the charge of the system, the larger the Coulomb potential barrier. Higher mass nuclei have more protons in their core, resulting in a higher charge. Additionally, the dripline nuclei of heavy mass isotopic chains are less known and harder to produce for high precision studies.

Compared to the neutron dripline the location of the proton dripline is more well known. Coulomb repulsion causes neutron-deficient nuclei to be unstable, allowing proton dripline nuclei to be studied through spontaneous proton emission [35]. For neutron-rich nuclei, the neutron-binding energy slowly decreases as more neutrons are added to the system, making the neutron dripline nuclei hard to study. The ability to study proton dripline nuclei through spontaneous proton emission increases the knowledge of the dripline nuclei, further studying the nuclei gives a greater insight to nuclear forces. This is one of the reasons an increased effort has been made to study the unique structure of proton dripline nuclei. Looking specifically for halo phenomena two nuclei with studies and arguments supporting a halo phenomena are ^{22}Al and ^{23}Al . They have multiple theoretical and experimental arguments for and against a largely extended proton distribution.

1.3 Arguments for Aluminum-22 and 23

Work was done to study both ^{22}Al and ^{23}Al to determine the structure of their nuclei. Results from studying the nuclei resulted in both supporting and nonsupporting arguments about the formation of proton halos, but no one study was strong enough alone to directly address the proton distribution. This section will outline some of the arguments regarding the possible halo structure.

1.3.1 Small Proton Separation Energy

The first precision mass measurement of proton dripline nucleus, ^{22}Al , was performed at the Low Energy Beam Ion Trap (LEBIT) facility at the Facility for Rare Isotope Beams

(FRIB) with a 9.4 T Penning trap mass spectrometer [4]. The proton separation energy was measured to be 100.4(8) keV which is exceptionally small, supporting the existence of a proton halo structure. The measurement was then compared with USD Hamiltonians and a particle-plus-rotor model. The comparison of the two models are contradicting. The USD Hamiltonians predict minimal $1s_{1/2}$ occupation in the proton shell in a deformed ^{22}Al ground state. Using the particle-plus-rotor model in the continuum the model supports proton halo formation with a large quadruple deformation [4]. The measurement extends the argument of possible proton halo structure but emphasizes a need for a measurement that can directly address the possible halo structure.

The systematic trend in the mass region was studied to determine the small proton separation energy in ^{22}Al and ^{23}Al [3]. The LEBIT precision mass measurement value agrees with the observed proton separation for ^{22}Al . For ^{23}Al the proton separation energy is 140.9 keV which is small and would support proton halo formation.

1.3.2 Enhancement of Reaction Cross Section

The first observed halo structure nuclei were originally indicated to be unique due to the enhanced reaction cross section. The reaction cross sections of $^{23-28}\text{Al}$ were measured with a Carbon target [2]. An increase in reaction cross section was observed for ^{23}Al when compared to $^{24-28}\text{Al}$. The measured reaction cross sections from Reference [2] are shown in Figure 1.8. Combining the large reaction cross section with the known small proton separation energy suggests that ^{23}Al is a proton halo. However, the measurement of the reaction cross section has large uncertainty and these parameters alone are not enough to decisively say ^{23}Al is a proton halo. Within one sigma of error, ^{23}Al could have the same size reaction cross section as ^{24}Al which would not support a halo structure in ^{23}Al . It can be argued that the trend moving towards ^{22}Al would continue to increase and ^{22}Al would have an even larger reaction cross section. Without a measured value, this increasing trend cannot be confirmed or used as an argument towards the possible halo structure in ^{22}Al .

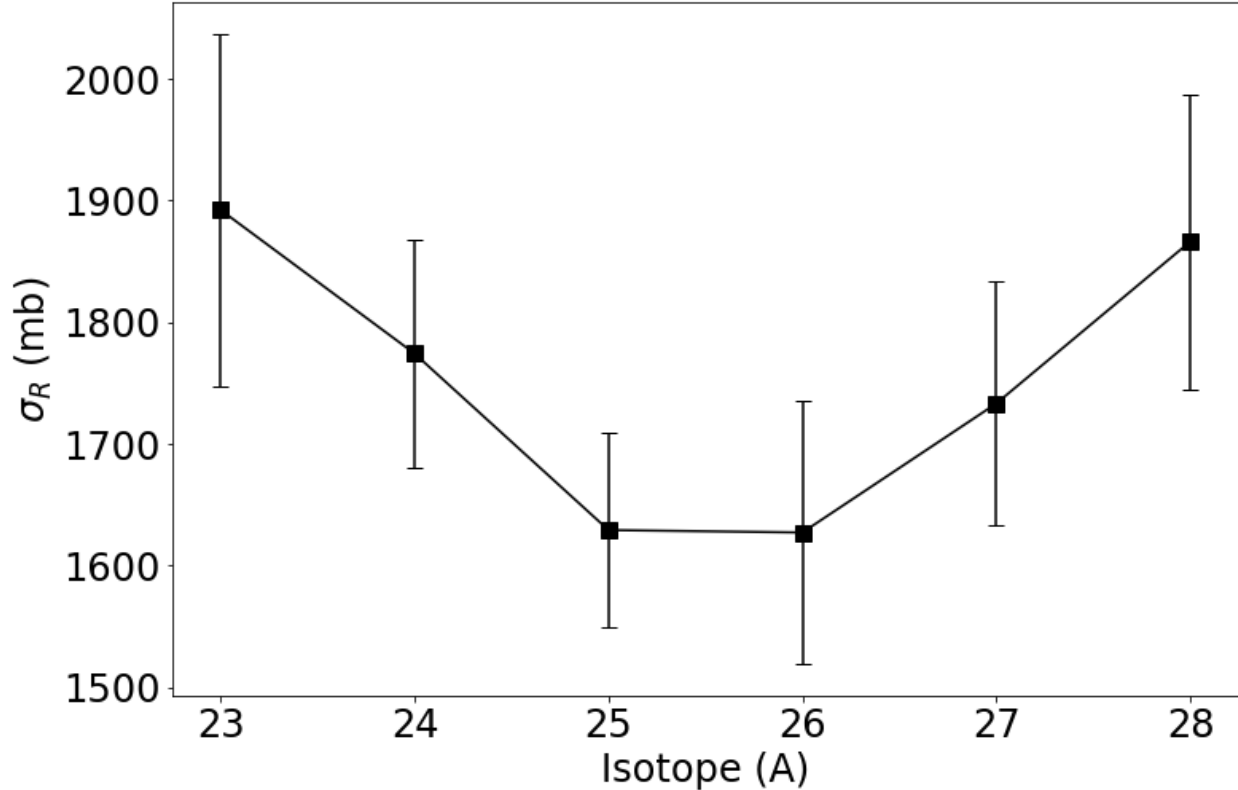


Figure 1.8 Aluminum isotopes reaction cross sections. The measured reaction cross sections, σ_R , are plotted as a function of mass number for the measured Al isotope chain. The data is taken and figure reproduced from Reference [2]. An increase in reaction cross section can be seen moving towards $^{22-23}\text{Al}$ but, with a large uncertainty.

1.3.3 Quadrupole Deformation

The quadrupole deformation parameter, β_2 , was calculated for ^{23}Al to be 0.391 from the axially deformed relativistic mean field formalism [5]. The calculation indicates ^{23}Al has a very large quadrupole deformation. A large deformation could indicate a single proton halo with a ^{22}Mg core. In addition to the deformation ^{23}Al differs in its two outer most orbitals compared to ^{27}Al . In ^{27}Al the energy levels of the outermost nucleons are close to the inner nucleon energy levels and show a small area of distribution. While in ^{23}Al the $2s_{1/2}$ and $1d_{5/2}$ outer most protons have much different energy levels compared to the inner nucleons and show an extended area of existence [5]. This supports a larger proton distribution and possible halo structure when comparing to ^{27}Al . However, the quadrupole moment has not yet been experimentally measured and the quadrupole deformation value relies on theoretical

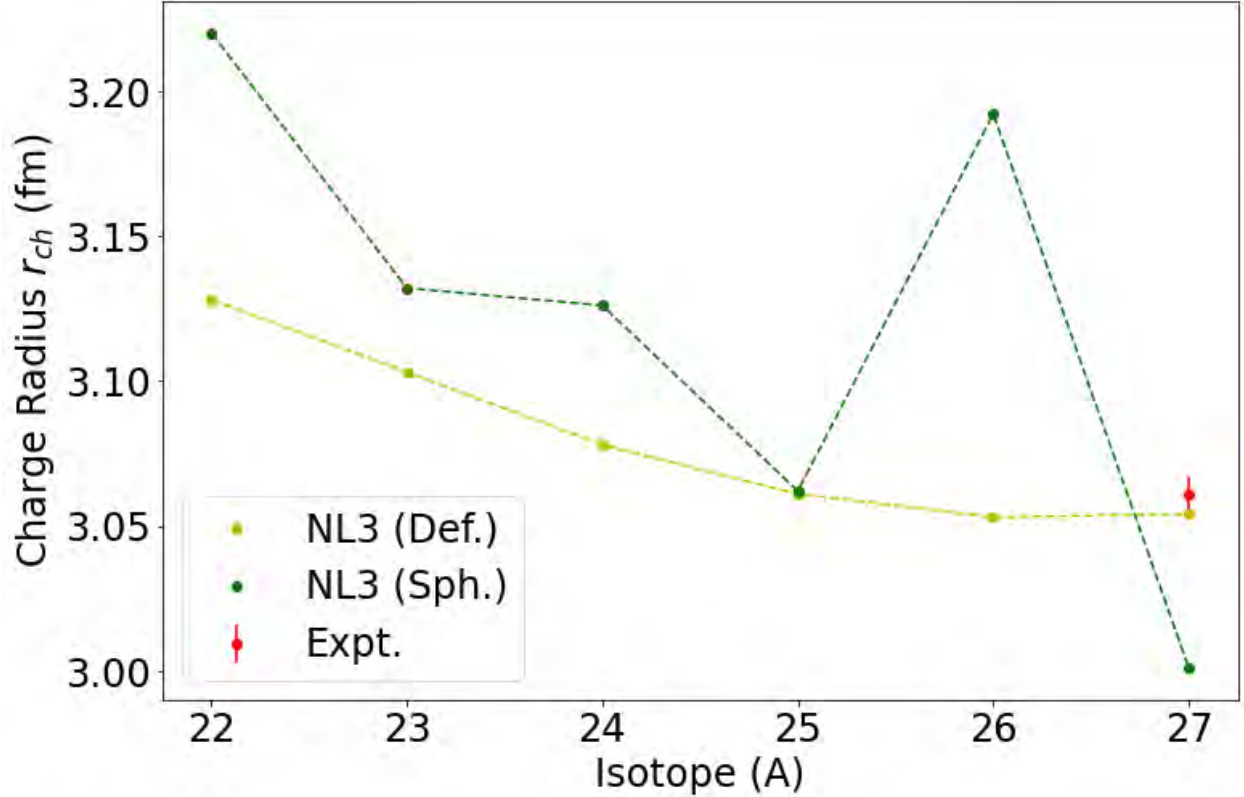


Figure 1.9 Charge radius predictions for $^{22-27}\text{Al}$. The RMF calculations from Reference [5] are plotted for $^{22-27}\text{Al}$ for both spherical (Sph.) and deformed (Def.) densities as a function of A . The experimental (Expt.) value for ^{27}Al is also included for comparison.

calculations and assumptions within those calculations. Experimental results to confirm and benchmark these calculations are needed to make a definitive statement on the structure of ^{22}Al and ^{23}Al .

1.3.4 Increasing Radial Extent

The relativistic mean field (RMF) theory was used to study many properties of both possible and known proton halo nuclei. Calculations from RMF formalisms using both deformed and spherical density solutions were used to calculate the charge radius, r_{ch} , of the entire Aluminum isotope chain [5]. The results of their calculations for $^{22-27}\text{Al}$ are plotted in Figure 1.9 along with the experimental charge radius for ^{27}Al . The NL3 parameter set was used in the calculations for both the spherical and deformed densities [36]. A large increase in charge radius for ^{22}Al is seen in the spherical density calculation. The spherical density calculation varies from the experimental value for ^{27}Al and is considered to be unreliable

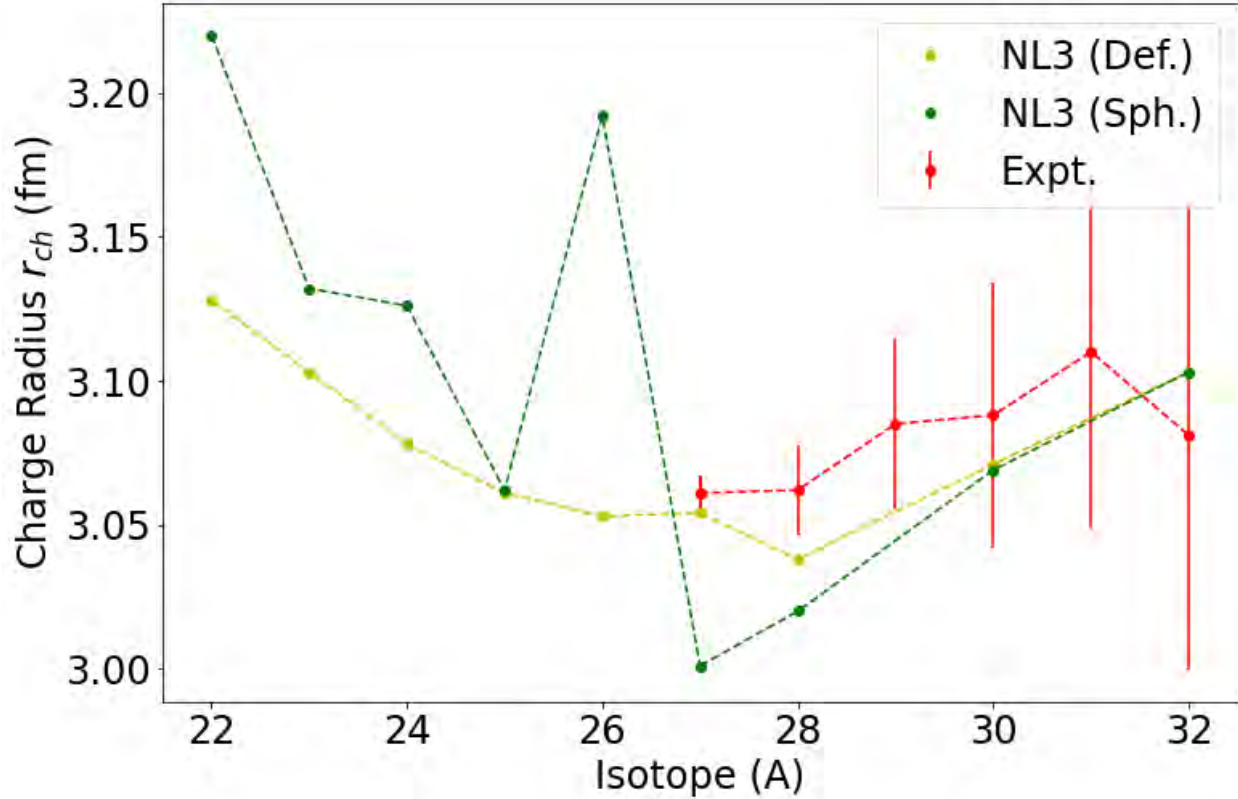


Figure 1.10 Charge radius predictions for $^{22-27}\text{Al}$ shown with literature values for $^{27-32}\text{Al}$. The RMF calculations from Reference [5] are plotted for $^{22-28, 30, 32}\text{Al}$ for both spherical (Sph.) and deformed (Def.) densities as a function of A . The experimental (Expt.) data from Reference [37] is converted to charge radius and plotted to compare with theory values.

when extended towards ^{22}Al , which may lead to a large disagreement between the theory and a future ^{22}Al experimental value. For the deformation density calculation the theory value is in better agreement with the experimental value for ^{27}Al , when compared to the spherical density calculation. The deformed density calculation shows a continuous increase in charge radius moving towards ^{22}Al , supporting an enlarged proton distribution for both ^{22}Al and ^{23}Al , supporting the existence of a halo structure.

Moving towards the neutron rich isotopes, higher number of nucleons (A), only the even mass number (odd-odd) isotopes were calculated using this RMF calculation method. The full isotopic chain of Aluminum isotopes calculated using RMF in [5] is plotted in Figure 1.10. Looking at just theory values it can be seen that the neutron-deficient isotopes are

predicted to have a larger charge radius, supporting a proton halo structure. The increase of charge radius for neutron-deficient nuclei compared to neutron rich nuclei is more pronounced in the spherical density calculations. Following these theoretical calculations the neutron rich isotopes differential mean square charge radii were measured using collinear laser spectroscopy at the ISOLDE-CERN facility [37]. The charge radii results are plotted with the RMF calculations in Figure 1.10. It is important to note that the experimental charge radius values are from the differential mean square charge radius and the plotted experimental charge radii values are dependent on the stable ^{27}Al charge radius which was used as the reference to deduce the absolute charge radii of radioactive $^{28-32}\text{Al}$ isotopes. Comparing these literature values to the theoretical calculations, there is a general trend of the experimental values being larger, although both the ^{30}Al and ^{32}Al calculations are within error of the literature values. Comparing the theory predictions for the neutron-deficient nuclei to the literature values for the neutron rich nuclei, both ^{22}Al and ^{23}Al are predicted to be large in comparison. These RMF calculations indicate a large possibility of an extended proton distribution for neutron-deficient Aluminum isotopes, motivating a need for experimental data to confirm the trend.

1.3.5 Large Spin

The spin of ^{23}Al is $5/2^+$ [38] and the spin of ^{22}Al is known to be large, suggested by experiments to be 4^+ , including β decay [39]. A halo structure in ^{22}Al would most likely consist of a ^{21}Mg core with a valence proton. For the valence proton coupled to the ground state of ^{21}Mg , which has spin $5/2^+$, the spin of ^{22}Al and its valence proton cannot be less than $3/2$. The conventional single-particle shell model indicates the valence proton would occupy the $1d_{5/2}$ orbital [40]. This orbital occupation does not support the existence of a proton halo, although it does result in the correct spin parity. The d orbital, $l = 2$, has a large centrifugal barrier compared to an s orbital. With the valence proton in a d orbital the formation of a proton halo is highly unlikely. For the valence proton to occupy the $2s_{1/2}$ orbital, the ^{21}Mg core would need to be in an excited state. For ^{22}Al to have a 4^+ ground

state spin with some $2s_{1/2}$ occupation, the ^{21}Mg core will need to be in a $7/2^+$ or $9/2^+$ state. The lowest energy level of ^{21}Mg that has the required spin is 3347 keV, leading to a 3447 keV separation energy for ^{22}Al [40] which is much larger than the experimentally measured 100.4 keV separation energy. This large proton separation energy makes the existence of a proton halo in this configuration unlikely. Although the spin and these configurations make a proton halo seem very unlikely, it is possible there is a small s -orbital component that would allow for proton halo formation. Small s -orbital components have been found in nuclei with similar properties including ^{17}B through analysis of the momentum distributions and cross sections [41]. The small occupation was explained in the work by deformed relativistic Hartree-Bogoliubov theory in continuum (DRHBc) [41]. In addition, different theoretical approaches can be used to model new detailed descriptions that support halo structure since ^{22}Al is largely effected by a variety of deformations, pairing correlations, and continuum effects that can be included and varied in each theoretical model [40].

1.3.6 Mirror Pair Comparison

In addition to the ground state possibly having an extended proton distribution, the excited states of Aluminum have been thought to display a largely enhanced proton distribution. The properties of beta decay from ^{22}Si to the low-lying states of ^{22}Al were measured through beta delayed one proton emission on a silicon array with germanium detectors [42]. From observed properties of the one proton emission the ft reduced transition probabilities were determined. The data was then combined with data on the mirror nucleus ^{22}O to find a mirror asymmetry of 209(96)% for the 1^+ excited state in ^{22}Al . Shell-model calculations can reproduce the result with interaction related to the $s_{1/2}$ orbit and describes a loosely bound nuclei. This favors significant proton occupation in the $s_{1/2}$ orbit which may have an extended distribution, supporting a halo structure in the excited states of ^{22}Al [42]. The present work does not study the excited states, only the ground states of ^{22}Al and ^{23}Al . The results presented only confirm or deny the predictions of the halo phenomena in the ground state and the unique structure of the excited states of Al remain to be studied.

1.4 Need for Charge Radius Measurement

Combining the large reaction cross section, extended density distribution, small proton separation energy, and large quadrupole deformation parameter for ^{22}Al it can be argued that both ^{22}Al and ^{23}Al have a proton halo structure. However, the assumed large spin and large uncertainty in reaction cross section argue against the possible halo structure. Currently, no single argument can definitively state whether or not a halo structure is present which motivates a need for experimental data that directly addresses the proton distribution of the nuclei.

The charge radius of a nucleus is a property that can be measured experimentally and directly addresses the proton distribution. Laser spectroscopy can determine the differential mean square charge radius of rare isotopes. Until recently, laser spectroscopy could not be performed on the dripline and near dripline nuclei due to their low production rates. At the facility for rare isotope beams (FRIB) facility the production rate of ^{22}Al and ^{23}Al are high enough that combined with advancements to the spectroscopy technique at FRIB, laser spectroscopy could be performed on $^{22-25}\text{Al}$ to address the possible proton halo structure.

CHAPTER 2

HYPERFINE INTERACTION

2.1 Hyperfine Interaction

The hyperfine interaction is the interaction between the angular momenta of orbital electrons and electromagnetic moments of the nucleus. The hyperfine energy levels are characterized by the coupling of a nonzero nuclear spin, I , with the total electron angular momentum, J , where their sum is defined as $F = I + J$. The electronic fine structure energy levels are defined only by J . Allowed atomic transitions between hyperfine structure levels must have a difference of 0, 1, or -1 between their F values, $\Delta F = 0, \pm 1$. A schematic showing the allowed atomic transitions between hyperfine structure levels is shown in Figure 2.1. The shift of the hyperfine levels from the fine structure levels are given by a multipole expansion of the nuclear moments. The work outlined in this thesis is only sensitive to the first two terms arising from the nuclear magnetic dipole moment and electric quadrupole moment. However, the expansion can be taken to higher orders, which generally requires much higher sensitivity to detect in experiments. The equation for the change in energy from the fine energy levels to the hyperfine levels is shown in Equations 2.1 and 2.2 [43].

$$\Delta E_{HFS} = \Delta E_{dipole} + \Delta E_{quadrupole} + \Delta E_{octupole} + \dots \quad (2.1)$$

$$\begin{aligned} \Delta E_{HFS} = & \frac{A}{2}K + \frac{B}{4} \frac{\frac{3}{2}(K(K+1)) - 2IJ(I+1)(J+1)}{IJ(2I-1)(2J-1)} + \\ & \frac{5C}{4} \frac{K^3 + 4K^2 + \frac{4}{5}K(-3IJ(I+1)(J+1) + I(I+1) + J(J+1) + 3) - 4IJ(I+1)(J+1)}{IJ(I-1)(2I-1)(J-1)(2J-1)} + \dots \end{aligned} \quad (2.2)$$

In these equations A , B , and C are the hyperfine coefficients and $K = F(F+1) - J(J+1) - I(I+1)$. In this expression it can be seen that an energy level with $J = 0$ or $I = 0$ does not see a change in energy for the hyperfine energy levels from the fine structure levels. For an energy level with $J = \frac{1}{2}$ the transition is not sensitive to the electric quadrupole or higher moments. This is important to consider when choosing a transition to use for a laser spectroscopy experiment.

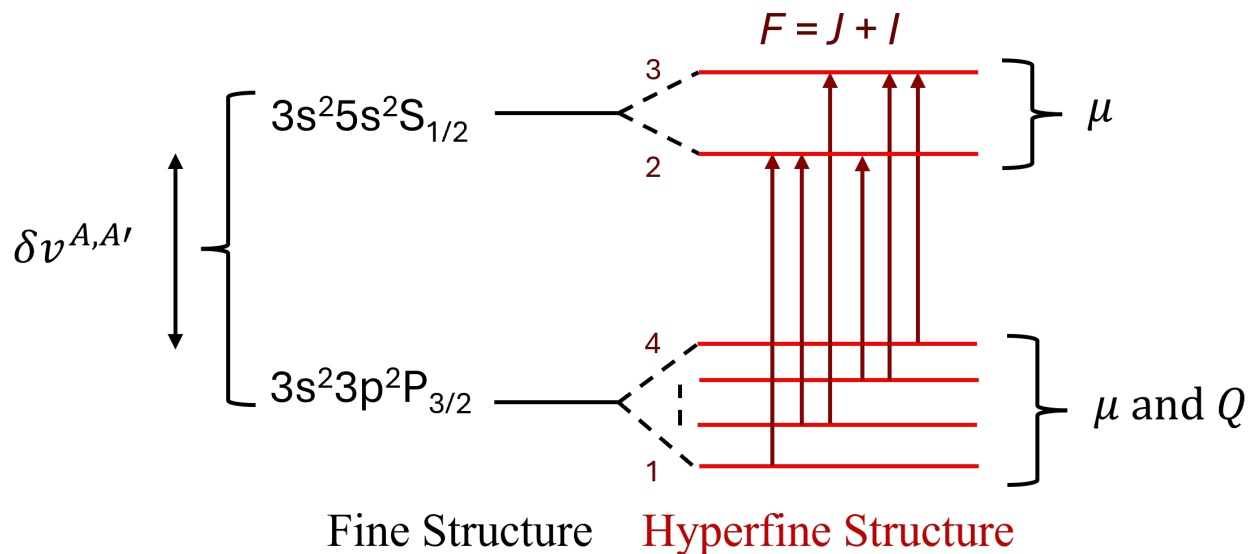


Figure 2.1 Atomic transition schematic. A schematic of an atomic transition is shown, the transition level splitting is not drawn to scale for clarity. For each fine structure level the hyperfine structure levels are shown, defined by F . The allowed transitions, defined by $\Delta F = 0, \pm 1$, are shown by dark red arrows. The isotope shift, $\delta v^{A,A'}$, is sensitive to the shift of fine structure levels between rare isotopes and the corresponding stable isotope. The magnetic dipole and electric quadrupole moments, μ and Q , are sensitive to the hyperfine energy level splittings.

A hyperfine spectra of allowed hyperfine transitions can be used to study the differential mean square charge radius, dipole moment, and quadrupole moment. The hyperfine spectra are measured by a frequency scan around the fine structure frequency, the details of the spectra and frequency scan are outlined in the Experimental Data chapter. The hyperfine spectra is fit using a pseudo-Voigt profile and the fitting details are outlined in the Analysis chapter. From the fit result, among other parameters, the centroid of the hyperfine spectrum and hyperfine coefficients are determined. These fit parameters can then be used to determine properties of the isotope being studied.

2.2 Hyperfine Structure

2.2.1 Magnetic and Quadrupole Moment

The magnetic dipole moment, μ , gives insight into the configuration of the nucleons, spin, and angular momentum. The magnetic moment is produced by the intrinsic spin of

the protons and neutrons along with the orbital angular momentum of the protons. The magnetic moment can be found at the one-body level in the z direction in coordinate space using Equation 2.3 [44].

$$\mu_{1B} = \mu_N \sum_i (g_i^l l_{i,z} + g_i^s \sigma_{i,z}) \quad (2.3)$$

The sum is taken over the number of nucleons, g_i^l is the orbital g -factor, g_i^s is the spin g -factor, $l_{i,z}$ is the z component of the orbital angular momentum operator, and $\sigma_{i,z}$ is the z component of the spin operator [44]. The spectroscopic electric quadrupole moment, Q , gives insight into the charge distribution, deviation from spherical symmetry, and static deformation. The quadrupole moment is produced from the proton distribution in the nucleus. If $Q = 0$ the nucleus is spherical, if $Q < 0$ the nucleus is flattened along the axis of symmetry (oblate), and if $Q > 0$ the nucleus is stretched along the axis of symmetry (prolate). The quadrupole moment can be calculated from the E2 operator, $(E2)^{op}$, as shown in Equation 2.4 [45].

$$Q_s = \sqrt{\frac{16\pi}{5}} \langle \Psi | (E2)^{op} | \Psi \rangle_{M=J} \quad (2.4)$$

$$(E2)^{op} = \sum_{i,\tau_z} e_{\tau_z} r_{i,\tau_z}^2 Y^2(\hat{r}_i, \tau_z) e \quad (2.5)$$

The sum is taken over the number of protons and neutrons represented as τ_z , e_{τ_z} is the free-nucleon effective charges, $e_{p,n} = 1, 0$ or effective charges obtained from fitting available E2 data, and $Y^2(\hat{r}_i, \tau_z)$ is the spherical harmonic function and a component of the operator acting on the nucleons [46].

The magnetic dipole and electric quadrupole moment are determined from the hyperfine coefficients found from the shift of the atomic hyperfine energy levels. An energy level schematic showing the level splitting sensitive to the moments is shown in Figure 2.2 and 2.3. The energy shift of the hyperfine structure is the relative shift between the atomic hyperfine level and the unperturbed fine structure level [43]. For this work the energy shift equation, Equation 2.1, is reduced to the sum of the nuclear magnetic dipole and electric quadrupole moments since this work is not sensitive to higher moments than the electric

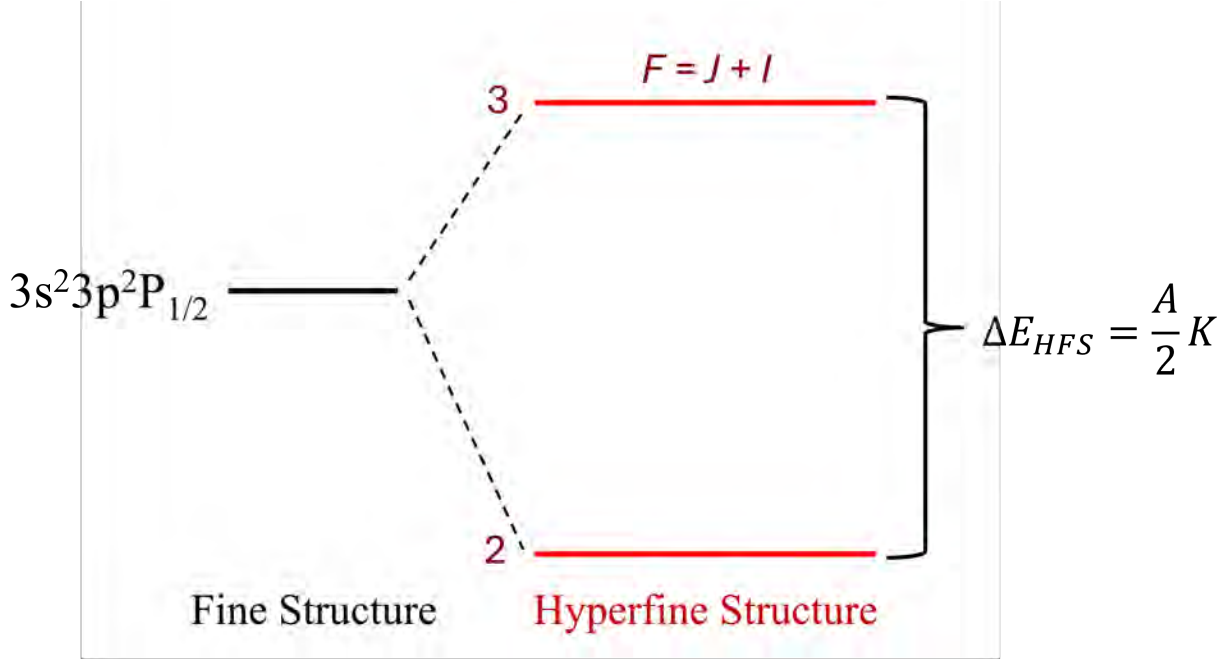


Figure 2.2 Energy level schematic showing splitting proportional to μ . The hyperfine energy levels are shown for the $3s^2 3p^2 P_{1/2}$ fine energy level of ^{27}Al . The nuclear spin of ^{27}Al is $\frac{5}{2}$, $I = \frac{5}{2}$. The total electron angular momentum of the $3s^2 3p^2 P_{1/2}$ level is $\frac{1}{2}$, $J = \frac{1}{2}$. Resulting in two values for F , 2 and 3. The magnetic dipole perturbs the hyperfine energy levels. μ is derived from the hyperfine coefficient that is determined by the size of splitting of the hyperfine energy levels. This particular level is not sensitive to the quadrupole moment since $J = \frac{1}{2}$.

quadrupole moment. The simplified equation can be written as

$$\Delta E_{HFS} = \Delta E_{dipole} + \Delta E_{quadrupole} \quad (2.6)$$

2.2.2 A and B Hyperfine Coupling Constants

The magnetic dipole and electric quadrupole moments can be written in terms of the hyperfine coefficients A and B and the isotopes quantum numbers, as shown in Equation 2.7 simplified from Equation 2.2.

$$\Delta E_{HFS} = \frac{A}{2} K + \frac{B}{4} \frac{\frac{3}{2}(K(K+1)) - 2IJ(I+1)(J+1)}{IJ(2I-1)(2J-1)} \quad (2.7)$$

where A and B are the hyperfine coefficients, I , J , F , and K are defined the same as above. The measured hyperfine spectra gives a hyperfine energy shift that is used with the known quantum numbers to find A and B . The A hyperfine coefficient is defined by the nuclear

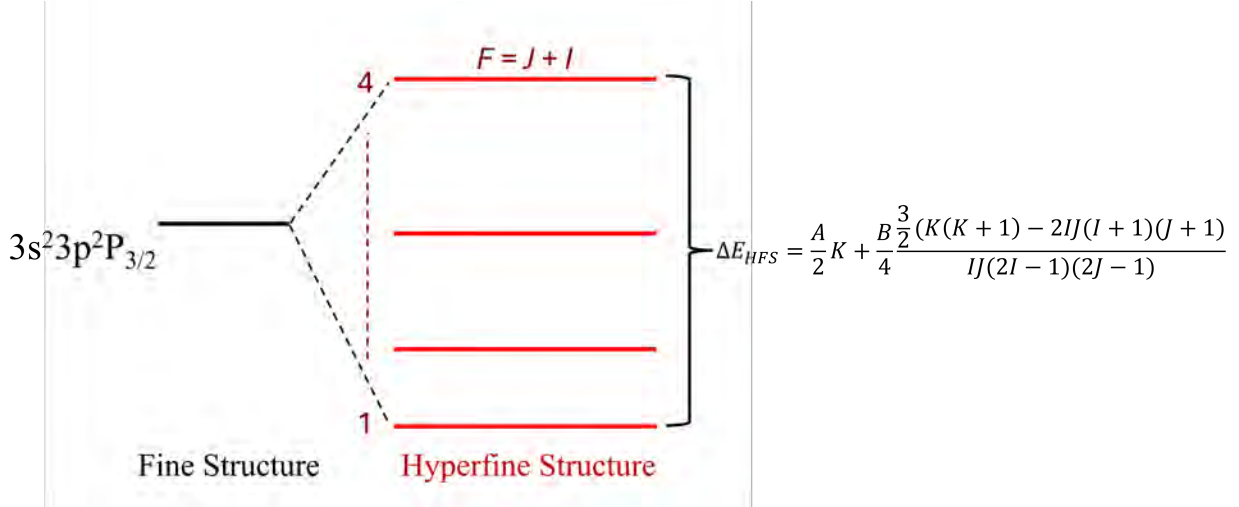


Figure 2.3 Energy level schematic showing splitting proportional to μ and Q . The hyperfine energy levels are shown for the $3s^2 3p^2 P_{3/2}$ fine energy level of ^{27}Al . The nuclear spin of ^{27}Al is $\frac{5}{2}$, $I = \frac{5}{2}$. The total electron angular momentum of the $3s^2 3p^2 P_{3/2}$ level is $\frac{3}{2}$, $J = \frac{3}{2}$. Resulting in four values for F , 1, 2, 3, and 4. The magnetic dipole and electric quadrupole moments perturb the hyperfine energy levels. Both moments are derived from hyperfine coefficients that are determined by the size of splitting of the hyperfine energy levels.

magnetic dipole moment, μ , magnetic field generated at the nuclear site due to the valence electrons, $B_e(0)$, I , and J as defined previously, shown in Equation 2.8 [43].

$$A = \frac{\mu B_e(0)}{IJ} \quad (2.8)$$

The B hyperfine coefficient is defined by the spectroscopic quadrupole moment, Q_s , time-averaged partial differential being the average electric field gradient generated by the electrons at the nucleus, $\langle \frac{\partial^2 V}{\partial z^2} \rangle$, and the fundamental electron constant, e , shown in Equation 2.9 [43].

$$B = eQ_s \langle \frac{\partial^2 V}{\partial z^2} \rangle \quad (2.9)$$

The hyperfine coefficients are found for each rare isotope studied and the stable reference isotope. Combining the hyperfine coefficients for the isotope and its corresponding stable isotope both the magnetic dipole and electric quadrupole moment can be determined, as long as the transition being studied has sensitivity. The A hyperfine coefficient is used to find the magnetic dipole moment. The ratio of an isotopes A with its corresponding stable isotopes

A' is equivalent to the ratio of their magnetic dipole moments and spin of the nucleus, as shown in Equation 2.10.

$$\frac{A}{A'} = \frac{\mu}{\mu'} \frac{I'}{I} \quad (2.10)$$

The A hyperfine coupling constant is sensitive to the magnetism distribution of a nucleus, seeing a difference in the hyperfine interaction between an assumption of a point-like distribution and actual distribution of magnetism. The ratio of A hyperfine coupling constants for given states between different isotopes can be assumed to be constant for a point like distribution. However, in precise measurements the ratio can be seen to deviate from the constant. This deviation due to the actual distribution of magnetism is referred to as the hyperfine anomaly, ${}^A\Delta^{A'}$, [47]. The hyperfine anomaly can be included in the ratio of A hyperfine coefficients as shown in Equation 2.11.

$$\frac{A}{A'} = \frac{\mu}{\mu'} \frac{I'}{I} (1 + {}^A\Delta^{A'}) \quad (2.11)$$

The value of ${}^A\Delta^{A'}$ is generally a magnitude of 10^{-3} or less [48]. Laser spectroscopy measurements generally report hyperfine coefficients to a precision of 10^{-2} , including this work. This level of precision is outside the sensitivity of ${}^A\Delta^{A'}$ and very small relative to experimental uncertainties [43], therefore ${}^A\Delta^{A'}$ can be assumed to be zero. Solving the A ratio with ${}^A\Delta^{A'} = 0$ for the magnetic dipole moment of the isotope of interest results in Equation 2.12.

$$\mu = \frac{AI}{A'I'}\mu' \quad (2.12)$$

where $'$ indicates a variable for the stable isotope. The B hyperfine coefficient is used to find the electric quadrupole moment. The ratio of an isotopes B with its corresponding stable isotopes B' is equivalent to the ratio of their electric quarupole moments, as shown in Equation 2.13.

$$\frac{B}{B'} = \frac{Q}{Q'} \quad (2.13)$$

Solved for the electric quadrupole moment of the isotope of interest in Equation 2.14.

$$Q = \frac{BQ'}{B'} \quad (2.14)$$

The ratio of hyperfine coefficients give the moments of the isotope being studied, however, this method gives moments that are dependent on the corresponding stable isotopes moments. This method is dependent on previous knowledge of a stable reference isotope and includes the reference values uncertainty and are not independently determined. Theoretical calculations for the magnetic field and electric field gradient are required to extract the magnetic and quadrupole moment.

2.3 Isotope Shift of Hyperfine Spectra

The isotope shift, $\delta v^{A,A'}$, is the difference in the center frequency, centroid, of the hyperfine spectrum of the isotope of interest and the corresponding reference isotope. The centroid is the frequency of the atomic transition being studied and the fine structure levels. Typically the reference isotope is the stable isotope of the element of interest, but it can be radioactive. The absolute charge radius of the reference isotope must be known, stable or radioactive, to deduce the absolute charge radius of the elements of interest. For this work the reference isotope is the stable isotope of Aluminum, ^{27}Al . An energy level schematic showing the shift of fine structure levels is shown in Figure 2.4.

The centroid value is extracted from the hyperfine spectra through fitting the center of each peak in the spectrum. The details of the fitting procedure are detailed in the Analysis chapter. Equation 5.1 details the relation between each peak center location and the centroid. Once the centroid values are obtained, the difference between the isotope's centroid value and the reference isotope can be taken to find the isotope shift, as shown in Equation 2.15.

$$\delta v^{A,A'} = \text{centroid}_{\text{isotope}} - \text{centroid}_{\text{reference}} \quad (2.15)$$

The differential mean square charge radius, $\delta \langle r^2 \rangle^{A,A'}$, is determined by combining the measured isotope shift with atomic factors calculated theoretically or determined using a King plot analysis [49].

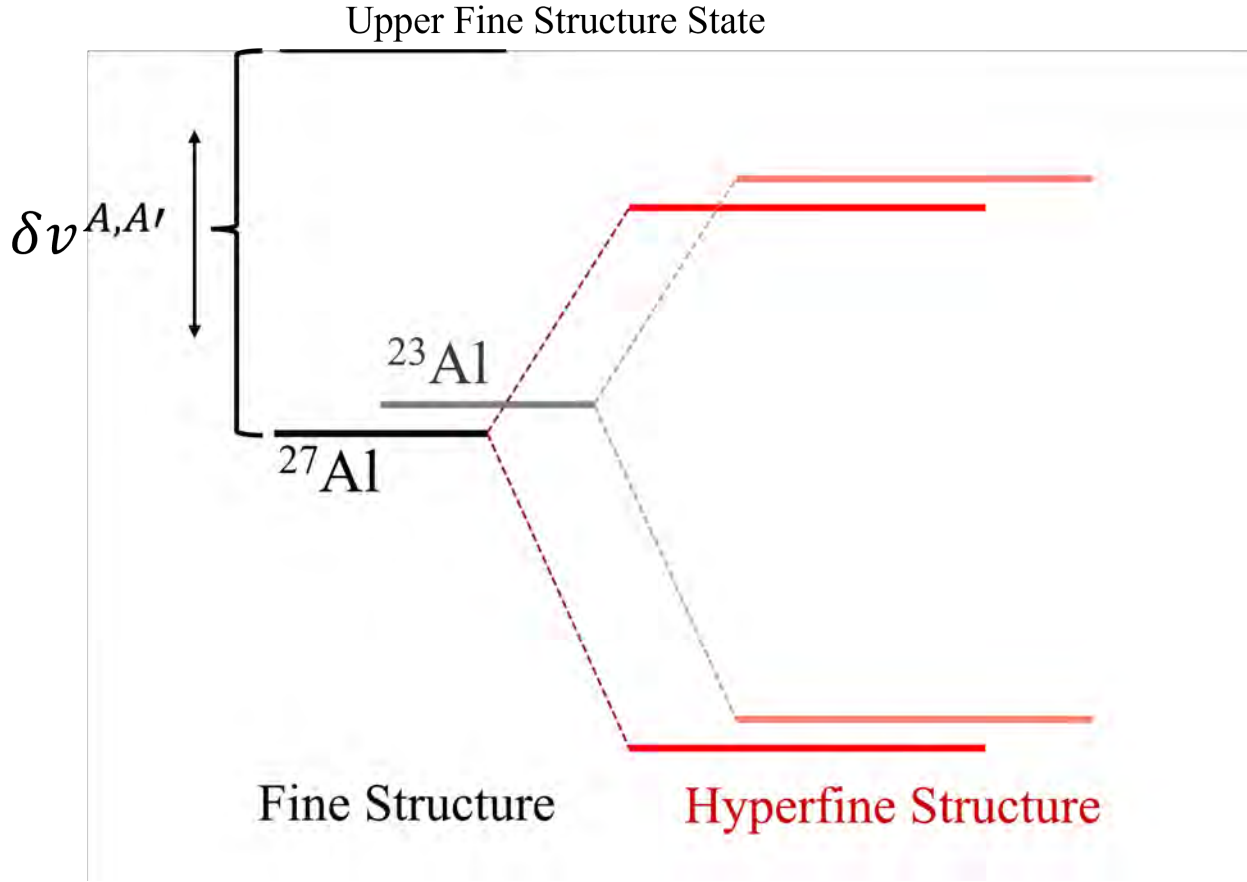


Figure 2.4 Energy level schematic showing isotope shift. The fine and hyperfine energy levels are shown for the $3s^23p^2P_{1/2}$ fine energy level of ^{27}Al and ^{23}Al . The charge radius is sensitive to the shift of fine structure transitions between rare isotopes and the corresponding stable isotope. The fine structure energy levels are sensitive to nuclear size and their shift gives information about relative size between nuclei. In this example the isotope shift between ^{27}Al and ^{23}Al is highlighted, note the isotope shift value is not drawn to scale.

2.3.1 Differential Mean Square Charge Radius

The differential mean square charge radius gives insight into the charge distribution, static, and dynamic (vibration) deformation. A liquid drop model approach with a homogeneous distribution, assuming there is no spatial distinction between constituent nucleons, gives an equation for the mean square charge radius shown in Equation 2.16 [43].

$$\langle r^2 \rangle = \frac{3}{5} r_0^2 A^{\frac{2}{3}} \quad (2.16)$$

Where $r_0 \approx 1.2$ fm and A is the atomic mass. Details of the nuclear structure arising from interactions between protons and neutrons are shown by deviations from this equation.

Deviations from this equation can be accounted for by including deformation parameters, β_i , and expanding the equation. Equation 2.17 shows the expansion, in terms of the spherical harmonics, including parameters to represent a deformed distribution, where $\langle r^2 \rangle_0$ is the mean-square charge radius of the nucleus if it were spherical and β_i are the deformation parameters of order i [43].

$$\langle r^2 \rangle = \langle r^2 \rangle_0 \left(1 + \frac{5}{4\pi} \sum_{i=2}^{\infty} \langle \beta_i^2 \rangle \right) \quad (2.17)$$

The deformation parameters that need to be included to the liquid drop model to replicate experimental data give insight to the nucleus deformation.

The charge radius is a measurement of the proton distribution of a nucleus. The absolute charge radius of nuclei can be measured with techniques such as electron scattering [50]. The cross sections measured in electron scattering experiments can be used to determine the electric and magnetic form factors. The form factors are directly related to the charge density and fitting the form factors and charge density parameters to the cross-section data allows the root mean square radius to be extracted [50]. Electron scattering was used to find the charge radius of ^{27}Al [51] [52]. However, these techniques for absolute charge radii measurements work best for stable or long lived nuclei close to stability and cannot be applied to all nuclei out to the dripline. To measure the charge radius of nuclei for full isotopic chains, including the dripline nucleus, the change in nuclear charge radii relative to the well measured stable isotope can be determined. This determined difference in charge radii is the differential mean square charge radius, which can be found from a measured isotope shift.

2.3.2 Determination of the Differential Mean Square Charge Radius

An energy level schematic showing the level splitting sensitive to the charge radius is shown in Figure 2.4. The isotope shift is equal to the mass shift plus the field shift, as shown in Equation 2.18.

$$\delta v^{A,A'} = \delta v_{massshift}^{A,A'} + \delta v_{fieldshift}^{a,A'} \quad (2.18)$$

The isotope shift is a result of changes in nuclear mass and size of isotopes along an isotopic change [43]. The mass shift is a combination of the normal mass shift, NMS, which comes from the reduced mass and the specific mass shift, SMS, which comes from the correlation between the electrons. The mass shift accounts for the overall change of mass for each isotope and is equal to M_i times a combination of the rare isotope mass and stable ^{27}Al mass. The equation for mass shift is shown in Equation 2.19 where A and A' are the atomic masses of the stable and rare isotope respectively [43].

$$\delta v_{massshift}^{A,A'} = \delta v_{i,NMS}^{A,A'} + v_{i,SMS}^{A,A'} = M_i \frac{A - A'}{AA'} \quad (2.19)$$

The field shift is a combination of the change in differential mean square charge radius and an atomic electronic factor proportional to the change of the electronic charge density at the nucleus for the transition, i , being studied. The field shift accounts for any change in the spatial distribution of the nuclear charge [43]. Mathematically, the field shift is equal to F_i times the Seltzer moment, $\Lambda^{AA'}$, as shown in Equation 2.20, where $C_{1,2,3}$ are constants [43].

$$v_{fieldshift}^{a,A'} = F_i \Lambda^{AA'} \quad (2.20)$$

$$\Lambda^{AA'} = \delta \langle r^2 \rangle^{A,A'} + \left(\frac{C_2}{C_1}\right) \delta \langle r^4 \rangle^{A,A'} + \left(\frac{C_3}{C_1}\right) \delta \langle r^6 \rangle^{A,A'} + \dots \quad (2.21)$$

F_i is an atomic factor found from the dependence on the optical transition. $\Lambda^{AA'}$ represents the different moments of the nuclear charge distribution [53]. The contributions of terms higher than second order in $\Lambda^{AA'}$ are negligible in light mass measurements, such as Aluminum. Higher orders become important for heavier masses, for this work they can be set to zero resulting in a simplified equation for $\Lambda^{AA'}$ as shown in Equation 2.22.

$$\Lambda^{AA'} = \delta \langle r^2 \rangle^{A,A'} \quad (2.22)$$

Subbing in the simplified $\Lambda^{AA'}$ a simpler field shift equation can be found as shown in Equation 2.23.

$$v_{fieldshift}^{A,A'} = F_i \delta \langle r^2 \rangle^{A,A'} \quad (2.23)$$

$$\delta\langle r^2\rangle^{A,A'} = \delta\langle r^2\rangle^{A-A'} = \langle r^2\rangle^A - \langle r^2\rangle^{A'} \quad (2.24)$$

Combining the equations for the mass and field shift results in a relationship between the isotope shift and differential mean square charge radius, shown in Equation 2.25.

$$\delta v^{A,A'} = M_i \frac{A - A'}{AA'} + F_i \delta\langle r^2\rangle^{A,A'} \quad (2.25)$$

The atomic masses are known from literature values [4] [3] and the atomic factors are theoretically calculated. The isotope equation can be solved for the charge radius and rewritten as shown in Equation 2.26.

$$\delta\langle r^2\rangle^{A,A'} = \frac{1}{F_i} (\delta v^{A,A'} - M_i \frac{A - A'}{AA'}) \quad (2.26)$$

2.3.3 Atomic Theory Calculations

The atomic factors needed to determine the differential mean square charge radius were calculated by collaborator Leonid V. Skripnikov employing the relativistic coupled cluster method using the Direc-Coulomb Hamiltonian [54]. The method used incorporated quantum electrodynamics to handle high-order effects. Details of the calculation can be found in Reference [54]. The mass shift atomic factor was calculated to be $-0.7 \text{ GHz u} \pm 2.1$ and the field shift atomic factor was calculated to be $70.11 \text{ MHz/fm}^2 \pm 0.12$. Since the isotope shift values are so small, it leads to a very accurate theory calculation having a large uncertainty on the charge radius. Figure 2.5 shows the relative size of the isotope shift for each isotope. The data and line of best fit are plotted in blue and the centroid value is plotted as a vertical red dashed line. All of the spectra are centered at the centroid of ^{27}Al , making the difference in each centroid value on the plot the isotope shift. Although it is very small, the shift can be seen between each isotope.

2.3.4 King Plot Analysis

A King plot analysis is a method to combine well known charge radii measurements and isotope shifts to find the atomic factors. The charge radii values need to be precise and are taken either from literature values available from electron scattering [51] or combined analysis of electron scattering and μ -X ray measurements [55]. The linear relationship between

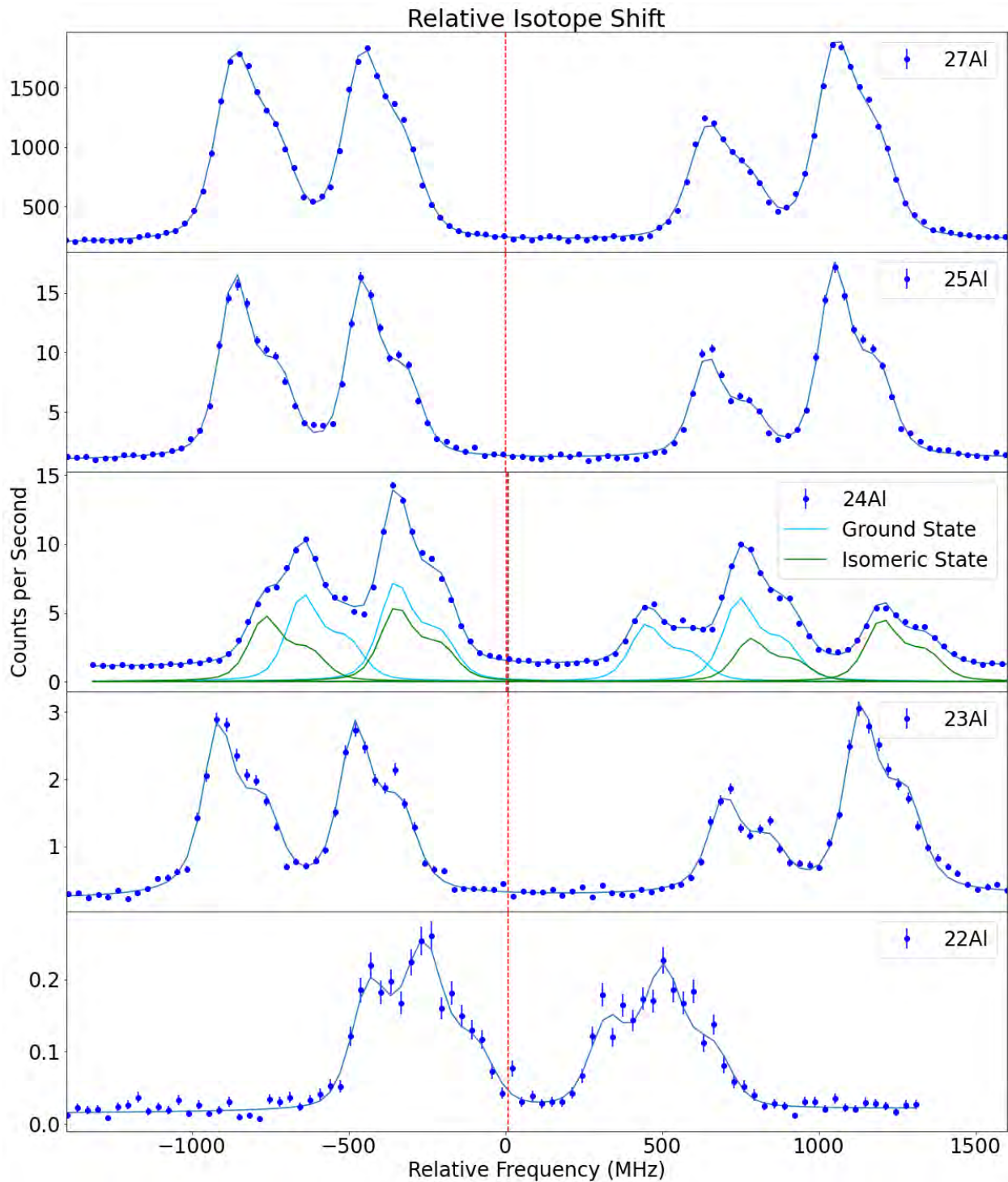


Figure 2.5 $^{22-25}\text{Al}$ and ^{27}Al hyperfine spectra. The blue points and solid blue line are the isotope's data and line of best fit using the CEC simulation fitting method. For ^{24}Al the light blue solid lines are the nuclear ground state peak components and the green solid lines are the nuclear isomeric state peak components. For each isotope the centroid value is plotted as a red vertical dashed line, the isomeric state in ^{24}Al is plotted as a dark red line. All spectra are centered at the centroid value of ^{27}Al .

the modified isotope shifts, $\frac{\delta v^{A,A'}}{\mu^{A,A'}}$, and the modified differential mean-squared charge radii, $\frac{\delta \langle r^2 \rangle^{A,A'}}{\mu^{A,A'}}$, is shown in Equation 2.27 [49].

$$\frac{\delta v^{A,A'}}{\mu^{A,A'}} = F_i \frac{\delta \langle r^2 \rangle^{A,A'}}{\mu^{A,A'}} + M_i \quad (2.27)$$

$$\mu^{A,A'} = \frac{m_A - m_{A'}}{(m_A + m_e)(m_{A'} + m_e)} \quad (2.28)$$

Where F_i is the field-shift atomic factor, M_i is the mass-shift atomic factor, m_A and $m_{A'}$ are the nuclear masses, and m_e is the electron mass. Using this linear relationship the modified isotope shifts can be plotted as a function of the modified differential mean-squared charge radii to determine F_i and M_i . If there are multiple stable isotopes for an element or long lived isotopes, this method is possible, at least three isotopes charge radii must be known. In some cases, such as Aluminum, only one or two isotopes radii are known and must rely on theoretical calculations for the atomic factors.

2.3.5 Relative Contribution of Mass and Field Shift to the Isotope Shift

Depending on the atomic masses and the transition being studied, the relative contribution of the mass and field shift will vary. At lighter masses the mass shift dominates but at higher masses the field shift dominates. A qualitative relative size of the field shift compared to the mass shift for different atomic numbers is shown in Figure 2.6. Equation 2.19 shows that the mass shift is dependent on M_i and the atomic masses of the isotope of interest and reference isotope. Substituting atomic masses across the nuclear chart for A and A' a quantitative effect on the contribution of the mass shift can be seen. Figure 2.7 shows the value of the atomic mass relationship, $\frac{A-A'}{AA'}$, as a function of A' . Through a small range of masses a decrease of value for the fraction is seen, when the range of masses is expanded a decay in the fraction's value is seen. For masses larger than 100 the atomic mass relationship becomes close to zero. An expansion of Figure 2.7 to higher masses is shown in Figure 2.8. This makes it easier to extract the charge radius at higher masses since the field shift component is the component that contains the charge radius. For light masses where the mass shift dominates, it makes the charge radius harder to extract. It also can be seen

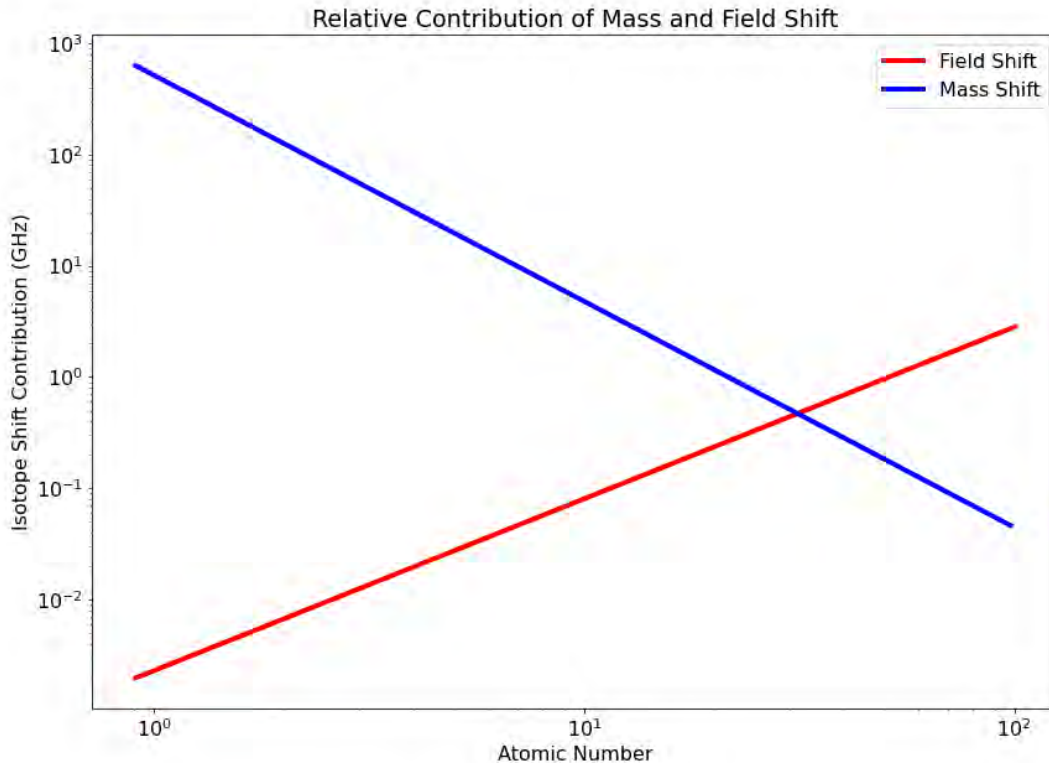


Figure 2.6 Relative mass and field shift contributions. The relative contribution of the mass and field shift is graphically shown from Reference [56]. As the atomic number increases the field shift component dominates relative to the mass shift.

that the relative contribution of the mass shift through an isotopic chain varies more for a lighter mass versus a heavier mass. To avoid mass shift dominated measurements transitions with a small M_i can be chosen. However, there is not always a transition with a small M_i that is possible to measure for a given element, making light mass nuclei harder to measure. When choosing a transition for an experiment, these factors are considered to find the largest relative field shift contribution.

2.4 Charge Radii Studies by Laser Spectroscopy

A general relation between the radius, r , and the number of nucleons, A , in a nucleus is made from the finding of scattering experiments, that the charge density of the nucleus is, in general, constant. Equation 2.29 where r_0 is a constant equal to approximately 1.2 fm,

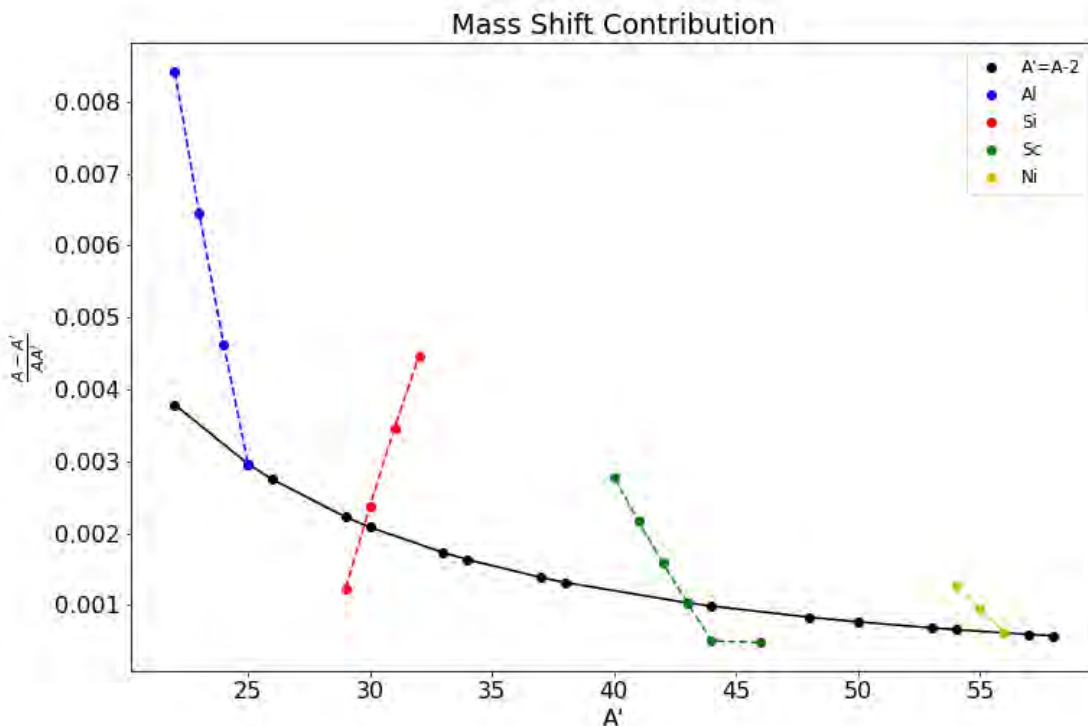


Figure 2.7 Mass shift contribution as a function of A . The atomic mass relationship from the mass shift equation, Equation 2.19, is plotted as a function of the rare isotope atomic mass, A' . The black points and solid line are the atomic mass relationship value of a selection of stable isotopes across the nuclear chart with the corresponding isotope that is two mass less. This shows a general trend of mass shift contribution depending on the atomic mass of each element, assuming M_i is the same. Each colored point represents an isotopic chain that has been measured at the BECOLA facility. The experimental results for Si, Sc, and Ni can be found in Reference [57], [58], and [59] respectively. Note, the Silicon isotopes measured were neutron rich unlike the other elements plotted, meaning $A' > A$ rather than $A' < A$. Since this comparison is focused on the overall relative scale, the absolute value was taken to plot Si with the other elements and demonstrate the relative size. The different elements show the variation of the mass shift contribution across an isotopic chain for different masses. Lighter masses have a larger mass shift contribution and more variation of the mass shift component across its isotopic chain.

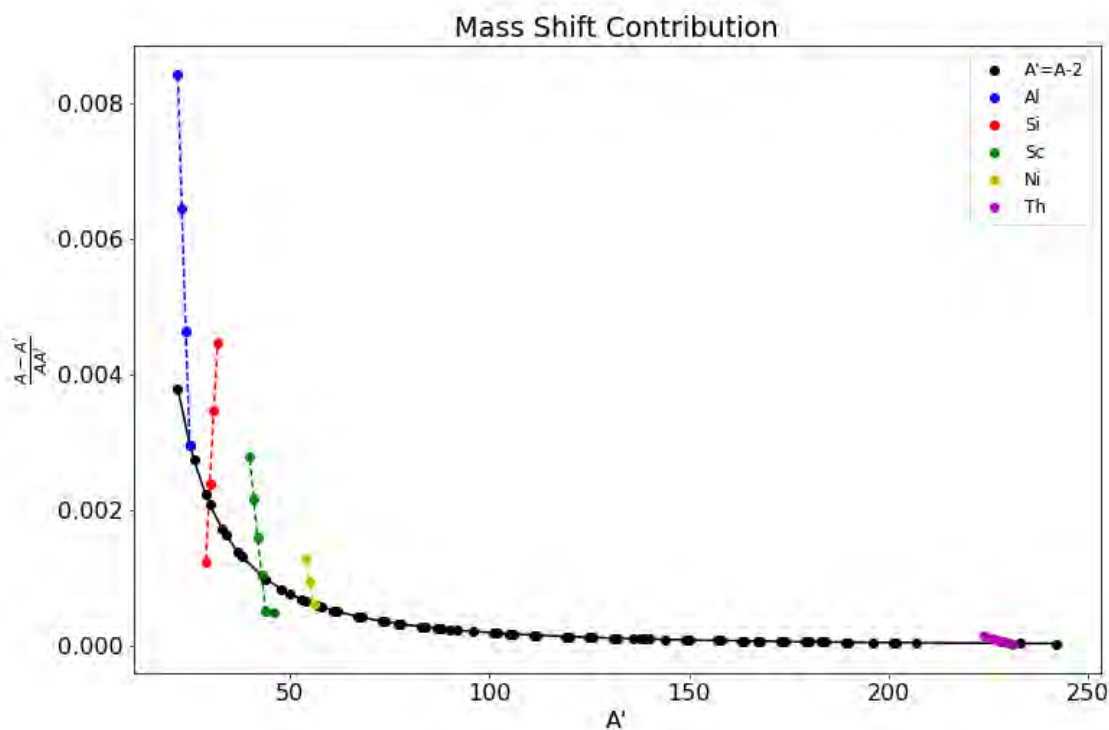


Figure 2.8 Mass shift contribution as a function of A expanded to higher masses. This figure expands on Figure 2.7 to higher masses. Expanding the plot to higher masses emphasizes the overall trend. Thorium is added as an isotopic chain that is in progress of being measured at BECOLA. The expanded plot shows that the trend starts to plateau to zero, showing how small of a contribution heavy mass nuclei can have from the mass shift.

shows this relation.

$$r = r_0 A^{1/3} \quad (2.29)$$

Using this relation as a general trend, approximations for the radius of nuclei can be made across the nuclear chart. Any deviation from the relation that is found experimentally provides insight into the structure of the nucleus and can reveal unique phenomena. Laser spectroscopy has been used to measure the differential mean square charge radii of nuclei all across the nuclear chart and test this general relationship.

In 1973 a new method of laser excitation of fast-moving atoms was published [60]. The method was being used for precision lifetime measurements. A few years later in 1976 the laser excitation method was applied to the hydrogen molecular ion HD^+ [61]. The work

studied partially resolved hyperfine structure and was utilizing doppler tuning and laser resonance. The following year, 1977, a work titled "Collinear Laser Spectroscopy on Fast Atomic Beams" was published [62]. Their work highlights an early spectroscopy experiment that reflects the collinear laser spectroscopy experiments performed today. In these and subsequent years more collinear laser spectroscopy publications were released including nuclear moments and mean-square radii results. One example is a work on Cs isotopes in 1978 [63] where the results include both the nuclear moments and mean-square radii in the results. The first spectroscopy experiments on radioactive nuclei were compiled into a single publication in 1988 [64]. Laser spectroscopy data collected since 1988 is scattered among refereed journals. Reference [65] contains a compiled list of refereed journals published and their results. Figure 2.9 shows all of the isotopes measured using optical spectroscopy experiments from Reference [65].

Laser spectroscopy measures atomic hyperfine structure of rare isotopes and stable reference isotopes. By comparing their centroid energy an isotope shift can be found and used to extract a differential mean square charge radius. The details of determining the differential mean square charge radius can be found in the determination of the differential mean square charge radius sub-section. This method of determining the differential mean square charge radius results in measurements of isotopic chains from stable to dripline, or as close to the dripline as possible, isotopes. Providing insight into the nuclear structure of rare isotopes far from stability. Through spectroscopy, nuclear structure theories and nuclear models have been tested. Examples include finding kinks in isotopic chains [66], studying bubble nuclei (recent BECOLA experiment on ^{34}Si), or as in this work, trying to identify possible halo candidates. The wide reach of laser spectroscopy to study the charge distribution of nuclei across the nuclear chart has made it a valuable asset to bench marking nuclear theory.

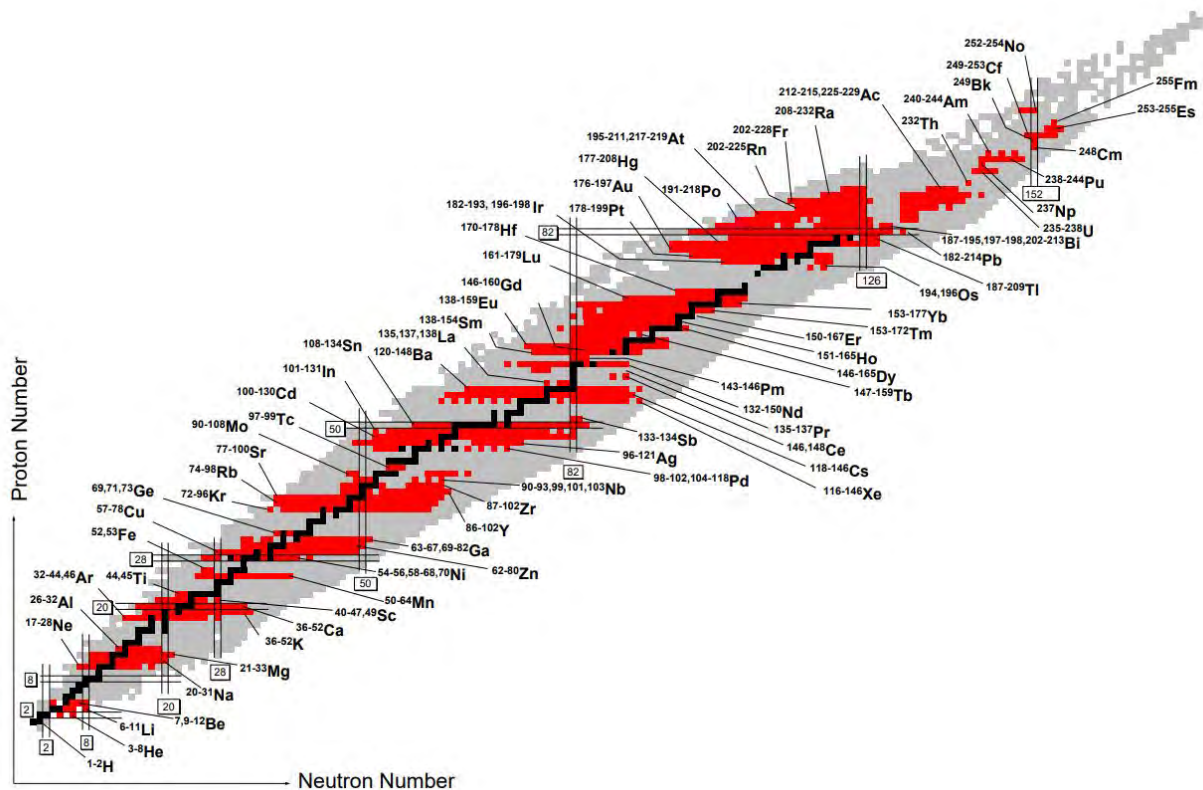


Figure 2.9 Nuclei measured using laser spectroscopy. A nuclear chart is shown from Reference [65], on the x-axis is the number of neutrons and the y-axis is the number of protons. The black squares indicate the stable isotopes on the nuclear chart. The red squares indicate isotopes that have been measured using optical spectroscopy experiments.

CHAPTER 3

EXPERIMENT

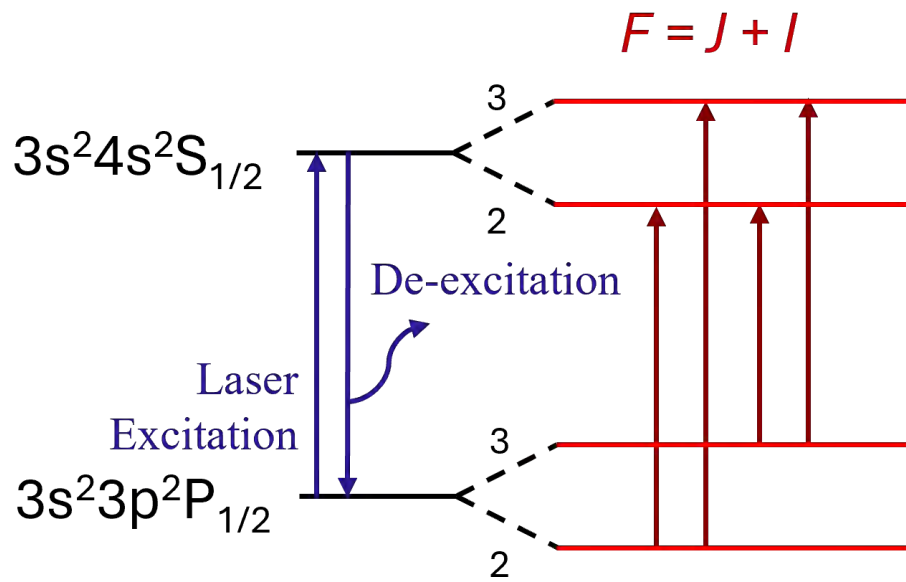
3.1 Laser Spectroscopy Techniques

Laser spectroscopy utilizes resonant laser excitations to study the hyperfine structure of atomic nuclei across the nuclear chart. There were two different techniques for laser spectroscopy used in preparation of the online aluminum experiment which are outlined in this section. Both techniques were tested offline using selected transitions and one technique was chosen for the online run.

3.1.1 Fluorescence

One technique for laser spectroscopy is the use of Fluorescence spectroscopy. Fluorescence spectroscopy uses laser light, set to the resonant laser frequency, to excite an electron from the lower state to the upper state. When the electron de-excites back to the lower state, it emits a photon with energy corresponding to the energy difference between the states. That emitted photon can be detected by photo multiplier tubes (PMT). Scanning over the small range around the fine structure frequency, the resulting resonant photons are counted by the PMTs and a hyperfine spectrum is measured. A schematic of the fluorescence transitions measured for Aluminum are shown in Figure 3.1.

One major challenge in fluorescence measurements is the high photon background. Sending a laser through a beamline where resonant photons are being counted creates a very high background level due to the scattered laser light. The PMTs used for detection are not able to distinguish scattered laser light photons and resonant photons because the PMT is unable to determine the wavelength or source of the incoming photons. In some cases a transition can be used where there is a large difference in wavelength for the laser light and produced resonant photons. The difference occurs from the excited photon decaying to a different state than it was excited from. This large difference can allow a filter to be used to eliminate laser background. An example of this filtering being used is in a previous BECOLA experiment measuring Silicon isotopes, the laser was set to 391 nm and the resonant photons were 288



Fine Structure

Hyperfine Structure

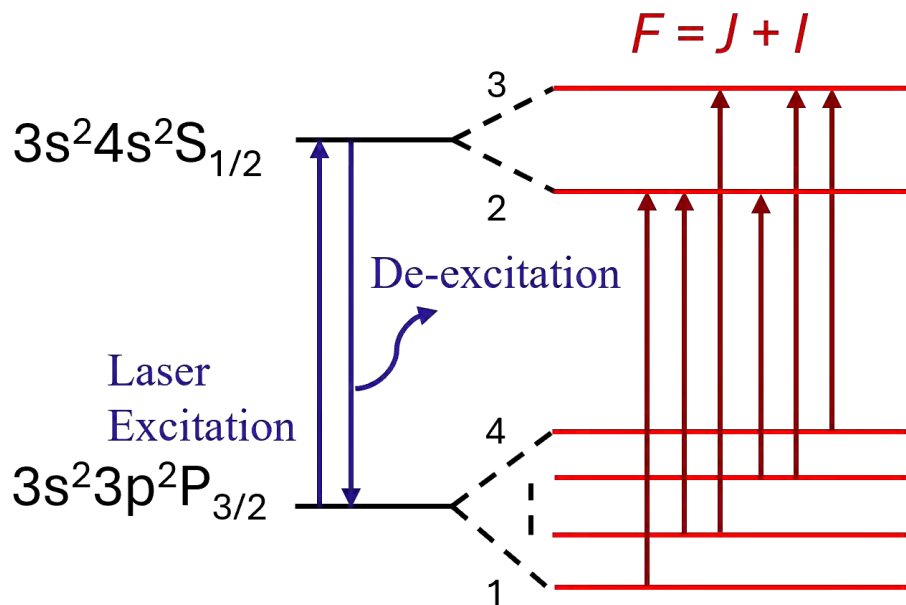


Figure 3.1 Transition level schematics of fluorescence detection measured transitions. A schematic of each fluorescence measured transition in Aluminum is shown. The laser excites electrons from the lower $3p^2 P_{1/2}$ or $3p^2 P_{3/2}$ energy level to the upper $4s^2 S_{1/2}$ energy level. Following the excitation, the electron de-excites into the lower state and emits a photon that can be detected by the PMTs.

nm [57]. This difference allowed a filter to be placed, in combination with an optimum PMT, that eliminated the scattered photon background creating virtually background-free spectroscopy. However, it is not always possible to find an excitation that decays to a different state. For the Aluminum fluorescence transitions measured, all the electrons excited decay back into the ground state they were excited from. The transitions tested were the $3p\ ^2P_{1/2}$ to $4s\ ^2S_{1/2}$ and $3p\ ^2P_{3/2}$ to $4s\ ^2S_{1/2}$ transitions. In both cases the decay branches from the $4s\ ^2S_{1/2}$ state all lead to the ground states the electrons were excited from. It is possible to look at exciting to higher excited states for a possible transition with different decay branches. The first energy level this occurs is the $5s\ ^2S_{1/2}$ state at an energy of $37,689.407\ \text{cm}^{-1}$. This state is dominated by decay into the ground state, but has a 10 to 15 percent decay branch to the $4p\ ^2P_{3/2}$ state at an energy of $32,965.639\ \text{cm}^{-1}$. Although this transition and decay branch would make for an ideal background-free fluorescence spectroscopy measurement, the BECOLA facility cannot produce the proper wavelength and laser conditions required to excite electrons to the $5s\ ^2S_{1/2}$ for a fluorescence measurement. This leads to no such case to create a background-free measurement using the existing setup for a fluorescence spectroscopy experiment.

To minimize the background, the ion beam can be bunched in time and data can be taken only when the ion beam is in the interaction region [67]. Bunching the ions creates a small time window when the ions are in the detection region to decrease the amount of time the detector is counting background photons from the laser. In a continuous measurement (no bunching) a small number of ions are continuously arriving at the detection region over the full time of the frequency scan. The entire time the PMT is counting and seeing the full laser power. In a bunching method the PMT sees all of the ions at once with the laser background, then stops counting while another bunch of ions accumulates, ignoring background counts. Using a one second repetition rate and a one microsecond bunch width gives a 10^6 background suppression. This method is efficient in reducing the background for rare isotopes, but for some isotopes with low production rates the background is still too

high and the small signal to noise ratio requires a higher ion rate than available. Bunched beam collinear laser spectroscopy with fluorescence detection has been applied at BECOLA to isotopes with rates on the order of 10 ions per second, for example ^{36}Ca [68]. The low rate isotopes studied with this method have simple hyperfine structure with zero spin nuclei and are relatively fast transitions. For isotopes with more complex hyperfine structures with finite spin or slower transitions, higher rates are needed. Some isotopes, including dripline nucleus ^{22}Al , require a higher ion rate than available for this method. The efficiency of this measurement technique for allowed Aluminum transitions is too low that a very long accumulation time, longer than possible for an experiment at FRIB, would be needed to achieve the desired statistics. Wanting to reach the dripline nucleus, a new technique was developed at the BECOLA facility. The extension and development is discussed in detail in the RISE sub-section.

3.1.2 Resonant Ionization

The use of resonant ionization can increase efficiency for low production rare isotopes and give a wider variety of transitions to be chosen from for spectroscopy experiments. Resonant ionization uses multiple laser to create resonant ions that can be detected with an ion detector. The multiple lasers interact with the atom beam one after another with tens of nanoseconds between them depending on the transition probabilities (Einstein coefficients) of excitation steps involved in the scheme. The Einstein coefficient of the transition used for the Aluminum experiment is $1.334 \times 10^7 \text{ s}^{-1}$. The first laser is a resonant laser that excites an electron from the ground state to the excited state, the same as fluorescence. Once the electron is excited a second laser interacts with the atom beam to excite the electron to the continuum, making an ion that can be detected. More than two lasers can be used depending on the energy the electron needs to be excited to reach the continuum. A schematic showing a resonant ionization transition for Aluminum is show in Figure 3.2.

The use of an ion detector rather than a PMT provides high detection efficiency and eliminates the high background caused by scattered photons. For the Aluminum experiment

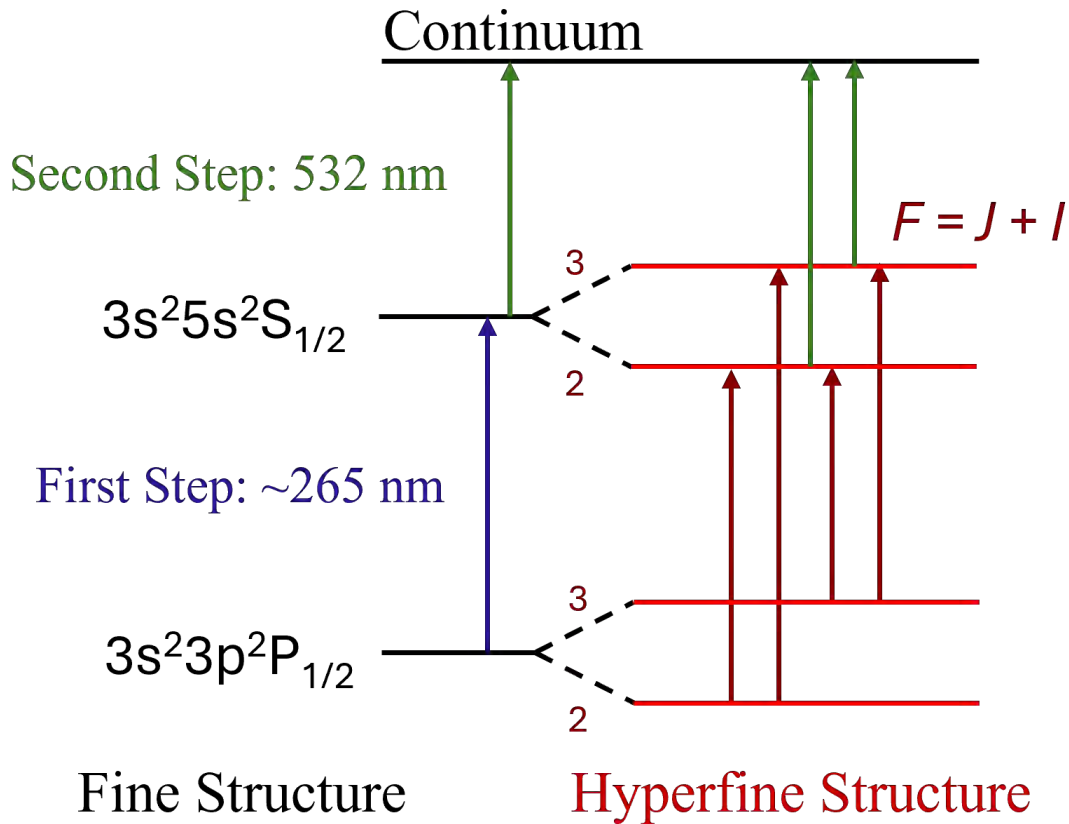


Figure 3.2 Resonant ionization transition level scheme. A transition for a resonant ionization measured transition in Aluminum is shown. The first laser excites electrons from the $3p\ ^2P_{1/2}$ energy level to the $5s\ ^2S_{1/2}$ energy level. The Einstein coefficient of this transition is $1.335 \times 10^7\ s^{-1}$. Directly after the laser excitation a second laser non-resonantly excites the electron to the continuum. This creates an ion that can be detected by an ion detector.

the resonant frequency was in the ultraviolet (UV) range. The quantum efficiency of the BECOLA PMT to detect a UV photon is about ten percent, versus an ion detection efficiency of about one hundred percent for the resulting resonant ions. The laser used to excite the ion to the continuum, allowing for it to be detected, is used at a very high power and is a non-resonant excitation. The main source of background for resonant ionization measurements are collisionally produced ions and non-resonant laser ionizations. The non-resonant ions typically have a much smaller or at most comparable size cross section compared to the resonant ions. Since the background is coming from the incoming ions, the background level scales with the amount of incoming ions. This is critical in measurements on isotopes with

very low production rates. Unlike a fluorescence measurement, if less ions are entering the beamline, leading to a smaller amount of resonant ions, the background also decreases.

Before exciting the atoms for spectroscopy, the ions produced and delivered to the beamline can be neutralized, for the Aluminum experiment incoming ions were neutralized with finite efficiency. The details of how they are neutralized and why are outlined in the Charge Exchange Cell sub-section. Following the neutralization process, there is an electrostatic kicker that deflects any ions that were not neutralized in the charge exchange cell. This deflection should eliminate any collision induced ions or ions that were not neutralized in the charge exchange cell. Due to the large laser power the atoms can absorb multiple photons and be ionized non-resonantly after the kicker, causing a large background. Another large contribution to the background comes from some atoms colliding with residual gas in the vacuum chamber and being ionized by the collision. Compared to a fluorescence measurement the background for a resonant ionization transition is typically lower and scales with the number of ions. However, in some cases the non-resonant laser can excite many atoms and create a large background. Although it scales with the amount of ions coming in, the large background leads to a poor signal to noise ratio and prevents efficient measurement of an isotope with low production rate. An example of this occurring is in resonant ionization transitions for Nickel-58. Using either high power 355 nm laser light or 532 nm laser light to non-resonantly excite electrons to the continuum causes a large background, causing a small signal-to-noise ratio. Sample spectra for a transition using 355 nm and 532 nm laser light are shown in Figure 3.3 and 3.4 respectively. Due to the large background caused by non-resonant laser excitations for Ni transitions, a fluorescence transition or an ionization transition which does not involve a non-resonant laser would be preferred. To achieve an ionization without a non-resonant laser, the Rydberg states can be utilized. A Rydberg energy level is an energy level that sits directly below the ionization potential. Laser light can excite the electron to a Rydberg state and an electric field can be applied to ionize. This ionization process was commissioned for the BECOLA facility with Ni. An example of

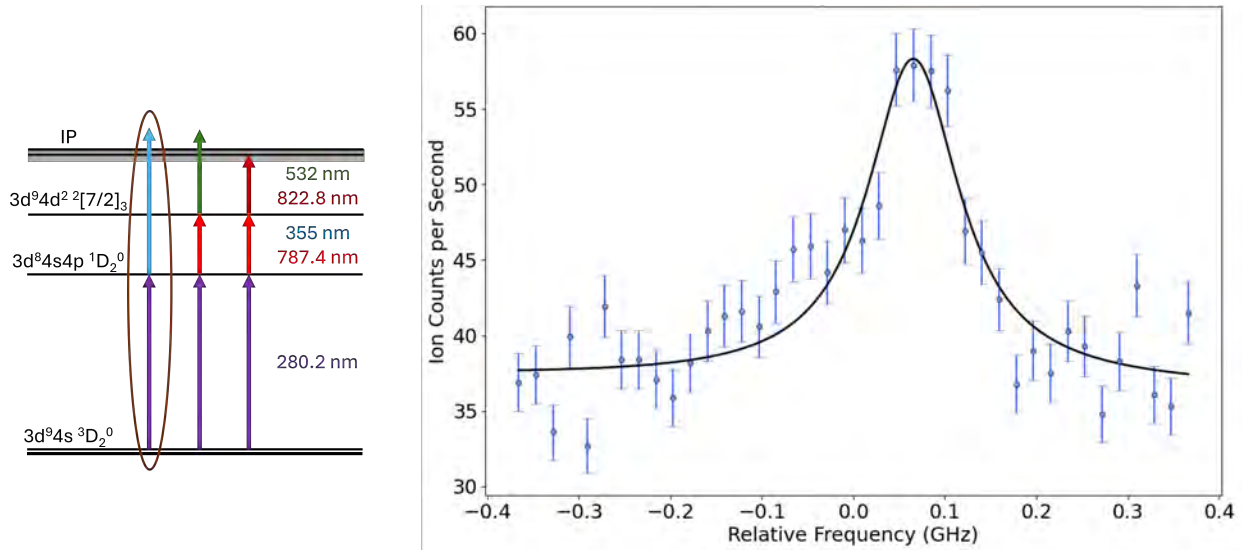


Figure 3.3 Ni spectrum using 355 nm laser light. An example spectra and level scheme for a two step resonant ionization transition measured in ^{58}Ni is shown. The three level schemes measured in Ni are shown with the scheme of the example spectra shown circled. In this particular example the non-resonant 355 nm laser light induces a large background in the spectrum, limiting the overall efficiency and signal to noise ratio of the spectrum.

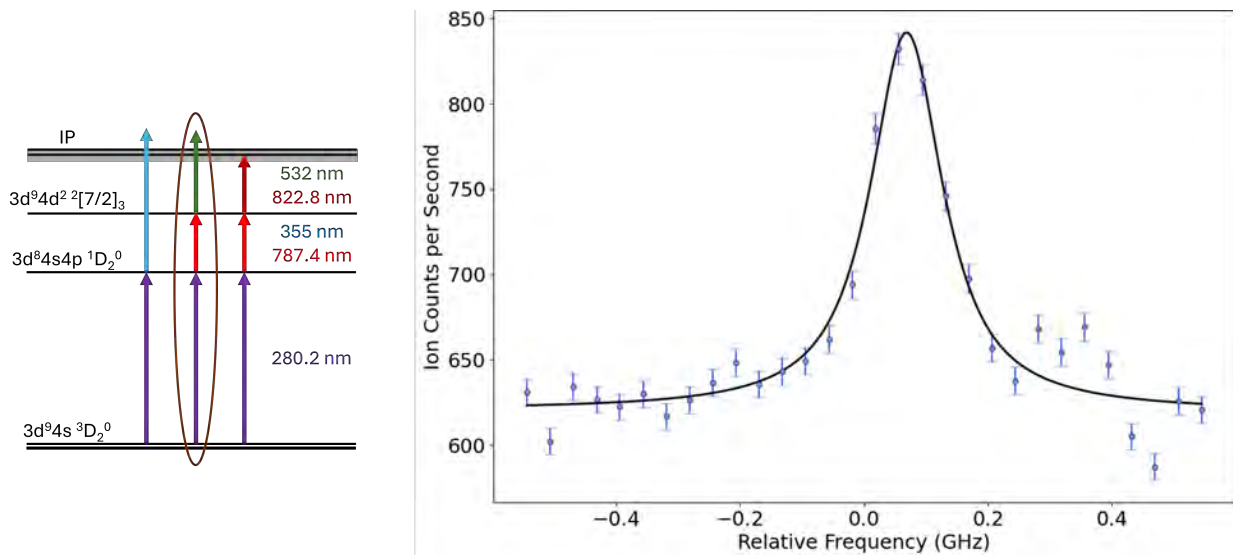


Figure 3.4 Ni spectrum using 532 nm laser light. An example spectra and level scheme for a three step resonant ionization transition measured in ^{58}Ni is shown. The three level schemes measured in Ni are shown with the scheme of the example spectra shown circled. In this particular example the non-resonant 532 nm laser light induces a large background in the spectrum. Although the background production is less than 355 nm laser light, the overall efficiency and signal to noise ratio of the spectrum is not ideal or high enough for an online run.

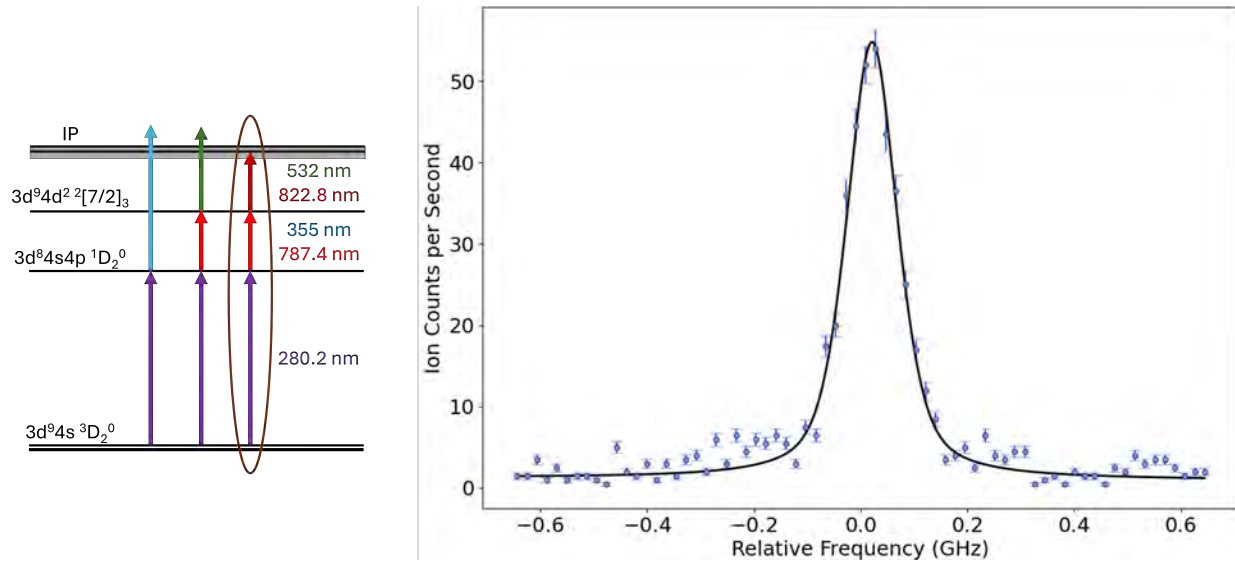


Figure 3.5 Ni Rydberg transition spectrum. An example spectra and level scheme for a Rydberg transition measured in ^{58}Ni is shown. The three level schemes measured in Ni are shown with the scheme of the example spectra shown circled. In this particular example, utilizing the Rydberg state to ionize eliminates the high background, creating a close to background free measurement. The overall efficiency and signal to noise ratio of the spectrum is more optimum for an online run and could potentially be used for the upcoming Ni experiment.

the resulting spectra is shown in Figure 3.5. This Ni work is the thesis project of a future graduate student and further details of Rydberg states will not be discussed in this work.

Fortunately, in the case of Aluminum there are minimal non-resonant laser excitations and they do not contribute a large background to the spectrum. Figure 3.6 shows a sample Aluminum spectrum which uses 532 nm laser light as a non-resonant step in the transition. The background level shown includes all sources of background for the measurement, not just background laser excitations. Including all sources of background, a background to peak ratio of about ten was achieved in the tested Aluminum transitions. The main contribution to the background is collisional ions in the beamline. Blocking all laser light, the background stays within typical fluctuations, emphasizing that the background caused by the 532 nm light is very minimal compared to the resonant signal.

Choosing between a fluorescence transition and resonant ionization transition is highly element and isotope of interest dependent. Many different transitions for both methods must

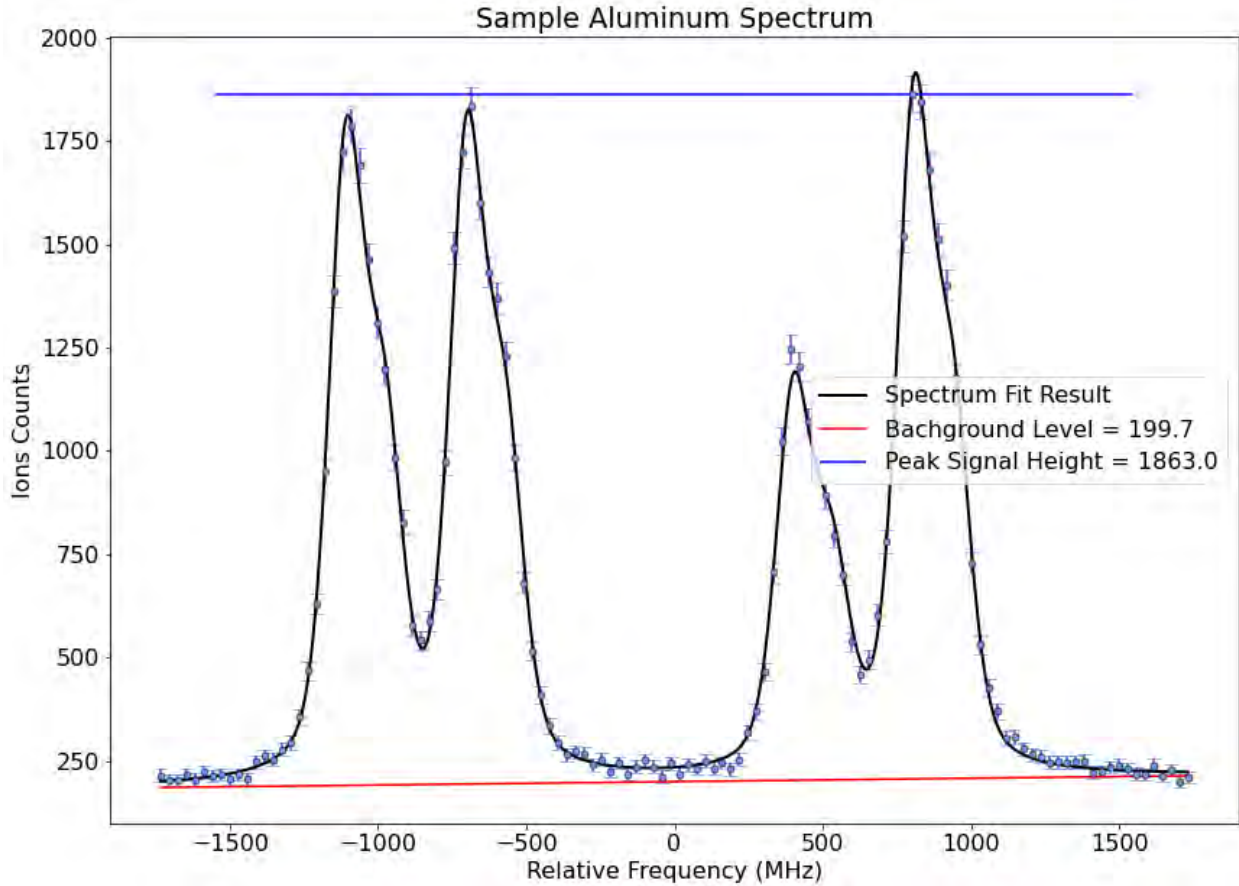


Figure 3.6 Background and peak signal height in ^{27}Al spectrum. A spectra of ^{27}Al is shown. The background level and peak height are emphasized to show the large bg to peak ratio. For this spectrum the ratio is 9.33. The spectrum shown uses 532 nm non-resonant laser light which does not contribute a large background for Aluminum.

be carefully considered and tested to determine the transition that will yield the highest efficiency for an experiment and produce the highest statistics in the smallest amount of time. The capability of the BECOLA facility to run both spectroscopy techniques gives an unique opportunity to select from a wide number of transitions. This capability allows for a wide variety of isotopes to be studied with high precision at one facility. The details of the transitions tested for the Aluminum experiment are outlined in the Appendix and Experimental Data chapter. For the online experiment measuring $^{22-27}\text{Al}$, a resonant ionization transition was chosen. The following sections and subsections discuss the details of the experimental setup focusing on the resonant ionization technique used for the Aluminum experiment.

3.2 Laser Setup

Lasers are a crucial component of laser spectroscopy since they are necessary to excite the electron. Depending on the isotope and the transition being studied, a wide variety of wavelengths and pulse energies are necessary. For the Aluminum experiment there were two lasers used in the online experiment. The lasers used for the online experiment are outlined in detail below. In addition to these lasers, a Ti:Sa continuous wave (CW) Sirah Matisse [69] doubled by a cavity-based Wavetrain Spectra Physics frequency doubler [70], was used for the offline fluorescence measurements of stable Aluminum-27.

The two step Aluminum transition of interest, shown in Figure 3.2, requires three lasers to produce the required two laser steps. The first step of the transition requires pulsed laser light at 265 nm. This is obtained by an injection seeded cavity [71]. The cavity requires two laser to produce the desired laser light, one to pump the cavity and one to seed the cavity. Details are outlined below. The second step requires high power pulsed 532 nm light and is obtained by a frequency doubled Nd:YAG laser. The two lasers need to be overlapped with the ion beam in the beamline. The 265 nm light for the first step is produced in the laser lab across the hall from the beamline and must be transported, while the 532 nm light is produced by a laser mounted directly next to the beamline due to the safety concern to send high power laser light over a long distance. The overall light transport configuration is shown in Figure 3.7.

In addition to overlapping the lasers position in the interaction region, the lasers timing must be synchronized to interact with the ion beam in the interaction region of the beamline, first by the 265 nm then directly after by the 532 nm. The timing of the lasers were set and synchronized by a pulse pattern generator, Quantum Composer, to ensure precision timing between the ion beam and each subsequent laser excitation.

3.2.1 Injection Seeded Cavity

For the first resonant step of the online Aluminum transition tripled light from an injection seeded Titanium sapphire (Ti:Sa) cavity [71] was used. The cavity was seeded by

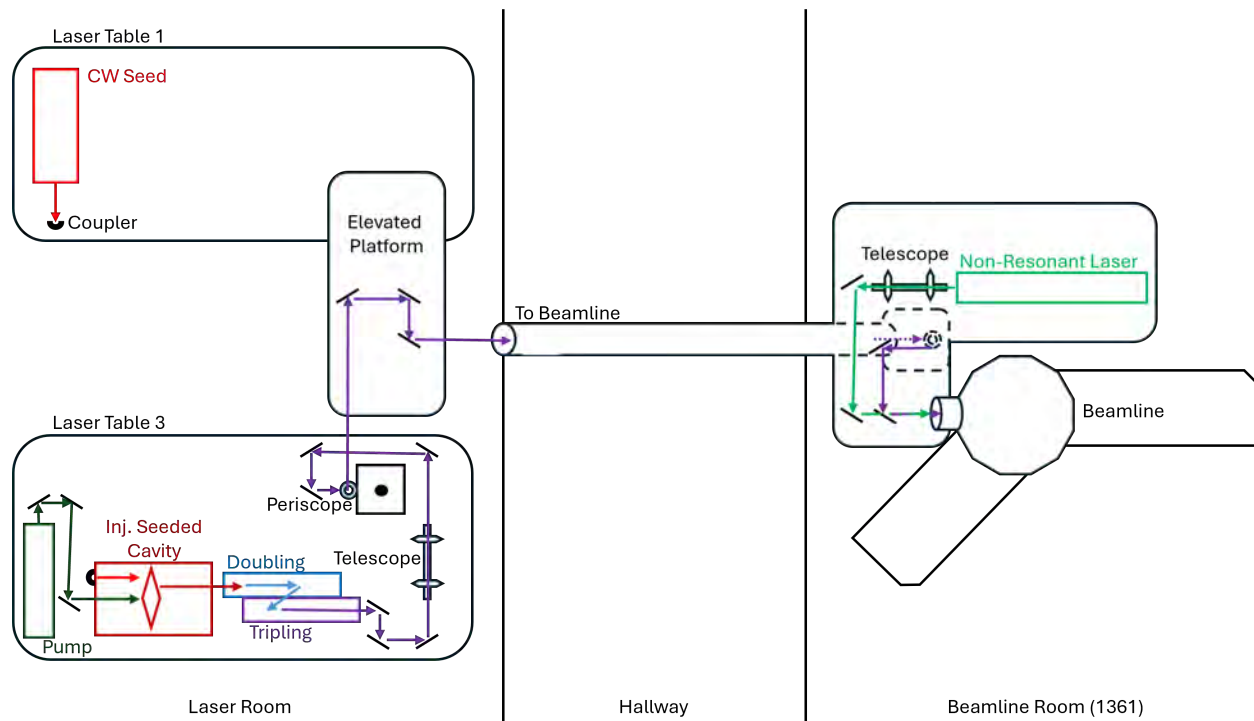


Figure 3.7 Laser transport simplified schematic. A not to scale simplified schematic of the laser light transport system used for the AI experiment is shown. Solid black lines indicate mirrors. Bright red arrows indicate seed light, darker red indicate injection seeded cavity light, dark green indicates the cavity pump light, blue indicates doubled cavity light, purple indicates tripled cavity light, and bright green indicates the non-resonant laser light. The periscope used to send the tripled cavity light up is indicated by 2 embedded circles. The square with solid black dot in the center is a pillar mounted on laser table 3 which holds the periscope optics. In the beamline room dashed lines indicate components which are elevated, including a set of two dashed embedded circles indicating the periscope to send the tripled cavity light to the same height as the beamline.

a Ti:Sa CW Matisse laser (Matisse-TS) [69]. The cavity was pumped by 532 nm light at 10 kHz from a single mode Ti:Sapphire Photonics Industries laser (DS20-532 TU-H) [72]. The cavity works by overlapping the seed and pump light in a bowtie configuration through a Ti:Sa crystal, locking on the desired wavelength determined by the seed. The seed laser wavelength is monitored and stabilized using a HighFinesse Angstrom WS30 high precision wavemeter [73] calibrated by a SIOS Meßtechnik GmbH Frequency-Stabilized He-Ne Laser (SL03) [74].

A schematic of the injection seeded cavity is shown in Figure 3.8. The seed light enters from the top left of the figure through an optical fiber. The seed light reflects off of red

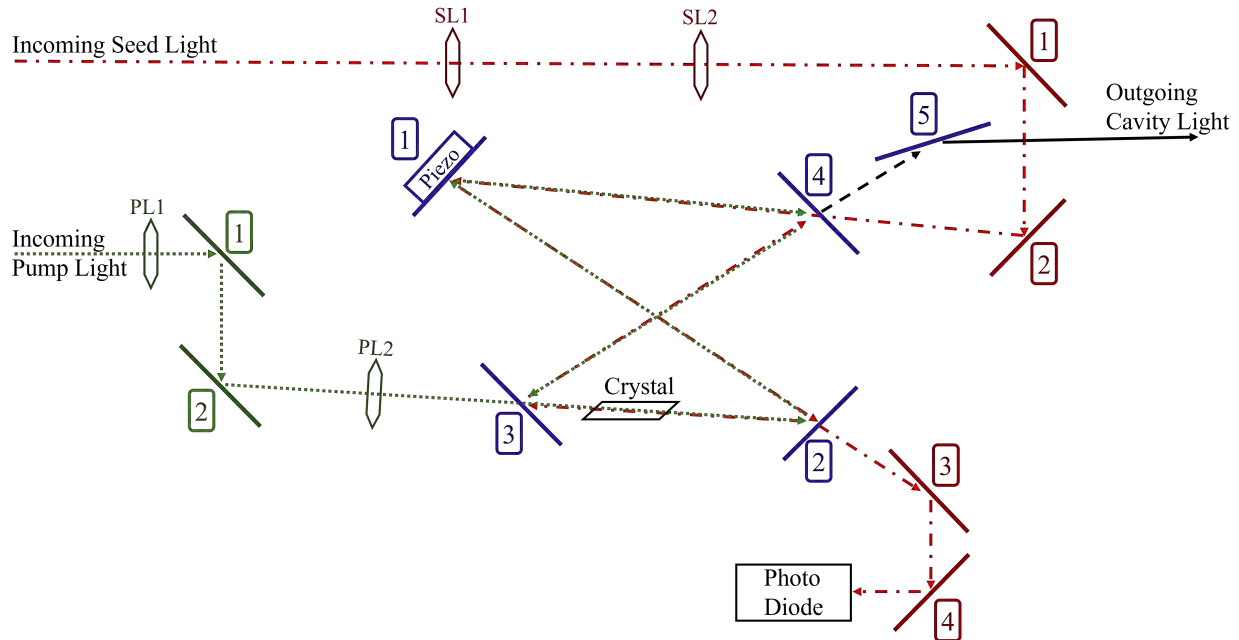


Figure 3.8 Injection seeded cavity schematic. A simplified schematic of the injection seeded cavity is shown. Mirrors are indicated by solid lines, the color of the mirror helps to indicate what laser light path it is on. The seed light is shown by a red dashed line, pump light by a green dashed line, produced cavity light by a black dashed line in the cavity and as a solid black arrow indicating the exit from the cavity. SL stands for seed lens and PL stands for pump lens. The seed light and pump light each have two lenses that act as a telescope to focus the laser light onto the crystal. Note, optical components such as isolators and polarizers were omitted for simplification. The schematic is not drawn to scale or with proper reflecting angles.

mirror 1 and 2 through the back of purple mirror 4 into the bow tie cavity, interacting with the crystal between purple mirror 2 and 3. A sample of the light is taken through purple mirror 2, reflected off red mirror 3 and 4 onto a photo diode. The sample of light taken is fed into the cavity's electronic system to lock the cavity to the correct wavelength. The pump light enters from the middle left of the figure onto green mirror 1 and 2 to be sent into the bow tie cavity and interact with the crystal. The cavity light produced exits through purple mirror 4 and is reflected off of purple mirror 5 to exit the cavity.

The cavity is locked use a TEM-Messtechnik LaseLock laser stabilization electronic system [75]. LaseLock is a compact electronic box which frequency stabilizes the Ti-sapphire injection seeded cavity. LaseLock monitors the frequency of the cavity to detect changes and provide feedback signals to correct and stabilize the cavity to the desired frequency [75].

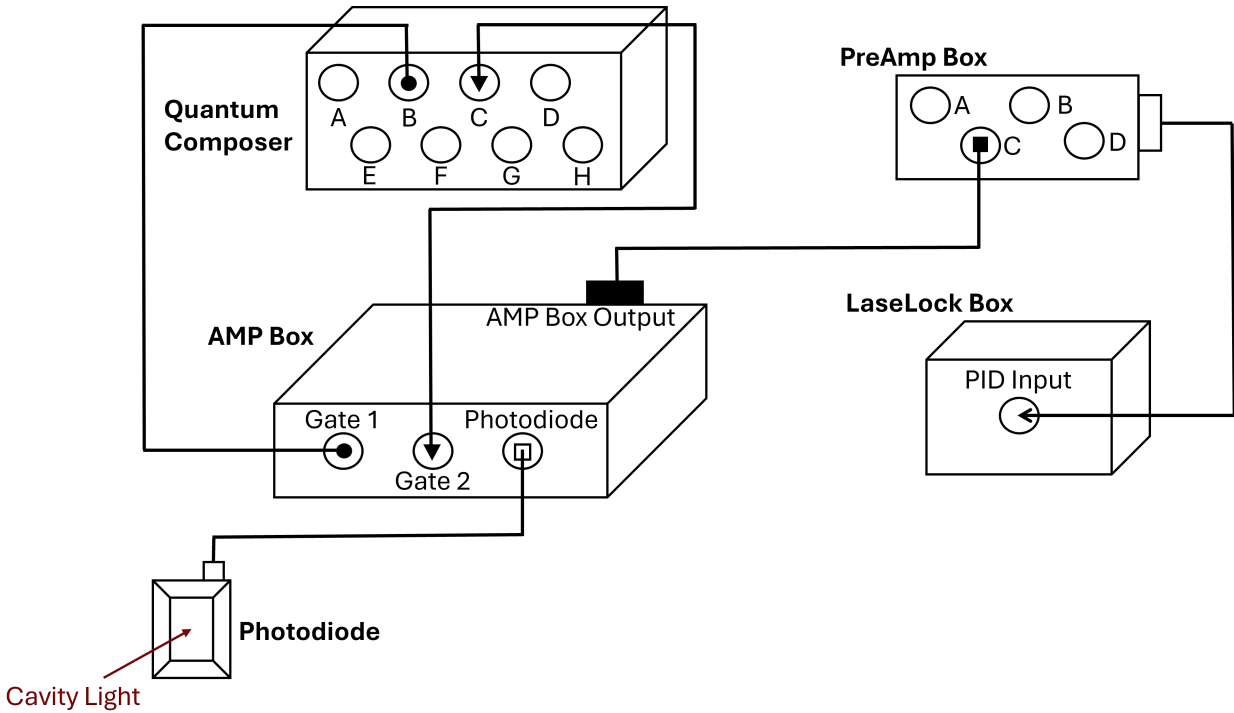


Figure 3.9 Injection seeded cavity locking signal from cavity to LaseLock. A schematic showing how the photodiode signal goes from the cavity into the LaseLock is shown. Details can be found in the text.

LaseLock is able to generate stable narrow line widths and eliminate any frequency drift. A schematic showing how the signals are fed into the LaseLock for frequency monitoring is shown in Figure 3.9. To monitor the cavity wavelength, the photo diode signal from the cavity is fed into an AMP Box. The AMP box has three input signals; two gate signals and the photodiode signal. The two gate signals are given from the Quantum Composer, which triggers the lasers and cooler buncher during the experiment. The gate signals are given by channel B and C from the Quantum Composer. Both channels are synced to channel A, which is the trigger signal to the pump of the injection seeded cavity. The gate signals are delayed from the pump trigger signal to filter out the pump laser component in the photo diode signal. The filtered signal is output from the AMP box to the PreAmp box. The signal is input to the PreAmp box with a 50Ω resistor. The PreAmp box is from TEM-Messtechnik and accepts voltages ranging from -10 V to 10 V. It takes the input signal and prepares it to be fed into the LaseLock PID input. Purple mirror 1 in the cavity

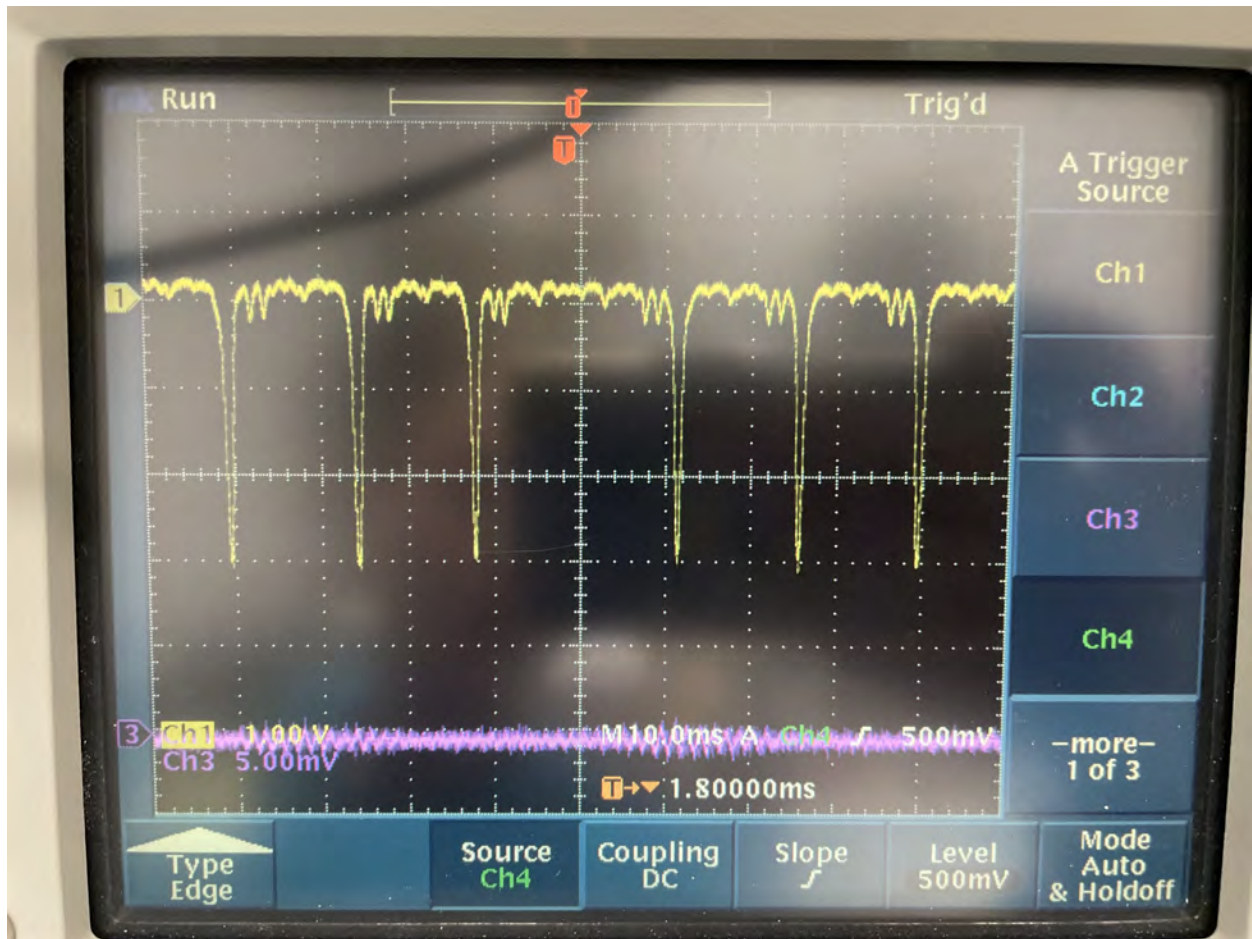


Figure 3.10 Injection seeded cavity fringe pattern. A photo of an oscilloscope showing the resulting fringe pattern from scanning the purple mirror 1 in the cavity is shown. The cutoff frequency was set to 880 Hz. The yellow line is the fringe pattern. Each vertical square on the y axis is 1 volt. The fringes are over 2 volts high. To account for fluctuations and for the best stability a 1.6 volt setpoint was chosen.

is mounted on a piezo mount which is controlled by the LaseLock. When the piezo motor is scanned a fringe pattern is produced as shown in Figure 3.10. To better view the fringe pattern the cutoff frequency is set to 880 Hz. The fringe pattern is used to determine the setpoint to lock the cavity. For Aluminum the lock setpoint was 1.6 volts to lock to the top of the fringe pattern, with 0.1 volt fluctuations to account for changes in cavity conditions over the months running Aluminum. An 80 Hz cutoff frequency was also set on the regulator to increase the stability of the lock. Once the cavity is locked, the filtered PID input to the LaseLock is used to monitor the variation from the voltage setpoint. The LaseLock will move the piezo mirror in the cavity as needed to maintain the set voltage. In addition

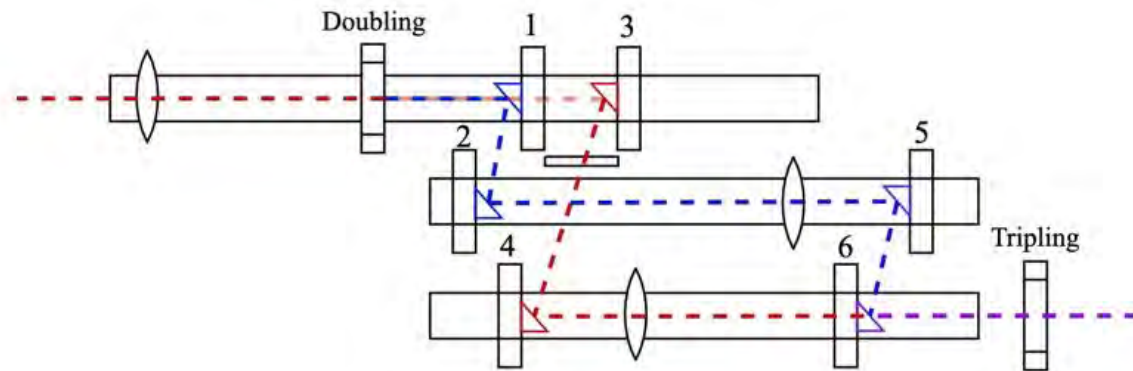


Figure 3.11 Laser light tripling schematic. A schematic of the tripling configuration is shown. Tapered ellipses indicate lenses and triangles indicate mirrors. Mirrors are colored to indicate which laser light path they are one. A half wave plate is shown as a black rectangle between red mirror 3 and 4, the wave plate adjusts the fundamental light polarization to match the doubled light. Fundamental light from the injection seeded cavity is indicated by a red dashed line, doubled light is blue, and overlapped fundamental light with doubled light is shown as purple. Laser light exits the tripling unit to be transported to the beamline after the tripling crystal at the bottom right hand side of the figure.

to locking the cavity, the wavelength output from the cavity is monitored using the high precision wavemeter. The seed laser receives the wavelength readout and has its own PID system to maintain the frequency setpoint.

After the cavity light is produced the light was tripled first by using a bismuth triborate (BIBO) crystal to frequency double the light, then overlapping the fundamental light output from the cavity with the produced doubled light into a beta barium borate (BBO) crystal to frequency triple the light. A schematic of the tripling process is shown in Figure 3.11. Light exiting the injection seeded cavity is shown as a red dashed line from the left hand side of the figure going towards the "Doubling" crystal. The laser light first encounters a lens, lenses are represented as tapered ellipses, where it is focused onto the face of the doubling crystal. The doubling crystal is a BIBO crystal that will double a fraction of the incoming light. The laser light that was doubled, shown with a blue dashed line, will reflect off of mirror 1 after exiting the crystal and then reflect to mirror 2. Laser light that was not

doubled (fundamental) will reflect off of mirror 3 after exiting the crystal and then reflect to mirror 4. Since doubling laser light changes the polarization, the fundamental light will pass through a polarization plate between mirror 3 and mirror 4, represented as a rectangle, this will ensure polarization matching for the two laser lights to be combined and tripled. Both the doubled and fundamental laser paths will then go through a lens to independently set their focus at the face of the tripling crystal. The doubled laser light will then reflect off of mirror 5 and 6 to overlap with the fundamental light, which passes through mirror 6. The overlapped light, shown as a purple dashed line, then passes through the BBO tripling crystal and produces tripled light. The resulting tripled light ranged from 256-265 nm for each of the isotopes studied and all of the transitions tested offline. To view the tripled light after the BBO crystal during alignment a Pellin Broca Prism (Thorlabs ADBU-20) was used to separate the light exiting the crystal by wavelength. For the Aluminum experiment 1.67 W of fundamental light exited the injection seeded cavity producing 200 mW of doubled light and 18-28 mW of tripled light. 10 mW of laser power coming out of the tripling crystal was transported to the beamline to be used for spectroscopy.

The crystals used for doubling and tripling depends on the wavelength needing to be generated. Crystal software such as Select Non-Linear Optics (SNLO) by Dr. Arlee Smith from AS-Photonics [76] or iPhasematch by Yushi Kaneda [77] can be used to determine the required angle cut of the crystal. An example from SNLO is shown in Figure 3.12. For ^{27}Al the fundamental light was about 769 nm. To determine the doubling crystal angle the fundamental wavelength is put in for both the Red 1 and Red 2 inputs. Selecting a BBO crystal the crystal angle is output as "At theta" as 30.4 degrees. To use a BIBO crystal rather than BBO, the required angle is $180 - 30.4 = 149.6$ degrees. Crystals are typically purchased for a laser system at interval cut angles. The closest crystal angle to the required angle is used and mounted on an adjustable mount. This allows for the required angle to be obtained manually and optimized on the output laser power at the desired wavelength. For Aluminum a 31.9 degree BBO and 151.2 degree BIBO crystal were used for doubling to

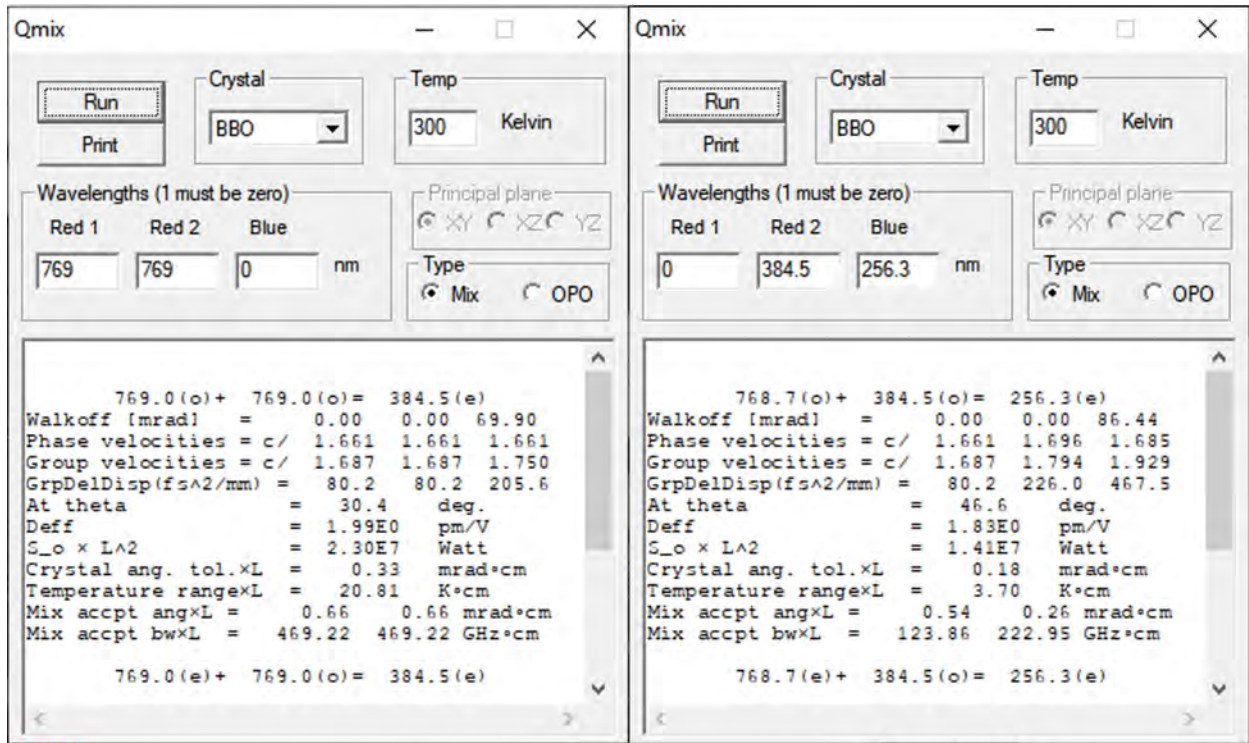


Figure 3.12 SNLO crystal choosing software. An example screen of using the SNLO software is used [76]. On the left hand side is an example for determining the doubling crystal angle and on the right hand side is an example of determining the tripling crystal angle. The example inputs are for ^{27}Al . The resulting output angle is "At theta".

determine which yielded the highest laser power at the desired wavelength. Testing revealed the BIBO worked better and the 151.2 degree BIBO crystal on an adjustable mount was used for the online experiment. To determine the tripling crystal angle the doubled laser wavelength is put in for the Red 2 input and the desired tripled wavelength output is put in for the Blue input. Doubled 769 nm fundamental light is 384.5 nm and tripled is 256.3 nm. The resulting required angle is 46.6 degrees. For the online experiment a 44.3 degree BBO crystal on an adjustable mount was used. For each isotope of Aluminum the required crystal angle is similar to ^{27}Al and can be obtained with small tilting angle adjustments to the crystal mounts.

3.2.2 Merion

The second non-resonant, brute force, step was performed by a 100Hz diode-pumped pulsed Nd:YAG Lumibird Merion laser (MW) at 532nm [78]. For the Aluminum experiment

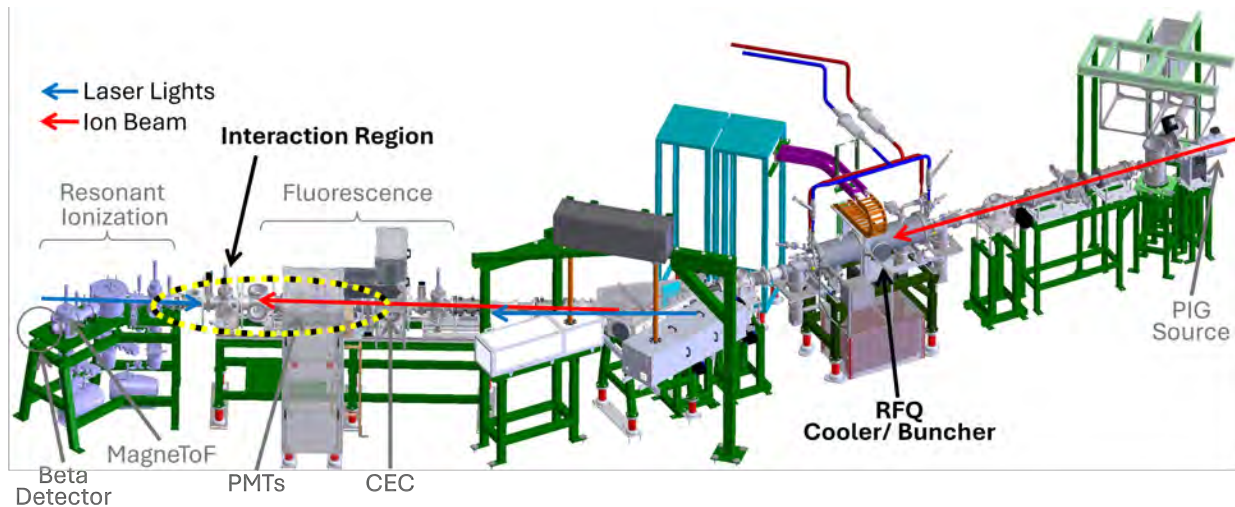


Figure 3.13 Interaction region. A schematic of the BECOLA beamline [96] is shown highlighting the location of the cooler buncher and interaction region.

the Merion was run at 3.4W.

3.2.3 Quantum Composer

The timing of the lasers needs to be precisely set to ensure the laser meets the ion beam in the interaction region of the beamline, first step followed by second step. To do this a 9520 Series Pulse Generator for Timing and Synchronization from Quantum Composers [79] was used to generate pulses of all of the trigger signals, including the lasers and cooler buncher. This gives all of the components the same clock with one nanosecond precision. The injection seeded cavity is triggered by sending a signal to the pump laser’s diodes and Q-switch, firing the laser pulse. The non-resonant step laser is triggered and fired by sending two pulses, one to the diodes and one to the Q-switch of the Merion. The timing of the ions is controlled by sending a pulse to the DAQ system that controls the timing of the cooler buncher, details are outlined in the RFQ Cooler/ Buncher sub-section, to release the ion bunches into the beamline. The timing between the ion beam and laser beams is determined by the time of flight of the element of interest from the cooler buncher to the interaction region. The relative location between the cooler buncher and interaction region, which is the point in the beamline where the lasers and ions meet, is shown in Figure 3.13. In the case of Aluminum the ion bunch takes around 23 to 25 microseconds to reach the interaction

region, depending on the isotope. The Quantum Composer timing was optimized on the resonant signal to determine the best laser-ion timings. The Quantum Composer is in the laser room, across the hall from where the input signal to the DAQ for the buncher release time is located. This means a very long, over 10 meter, BNC cable was used to transport the signal. This causes the setpoints on the Quantum Composer to vary compared to the observed separation in time. The delay set on the Quantum Composer for the first laser is 2.91×10^{-6} s and the buncher release time is set to 2.83×10^{-4} s. The DAQ sees the lasers arriving at 20.5 microseconds and the ions around 23 to 25 microseconds, about a 3 to 5 microsecond separation. The two lasers are set about 40 nanoseconds apart from each other, ensuring the first step is excited before the second step laser excites the electron further or the first step de-excites since the Einstein coefficient of the Aluminum transition is 1.335×10^7 s⁻¹. The Einstein coefficient is inversely related to the lifetime and is the sum of all decaying branches. The first step laser has a 40 ns time fluctuation, a 40 ns separation between the first and second step ensure the first step does not overlap with or come after the second step. The timing of the two lasers are shown in Figure 3.14. This timing is transition dependent, for example, the first step of a transition may decay very quickly from the excited state, requiring the second step laser to arrive at the same time as the first step. The exact timing between the lasers as well as between the lasers and ion beam is optimized during offline measurements by maximizing the intensity of resonant signals in preparation for online experiments.

3.2.4 Laser Installation

Both the injection seeded cavity and the Merion were a part of the installation and commissioning to add the resonant ionization capability to the BECOLA facility. The laser used to seed the injection seeded cavity was already installed and commissioned previously in the BECOLA facility. The only alteration needed was to connect a fiber from the laser to the input of the injection seeded cavity. The pump laser used for the injection seeded cavity was brought from a previous project at Oakridge National Laboratory (ORNL) and

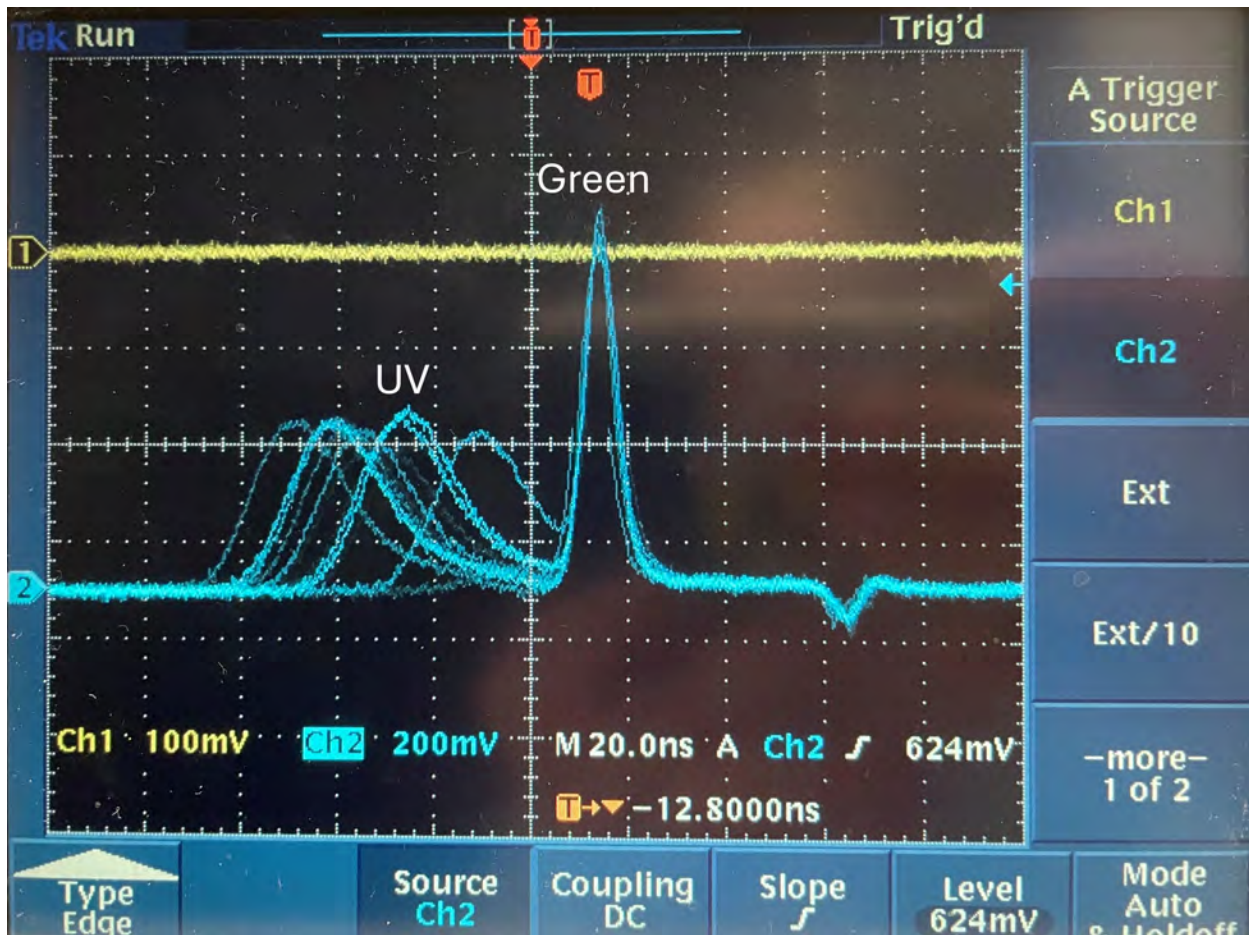


Figure 3.14 Relative laser timings. A photo of an oscilloscope showing the timing of the two lasers is shown. The timings are read using a photodiode, the photodiode signal is shown in blue. The first pulse is from the UV light, followed by the second pulse which is the green light. The injection seeded cavity has a 40 ns time fluctuation in its timing. The center of the UV timing pulse and the green are 40 ns apart.

was installed to pump the cavity. The laser did not require any modification and only required a telescope to adjust the focus and mirrors to adjust the alignment into the cavity. The injection seeded cavity itself, along with the electronics for it and elements inside of it, was newly brought to the BECOLA facility to be installed for resonant ionization. The cavity required assembly, alignment, optimization, and testing to be implemented for this experiment. The Merion was also newly purchased and commissioned for this experiment. The Merion arrived able to produce the 532 nm laser light at the desired pulse repetition rate, the plumbing for the chiller and laser head, power cables, mounting of the laser, and running settings all needed to be modified. Each laser's path was also newly setup and

prepared for this experiment, including both focusing elements and transport optics.

3.2.5 Laser Light Transport

The injection seeded cavity and tripling unit used to produce the laser for the first step of the transition are in a separate room across the hall from the BECOLA beamline. This means the laser light needs to be transported across the hall to the beamline. This has been done previously in the group mainly with an optical fiber. Since the tripled light is in the UV wavelength range, it cannot be transported in an optical fiber due to UV light solarization. Due to this constraint a laser transport system was designed and installed to safely and efficiently get the laser light from the laser room to the beamline. In addition, laser light required for resonant ionization is higher power than is required for fluorescence measurements and is too high to be transmitted with an optical fiber. The new transport system was designed to be used for all resonant ionization lasers that could be used in future experiments with the new resonant ionization system at BECOLA.

The first step of setting up the transport system was to build a physical platform in the laser room to place mirrors that can send the light to the beamline. A photo of the platform is shown in Figure 3.15. An existing pipe was in place to connect the two rooms, but is very close to the ceiling to allow for pedestrian traffic in the hallway. The existing pipe connected the platform to the collinear side of the beamline, a second pipe was installed to connect the platform to the anticollinear side of the beamline. This allows resonant ionization experiments to be setup from either side of the beamline. The platform was constructed along with vertical pillars on each laser table to periscope the light to the height of the platform. With the platform in place it was possible to send the UV light between the two rooms. However, the platform itself was very susceptible to building movement and noise. This would cause the UV beam spot to be very unstable and change position, misaligning the laser. This drops the overall efficiency of the measurement since any misalignment is a number of ions not being excited by the laser. To account for this movement an MRC active laser beam stabilization system [80] was installed to maintain the laser position.



Figure 3.15 BECOLA bridge. A photo of the platform, nicknamed "BECOLA bridge", which sends laser light from the laser room to the beamline is shown. The red arrow indicates where the laser light travels.

A simplified overview of the laser light transport system is shown in Figure 3.7. In the laser room there are four laser tables holding a variety of lasers. For this Al experiment only lasers on table one and three were used. Laser table one holds the laser that produces the CW seed for the injection seeded cavity. A coupler couples the CW seed laser light into an optical fiber. The other end of the optical fiber is directly inserted to the injection seeded cavity. Laser table three holds the injection seeded cavity, its pump, tripling unit, and telescope. The detailed schematics of the cavity and tripling unit are shown in Figure 3.8 and 3.11 respectively. The pump laser light is sent into the injection seeded cavity with the seed light. The laser light produced by the cavity is sent through a tripling unit to first double

then triple the laser light. The tripled cavity light is the laser light needed for resonance at the beamline. It is first sent through two telescopes to set a good focus at the beamline interaction region. The first telescope uses two cylindrical UV coated lenses to adjust the vertical spread of the beam, correcting the beam spot from an elliptical shape to a spherical shape. For the Aluminum experiment the cylindrical telescope used a 100 mm focal length lens followed by a 300 mm focal length lens. The second telescope used two spherical UV coated lenses to adjust the diameter of the beam spot. For the Aluminum experiment the spherical telescope used a -75 mm focal length lens followed by a 125 mm focal length lens. The distance between the lenses were adjusted while looking at the beam size and profile at the interaction region, setting the UV profile to a 1 cm diameter rectangular spot. A combination of the beam profile exiting the crystals and the large distance the laser light needed to be transported made a spherical beam spot unobtainable. Following the telescopes it is periscoped up to the same height as the elevated platform to be sent through the pipe connecting the laser room and beamline room through the hallway. Once it arrives in the beamline room it is periscoped down to the beamline height. The second step non-resonant laser is mounted in the beamline room with a telescope to adjust the focus at the interaction region. Both the tripled cavity light and the non-resonant laser light are overlapped and sent into the beamline.

The stabilization system [80] works in two stages with detectors (4QD) to sense the movement of the laser and piezo mirrors (P4S30) to adjust the position. The first piezo mirror works with the first detector and the second piezo mirror works with the second detector. The first piezo mirror was installed on the launching platform in the laser room along the injection seeded laser light path, shown in Figure 3.16. The first detector was then placed directly after the transport pipe in the beamline room. A pickoff mirror was used to reflect a small amount of power off of the laser light path to the detector. The picked off laser light was then sent through a lens to focus the laser light onto the surface of the detector. To account for changes in the overall laser power being sent for spectroscopy a continuous

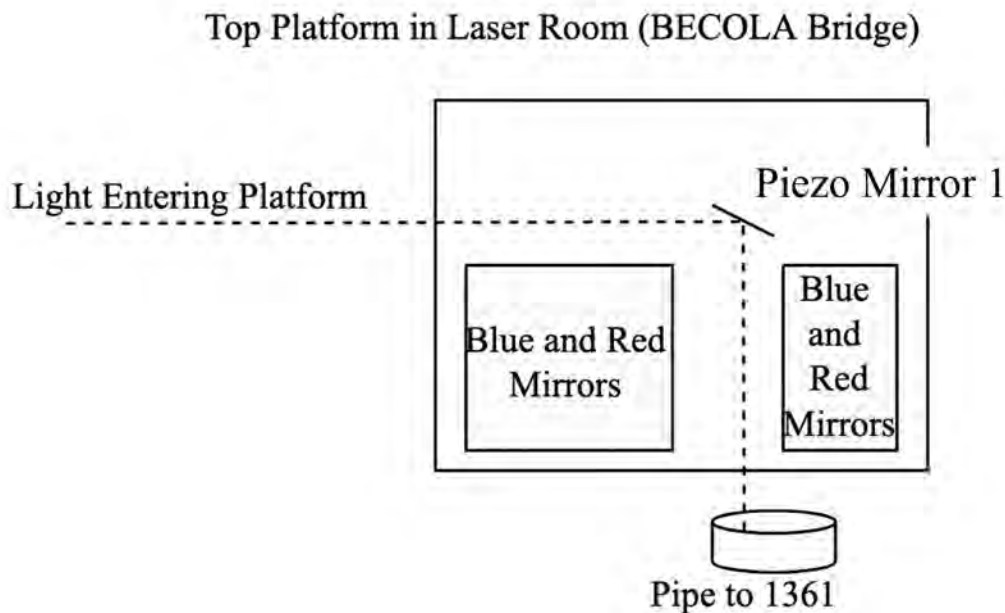


Figure 3.16 First piezo mirror of the feedback detection system location schematic. A schematic of the first piezo mirror for the feedback detection system is shown. The first piezo mirror is on the launching platform in the laser room. The dashed line indicates the laser light path.

neutral density wheel was placed between the lens and detector. This allows for the amount of power getting sent to the detector to be easily changed by hand. The second piezo mirror was placed after the first detector pickoff on the top platform in the beamline room. A schematic of the top platform above the beamline in room 1361 with the first detector and second piezo mirror is shown in Figure 3.17. The second detector was placed next to the beamline with a pickoff, focusing, and filter setup identical to the first detector. A schematic of the second detector's location is shown in Figure 3.18. The mirrors and detectors connect to a central control box which controls the piezo movement according to the detectors signal. With the two stages installed the laser movement was eliminated and stabilized.

3.3 Beamline Setup

The BECOLA facility, shown in Figure 3.19, is located in the stopped beam experimental area at FRIB at MSU. Both fluorescence and resonant ionization spectroscopy techniques are used at the facility, accepting radioactive and stable ion beams at an approximate energy

Platform Above Beamline (Room 1361)

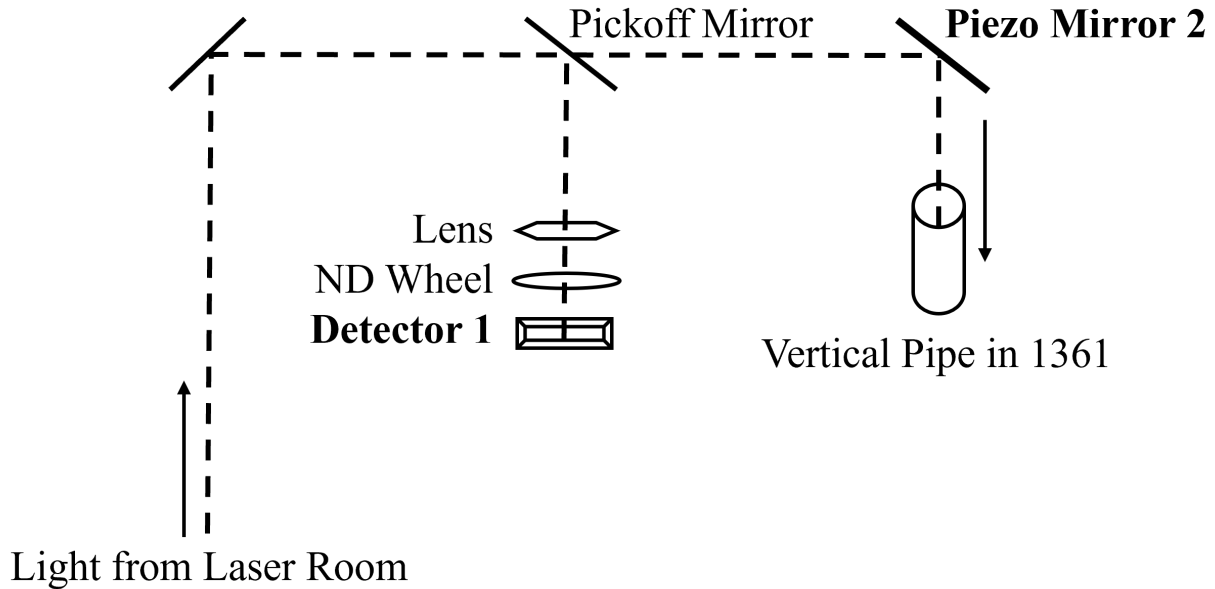
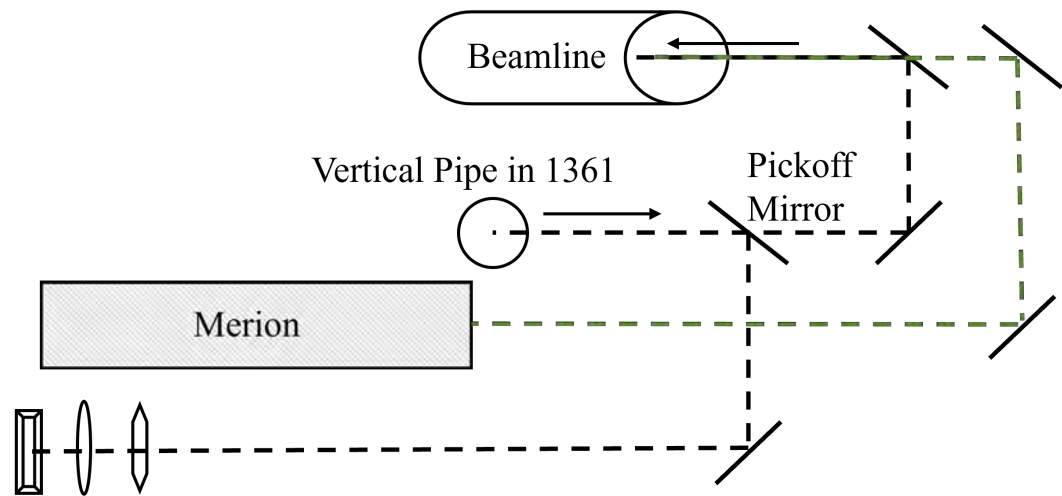


Figure 3.17 First detector and second piezo mirror of the feedback detection system location schematic. A schematic of the first detector and second piezo mirror for the feedback detection system is shown. They are both located in the top platform above the beamline in room 1361. The dashed line indicates the laser light path. Detector 1 works with Mirror 1 shown in Figure 3.17 and Mirror 2 works with Detector 2 shown in 3.18.

of 30 keV.

At FRIB [81] rare isotope beams are produced using a linear accelerator (LINAC) [82] and sent to the Advanced Rare Isotope Separator (ARIS) fragment separator [83] to select the isotope beams of interest. Following the fragment separator the ion beam can be delivered to a variety of experiments in the fast beam, stopped beam, and reaccelerated beam experimental areas. The BECOLA facility is in the stopped beam experimental area and will be the focus of this work. To stop the incoming fast ion beam and deliver a high quality low energy ion beam at the desired 30 keV energy, the fast ion beam from the ARIS fragment separator is delivered to one of the gas stoppers [84][85]. The gas stoppers stop the ion beam and deliver a 30 keV ion beam to the stopped beam experimental area, including the BECOLA facility. An overall schematic of the layout of FRIB can be found in Figure 3.20.

Platform Next to Beamline (Room 1361)



Detector 2 - ND Wheel - Lens

Figure 3.18 Second detector of the feedback detection system location schematic. A schematic of the second detector for the feedback detection system is shown. It is located next to the beamline in room 1361. The dashed line indicates the laser light path, black for UV and green for the Merion.

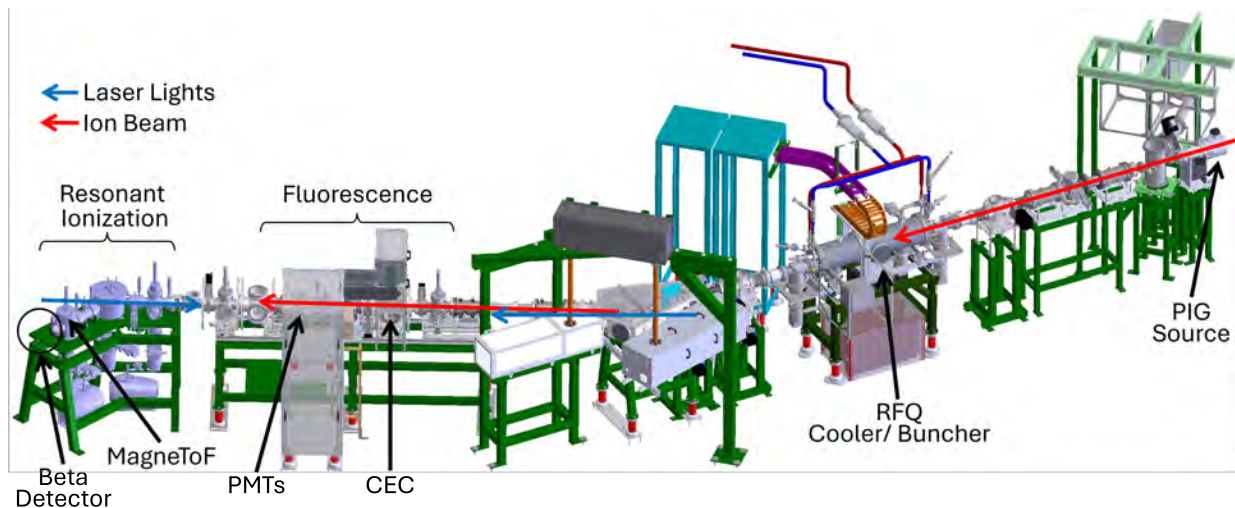


Figure 3.19 BECOLA beamline schematic. A schematic of the BECOLA beamline [96] is shown. The different beamline components laid out in this section are labeled appropriately; PIG source, cooler/ buncher, CEC, PMTs, MagnetoF, and beta detector. Note, the beta detector is not shown in the schematic and a circle is used to show where it is mounted. The red line indicates the ion beam path through the beamline and the blue line indicates the laser light path into the beamline from both the collinear and anti-collinear direction. The section of the beamline used for fluorescence and resonant ionization are indicated.

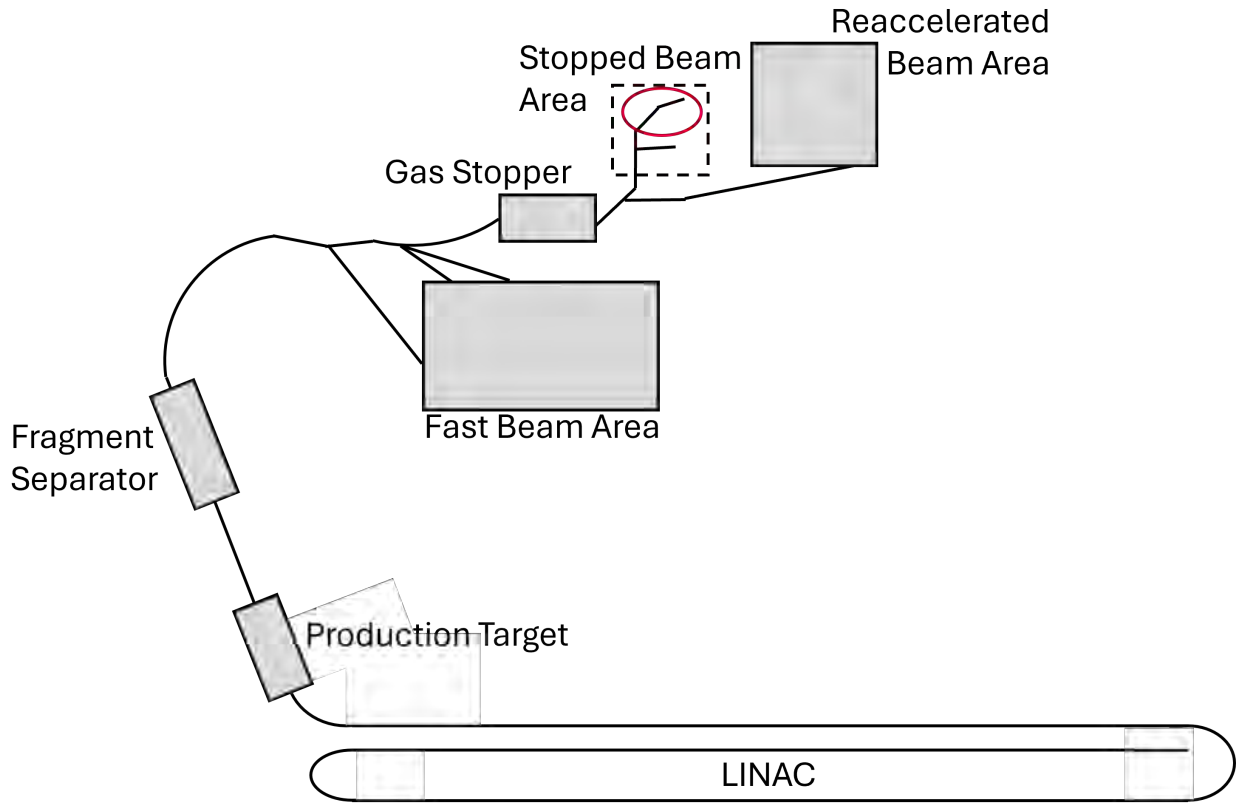


Figure 3.20 Simplified schematic of FRIB layout. A simplified schematic of the FRIB layout is shown. A detailed layout can be found in Reference [86]. The BECOLA facility is indicated by a red circle.

Once the ion beam is taken into the BECOLA facility it is injected into a radio frequency quadrupole (RFQ) cooler buncher. The cooler buncher cools the incoming ion beam and uses RF and DC potentials to trap the ion beam and transform it into ion beam bunches. The bunches can then be reaccelerated into the beamline at a typical energy of 30 keV at the corresponding time to the laser light. The ion beam, now in a bunch, continues down the beamline to a charge exchange cell. The charge exchange cell can neutralize the ion beam to create an atom beam. The bunched atom beam then meets the laser to excite the first step of the transition of interest. Once the first step is excited either the transition de-excites and emits a photon which can be detected by a PMT in the fluorescence detection region. Or the atom beam immediately interacts with more laser lights to create an ion that can be steered to an ion detector at the end of the beamline. The details of the beamline are

outlined below.

3.3.1 LINAC - main accelerator

The main accelerator at FRIB is the LINear ACcelerator (LINAC) [82]. For this experiment on Al a ^{28}Si beam was accelerated in the LINAC to 290 MeV per nucleon. This primary beam was then impinged on a 17.67 mm target of ^{12}C at the production target area of the FRIB facility. The resulting ion beam was then sent to the ARIS fragment separator [83]. Using the ARIS separator each isotope mass of interest was selected from the ion beam. The beam of selected mass was then injected into the gas cell of the gas stopper.

3.3.2 Gas Stopping

Beam from the ARIS fragment separator can be injected into one of two gas cells in the gas stopping area. The first is a large-volume RF-based gas catcher which contains RF ion-guiding ability along the chamber and a large overall internal volume [84] [87]. Before entering the gas catcher the ions kinetic energy is reduced by passing through a series of solid degraders and a monochromatic wedge while also reducing the spread in beam energy. Once ions are in the gas catcher they collide with helium buffer gas to be thermalized. A static drift field is applied to move the ions to a section of the catcher that has a large gas flow able to extract the ions from the cell. The RF potential applied along the cell maintains the focus of the ions to the hole for extraction. The second is an Advanced Cryogenic Gas Stopper (ACGS) with an RF wire-carpet, cryogenic cooling, and a planar geometry [85]. Same as the first gas cell described, before entering the cell the ions go through a series of Al degraders to decrease the energy of the ion beam. Then the ions are injected into the cryogenic stopping chamber where ions are stopped through collisions with the helium gas. The benefit of cryogenic cooling of the helium gas chamber is to reduce molecular formation that would become a beam contaminant. At cryogenic temperatures, the kinetic energy of the ions is reduced via collisions with cold He atoms and any contaminating gases freeze in the stopper to suppress unwanted molecular formation. The RF wire-carpet [85] extends the length of the chamber and quickly transports ions through the cell to the exit wall of the

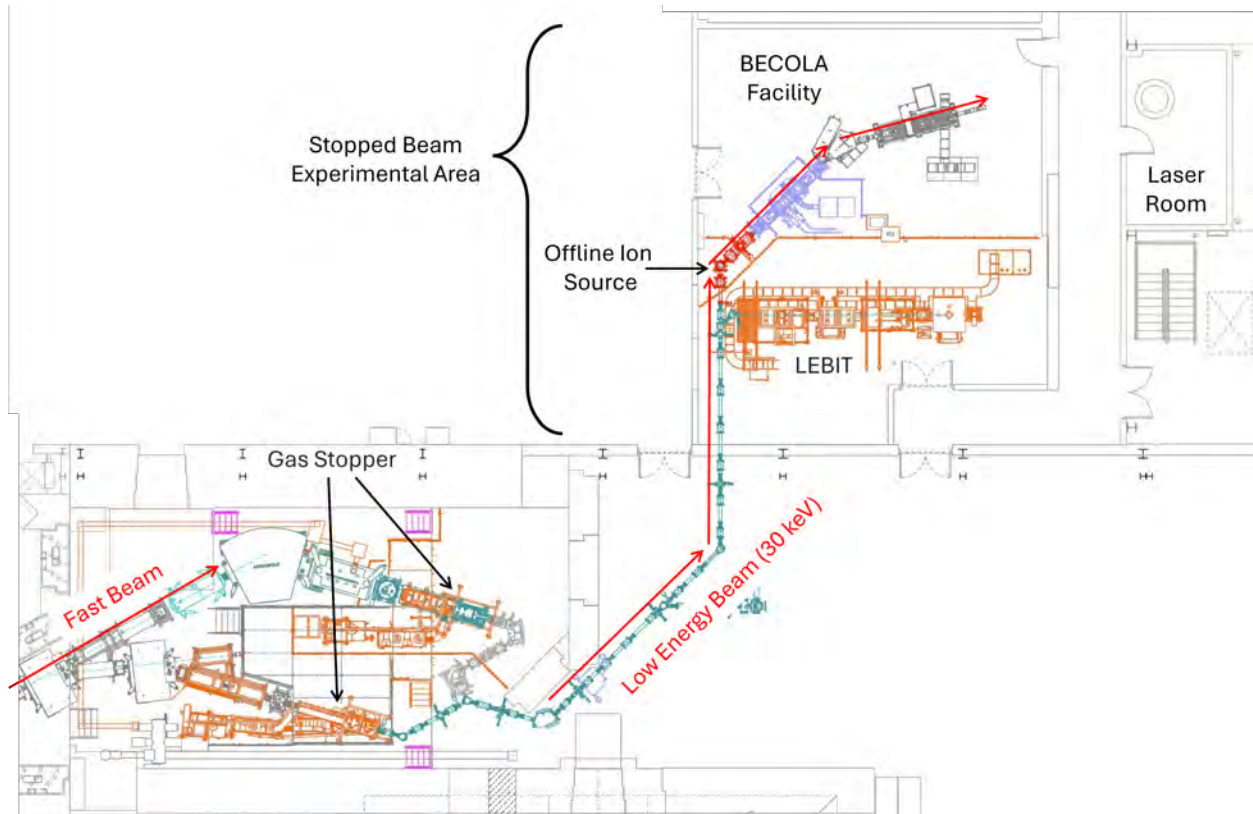


Figure 3.21 Stopped beam experimental area layout. A schematic of the stopped beam experimental area [84]. Fast ion beam from the main linear accelerator or batch mode ion source at FRIB enters the from the bottom left hand side of the figure. The beam then passes through a gas stopper which then delivers a 30 keV ion beam to either the LEBIT or BECOLA facility in the stopped beam experimental area. This figure also points out the laser room across the hall from the BECOLA beamline that holds the lasers needed for spectroscopy.

chamber. A small nozzle at the exit has a strong gas flow to extract the ions. After the ions are extracted from either cell they are sent to the stopped beam experimental area.

3.3.3 Stopped beam experimental area

The stopped beam experimental area, Figure 3.21, is located after the gas stopper [84]. Beam from the ARIS fragment separator is delivered to one of the gas cells, thermalized, extracted at an energy of 30 keV, and then delivered to the stopped beam experimental area. In addition to beam from the gas stopper a Batch Mode Ion Source (BMIS) [88] located in the FRIB experimental vault N4 next to the gas stopper can be used to deliver beam to the stopped beam experimental area. The BMIS is used for production of long-lived

isotopes, which can be used for laser spectroscopy to support online experiments from the LINAC or for independent experiments. The BMIS is able to produce unstable isotopes in parallel with the LINAC and can be run when the LINAC is producing beams for other areas in the lab. This allows time for experiments to be run on new elements such as the BECOLA Silicon experiment [57] or to support upcoming LINAC experiments such as the upcoming BECOLA Thorium experiment. The upcoming Thorium experiment will be the heaviest mass the BECOLA facility has ever received and a new element for the gas stopper to deliver to the BECOLA facility. To prepare for the LINAC experiment on rare Thorium isotopes moving towards the dripline, the BMIS can deliver radioactive isotopes of Thorium to test the gas stopper chemistry and perform spectroscopy. The BECOLA facility cannot produce unstable radioactive beams independently. This preparation using the BMIS source will allow for a more successful LINAC experiment and limit the number of hours needed to run the LINAC for one experiment.

In addition to the BECOLA facility in the stopped beam experimental area are the Low Energy Beam Ion Trap (LEBIT) [89] beamline where high precision mass measurements are performed, and general experimental ports where external users can set up their equipment and run experiments.

3.3.4 PIG source

A Penning Ionization Gauge (PIG) [90] ion source was used to produce stable ^{27}Al ions for offline measurements to prepare for the online Al experiment, measure additional transitions, and throughout the online experiment to measure calibration runs. The Penning Ionization Gauge (PIG) ion source is a discharge plasma sputtering source. Two cathodes of the element of interest, in this experiment Aluminum, are placed on either side of an anode. Cathodes used in this work are shown in Figure 3.22. The source itself is filled with a Neon gas to maintain the plasma. Other buffer gases can be used such as Argon depending on the element being produced. A potential is applied to the cathodes and anode to create a potential difference between the anode and cathodes. This potential difference triggers the



Figure 3.22 Aluminum cathodes from PIG source. A set of used Aluminum cathodes that were used for offline measurements are shown. The cathodes are slowly eaten away in the source as the buffer gas is accelerated into them. The surface of the cathodes are concave and show marks from where the buffer gas ions collided into the cathodes to release Aluminum ions into the BECOLA beamline. In the cathode on the left a small hole can be seen in the center. This is where the Aluminum ions are extracted out of the source into the beamline by the extraction electrode.

discharge to create plasma and accelerates the Neon buffer gas into the cathodes releasing Al atoms which are ionized in the plasma via the electron impact. The plasma is contained within the source due to an axial magnetic field. To extract the ions an extractor, extraction electrode, is at the front of the source with an applied potential to pull the ions through a small hole in one cathode, releasing them into the beamline. A schematic of the PIG source is shown in Figure 3.23.

For the Aluminum experiment the PIG source was operated with the following conditions. The cathode voltage was set to -290 volts and the anode to 150 volts. The leakage current of the cathode was 29 mA. The magnet to confine the plasma was set to 1.5 A. The buffer gas valve was set to 16 percent. For maximum ions extracted from the source the extractor

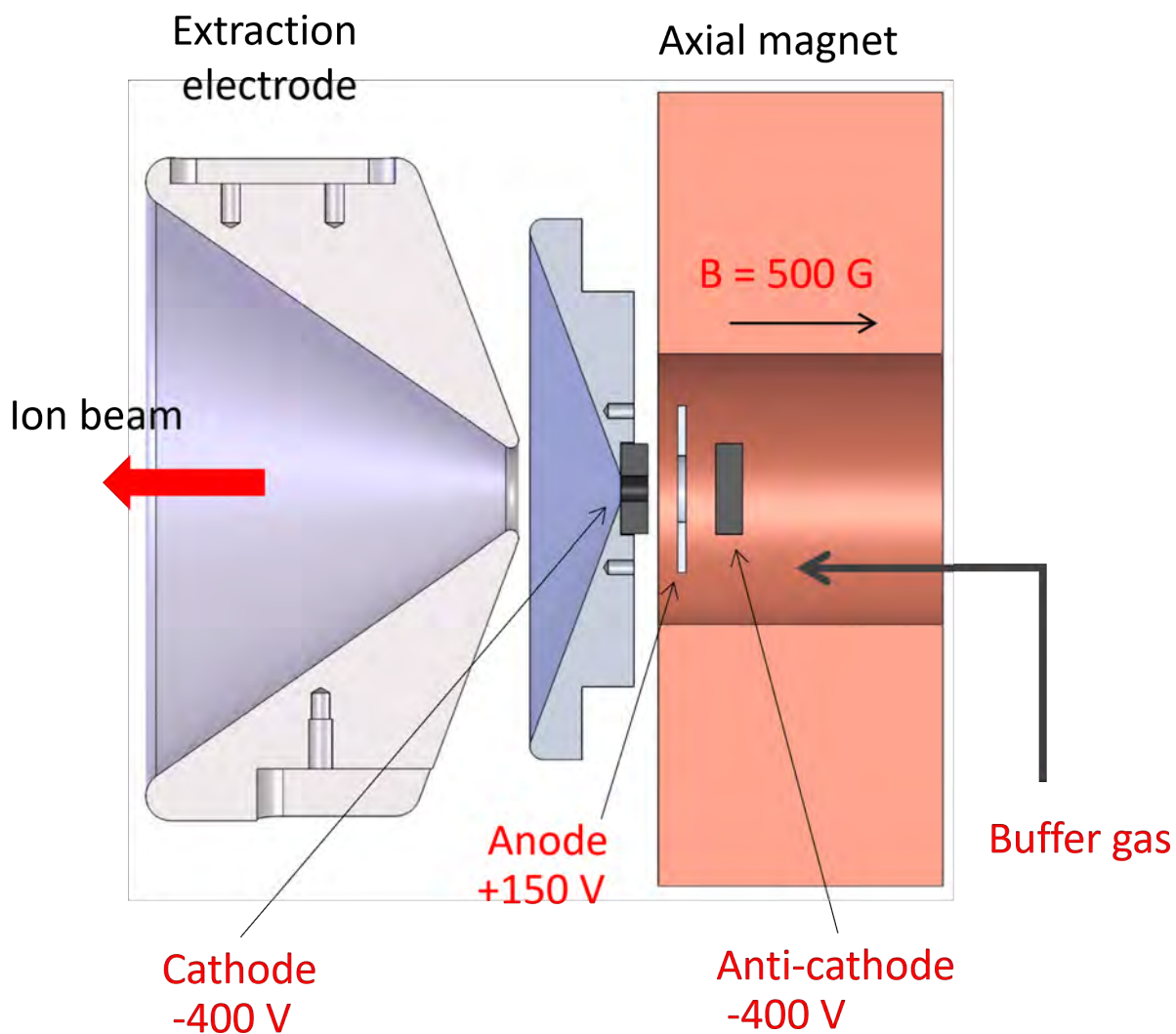


Figure 3.23 PIG source schematic. A schematic of the PIG source from Reference [91] is shown. The elements of the source are labeled accordingly. The buffer gas fills the orange colored section of the source. Ions are extracted out of the cathode into the beamline to the left of the figure.

was set to -3200 volts. To tune the ion optics position through the beamline the extractor is set to create the maximum number of ions coming out of the source. For the measurement of stable ^{27}Al the maximum number of ions is too much and distorts the hyperfine spectra due to the excessive space charge. Once the ion optics are tuned and adjusted, the extractor is reduced to -320 volts. In addition to reducing the extractor voltage, the steering of the ions into the beamline can be de-tuned to further reduce the number of ions. All ^{27}Al measurements were performed with about 2 pA of beam measured right after the RFQ at the BOB0. Spectroscopy was performed with 100 Hz repetition rate and the number of ions was kept around 1×10^5 ions per bunch.

3.3.5 RFQ Cooler/ Buncher

Whether the ion beam entering the BECOLA beamline comes from the gas stopper, the BMIS, or the offline PIG source, all beams are injected into the Radio Frequency Quadrupole (RFQ) cooler and buncher [92]. The cooler buncher works in two sections, one for cooling and one for bunching. The first section the ion beam encounters is the cooling section. The cooling section is filled with a He buffer gas at 0.05 Torr (at a set pressure), which the ion beam collides with, slowing it down and reducing the energy. The quadrupole RF field radially confines the ions. An applied DC potential gradient axially drags the ions towards the trapping region. In the trapping section, the DC potential depth is matched with the pseudo potential of the RF to achieve a high trapping efficiency. The DC potential voltage is then switched, reduced, to release the ions in a bunch. The time between releasing the bunches controls the amount of ions in each bunch, and the exact time the bunches are released is synchronized with the laser systems to ensure the ion bunch interacts with the lasers in the proper region of the beamline. A schematic for the cooler buncher can be found in Figure 3.24.

The cooler buncher settings must be adjusted for different masses to ensure the ions are trapped efficiently and stable in the bunching region. The stability of the isotope of interest in the cooler buncher can be determined using the Mathieu stability parameter, q , which

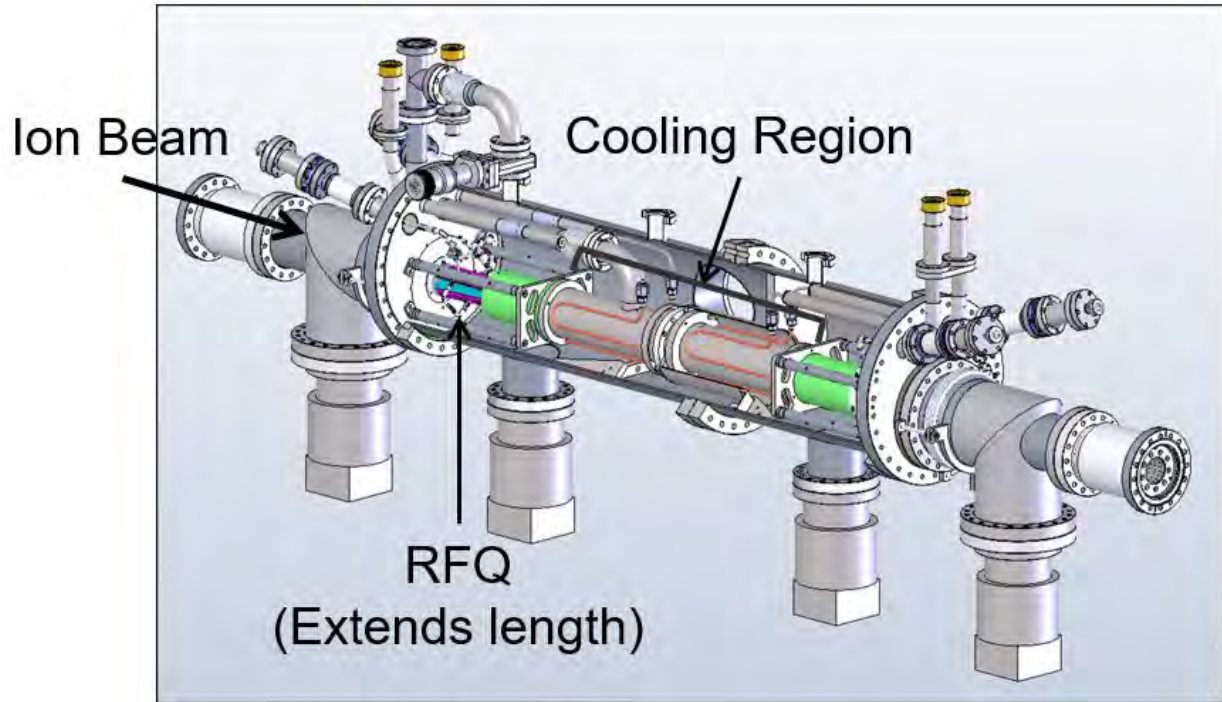


Figure 3.24 Cooler buncher schematic. A schematic of the cooler buncher from Reference [92] is shown. The incoming ion beam enters from the top left of the figure and then is cooled and bunched in the corresponding regions and continues through the beamline to the bottom right of the figure.

is given by Equation 3.1 where e is the charge of the ion, V_{RF} is the peak to peak radio frequency (RF) amplitude, m is the mass of the ion, r_0 is the distance from the central axis to the RFQ electrode, and ω_{RF} is the RF angular frequency [92].

$$q = \frac{2eV_{RF}}{mr_0^2\omega_{RF}^2} \quad (3.1)$$

To ensure the ions are stable in the buncher, the Mathieu parameter must be less than 0.9 [92].

In addition to setting the Mathieu parameter, the proper potential depth for the isotope of interest in the cooler buncher must be considered. The pseudo potential is important to efficiently accept ion beams with a large energy spread, the pseudo potential must be deeper than the energy spread in addition to matching with the DC potential in the trapping section. The depth of the psuedo potential can be calculated by Equation 3.2 where e , V_{RF} , m , r_0 ,

and ω_{RF} are defined as before and r is the distance of the ions to the RFQ electrode [92].

$$V_{psuedo}(r) = \frac{eV_{RF}^2}{4mr_0^4\omega_{RF}^2}r^2 \quad (3.2)$$

The ions can be assumed to be on the central axis, $r = r_0$. This reduces the psuedo potential to Equation 3.3.

$$V_{psuedo} = \frac{eV_{RF}^2}{4mr_0^2\omega_{RF}^2} \quad (3.3)$$

Combining the equations for both the psuedo potential and the Mathieu parameter, the psuedo potential can be written in terms of the Mathieu parameter as shown in Equation 3.4.

$$V_{psuedo} = \frac{qV_{RF}}{8} \quad (3.4)$$

The Mathieu parameter and pseudo potential must be altered to ensure the proper condition for the ions.

Of the parameters in the Mathieu parameter and psuedo potential equation, only V_{RF} and ω_{RF} can be varied. The remaining parameters are set by the incoming ion properties or the physical geometry of the cooler buncher. For the injection section, the RF is applied through an impedance matching circuit and an LC resonator. For the bunching section, the RFQ electrodes were connected in parallel to a 50 Ω resistor with an applied frequency around 1 MHz which is approximated as DC. V_{RF} can be varied directly using the function generator signal and amplifier settings which are used to set the RF amplitude. ω_{RF} cannot be varied directly, but can be adjusted indirectly through changes of the LC resonator and impedance matching circuit. To find ω_{RF} in units of radians per second Equation 3.5 can be used, where L is the inductance of the circuit and C is the capacitance.

$$\omega_{RF} = \frac{1}{\sqrt{LC}} \quad (3.5)$$

The capacitance must be varied manually to alter the LC circuit of the system. Previously, the circuit was setup using a variable air capacitor and a cylindrical coil air core inductor. During the Aluminum work the BECOLA facility was also taking measurements on Thorium.

This meant the cooler buncher needed to be able to switch easily between masses across a range from 22 to 232 atomic masses. The existing circuit was not set up for varying parameters for such a large range. To add a larger mass range capability to the BECOLA beamline the variable air capacitor was switched to a 4000 pF variable vacuum capacitor. This change allowed for the full range of capacitance needed for the full mass range, however the large capacitance change altered the impedance matching of the system. To restore proper impedance matching, the inductor was also changed to a large disc air core inductor. These alterations allow for an LC circuit capable of varying the ω_{RF} for the large mass range. The previous and upgrading LC circuits are shown in Figure 3.25 and 3.26 respectively.

For the Aluminum experiment the injection into the cooler buncher was set to 3.2 MHz with a 0.8 V amplitude amplified to a 482 volt peak to peak amplitude. Resulting in a 0.697 Mathieu parameter and 41.970 psuedo potential. The bunching section was set to 1.3 MHz with a 0.36 volt amplitude. Upstream 6 W were applied and 17 W applied downstream.

3.3.6 Charge Exchange Cell

For some elements, including Aluminum, the neutral state electronic structure is favorable for laser spectroscopy. To get the ion beam into the neutral state a Charge Exchange Cell (CEC) [93] is needed. The CEC neutralizes the ion beam through ion-atom charge-exchange reactions. The CEC is filled with circulating Sodium vapor. There is a reservoir of sodium at the bottom of the cell that creates a vapor when heated. The vapor rises through the cell crossing the interaction region, where the ion beam crosses through the cell, to the top of the cell. At the top of the cell there is a condensing region which condenses the sodium vapor which then falls back into the reservoir at the bottom. This heating and condensing creates a circulating sodium vapor process, maintaining sodium vapor at the interaction region with the ion beam. The incoming ion beam can then acquire a loosely bound electron from the circulating vapor. Equation 3.6 shows the chemical equation of the electron exchange, where ΔE is the exchanged energy in the electron transfer process.



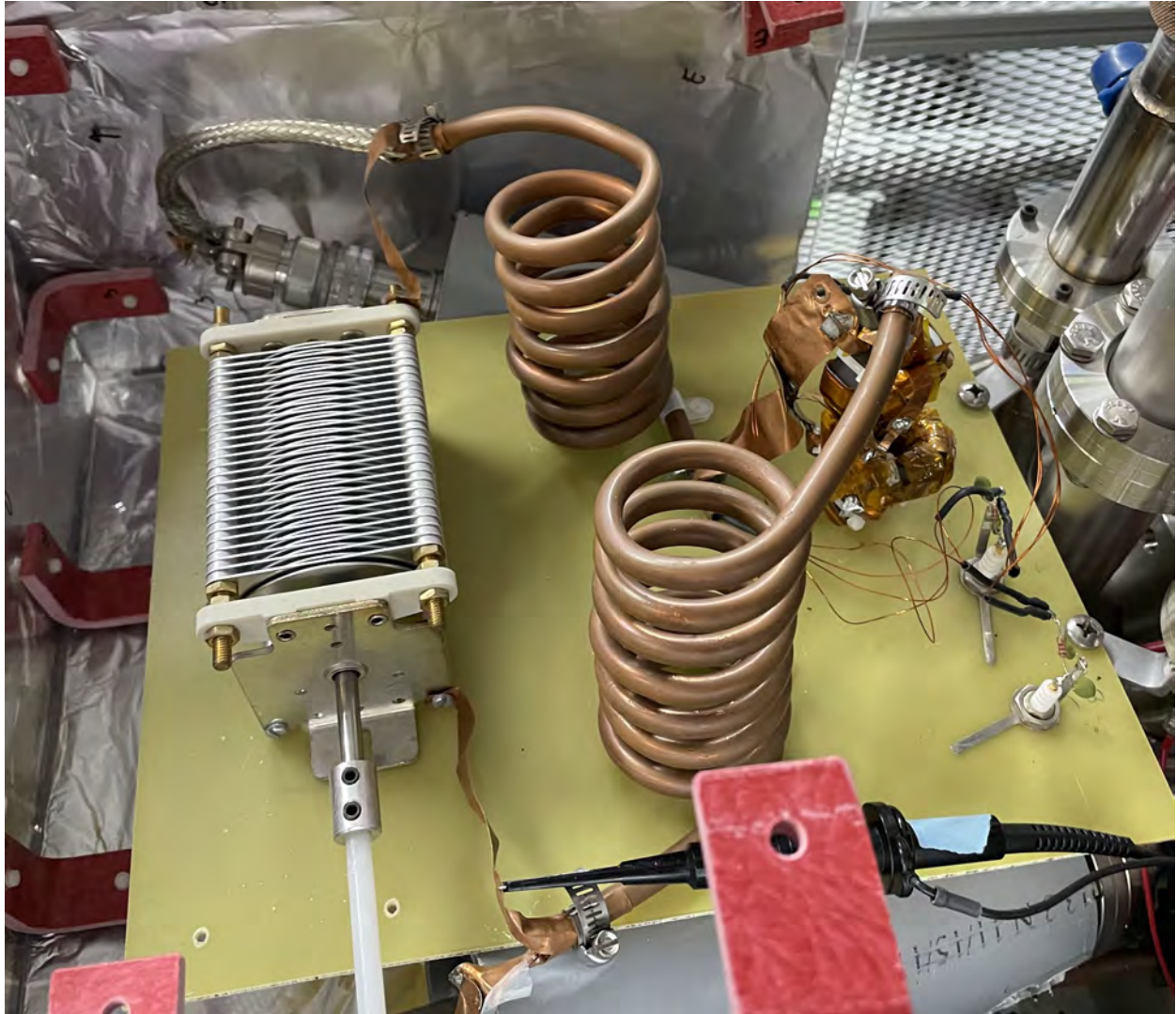


Figure 3.25 Original LC circuit for the cooler buncher. The previously used LC circuit is shown with the variable air capacitor on the left and coil inductor on the right. The impedance matching was achieved with a 3-core transmission line transformer.



Figure 3.26 Upgraded LC circuit for the cooler buncher. The upgraded LC circuit is shown with the variable vacuum capacitor on the left and disc inductor on the top right. The impedance matching was achieved by a 1:49 step down transformer.

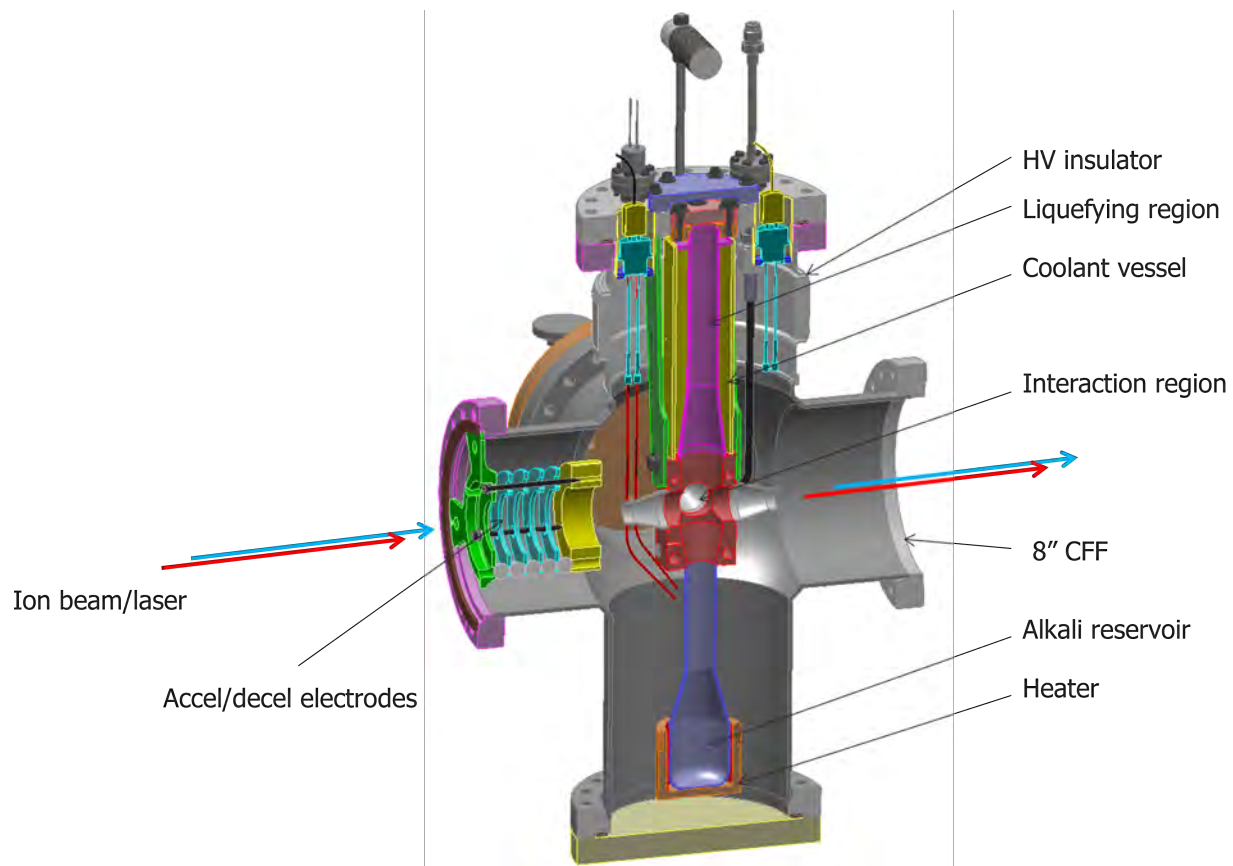


Figure 3.27 CEC schematic. A schematic of the CEC from Reference [93] is shown. ion beam enters the cell from the left hand side of the figure and exits as an atom beam to the right. Components of the cell are labeled accordingly.

After the ion beam is neutralized the atom beam interacts with the lasers in an interaction region to excite the desired transition. A schematic and photo of the charge exchange cell are shown in Figures 3.27 and 3.28 respectively.

For the Aluminum experiment the power supply to set the CEC temperature was set to 3.6 A. The temperature of the sodium reservoir was kept around 450 degrees and the condensing region around 105 degrees.

3.3.7 PMT

When doing fluorescence measurements resonant photons are detected, to detect them photomultiplier tubes (PMTs) are used. Fluorescence detection was only used for two of the transitions tested offline for Aluminum, resonant ionization was used for most transitions tested offline and the online experiment. A PMT detects photons and then multiplies the



Figure 3.28 CEC. A photo of the CEC taken when the cell was removed from the beamline to be cleaned is shown. The cell usually hangs into the beamline to intersect with the ion path.

photo electrons from the cathode in a cascade process creating voltage pulses to be digested and fed into the DAQ. The photon detection region that houses the PMTs is in a photon detection region designed to limit background and optimize resonant counts. An ellipsoidal reflector was used to collect the resonant photons. Resonant photons were emitted from one of the focal points of the reflector and focused to the other, where the PMT was installed. Background light originating from any other location than the focal point is focused to the outer edge of the PMT, creating spacial separation to enhance the signal to noise ratio. The interior surface of the vacuum chamber in the interaction region is black coated to reduce the scattered laser light from getting to the PMT and causing background. Apertures are in place to cut any halo laser light the incoming laser light may have. Details of the photon detection system and PMTs are outlined in [94]. A schematic of the photon detection region is shown in Figure 3.29.

3.3.8 RISE

Prior to the work on Aluminum the BECOLA beamline ended after the photon detection region and only fluorescence was used for spectroscopy. Through collaboration with the Massachusetts Institute of Technology (MIT) an extension to the beamline was made. The Resonant Ionization Spectroscopy Experiment (RISE) extension is highlighted in Figure 3.30. The extension includes a field ionization region, MagneToF detector, and other ion optic components. This extension was added in addition to the laser system upgrades, allowing the BECOLA beamline to perform both fluorescence and resonant ionization spectroscopy. The extension was installed and commissioned with the offline Aluminum work throughout 2022 and 2023. The first online beam taken into the RISE extension was the online Aluminum experiment in May 2024, the first online resonance detected using RISE is shown in Figure 3.31.

3.3.9 MagneToF

The MagneToF detector [95] is an ion detector used for resonant ionization and the Aluminum experiment. It is a fast-timing electron multiplier that has single ion counting

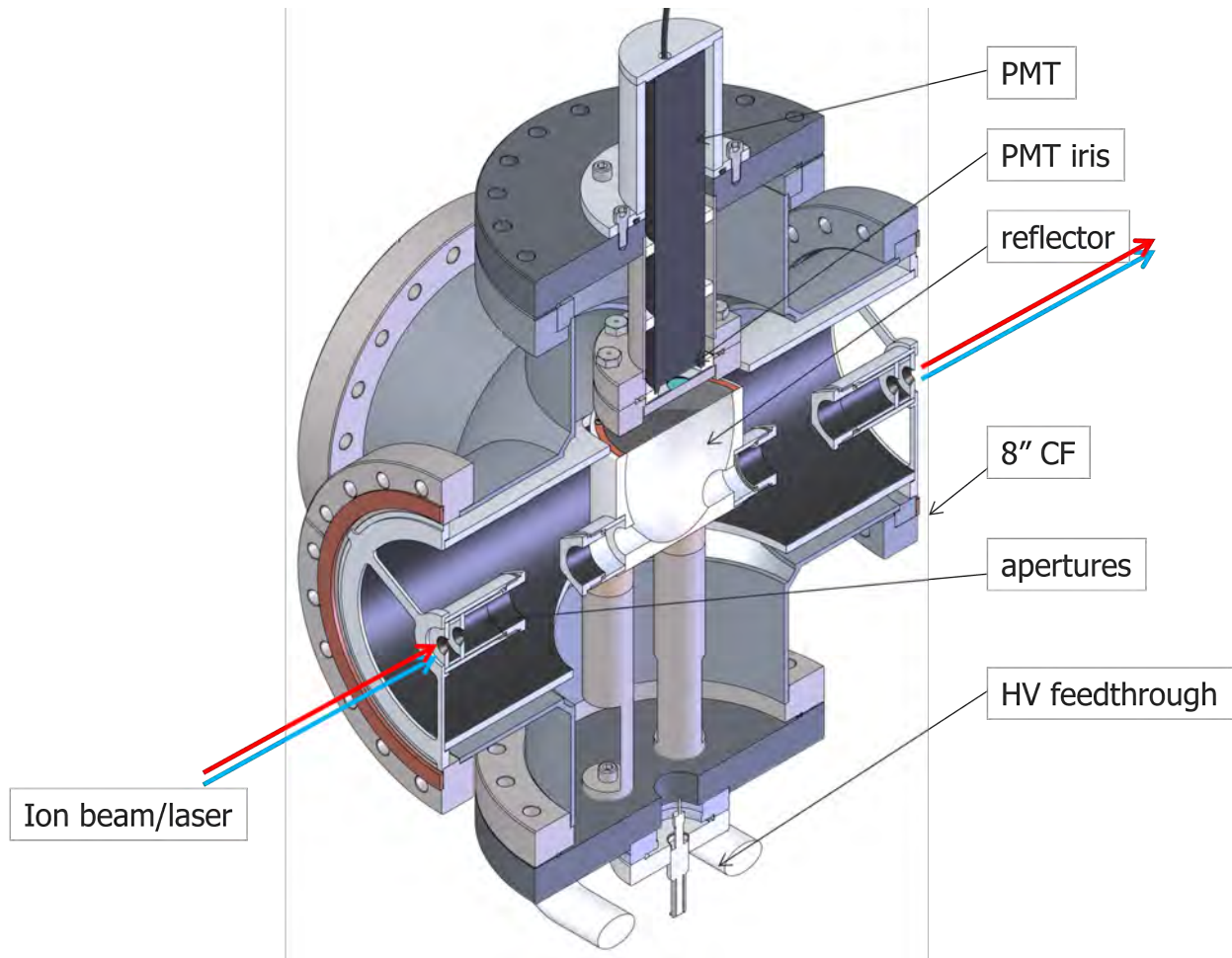


Figure 3.29 Photon detection system schematic. A schematic of the photon detection system from Reference [94] is shown.

ability and nanosecond time resolution. The MagneToF detector has a faster response time and higher time resolution than a PMT and is not largely affected by laser background. The signal from the detector was fed to a discriminator to remove electronic noise and possible double pulse counting to reduce background noise. The threshold for detecting an ion can be adjusted and was optimized for the Aluminum experiment. A photo of the MagneToF detector outside of and installed in the beamline can be found in Figure 3.32 and 3.33 respectively.

3.3.10 Beta Detector

For very low count isotopes and isotopes with a large stable beam contaminant a beta detector was designed in collaboration with OakRidge National Lab (ORNL). Although the

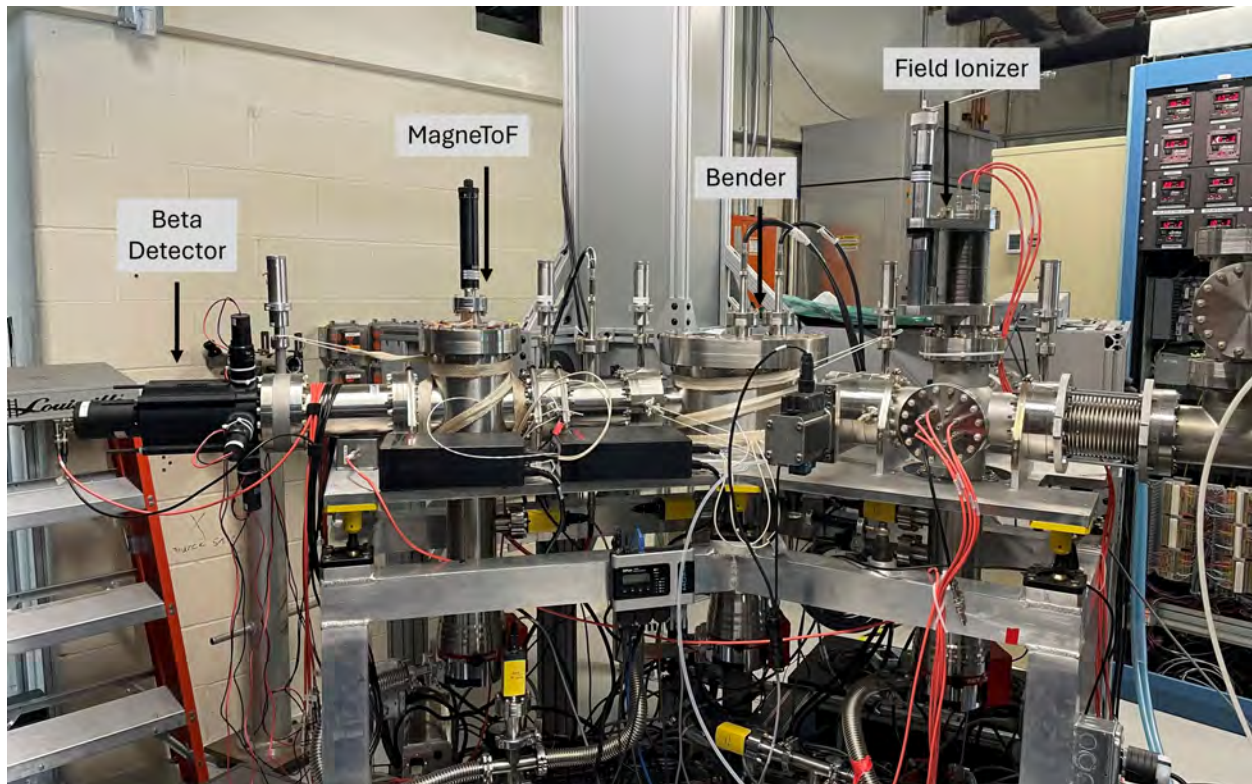


Figure 3.30 RISE extension. A detailed zoom in of the RISE extension is shown. All elements added to the BECOLA beamline for the RISE extension are shown and discussed elements are labeled accordingly.

beta detector was not used for the Aluminum experiment, it will provide great opportunity to detect radiations from rare isotopes and increases the capability and reach of the BECOLA beamline. The beta detector installed at the end of the BECOLA beamline is shown in Figure 3.34. The detector is made up of plastic scintillators coupled with five PMTs. Four of the PMTs are arranged around a single thin plastic scintillator and make up the "delta E". The fifth PMT is located past them with a thick plastic scintillator and makes up the "big E" section. Signals are counted based on coincidence counts of the PMTs. Laser ionized ions are stopped on the surface of the glass window before the beta detector and decaying beta particles are then detected. The delta E is setup in an "or" configuration. The delta E gives a signal count if any of the small PMTs in the delta E detect a beta particle on the thin plastic scintillator. For the detector to produce a signal the delta E and the big E must both produce a signal in coincidence on their respective scintillators. The geometric

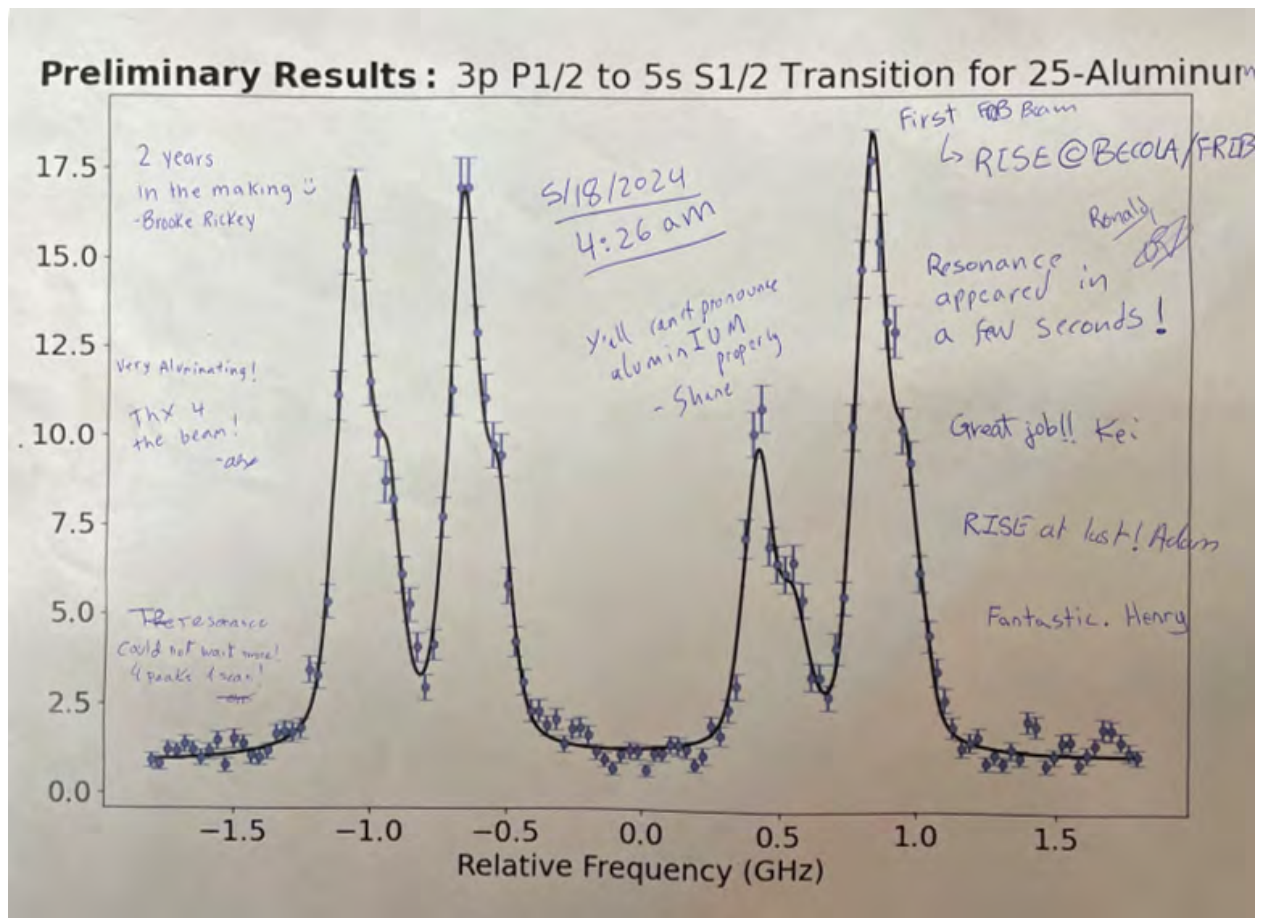


Figure 3.31 First resonance with online beam using the RISE extension. The very first resonance from the new RISE extension using online ion beam is shown. The spectrum is from the first set of scans of ^{25}Al . Notes and signatures from the collaboration members who took shifts for the Aluminum experiment are drawn on to commemorate the first online resonance.

configuration of the detector can be modified for different experiments and sensitivities.

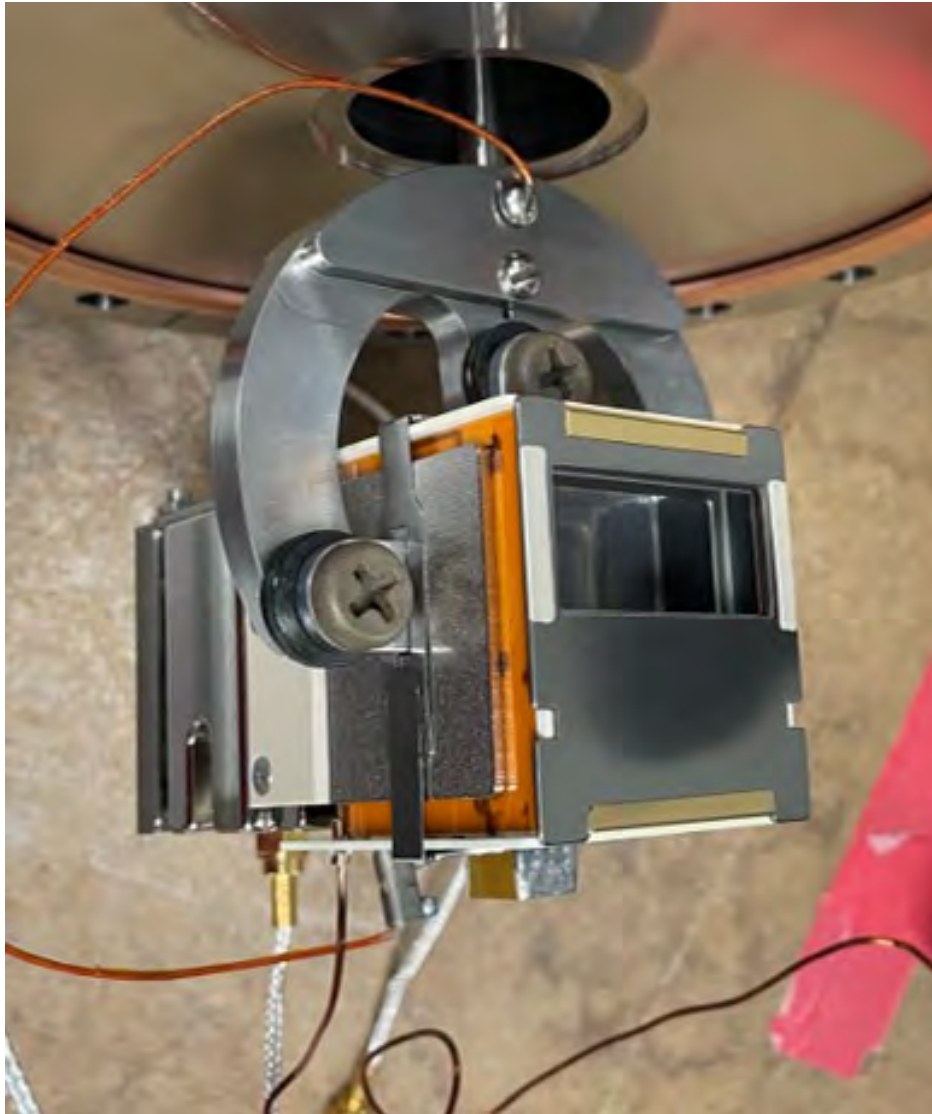


Figure 3.32 MagneToF detector. The MagneToF detector mounted on its holder outside of the beamline is shown. Ions enter the detector through the clear screen seen in the figure, where they are counted and the signal is sent to the DAQ.

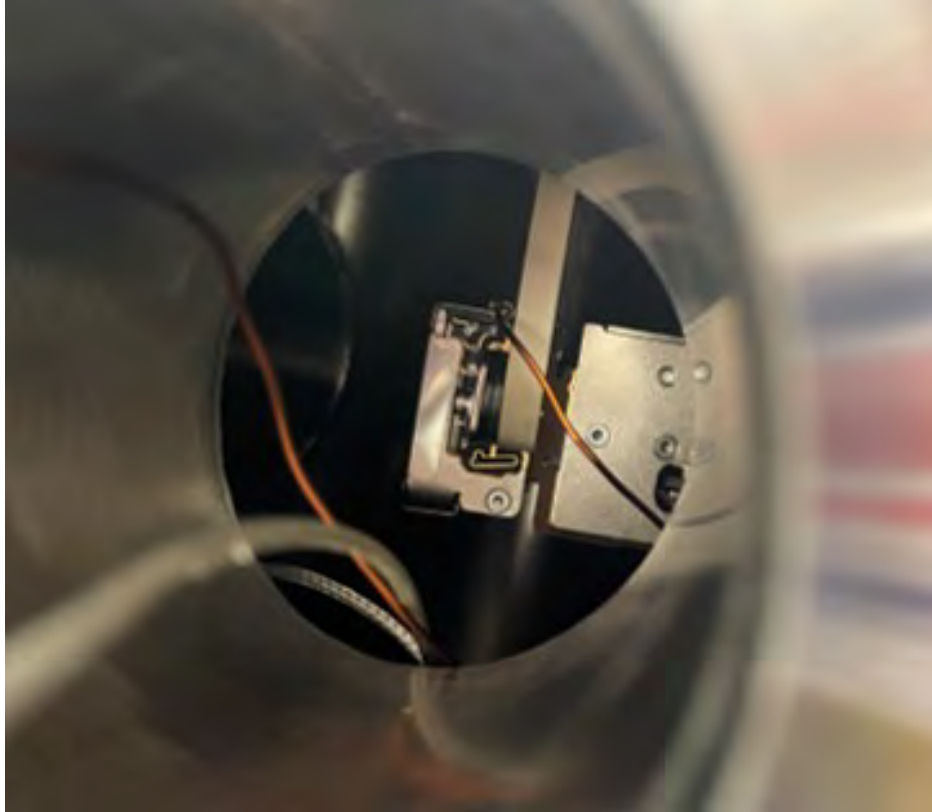


Figure 3.33 MagneToF detector inside beamline. The MagneToF detector is shown hanging in beamline. Ions enter the detector from the left hand side of the figure. The cables coming out of the page in the figure are the cables to send the signal detected to the DAQ and the power supply for the detector.

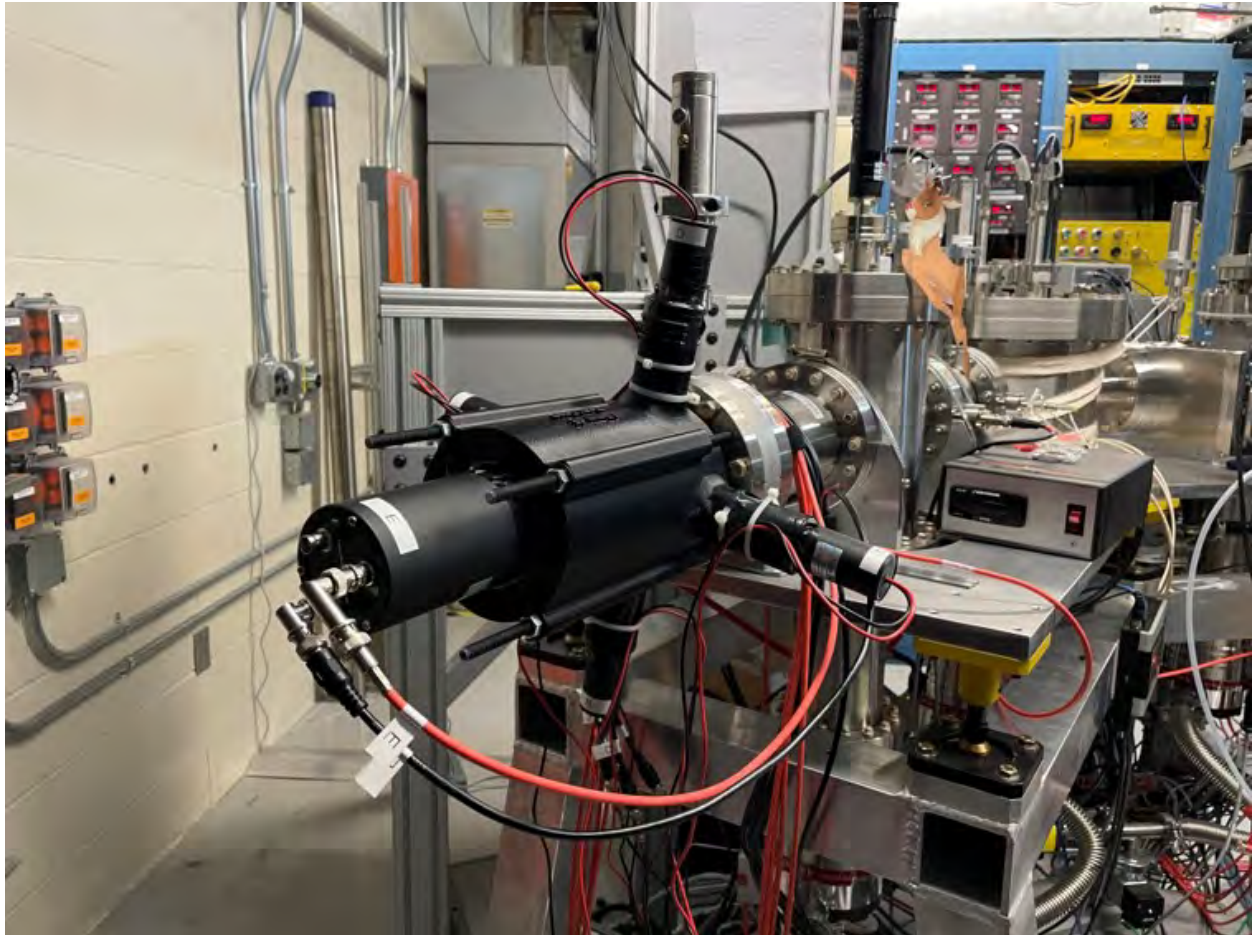


Figure 3.34 Beta detector. The beta detector mounted to the end of the BECOLA beamline is shown. Each PMT that makes up the detector has a cable for the signal to the DAQ and to a power supply.

CHAPTER 4

EXPERIMENTAL DATA

4.1 Hyperfine Spectra

For laser spectroscopy experiments, the laser being used to probe the transition is set to the fine structure frequency. A hyperfine spectra is obtained by scanning the laser frequency over a small range around the fine structure frequency. This frequency can be determined from the energy levels of the transition. The transition energy is determined by the difference between the energy of the excited state and the energy of the initial state, typically the ground state. The laser frequency can then be determined by Equation 4.1, where a sum is used for collinear measurements and difference for anticollinear measurements, q is the charge state of the atom being studied, U is the total potential energy of the beam, and m is the mass in $\frac{MeV}{c^2}$.

$$\text{laser frequency} = \text{transition energy} \times \gamma(1 \pm \beta)$$

$$\begin{aligned} \gamma &= \frac{1}{\sqrt{1 - \beta^2}} \\ \beta &= \sqrt{1 - \frac{1}{1 + q^2(\frac{U}{m})^2 + \frac{2qU}{m}}} \end{aligned} \quad (4.1)$$

The resulting laser frequency will be in the same units as the input transition energy.

The transition's hyperfine spectrum is then produced by scanning the laser frequency through a small range around the set fine structure frequency. For laser spectroscopy, the ions in the beamline see a Doppler shifted laser frequency. For collinear spectroscopy the Doppler shifted frequency the ions see can be found by Equation 4.2.

$$f_{ions} = f_{laser} \sqrt{\frac{1 - \beta}{1 + \beta}} \quad (4.2)$$

β can be solved for as a function of total potential, shown in Equation 4.3, where e is the elementary charge, c is the speed of light, U and m are defined as above [96].

$$\beta = \sqrt{1 - \left(\frac{mc^2}{eU + mc^2}\right)^2} \quad (4.3)$$

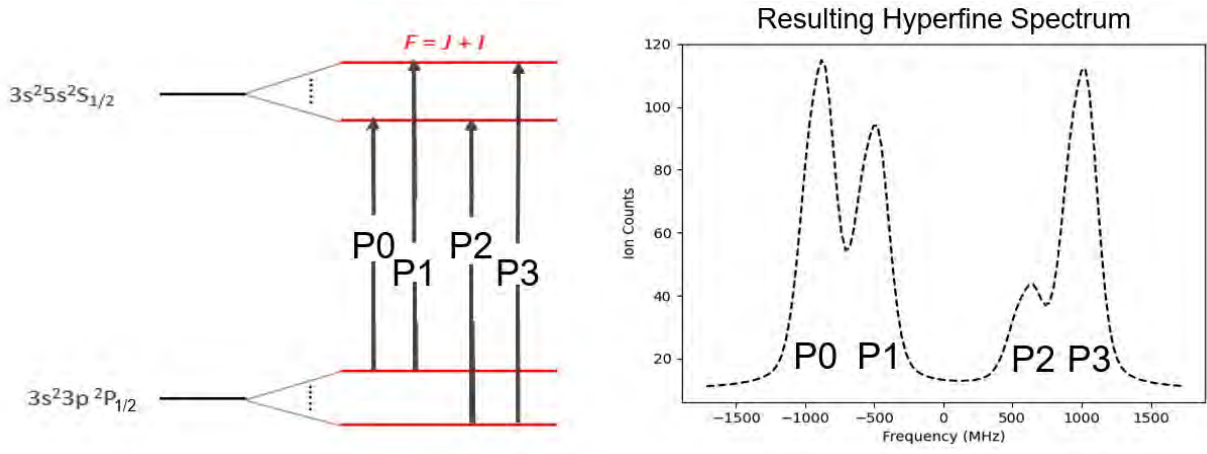


Figure 4.1 Corresponding hyperfine transition to peak in the hyperfine spectra. Each allowed transition in the hyperfine spectra directly corresponds to a resonant peak in the hyperfine spectra. The corresponding transition line is labeled to match the resonant peak in the simulated hyperfine spectrum example.

This allows the frequency seen by the ions to be varied by changing the applied potential to the ions rather than the laser frequency. U is the sum of the voltages applied to the beam including the main potential that determines the beam energy and a small scanning voltage applied to the charge exchange cell. This is an advantage since the laser frequency tends to be unstable when the frequency setpoint is varied to scan, creating possible uncertainty. The potential can be varied by applying a small voltage to the charge exchange cell or to the photon detection region for atom and ionic beam laser spectroscopy, respectively.

Scanning over the small range of frequencies, each allowed hyperfine transition is excited. At the frequency each transition is excited, a resonant peak is produced in the spectrum. Comparing the resulting hyperfine structure, each peak in the spectrum directly corresponds to an allowed transition. In Figure 4.1 an example for an Aluminum-27 transition is shown where each allowed transition is labeled to show the correlating resonant peak in the hyperfine spectrum. The resulting spectrum can be fit to extract parameters of the hyperfine structure. Fitting details are discussed in the Analysis chapter.

4.2 Stable ²⁷Al Offline Transitions

In preparation for the online Aluminum experiment, a transition had to be chosen that would obtain the best results; highest statistics with a large efficiency. Seven different

transitions, involving six different states, were measured to both commission the new RISE beamline extension and pick a transition for the online experiment. All transitions studied are detailed in the Appendix. The two transitions that were considered for the online run are summarized below. The hyperfine coefficients for all transitions studied were measured and can be found in Table 4.1 and Table 4.2.

Table 4.1 *A hyperfine coupling constants.* A hyperfine coupling constants from this work, theory, and previous literature values. Literature 1 are values from combining different infrared measurements in Reference [97]. Literature are values found by atomic beam magnetic resonance for the ground states and performing ultraviolet laser spectroscopy for the excited states in Reference [98]. Literature 3 are values from collinear laser spectroscopy measurements from [99].

$A(\text{MHz})$	Theory	Experiment	Literature 1	Literature 2	Literature 3
$3p\ ^2P_{1/2}$	510.90	502.92(0.41)	502.0(0.4)	502.04(0.97)	–
$3p\ ^2P_{3/2}$	99.22	94.47(0.05)	94.0(0.4)	93.76(0.71)	94.33(0.04)
$5s\ ^2S_{1/2}$	124.84	135.90(0.05)	–	–	–
$yd\ ^2D_{3/2}$	–	-108.22(0.16)	–	–	–
$yd\ ^2D_{5/2}$	–	-205.90(0.12)	–	–	–
$4s\ ^2S_{1/2}$	418.20	431.86(0.28)	421.00(15)	431.84(0.91)	–

Table 4.2 *B hyperfine coupling constants.* B hyperfine coupling constants from this work, theory, and previous literature values. Literature 1 are values from combining different infrared measurements in Reference [97]. Literature are values found by atomic beam magnetic resonance for the ground states and performing ultraviolet laser spectroscopy for the excited states in Reference [98]. Literature 3 are values from collinear laser spectroscopy measurements from [99].

$B(\text{MHz})$	Theory	Experiment	Literature 1	Literature 2	Literature 3
$3p\ ^2P_{3/2}$	17.61	19.69(0.04)	18.8(0.3)	19.12(0.86)	18.1(0.2))
$yd\ ^2D_{3/2}$	–	10.51(1.07)	–	–	–
$yd\ ^2D_{5/2}$	–	-3.52(0.49)	–	–	–

4.2.1 $3p\ ^2P_{1/2}$ to $5s\ ^2S_{1/2}$

The $3p\ ^2P_{1/2}$ to $5s\ ^2S_{1/2}$ transition contains 4 allowed hyperfine transitions. The atomic energy level scheme is shown in Figure 4.2. All 4 peaks are well resolved, the hyperfine spectra

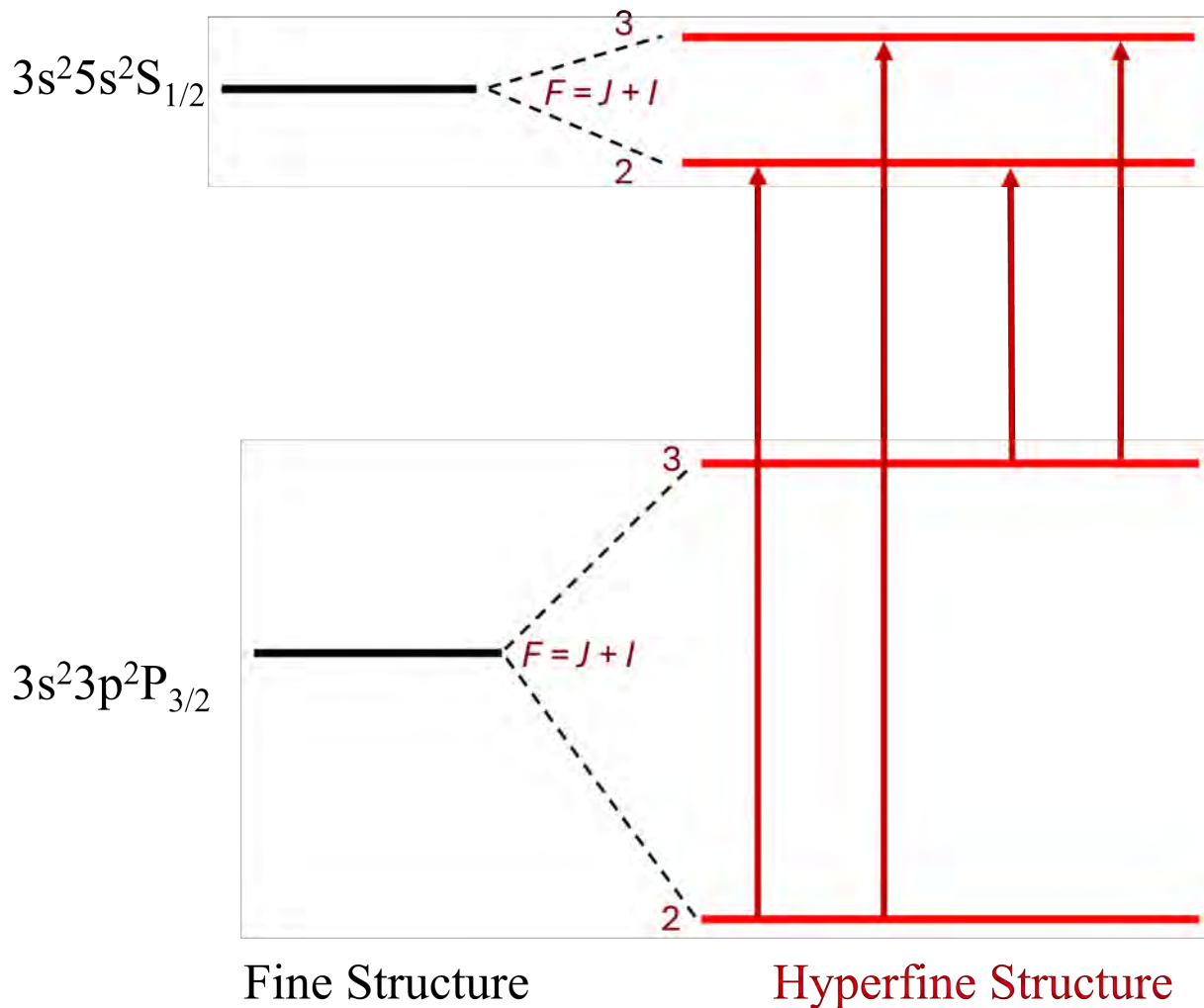


Figure 4.2 $3p\ ^2P_{1/2}$ to $5s\ ^2S_{1/2}$ transition energy level scheme. The atomic energy level scheme is shown for the $3p\ ^2P_{1/2}$ to $5s\ ^2S_{1/2}$ transition. The splitting between the fine structure levels is not drawn to scale. Dark red arrows indicate the allowed atomic transitions.

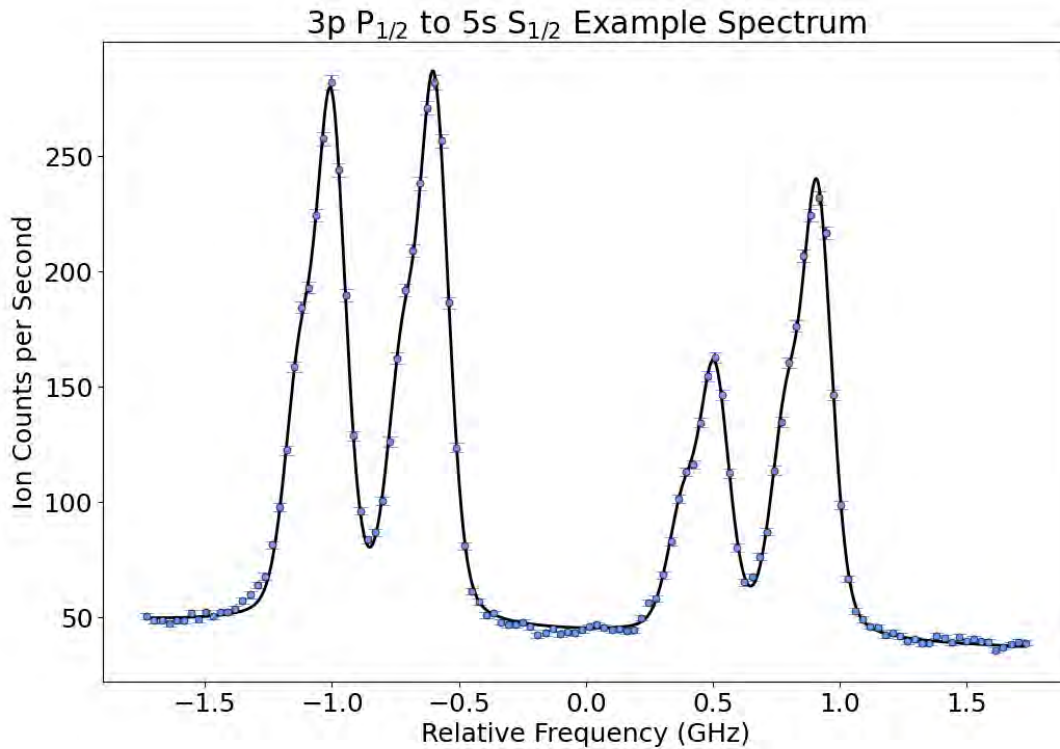


Figure 4.3 Hyperfine spectrum of the $3p \ ^2P_{1/2}$ to $5s \ ^2S_{1/2}$ transition for ^{27}Al . A spectrum of the $3p \ ^2P_{1/2}$ to $5s \ ^2S_{1/2}$ transition for ^{27}Al is shown.

is shown in Figure 4.3 and peak components in Figure 4.4. The hyperfine coefficients were measured offline and are included in Table 4.1 with an average efficiency of 2.96×10^{-5} . The efficiency is determined between the amount of counts in the resonant peak compared to the amount of ions entering the BECOLA beamline. The amount of resonant ions in the resonant peak is found by taking the maximum point of the highest peak in the hyperfine spectra. The amount of ions entering the beamline are found with a silicon detector located right after the cooler buncher. The amount of ions in the resonant peak are then divided by the amount of ions after the buncher to find an efficiency. The PIG source produces many containment ions that are not Aluminum in addition to the Aluminum ions of interest. The BECOLA beamline does not have a detector able to distinguish how many of the ions coming out of the source are Aluminum versus contaminants, anything coming out of the source is counted as an Aluminum ion entering the beamline. Due to the low purity, the efficiency

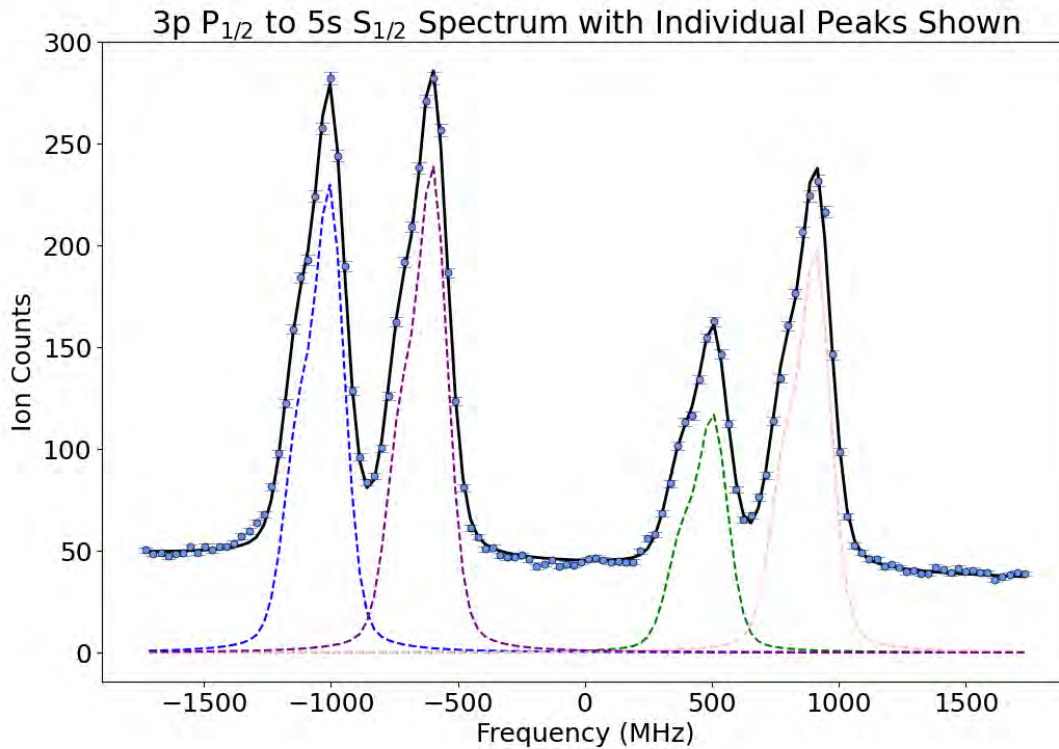


Figure 4.4 Peak components of the $3p \ ^2P_{1/2}$ to $5s \ ^2S_{1/2}$ transition for ^{27}Al . The individual peaks of the $3p \ ^2P_{1/2}$ to $5s \ ^2S_{1/2}$ transition for ^{27}Al are shown. Each allowed transition's peak is shown in a different color. The background level is subtracted from each individual peak for clarity.

measurement is a lower limit rather than an absolute efficiency. The resolution and efficiency would make this transition seem perfect for the online run. However, both the ground and excited state have a spin of $1/2$ so neither state is sensitive to the quadrupole moment. One goal of this experiment was to measure both the quadrupole moment and differential mean square charge radius for the Aluminum isotope chain. Simulation work was performed to simulate the hyperfine structure for this transition, for each isotope, to test feasibility of using this transition for the online experiment.

4.2.2 $3p \ ^2P_{3/2}$ to $5s \ ^2S_{1/2}$

The $3p \ ^2P_{3/2}$ to $5s \ ^2S_{1/2}$ transition contains 6 hyperfine transitions. The atomic energy level scheme is shown in Figure 4.5. The hyperfine spectra is shown in Figure 4.6 and peak components in Figure 4.7. The hyperfine coefficients were measured offline and are

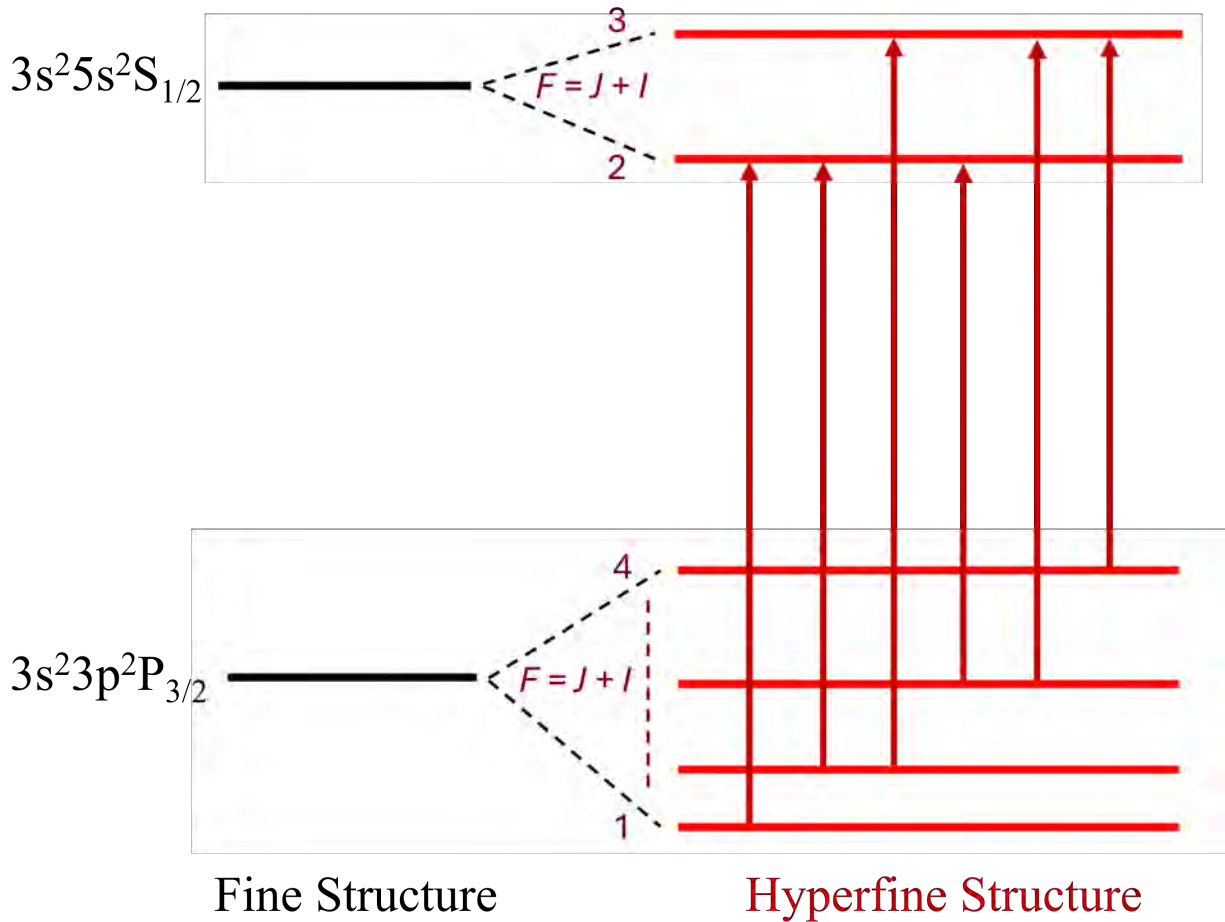


Figure 4.5 $3p\ ^2P_{3/2}$ to $5s\ ^2S_{1/2}$ transition energy level scheme. The atomic energy level scheme is shown for the $3p\ ^2P_{3/2}$ to $5s\ ^2S_{1/2}$ transition. The splitting between the fine structure levels is not drawn to scale. Dark red arrows indicate the allowed atomic transitions.

included in Table 4.1 and Table 4.2 with an average efficiency of 3.11×10^{-5} . The efficiency is determined between the amount of counts in the resonant peak compared to the amount of ions entering the BECOLA beamline. Some of the peaks are overlapped and unresolved in this transition. Theoretical calculations are able to be obtained and previous literature values for the $3p\ ^2P_{3/2}$ ground state are available [97] [98] [99]. Theoretical calculations applied the relativistic coupled-cluster (RCC) theory, starting with the Dirac-Hartree-Fock (DHF) method then including electron correlation effects due to the core-polarization and pair-correlation effects to all-orders the hyperfine coefficients for this and all transitions were found [100] [101]. Theoretical results are included in Table 4.1 and 4.2. The ground state has

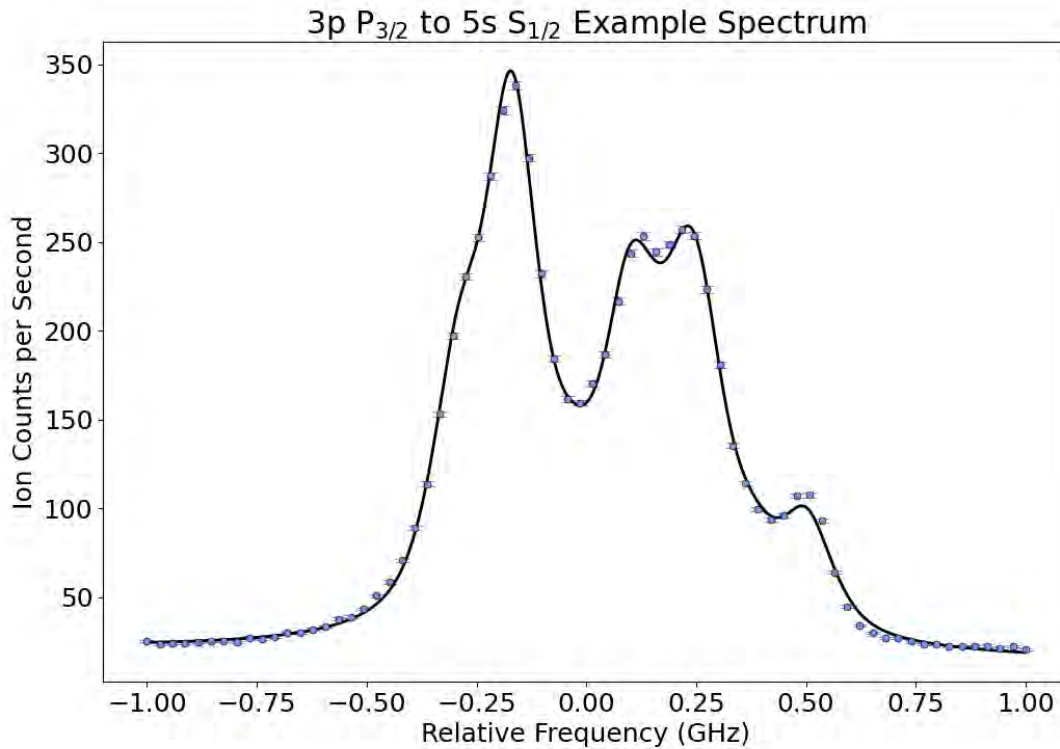


Figure 4.6 Hyperfine spectrum of the $3p\ ^2P_{3/2}$ to $5s\ ^2S_{1/2}$ transition for ^{27}Al . A spectrum of the $3p\ ^2P_{3/2}$ to $5s\ ^2S_{1/2}$ transition for ^{27}Al is shown.

a spin of $3/2$ which is sensitive to the quadrupole moment. With this state being the most promising of the transitions tried, simulations were done to see how much overlap between peaks would be seen for different isotopes in the online run. The overlap indicates if the peaks can be well resolved and if meaningful results can be obtained.

4.3 Simulations

To best prepare for the online run simulations of the rare isotopes spectra are needed. This allows for the amount of time needed to run each isotope, what parameters are able to be extracted, and their uncertainty estimates to be determined. Simulations are also critical when choosing the transition to use for the online experiment.

To make a simulation for each of the isotopes of interest, theoretical shell model calculations were obtained from Alex Brown [45] for the magnetic dipole moments of each isotope. The details and results of his calculations are outlined in the Results chapter. Using the

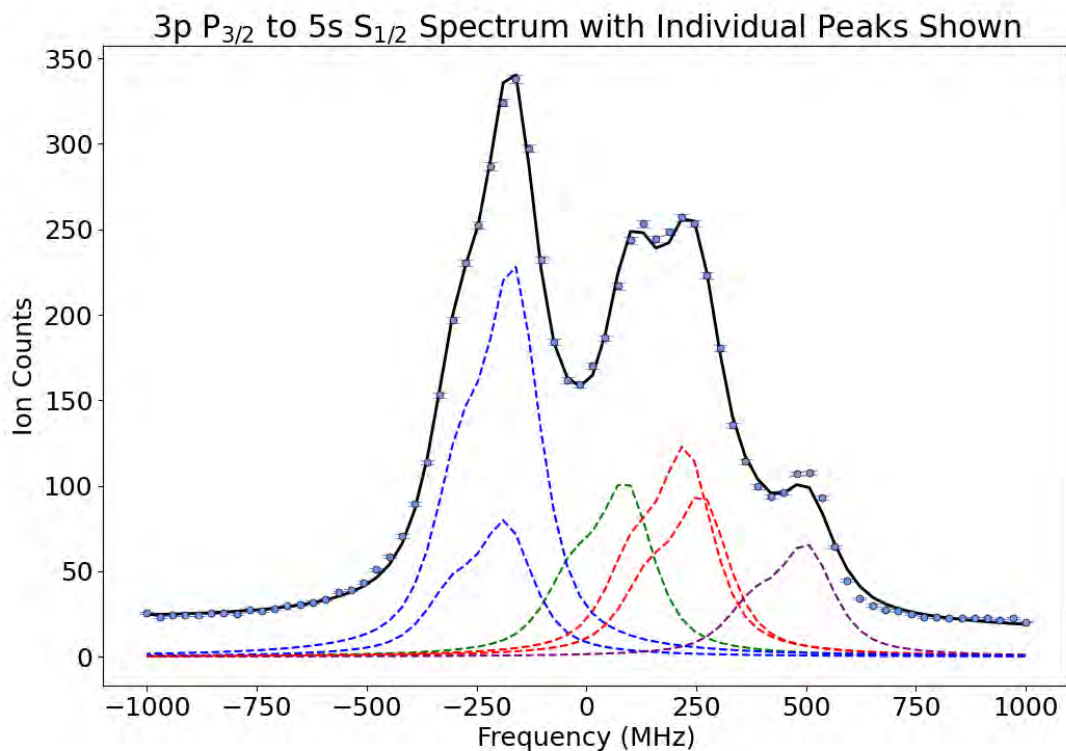


Figure 4.7 Peak components of the $3p \ ^2P_{3/2}$ to $5s \ ^2S_{1/2}$ transition. The individual peaks of the $3p \ ^2P_{3/2}$ to $5s \ ^2S_{1/2}$ transition for ^{27}Al are shown. Individual peaks that are the same color are tied together using a theoretical coefficient in the fitting procedure. The background level is subtracted from each individual peak for clarity.

theoretical moments and the measured stable hyperfine coefficients, a prediction for each isotope's hyperfine coefficients were made using Equation 2.12. Combining the hyperfine coefficient predictions with the quantum numbers of the isotope and transition, an estimation for the peak spacing can be determined. Equation 5.1 is used to find the location of each peak center and is explained in detail in the Analysis chapter.

4.3.1 Relative Peak Amplitudes

To simulate the relative peak amplitudes, the Racah coefficients were used. The Racah coefficients use the strength of each allowed transition to determine a theoretical prediction of the relative peak height. Determining these coefficients comes from finding the dipole matrix elements, $\langle F_g, m_g | er_q | F_e, m_e \rangle$, characterized by the strength of the atom and near-resonant electromagnetic radiation interaction [102]. The matrix element is transition dependent,

depending on both the ground state, $|F_g, m_g\rangle$, and excited state, $|F_e, m_e\rangle$, properties. The equation for the matrix elements utilizing Wigner 3-j and 6-j symbols is found in Equation 4.4 where m_g and m_e are the magnetic quantum numbers for the ground and excited hyperfine energy levels, each hyperfine level has $2m + 1$ degenerate energy levels assuming no Zeeman Effect is present [102]. The matrix element equation will only be nonzero for allowed transitions of $\Delta m \equiv m_e - m_g = 0, \pm 1$. L is the total electron angular momentum, S is the total electron spin, I , and J are quantum numbers as previously defined. The fourth term in parenthesis, $()$, is a Wigner 3-J symbol and the fifth and six terms in braces, $\{\}$, are Wigner 6-J symbols. The second term is a reduced matrix element $\langle L_g || er || L_e \rangle$, which is evaluated from theory and is explained in detail in reference [102].

$$\begin{aligned} \langle F_g, m_g | er_q | F_e, m_e \rangle = & (-1)^{2F_e + I + J_g + J_e + L_g + S + m_g + 1} \langle L_g || er || L_e \rangle \\ & \times \sqrt{(2F_g + 1)(2F_e + 1)(2J_g + 1)(2J_e + 1)(2L_g + 1)} \\ & \times \begin{pmatrix} F_e & 1 & F_g \\ m_e & -\Delta m & -m_g \end{pmatrix} \begin{Bmatrix} J_g & J_e & 1 \\ F_e & F_g & I \end{Bmatrix} \begin{Bmatrix} L_g & L_e & 1 \\ J_e & J_g & S \end{Bmatrix} \end{aligned} \quad (4.4)$$

$\langle L_g || er || L_e \rangle$ is only dependent on quantum number L , which is equivalent for all of a given atomic transition's hyperfine peaks. Since the matrix element is being used for relative peak heights the second term matrix element can be set to a global scaling parameter, d . Representing the first five terms from Equation 4.4 as c_m , the equation can be simplified to Equation 4.5.

$$\langle F_g, m_g | er_q | F_e, m_e \rangle = c_{m_F} \langle L_g || er || L_e \rangle \equiv c_{m_F} d \quad (4.5)$$

In this representation and how the equation has been defined c_m defines the relative amplitude between two Zeeman levels. The BECOLA beamline does not have a magnetic field applied, causing degenerate Zeeman levels. To account for this, all allowed Zeeman transitions for each hyperfine level must be summed. The summation and resulting relative amplitude, C_F , of a given peak is shown in Equation 4.6.

$$C_F = \sqrt{\sum c_{m_F}^2} \quad (4.6)$$

Although previous laser spectroscopy measurements at BECOLA have shown deviation from the Racah coefficients theoretically predicted relative peak heights, they serve as a close estimate for simulating unknown hyperfine spectra. Deviation is caused by allowed transitions in the hyperfine structure saturating at different laser powers than others.

4.3.2 Simulated Hyperfine Spectra

Combining the peak spacing found from theoretical μ values and the relative heights, a simulation was made for each isotope's spectrum. Simulation parameters such as the efficiency, relative background to peak ratio, and amount of ions of the isotope of interest were determined based on the stable ^{27}Al measurements, theoretical calculations, and estimated rates for radioactive Al isotopes. Simulation work focused on the two most promising transitions tested in the offline ^{27}Al work, $3p\ ^2P_{3/2}$ to $5s\ ^2S_{1/2}$ and $3p\ ^2P_{1/2}$ to $5s\ ^2S_{1/2}$. Using the ^{22}Al simulation as an example the simulation process and results from these two transitions are outlined below.

Using known quantum numbers and theoretical predictions for the hyperfine coefficients, a normalized spectrum was obtained using Equations 5.1 and 4.4 in combination with a peak function shown in Equation 5.2. A variety of peak models can be used to represent different line shapes, the pseudo-Voigt peak model was used for analysis of ^{27}Al data making it ideal for Al simulation work. The spectrum generated using theoretical values was normalized to one so it can be used as a probability distribution to generate spectra with estimated statistics. The resulting normalized spectra are shown for $3p\ ^2P_{3/2}$ to $5s\ ^2S_{1/2}$ and $3p\ ^2P_{1/2}$ to $5s\ ^2S_{1/2}$ for ^{22}Al in Figure 4.8 and 4.9 respectively.

It is shown in the normalized theoretical prediction that many peaks are overlapped and there is poor resolution of the individual peaks. The six peaks in Figure 4.8 overlap into one large peak. The four peaks in Figure 4.9 overlap into two sets of two peaks. Using the function of the normalized spectrum as a probability distribution a number of points were taken which correlate to the number of counts expected at the detector for the entire run. For example, for ^{22}Al an estimated rate of 525 ions per second were expected to be delivered

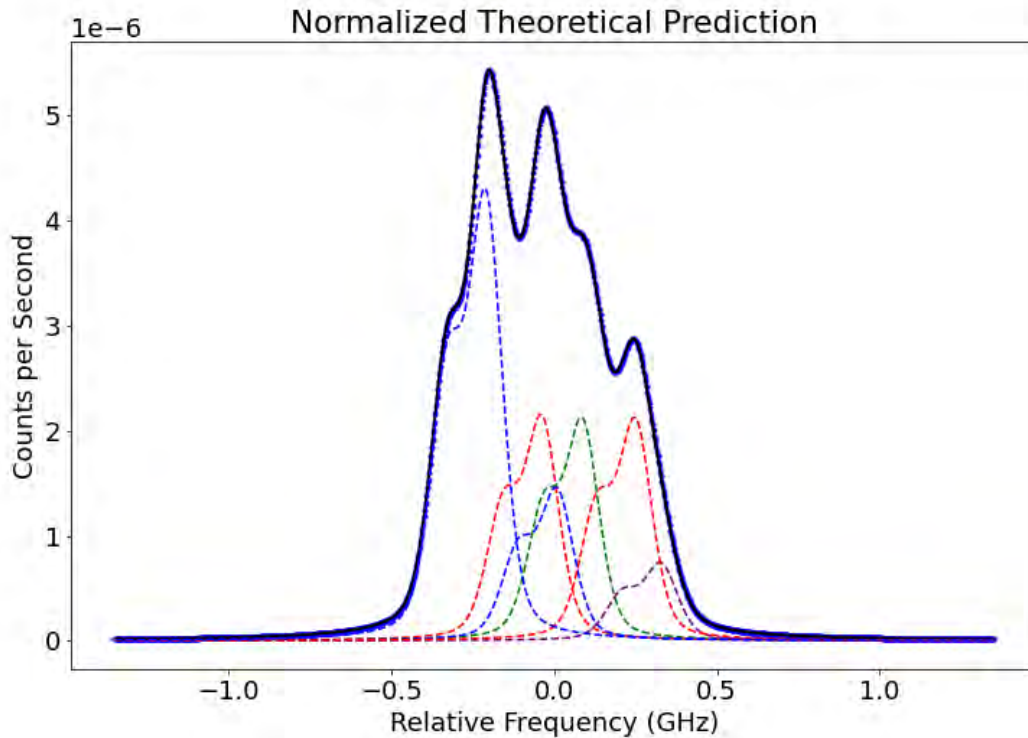


Figure 4.8 Theoretical prediction for the $3p \ ^2P_{3/2}$ to $5s \ ^2S_{1/2}$ transition for ^{22}Al . The normalized theoretical prediction for the $3p \ ^2P_{3/2}$ to $5s \ ^2S_{1/2}$ transition for ^{22}Al is shown. This prediction uses both theoretical predictions and properties measured in stable ^{27}Al to make an accurate prediction of the resulting spectra. This normalized spectra was used to make simulated data that could be fit and used to determine the goodness of this transition for ^{22}Al .

to the BECOLA facility. In offline measurements of ^{27}Al an efficiency of 5×10^{-5} was found from the number of ions leaving the cooler buncher to the number of resonant ions detected in the hyperfine peaks. Using these values the total amount of ions expected to be in the hyperfine spectra was found by multiplying the counts per second by the efficiency and by the total amount of time running, as shown in Equation 4.7.

$$points = counts \ at \ BOB0 \times efficiency \times time \quad (4.7)$$

The amount of time for running all Al isotopes was determined by the approved amount of beam time from the PAC result. The total approved beamtime for the Al experiment was 60 hours. Five of the approved hours would be used by the operators of the gas cell to transmit

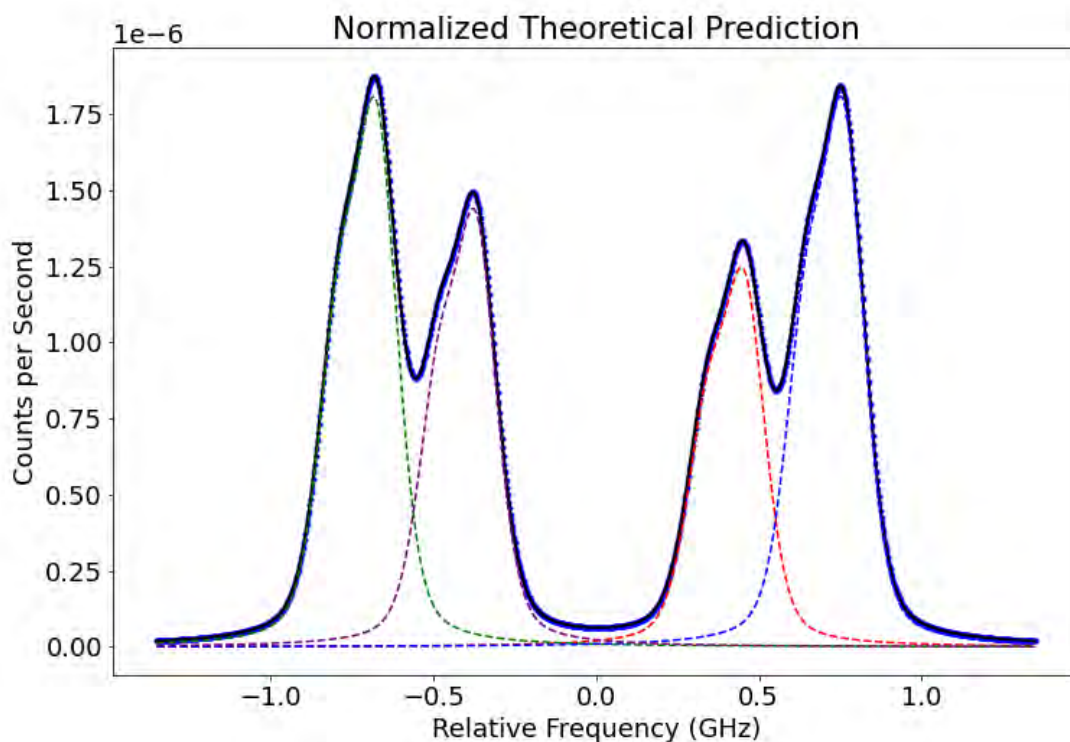


Figure 4.9 Theoretical prediction for the $3p \ ^2P_{1/2}$ to $5s \ ^2S_{1/2}$ transition for ^{22}Al . The normalized theoretical prediction for the $3p \ ^2P_{1/2}$ to $5s \ ^2S_{1/2}$ transition for ^{22}Al is shown. This prediction uses both theoretical predictions and properties measured in stable ^{27}Al to make an accurate prediction of the resulting spectra. This normalized spectra was used to make simulated data that could be fit and used to determine the goodness of this transition for ^{22}Al .

the beam from the ARIS fragment separator to the BECOLA beamline. Estimated about 16 hours would be required for calibration runs using offline ^{27}Al . The distribution of the remaining 39 hours to each isotope was determined based on simulation in coordination with beam operators to switch the mass. Using the normalized probability function and number of points, a random number generator was used to make realistically simulated data sets with variation of run time.

4.3.3 $3p \ ^2P_{3/2}$ to $5s \ ^2S_{1/2}$ Simulations

The focus of simulation work was the lowest rate isotope and hardest to measure, ^{22}Al . Each transition needed to be simulated to estimate the error on the centroid value as a function of run time. Starting from the $3p \ ^2P_{3/2}$ to $5s \ ^2S_{1/2}$ transition for ^{22}Al , the transition

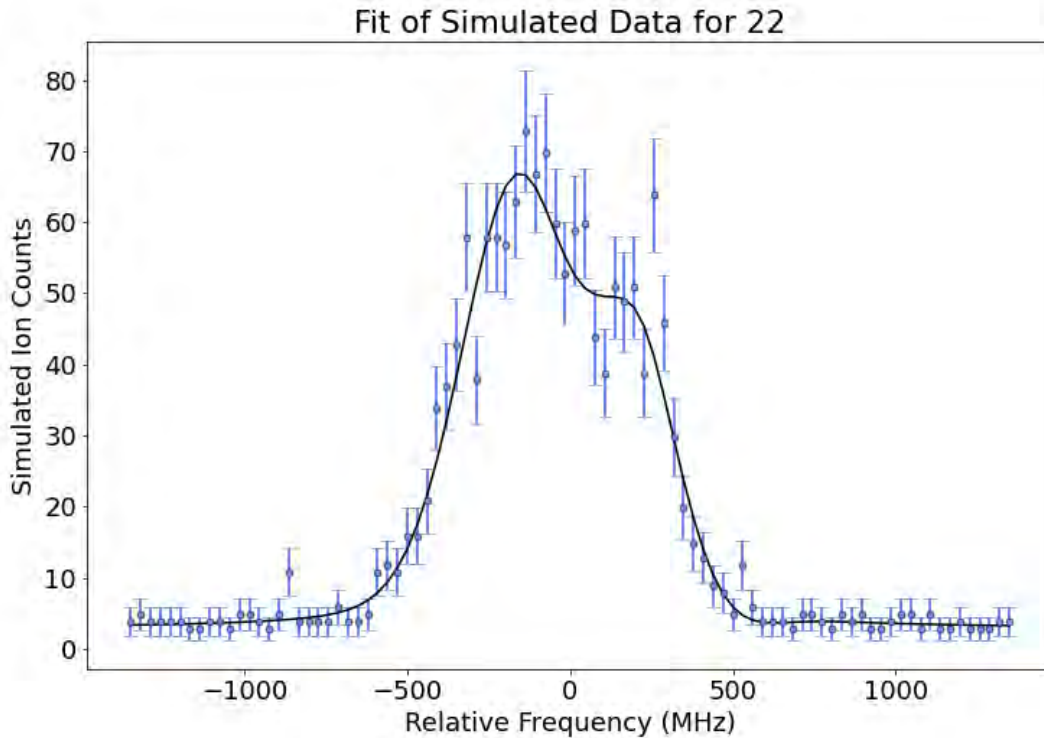


Figure 4.10 15 hour simulation for the $3p \ ^2P_{3/2}$ to $5s \ ^2S_{1/2}$ transition for ^{22}Al . An example 15 hour simulation of the $3p \ ^2P_{3/2}$ to $5s \ ^2S_{1/2}$ transition for ^{22}Al is shown. The fit is unable to identify the location of 6 individual peaks and their locations have a large uncertainty.

was simulated for a variety of times. After 15 hours of accumulation time it was seen that although the statistics and signal to noise ratio were improving, the data could not be fit without fixing fit parameters to theoretical values. A sample 15 hour simulation is shown in Figure 4.10. Even with fixed parameters, there is a large uncertainty on peak placement resulting in a large uncertainty on the centroid. Running the 15 hour simulation, centroid uncertainties ranging from about 14 to 26 MHz were seen for good data sets and fits. In less ideal cases uncertainties could not be estimated due to reaching fit parameter limits or the fit being unable to properly minimize. The six peaks are so close together that the fit is unable to identify individual peaks and collapses the peaks on top of each other, resulting in a fit that only represents two or three peaks rather than the six that are contained within.

After finishing the simulation work it was seen that the overlapping of the peaks would

get worse moving towards the dripline nucleus of interest, ^{22}Al . Even in a more favorable scenario the statistics of the measurement would be poor and have a large uncertainty on the properties of interest. This ruled out the possibility of using this transition for the online run.

4.3.4 $3p\ ^2P_{1/2}$ to $5s\ ^2S_{1/2}$ Simulations

Moving to the $3p\ ^2P_{1/2}$ to $5s\ ^2S_{1/2}$ transition for ^{22}Al , the transition was simulated for a variety of times. After 10 hours of accumulation time an improvement of the statistics and signal to noise ratio were seen. Unlike the previous transition, with these statistics the fit was able to distinguish all four peaks and yield centroid values with reasonable uncertainties. With a 10 hour accumulation time the centroid uncertainty varies between 10 and 20 MHz. A favorable sample 10 hour simulation is shown in Figure 4.11. Increasing the accumulation time to 15 hours reduces the uncertainty on the centroid to about 10 MHz, reaching as low as 5 MHz in good data sets. A sample 15 hour simulation is shown in Figure 4.12. Increasing the accumulation time even further to 20 hours reduces the uncertainty on the centroid to consistently about 5 MHz. A sample 20 hour simulation is shown in Figure 4.13. A 5 MHz uncertainty on the ^{22}Al centroid propagates to a statistical uncertainty of less than $0.1\ \text{fm}^2$ on the differential mean square charge radius. This level of uncertainty is enough to make a definitive statement of the possible halo structure in ^{22}Al . With these simulation results it was decided to use the $3p\ ^2P_{1/2}$ to $5s\ ^2S_{1/2}$ transition for the online run despite losing sensitivity to the quadrupole moment. The main motivation of this experiment was to measure the charge radius trend to address the possible halo structure in ^{22}Al and ^{23}Al . Before moving to the online run simulations of the other isotopes of interest were done to plan the run and ensure all isotopes would have reasonable uncertainties. Sample simulation results for ^{23}Al , ^{24}Al , and ^{25}Al are shown in Figure 4.14, 4.15, and 4.16 respectively.

4.4 Online Run

After running the different transitions offline with stable ^{27}Al and performing simulations, the $3p\ ^2P_{1/2}$ to $5s\ ^2S_{1/2}$ transition with estimated offline efficiency of 5×10^{-5} was chosen for

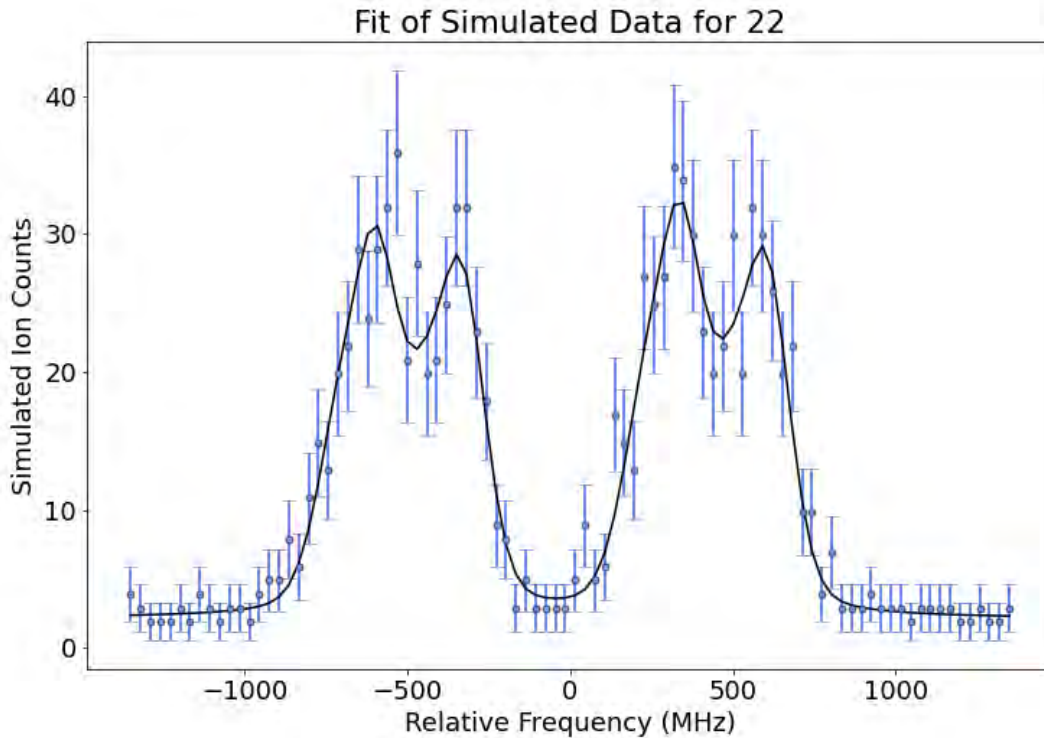


Figure 4.11 10 hour simulation for the $3p\ ^2P_{1/2}$ to $5s\ ^2S_{1/2}$ transition for ^{22}Al . An example 10 hour simulation for the $3p\ ^2P_{1/2}$ to $5s\ ^2S_{1/2}$ transition for ^{22}Al is shown. The four peaks are split into two pairs of two. Despite the small splitting between the peaks paired, the fit is able to distinguish four different peaks. The resulting centroid uncertainty for this favorable example is 9.6 MHz.

the online run. The nuclear ground state of four isotopes and one excited state, indicated by m , were measured during the online run; ^{22}Al , ^{23}Al , ^{24}Al , ^{24m}Al , and ^{25}Al . The life-time, spin, and parity [103] of the measured isotopes are listed in Table 4.3. The offline efficiency

Table 4.3 Aluminum isotope properties. The properties of the measured Aluminum isotopes are listed; ^{22}Al , ^{23}Al , ^{24}Al , ^{24m}Al , and ^{25}Al . Note, the spin of ^{22}Al is not definitively known.

	^{22}Al	^{23}Al	^{24}Al	^{24m}Al	^{25}Al
Life-time (ms)	91.1(5)	446(6)	2053(4)	130(3)	7166.6(2.3)
Spin & Parity	(4)+	$\frac{5}{2}+$	4+	1+	$\frac{5}{2}+$

was determined from the resonance spectrum of stable ^{27}Al produced by the offline FIG

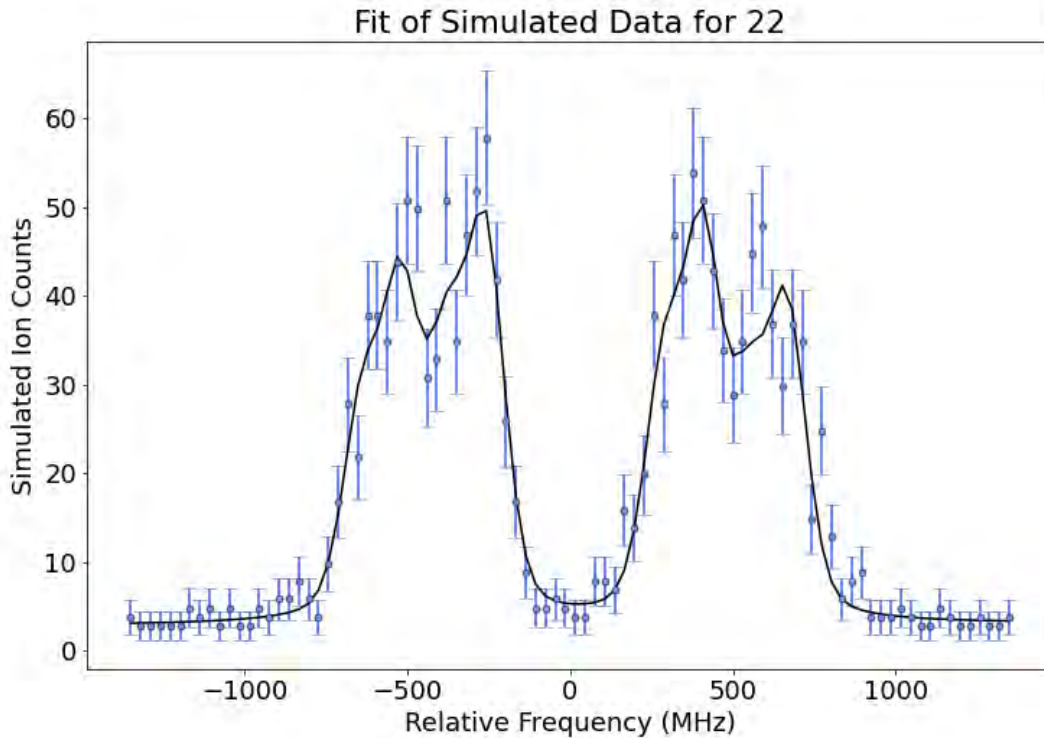


Figure 4.12 15 hour simulation for the $3p\ ^2P_{1/2}$ to $5s\ ^2S_{1/2}$ transition for ^{22}Al . An example 15 hour simulation for the $3p\ ^2P_{1/2}$ to $5s\ ^2S_{1/2}$ transition for ^{22}Al is shown. The statistics are better than the 10 hour accumulation time, resulting in a 5.7 MHz uncertainty on the centroid for this example.

source. The efficiency determination assumes that every incoming ion to the beamline is Aluminum. This is not a true statement, the PIG source is a "dirty" source, producing other ions besides the ^{27}Al ions of interest. The BECOLA beamline uses Faraday cups to measure the incoming beam current for stable beams, the measured current, in amps, can be converted into number of ions as shown in Equation 4.8.

$$\text{number of ions} = \frac{\text{beam current}}{1.602 \times 10^{-19}} \text{ s}^{-1} \quad (4.8)$$

The Faraday cups are not sensitive to what ions are incoming, it counts any ion entering the beamline. The unstable ion beam current or number of ions is measured using silicon detectors with a 70 V bias voltage. The silicon detectors are not sensitive to stable beam contaminants but are affected by other unstable contaminants. The online measurements

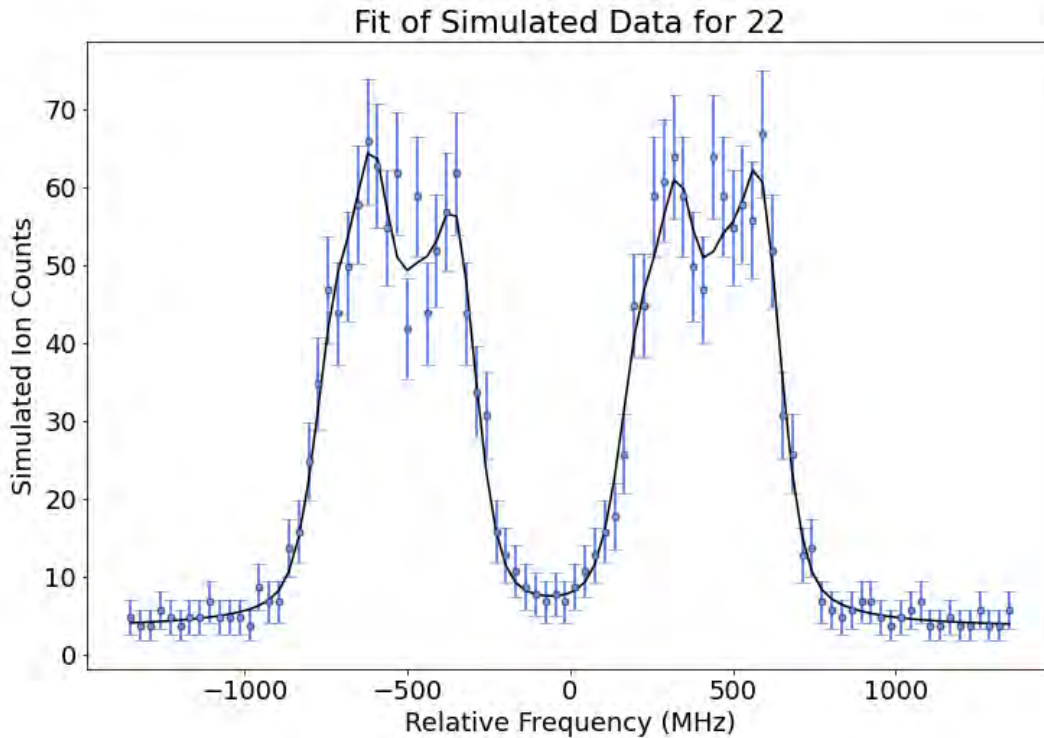


Figure 4.13 20 hour simulation for the $3p\ ^2P_{1/2}$ to $5s\ ^2S_{1/2}$ transition for ^{22}Al . An example 20 hour simulation for the $3p\ ^2P_{1/2}$ to $5s\ ^2S_{1/2}$ transition for ^{22}Al is shown. The statistics are better than the 10 and 15 hour accumulation time, resulting in a 4.5 MHz uncertainty on the centroid for this example.

have much purer beams, coming from the gas stopper, which will result in higher efficiencies for the online measurements compared to offline. However in some cases there is an unstable contaminant that affects the silicon detector counts. In the case of Aluminum, ^{22}Al and ^{23}Al decay to Mg whose decay was detected by the Silicon detector as a contaminant. The nuclear energy levels for these decays are shown in Figure 4.17 and 4.18. Using the lifetime of ^{22}Al and ^{23}Al the counts on the Silicon detector which are Mg can be estimated. Assumptions are made in the estimation which cause some uncertainty on the efficiency calculation. The efficiency will vary run to run due to systematics such as CEC temperature variation, ion beam movement, or laser light misalignment. Additionally, the efficiency will vary isotope to isotope due to the variation of transport efficiency to the BECOLA beamline and a difference in laser light alignment. This causes the overall efficiency for each isotope to vary. The details

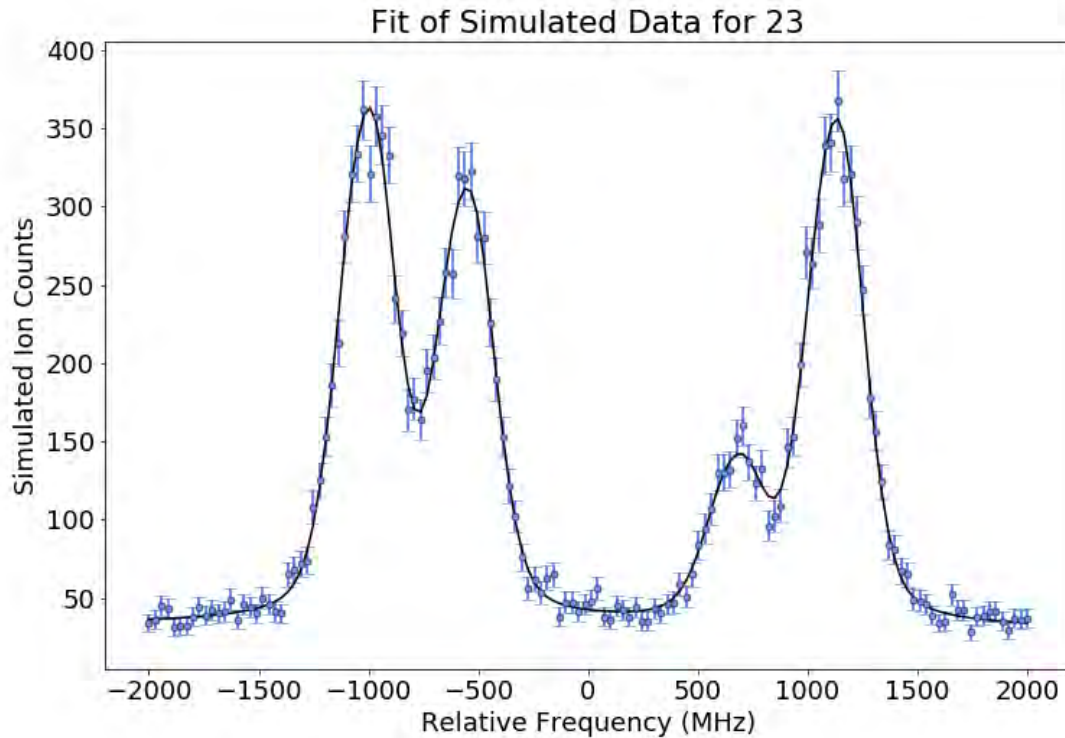


Figure 4.14 8 hour simulation for the $3p\ ^2P_{1/2}$ to $5s\ ^2S_{1/2}$ transition for ^{23}Al . An example 8 hour simulation for the $3p\ ^2P_{1/2}$ to $5s\ ^2S_{1/2}$ transition for ^{23}Al is shown. There is clear splitting among the four peaks of the spectra. Statistics are good and there is no large uncertainties in the fit.

for each online isotope's run and resulting hyperfine spectra are detailed in the sub-sections below.

4.4.1 ^{25}Al

The first isotope measured for the online run was ^{25}Al . Using Silicon Detectors along the BECOLA beamline, the amount of ions transmitted through the beamline can be determined. 36,000 ions were delivered to the BECOLA beamline per second. Injection and transmission losses through the cooler buncher results in 21,000 ions per second, neutralizing through the CEC results in 1,800 atoms that can be ionized. The resonant peak contains 17.5 resonant ions per second measured by the MagneToF. ^{25}Al was run for 2.73 hours. From the bunch leaving the cooler buncher to the resonant peak an overall efficiency of 8.3×10^{-4} was obtained. All peaks were well resolved and the resulting spectra is shown in Figure 4.19.

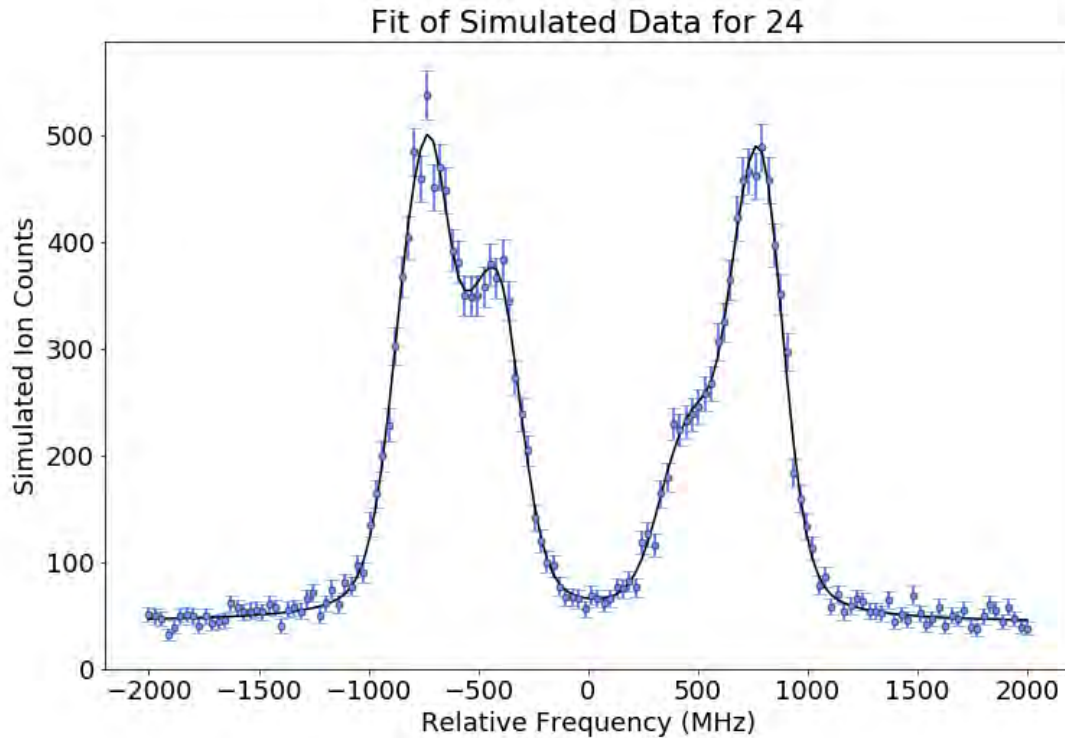


Figure 4.15 5 hour simulation for the $3p\ ^2P_{1/2}$ to $5s\ ^2S_{1/2}$ transition for ^{24}Al . An example 5 hour simulation for the $3p\ ^2P_{1/2}$ to $5s\ ^2S_{1/2}$ transition for ^{24}Al is shown. The splitting of the four peaks is smaller than in ^{23}Al , ^{25}Al , and ^{27}Al but larger than ^{22}Al . The fit is able to identify the four independent peaks and achieve good statistics. ^{24}Al has an isomeric state in addition to the ground state shown in this figure. The isomeric state will add four additional peaks into the spectra. The isomeric state and the associated fitting method is outlined in the Analysis chapter.

4.4.2 ^{23}Al

Following the completion of the ^{25}Al measurement, ^{23}Al was measured. Approximately 21,000 ions were detected on the Silicon detector as being delivered to the BECOLA beamline per second. Injection and transmission losses through the cooler buncher results in 9,000 ions per second detected, neutralizing through the CEC results in 390 neutral atoms detected that can be ionized. Using the lifetime of ^{23}Al the amount of Al which decays to Magnesium, Mg, and the amount of detected ions which are Al can be determined by Equation 4.9 where

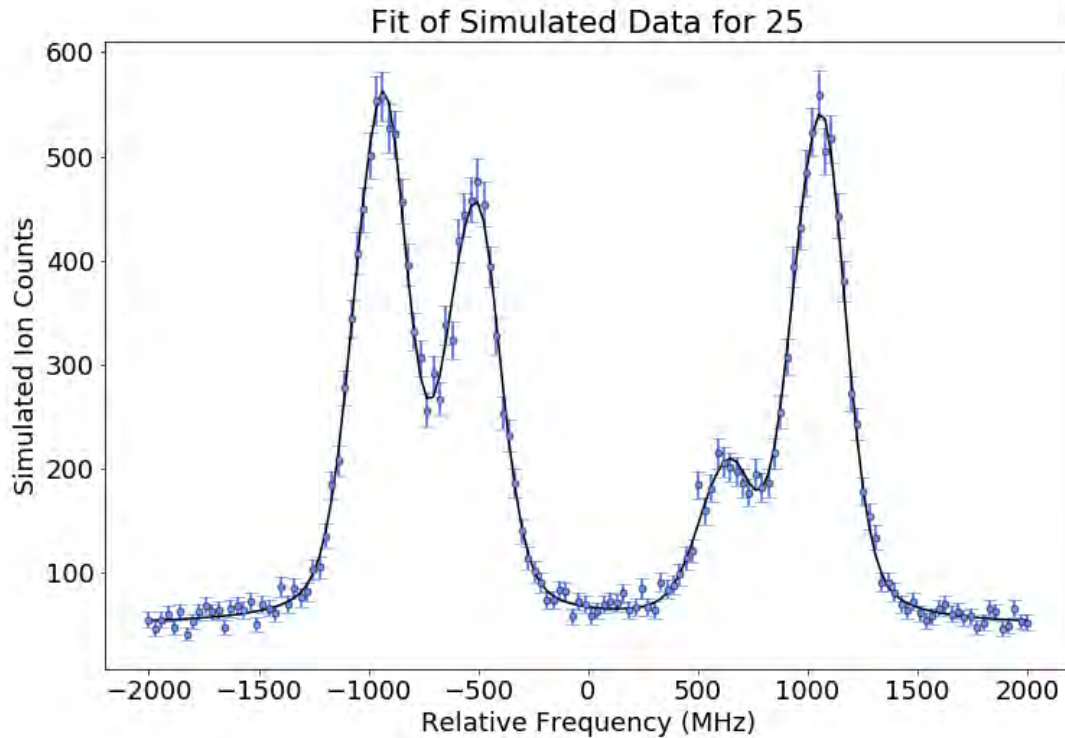


Figure 4.16 5 hour simulation for the $3p \ ^2P_{1/2}$ to $5s \ ^2S_{1/2}$ transition for ^{25}Al . An example 5 hour simulation for the $3p \ ^2P_{1/2}$ to $5s \ ^2S_{1/2}$ transition for ^{25}Al is shown. There is clear splitting among the four peaks of the spectra. Statistics are good and there is no large uncertainties in the fit.

t is the amount of time the Al has to decay.

$$Mg \ ions = \# \ of \ detected \ ions \times (1 - e^{-t/lifetime}) \quad (4.9)$$

$$Al \ ions = \# \ of \ detected \ ions \times e^{-t/lifetime}$$

The Al ions take approximately 40 ms to travel through the gas cell. Substituting 40 ms for t and 446 ms for the lifetime of ^{23}Al results in 19,199 of the 21,00 incoming ions being Al ions and 1,801 being Mg ions. The ions spend 10 ms in the cooler buncher, increasing t to 50 ms and using Equation 4.9 results in 8,046 of the 9,000 ions detected after the cooler buncher to be Al ions and 954 ions to be Mg ions. To determine the fraction of the detected neutral beam is Al, the ratio of the cross section of Al versus Mg was used. The cross section of Al divided by the cross section of Mg is equal to 3.8266. The ratio is used to determine

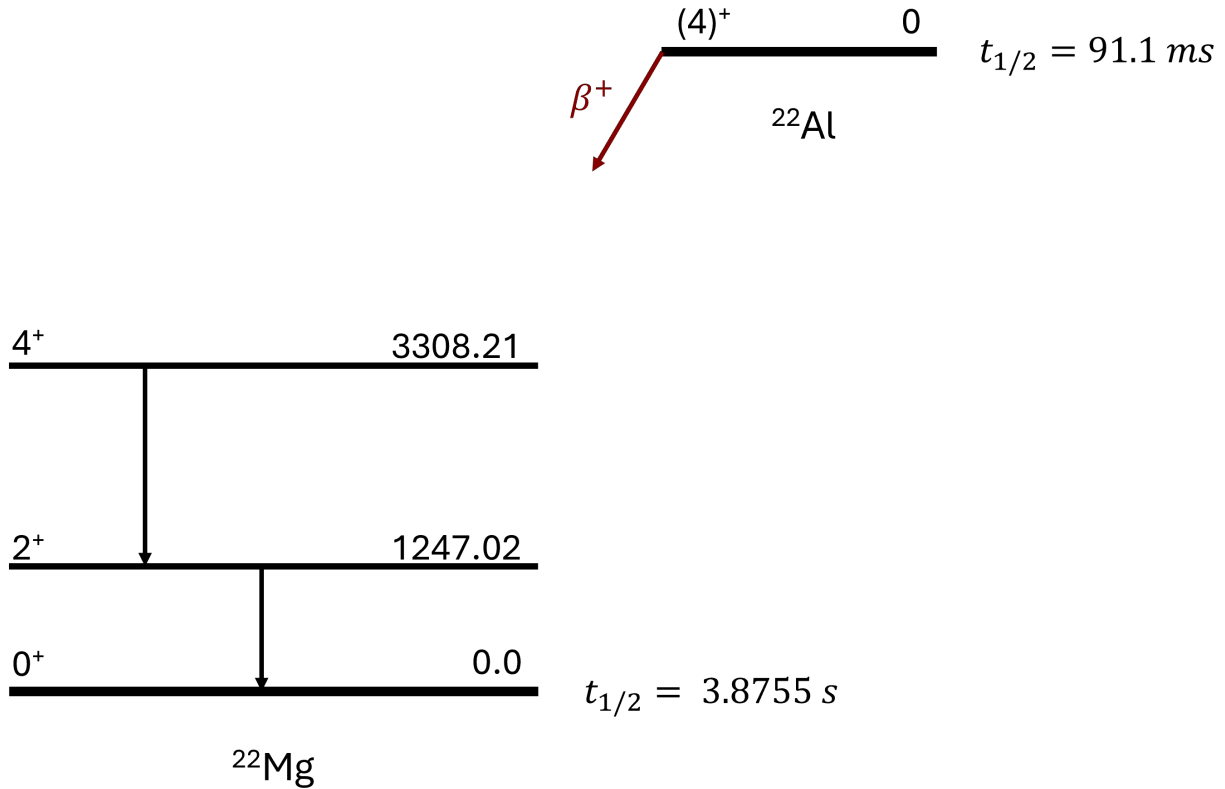


Figure 4.17 Nuclear energy levels of the ^{22}Al decay to ^{22}Mg . The nuclear energy levels are shown for ^{22}Mg . The nuclear ground state of ^{22}Al β^+ decays into ^{22}Mg .

the amount of Al atoms as shown in Equation 4.10.

$$\begin{aligned}
 Al_{neutrals} &= 3.8266 \times Mg_{neutrals} \\
 Total_{neutrals} &= Mg_{neutrals} + 3.8266 \times Mg_{neutrals} \\
 Mg_{neutrals} &= \frac{Total_{neutrals}}{4.8266}
 \end{aligned}
 \tag{4.10}$$

Using Equation 4.10 309 of the 390 neutral atoms detected were determined to be Al. The resonant peak contains 3 resonant ions per second measured by the MagneToF. Only Al atoms are resonantly excited and the Mg contamination is no longer present at the MagneToF. ^{23}Al was run for 8.7 hours. From the bunch leaving the cooler buncher to the resonant peak an overall efficiency of 3.7×10^{-4} was obtained. All peaks were well resolved and the resulting spectra is shown in Figure 4.20.

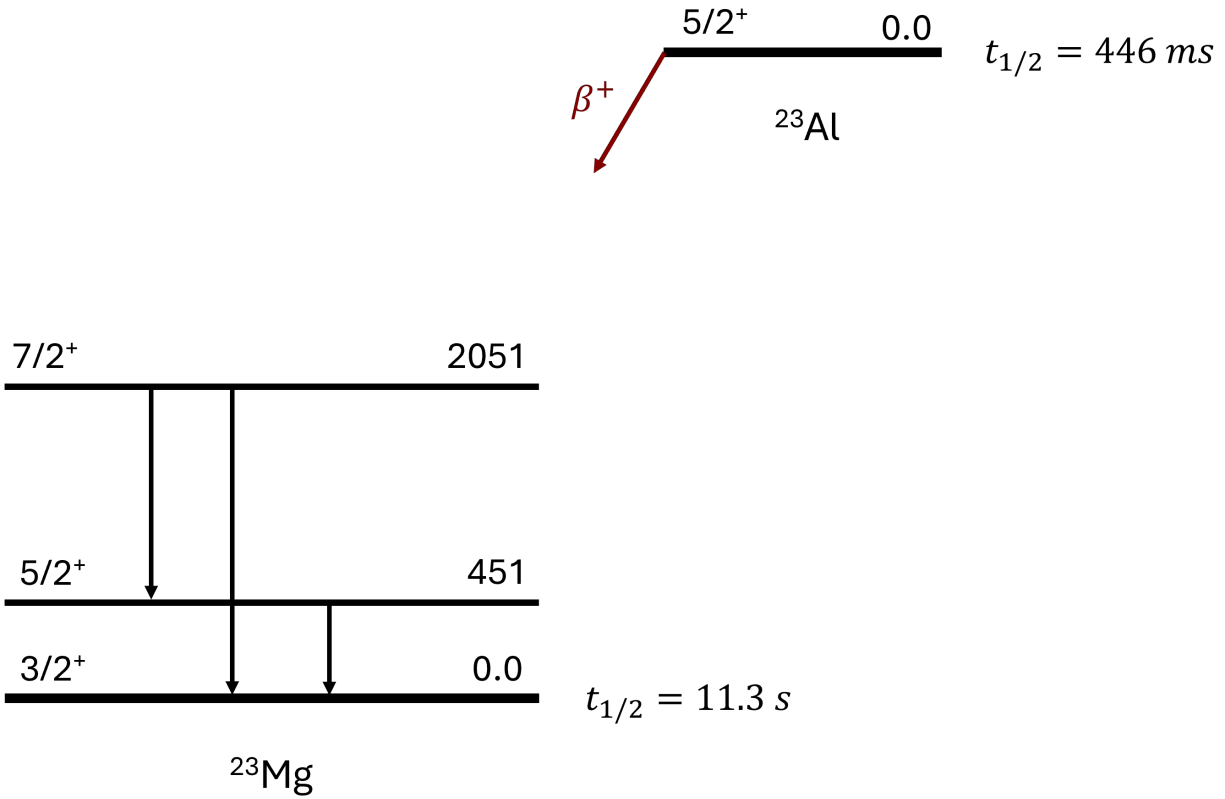


Figure 4.18 Nuclear energy levels of the ^{23}Al decay to ^{23}Mg . The nuclear energy levels are shown for ^{23}Mg . The nuclear ground state of ^{23}Al β^+ decays into ^{23}Mg .

4.4.3 ^{24}Al

The next isotope measured was ^{24}Al . ^{24}Al contains both the ground state and an isomeric state. Different settings were tested to vary the amount of the isomeric state present during spectroscopy. 28,000 ions were delivered to the BECOLA beamline per second. Injection and transmission losses through the cooler buncher results in 14,400 ions per second, neutralizing through the CEC results in 990 atoms that can be ionized. The resonant peak contains 14 resonant ions per second measured by the MagneToF. ^{24}Al was run for 8.14 hours. From the bunch leaving the cooler buncher to the resonant peak an overall efficiency of 9.7×10^{-4} was obtained. The lifetime of the isomeric state is 130(3) ms and primarily decays into the ground state with a lifetime of 2.053(4) s. A level scheme for ^{24}Al is shown in Figure 4.21. Increasing the accumulation time in the buncher, the isomeric state will decay into the ground state and change the percentage of ions in each state. During the experiment a

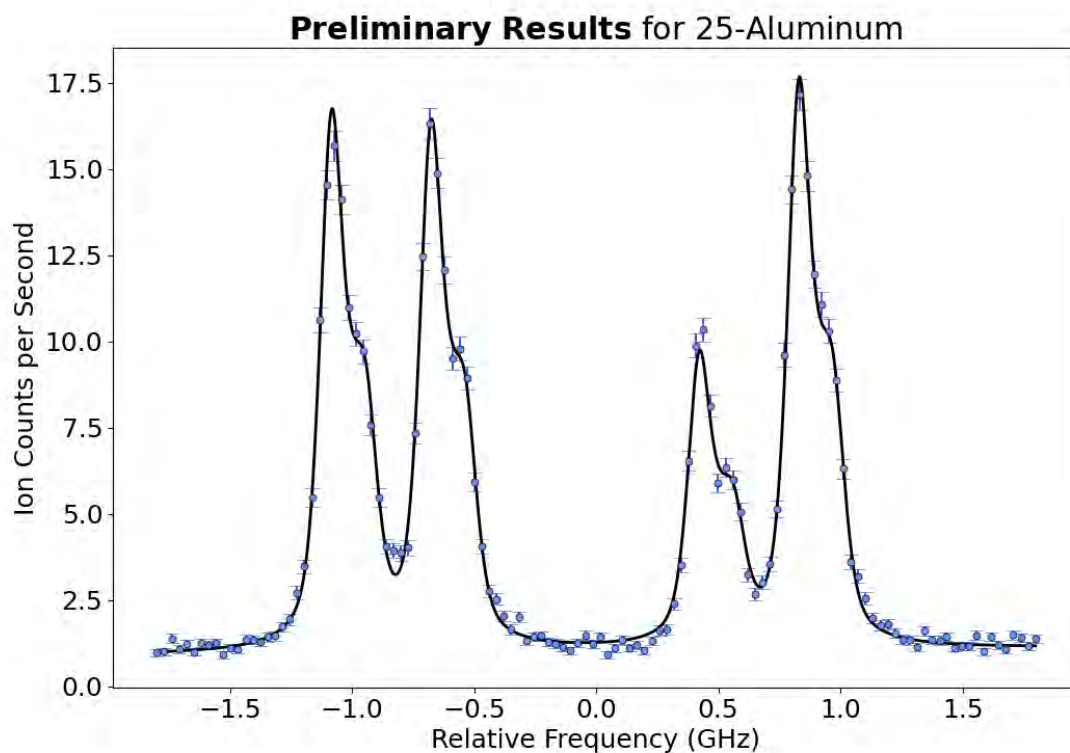


Figure 4.19 ^{25}Al hyperfine spectra. The measured spectrum of the $3p\ ^2P_{1/2}$ to $5s\ ^2S_{1/2}$ transition for ^{25}Al is shown.

variety of accumulation times were tested to help identify which components in the resulting hyperfine structure belong to the isomeric state. The details of this analysis is detailed in the ^{24}Al section in the Analysis chapter. The buncher is constantly being filled by the continuous ion beam from the gas stopper. To fully eliminate the isomeric component the incoming ion beam must be steered away from the buncher. Once the incoming ion beam is stopped from entering the buncher, the bunch must wait in the buncher for the isomeric state to decay, then be released into the beamline. This method will reduce the overall amount of incoming ions since the ion beam must be deflected for a portion of the run time. This leads to less statistics being accumulated during the measurement. Due to the loss of statistics fully eliminating the isomeric state would cause, it was decided to include the isomeric state in all of the measurements. This was supported due to the spectrum having atleast one fully isolated peak for each state. Details of how the spectrum was fit and used

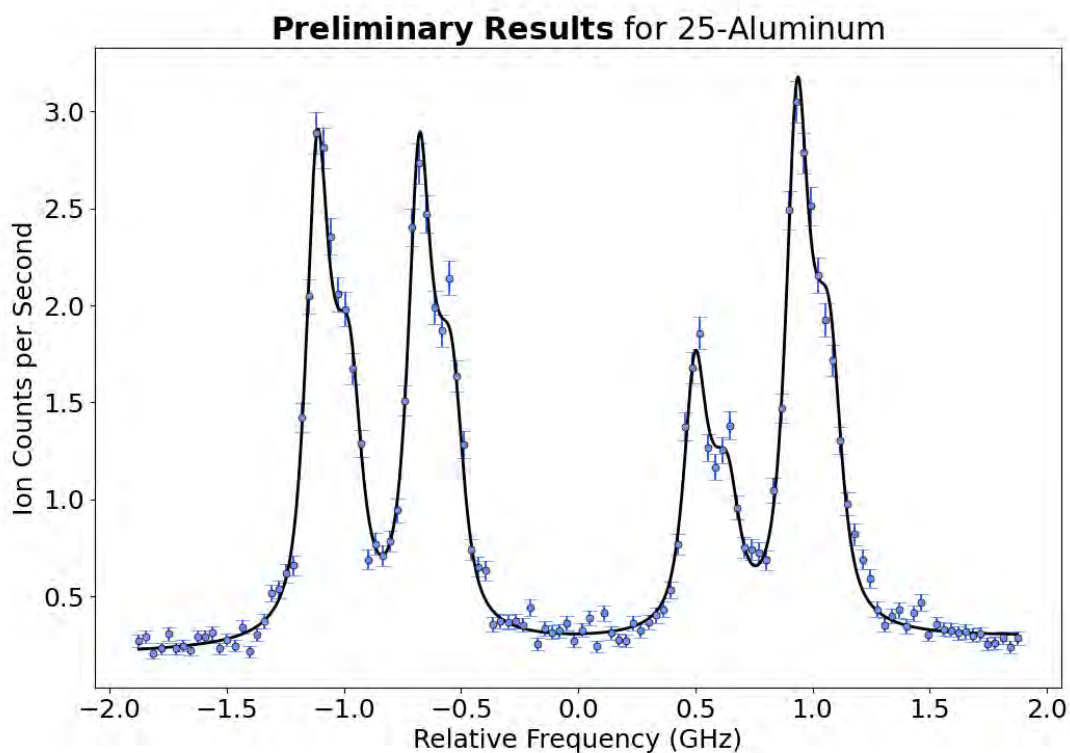


Figure 4.20 ^{23}Al hyperfine spectra. The measured spectrum of the $3p\ ^2P_{1/2}$ to $5s\ ^2S_{1/2}$ transition for ^{23}Al is shown.

spectra of varying amounts of the isomeric state are outlined in the Analysis chapter. The final resulting spectra is shown in Figure 4.22 with the isomeric and ground state peaks shown.

4.4.4 ^{22}Al

The final and most difficult isotope measured was ^{22}Al . 1,710 ions were detected on the Silicon detector as being delivered to the BECOLA beamline per second. Injection and transmission losses through the cooler buncher results in 600 ions per second detected, neutralizing through the CEC results in 24 atoms detected that can be ionized. Using Equation 4.9, assuming the ions spend 40 ms in the gas cell and substituting 91.1 ms in for the lifetime of ^{22}Al determines 1,102 of the 1,710 ions delivered to the BECOLA beamline to be Al and 608 to be Mg. Using Equation 4.9 again with the additional 10 ms the Al ions spent in the cooler buncher determines 347 of the 600 ions after the cooler buncher to be Al

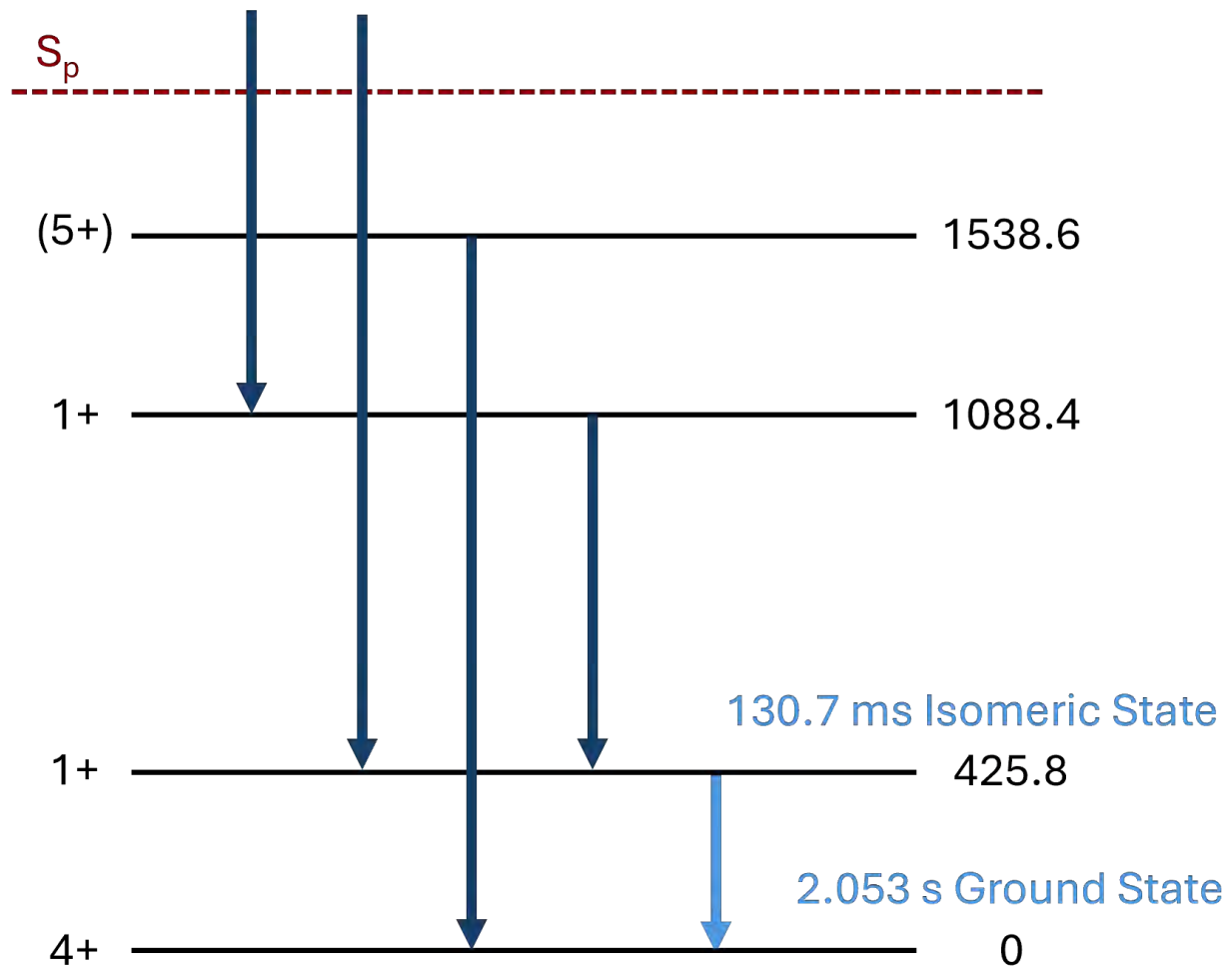


Figure 4.21 ^{24}Al nuclear energy level scheme. The nuclear energy level scheme for ^{24}Al is shown. The levels are labeled in black with spin on the left and energy level on the right. The decay of interest is highlighted in light blue from the isomeric state to the ground state. Any higher states do not affect the measurement of ^{24}Al because they will decay before reaching the BECOLA facility. Arrows coming from above the proton separation energy are from the 3875.4 and 2345.1 energy levels.

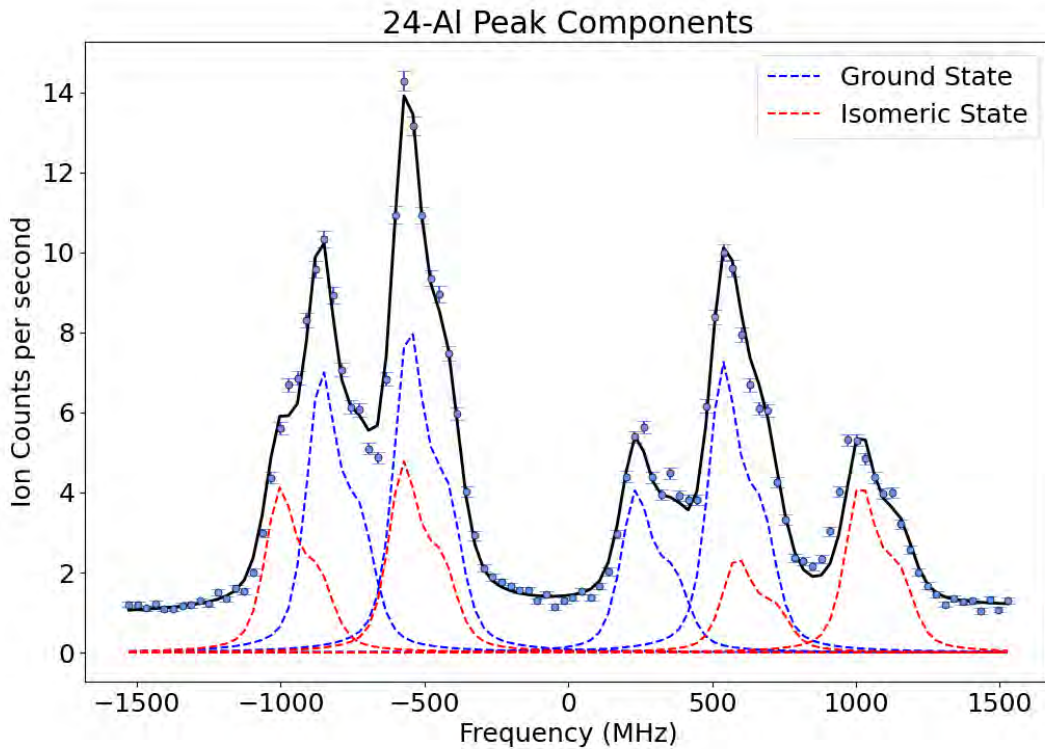


Figure 4.22 ^{24}Al hyperfine spectra. The measured spectrum of the $3p\ ^2P_{1/2}$ to $5s\ ^2S_{1/2}$ transition for ^{24}Al is shown. The isomeric and ground state components are shown in separate colors to indicate which part of the hyperfine structure belongs to which state. The background level of the different components was subtracted for clarity.

and 253 to be Mg. Using Equation 4.10 determines 19 of the 24 atoms after the CEC are Al and 5 are Mg. The resonant peak contains 0.25 resonant ions per second measured by the MagneToF. Only Al atoms are resonantly excited and the Mg contamination is no longer present at the MagneToF. ^{22}Al was run for 15.9 hours. From the bunch leaving the cooler buncher to the resonant peak an overall efficiency of 7.2×10^{-4} was obtained. Not all peaks are fully resolved in the spectra. With the lowest rate and smallest separation of peaks in the spectra, ^{22}Al had the worst statistics of the isotopes measured. The resulting spectra is shown in Figure 4.23.

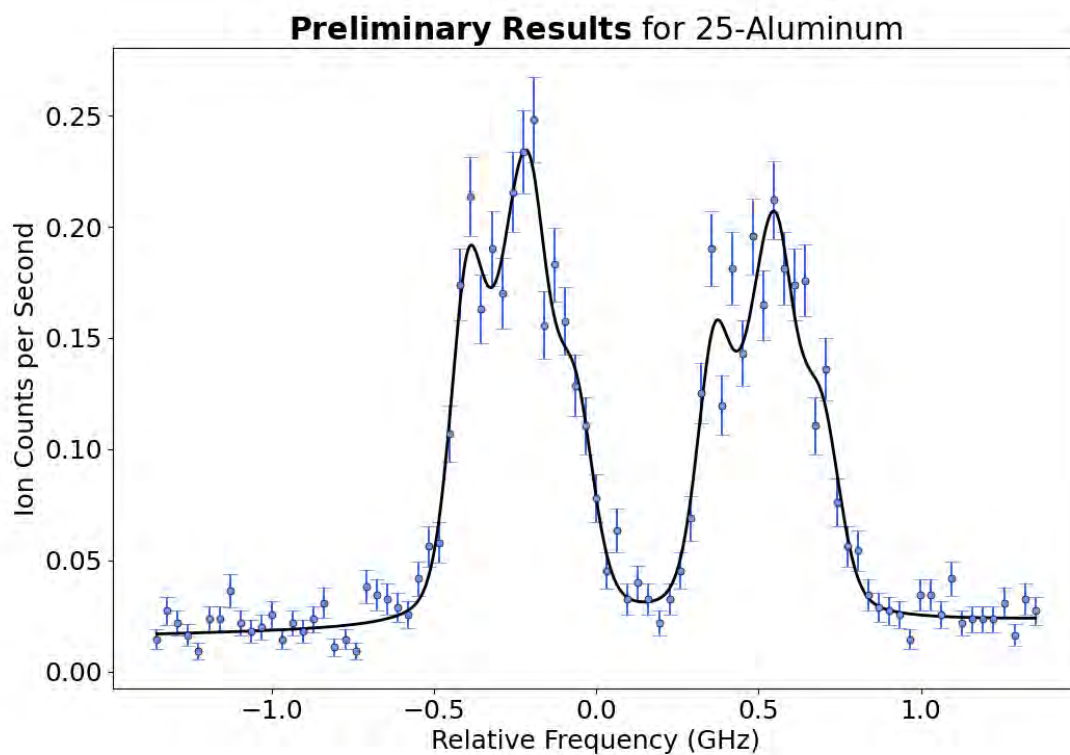


Figure 4.23 ^{22}Al hyperfine spectra. The measured spectrum of the $3p\ ^2P_{1/2}$ to $5s\ ^2S_{1/2}$ transition for ^{22}Al is shown.

CHAPTER 5

ANALYSIS

5.1 Fitting Function

To fit the hyperfine spectra data, a pseudo-Voigt profile was used for each peak. Each peak and corresponding side peak has a pseudo-Voigt profile which are summed together with a linear background.

There was a background in the data sets dominated by non-resonant ions. The baseline can vary due to a variation of experimental conditions correlated with the voltage scan and a linear slope can be present if there were any parameters slowly drifting in one direction throughout the day. The y intercept of the background is a free parameter with the initial guess being the average of the first 5 data points. The slope is a free parameter and in the Aluminum data sets the slope is typically very close to zero. This indicates there was no large drifts occurring in the background of the data taken, or any drift that did occur averaged out over the long data accumulation time.

The pseudo-Voigt profile for each peak shares a set of parameters across all peaks and side peaks. These shared parameters include sigma, the centroid, hyperfine coefficients, and the fraction. Sigma is half of the full width half maximum and constrains the width of each peak. The centroid is the energy difference between fine structure states. The fraction is defined as the relative weight of the Gaussian and Lorentzian components. The width of all the peaks is the same since the width comes from a combination of systematic factors. For example, the charge exchange cell running at too high of a temperature can broaden the peaks due to an increased number of collisions with the sodium vapor, sending too much laser power causes peak broadening, and doppler broadening can occur. The centroid, the center point of the spectrum, is a shared parameter across all peaks and is the parameter needed to find the isotope shift for each isotope relative to the reference. Hyperfine coefficients are specific to each isotope for a given transition and are shared across each peak. Combining the centroid with the hyperfine coefficients defines the location and spacing of each of the

peaks. The quantum numbers for a given transition are used to find the allowed excitations corresponding to each peak. Among these quantum numbers, F values are additionally used to define the contribution of each hyperfine coefficient to the corresponding peak. Equation 5.1 is used to combine the hyperfine coefficients, centroid, and F values to define the location of each peak center.

$$Peak\ Center = centroid - F_{A_{ground}}A_{ground} - F_{B_{ground}}B_{ground} + F_{A_{excited}}A_{excited} + F_{B_{excited}}B_{excited} \quad (5.1)$$

The pseudo-Voigt profile for each peak was coded into python using the LMfit package [104] defined as Equation 5.2 where A is the amplitude, μ is the peak center, σ is the same sigma defined above, α is the fraction previously defined, and $\sigma_g = \frac{\sigma}{\sqrt{2\ln 2}}$.

$$f(x; A, \mu, \sigma, \alpha) = \frac{(1 - \alpha)A}{\sigma_g \sqrt{2\pi}} e^{-\frac{(x-\mu)^2}{2\sigma_g^2}} + \frac{\sigma A}{\pi} \left(\frac{\sigma}{(x - \mu)^2 + \sigma^2} \right) \quad (5.2)$$

5.2 Side Peak

Each peak in the data has a side peak, visible as a shoulder in the data set, shown in Figure 5.1. This is due to the transfer of an electron from the alkali vapor to the ion beam in the charge exchange process, which can cause some ions in each ion bunch to be at a different energy. Originally this was handled as side peaks represented as a pseudo-Voigt profile tied to parameters in the main peak. Work was recently done led by Adam Dockery [105] to simulate the reactions occurring within the charge exchange cell to properly model the side peaks of the spectrum. Both methods of handling the side peaks are described below. The results of both methods were compared in detail and are in good agreement.

5.2.1 Side Peak Original Method

The original method for handling the side peaks assumed the main cause of the ions at a different energy were from inelastic collisions. This would result in each peak having a side peak at a fraction of the height and displacement in energy from the main peak. This was coded as creating a pseudo-Voigt profile where the center of the side peak is defined as the corresponding main peaks center plus a shared distance parameter across all side peaks. The

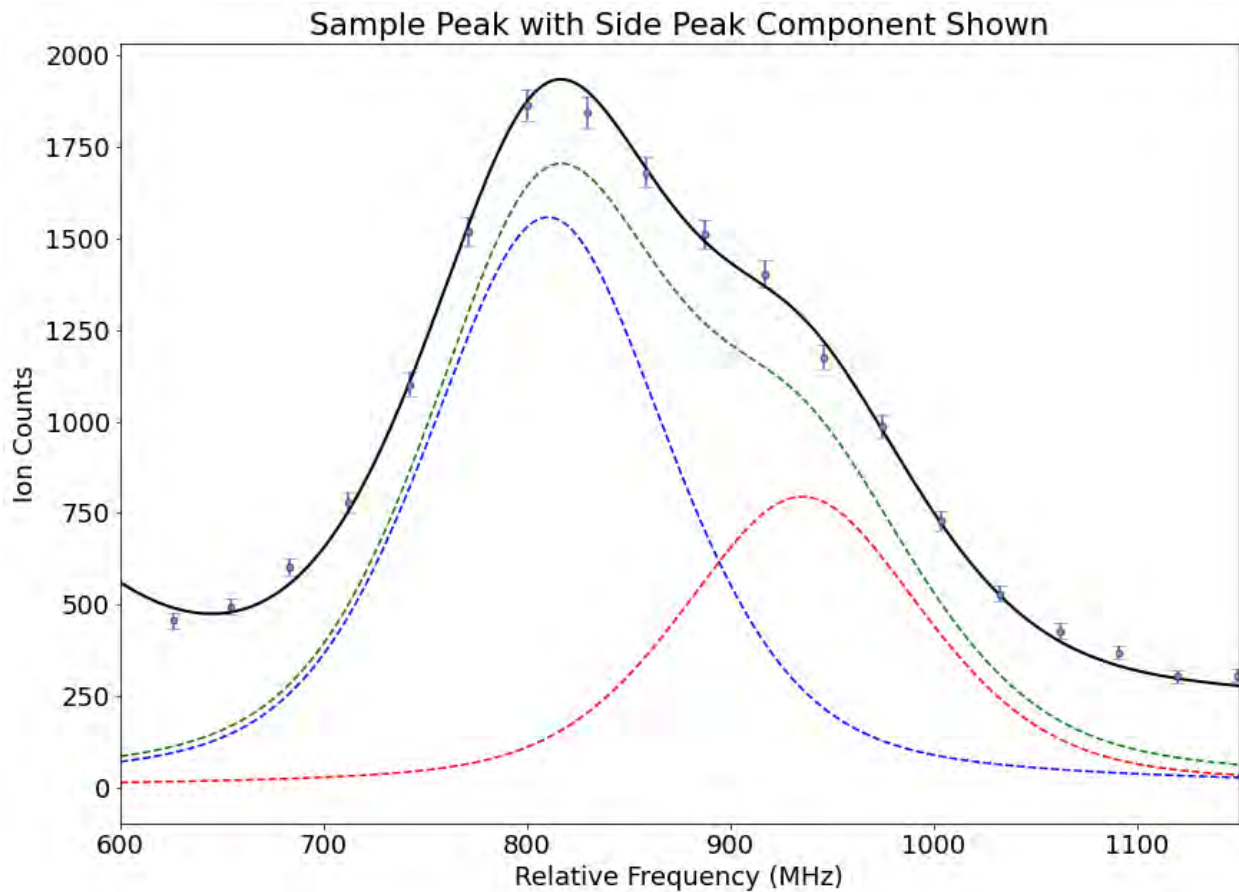


Figure 5.1 One side peak fit components. A zoomed in sample of one peak of data for ^{27}Al is shown. The light blue points are the data points taken. The solid black line is the line of best fit for the data. The green dashed line is the peak's main peak component plus side peak component, offset below the data points for clarity. The blue dashed line is the peak's main component and the red dashed line is the peak's side peak component, both also offset below the data points for clarity. The fitting function for the spectra is built of many components. In the original side peak method each peak has a main peak component and any number of side peaks, in this example just one is shown. When all of the components for one peak are summed the peak line shape is replicated including the "shoulder", as shown in green. Summing all the components for all of the peaks results in the line of best fit for the data, shown in black. Note, the fitted line begins to increase at the lowest frequency due to the next peak in the spectrum beginning at the following point.

amplitude of each side peak is defined as the amplitude of the corresponding main peaks amplitude times a shared parameter. Any number of side peaks can be used in this model, up to six side peaks were tested in the analysis of ^{27}Al . Each additional side peak added is the same distance as every side peak before, d_{side} , defining the side peak center, X_{side} , as the corresponding main peaks center, X_{main} , plus the shared parameter times the number side peak, SP_{number} , shown in Equation 5.3.

$$X_{side} = X_{main} + (d_{side}SP_{number}) \quad (5.3)$$

The amplitude of each additional side peak decreases exponentially. Defining each side peaks amplitude, A_{side} , as the corresponding main peaks amplitude, A_{main} , times a shared parameter to represent the fraction of the main peak, f , to the power of the number side peak, shown in Equation 5.4.

$$A_{side} = A_{main}f^{SP_{number}} \quad (5.4)$$

An infinite number of side peaks can be added modeling an exponential decay rather than a clear shoulder. The number of side peaks was tested and one to three side peaks were tested for each isotope to confirm consistency across different models.

5.2.2 Charge Exchange Simulation Method

During the time between the commissioning of the RISE beamline extension and the online Aluminum experiment a lot of data was taken for ^{27}Al for many transitions. During this time it was discussed if, using atomic theory, the collisions and reactions occurring within the charge exchange process could be simulated and modeled rather than using arbitrary side peaks to replicate the line shape. Through studying the behavior of ^{27}Al , the charge-exchange reaction and in-flight spontaneous decay were simulated to find contributing energy components and relative amplitudes. The details of the simulations can be found in [105]. The simulation finds the energy level the electron is transferred to in the charge exchange process and then follows what energy level it will decay to before interacting with the lasers. Finding the energy levels the electrons occupy can be used to find the number of side peaks

present in the charge exchange process and their properties, better defining the line shape of the data. The contributing energy components can be directly combined with the main peaks center distance to define the location of each side peak. Each side peaks location is defined as the corresponding main peaks center plus the corresponding energy component from the simulation, E_{side} , shown in Equation 5.5. Having a simulated value for the energy components eliminates the free parameter in the original side peak method that searched for the side peak location.

$$X_{side} = X_{main} + E_{side} \quad (5.5)$$

The simulation produces the relative amplitude of the main peak, $A_{rel_{main}}$, and each side peak, $A_{rel_{side}}$. The side peak amplitude is defined by the corresponding main peaks amplitude times the corresponding relative amplitude divided by the main peak relative amplitude, shown in Equation 5.6.

$$A_{side} = A_{main} \frac{A_{rel_{side}}}{A_{rel_{main}}} \quad (5.6)$$

An example peak with the side peaks defined by the CEC simulation is shown in Figure 5.2. When comparing this method for handling the side peaks the centroid and hyperfine coefficient values are in good agreement with the original side peak method but the error of the fitting parameters are reduced as well as the chi squared. A smaller reduced chi squared value signifies a better fit. For ^{22}Al the reduced chi squared was 2.151 for the one side peak fitting method and 2.079 for the CEC simulation fitting method. The uncertainty on the centroid was 5.10 MHz for the one side peak fitting method and 4.74 MHz for the CEC simulation fitting method.

5.3 Beam Energy Correction

When determining the isotope shift between two isotopes a large uncertainty comes from the total beam energy being unknown. While the laser frequency and applied voltage is known with some level of precision, there are additional components which affect the overall beam energy. In the BECOLA beamline these include energy losses in the CEC, gradients in the applied acceleration potential, and applied trapping potentials in the RFQ. To reduce

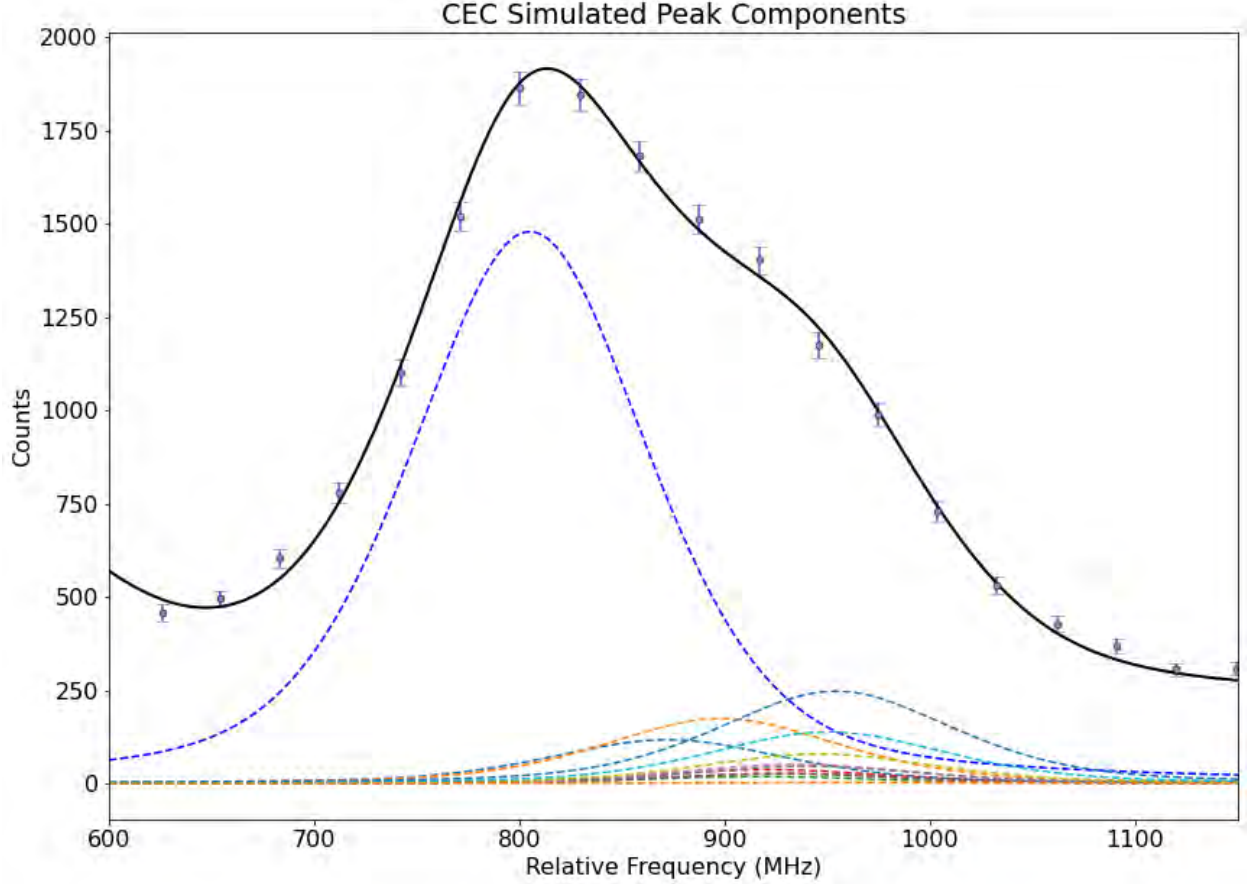


Figure 5.2 CEC simulation fit components. A sample peak with each side peak simulated by the charge exchange simulation is shown. The light blue points are the data points taken. The solid black line is the line of best fit for the data. The blue dashed line is the peak’s main peak component, offset below the data points for clarity. The remaining dashed lines are all of the simulated side peak components, also offset below the data points for clarity. Note, the fitted line begins to increase at the lowest frequency due to the next peak in the spectrum beginning at the following point.

uncertainty and have a more precise determination of the isotope shift value, the beam energy needs to be accurately determined. To do this a series of collinear and anticollinear measurements can be used to determine the rest-frame absolute transition frequency [106]. It can then be used to apply a beam energy correction to the measured hyperfine spectra. The specific transition chosen for this experiment has a very small isotope shift, making this measurement very sensitive to the beam energy correction.

Doing a collinear and anti-collinear spectroscopy measurement of the same transition back to back, the collinear, U_c , and anti-collinear, U_a , centroids are determined. Using

the collinear, v_c , and anti-collinear, v_a , laser frequencies, an initial guess for the rest frame frequency, v_0 , can be made. The initial guess, v_{0g} , is made by taking the square root of the product of U_c and U_a as shown in Equation 5.7 [106].

$$v_{0g} = \sqrt{U_c U_a} \quad (5.7)$$

Using v_{0g} with the laser frequencies, the sensitivity of the transition frequency to a change of beam energy can be determined. The equation to find the sensitivity, $\frac{\delta v_c}{\delta E_{kin}}$, is shown in Equation 5.8 [106]. Either the collinear or anti-collinear equations can be followed, indicated by a c or a subscript.

$$\begin{aligned} \frac{\delta v_c}{\delta E_{kin}} &= \frac{2v_{0g}}{mc^2} \frac{v_c^2}{v_c^2 - v_{0g}^2} \\ \frac{\delta v_a}{\delta E_{kin}} &= \frac{2v_{0g}}{mc^2} \frac{v_a^2}{v_a^2 - v_{0g}^2} \end{aligned} \quad (5.8)$$

The centroid voltage values, U_{calc} , are then calculated using Equation 5.9.

$$\begin{aligned} U_{calc_c} &= mc^2 \left(1 - \frac{v_c^2 - U_c^2}{v_c^2 + U_c^2} \right)^{-1/2} - mc^2 \\ U_{calc_a} &= mc^2 \left(1 - \frac{v_a^2 - U_a^2}{v_a^2 + U_a^2} \right)^{-1/2} - mc^2 \end{aligned} \quad (5.9)$$

The difference of the centroids is found by Equation 5.10.

$$\Delta U = U_{calc_c} - U_{calc_a} \quad (5.10)$$

Using the sensitivity, laser frequencies, and ΔU an improvement on the v_0 value can be made following Equation 5.11 [106].

$$\begin{aligned} v_{0,c} &= \sqrt{\left(v_c - \frac{\delta v_c}{\delta E_{kin}} \Delta U \right) v_a} \\ v_{0,a} &= \sqrt{\left(v_a - \frac{\delta v_a}{\delta E_{kin}} \Delta U \right) v_c} \end{aligned} \quad (5.11)$$

The sensitivity equation, Equation 5.8, and improved v_0 equation, Equation 5.11, can then be looped through to further improve v_0 . To do so, the improved v_0 is subbed in for v_{0g} in the sensitivity equation and then the updated sensitivity value is used in the improved v_0 equation. After iterating through the equations the change in the improved v_0 from the previous value will become negligible.

5.3.1 Determination of v_0 for Aluminum

Leading up to the online Al experiment, a series of collinear and anti-collinear measurements were performed. The experimental setup was set in a configuration for all of the laser light to propagate anti-collinearly through the beamline. The first and second step lasers were reflected using mirrors through a window on the anti-collinear side of the beamline. All online measurements were anti-collinear. To perform a collinear measurement, just the first step laser needed to be sent collinearly through the beamline. The second step laser could be sent in either direction. To switch the direction of the first step laser, a new laser light path could be setup to reflect the laser light through a window on the collinear side. This would have required a lot of additional mirrors to send the laser light from the laser room through a different pipe which would bring the laser light to the collinear side. On the collinear side the laser light would then need to have mirrors setup to overlap it's path with the ions and second step laser. In addition to this involving a lot of setup, when aligning UV, the second step laser would be coming at the optics that would need to be worked on unless the entire second step laser head was moved to the collinear table as well. Although this setup was possible, it was very complicated. For a precise value of v_0 to be determined it is important to switch between the collinear and anti-collinear measurements quickly to avoid any drift in systematics between measurements. To switch between the measurements quickly, a simpler setup was used. Instead of setting a new path for the laser light, a zero degree mirror (IDEX Optical Technologies SP-1-H 108541) that reflects the first step (UV) and transmits the second step (532 nm) laser light was placed at the collinear side window.

The first step laser light reflected directly off of the zero degree mirror back into the beamline. To align the laser light, the back reflection from the zero degree mirror was overlapped with the laser light entering the beamline from the anti-collinear side. Before doing any back reflection alignment, the anti-collinear alignment must be set and the second step laser light blocked. To be able to see the entering laser light and back reflection at the same time a thin cleaning tissue with a small hole was used. The tissue was first taped to

the anti-collinear window port to fully cover the window. Then a small hole at the center of the laser light beamspot on the tissue was cut out, ensuring just the main beam spot was going through the hole and not any fringes. The back reflection light was then visible on the tissue next to the entering laser light. The horizontal and vertical adjustments of the zero degree mirror were used to bring the back reflection to the same position as the entering laser light. Once the alignment was set, the tissue was removed and the second step laser light was unblocked.

In addition to changing the laser light propagation direction and alignment, the laser power, frequency, and timing needed to be adjusted. The laser frequency calculation in Equation 4.1 is different for collinear and anti-collinear measurements, the calculation for the difference was performed and the appropriate change in frequency was made. Due to using the back reflection from the zero degree mirror, the collinear laser light passed through three vacuum windows (Thorlabs VPWW42) rather than one. Each time the laser light passed through a window about 25 to 30 percent of the laser power was lost. For anti-collinear measurements 12.5 mW of laser power was used and 20 mW for collinear measurements. The increase in power was enough to compensate for the loss through the windows. The first step laser light took additional time to reflect back to the interaction region. Although the time is very small and the measurement could be performed without changing the timing, the timing was adjusted by 4 ns to maintain the same interaction region for the collinear and anti-collinear measurement.

Using the setup described three pairs of collinear and anti-collinear measurements were taken. A collinear and anti-collinear spectra are shown in Figure 5.3. Using Equations 5.7-5.11 a ν_0 was determined for each pair. The weighted average of the results was taken to determine a ν_0 of 1129899838.24 MHz with a 2.14 MHz uncertainty shown in Equation 5.12.

$$\nu_0 = 1129899838.24(2.14) \text{ MHz} \quad (5.12)$$

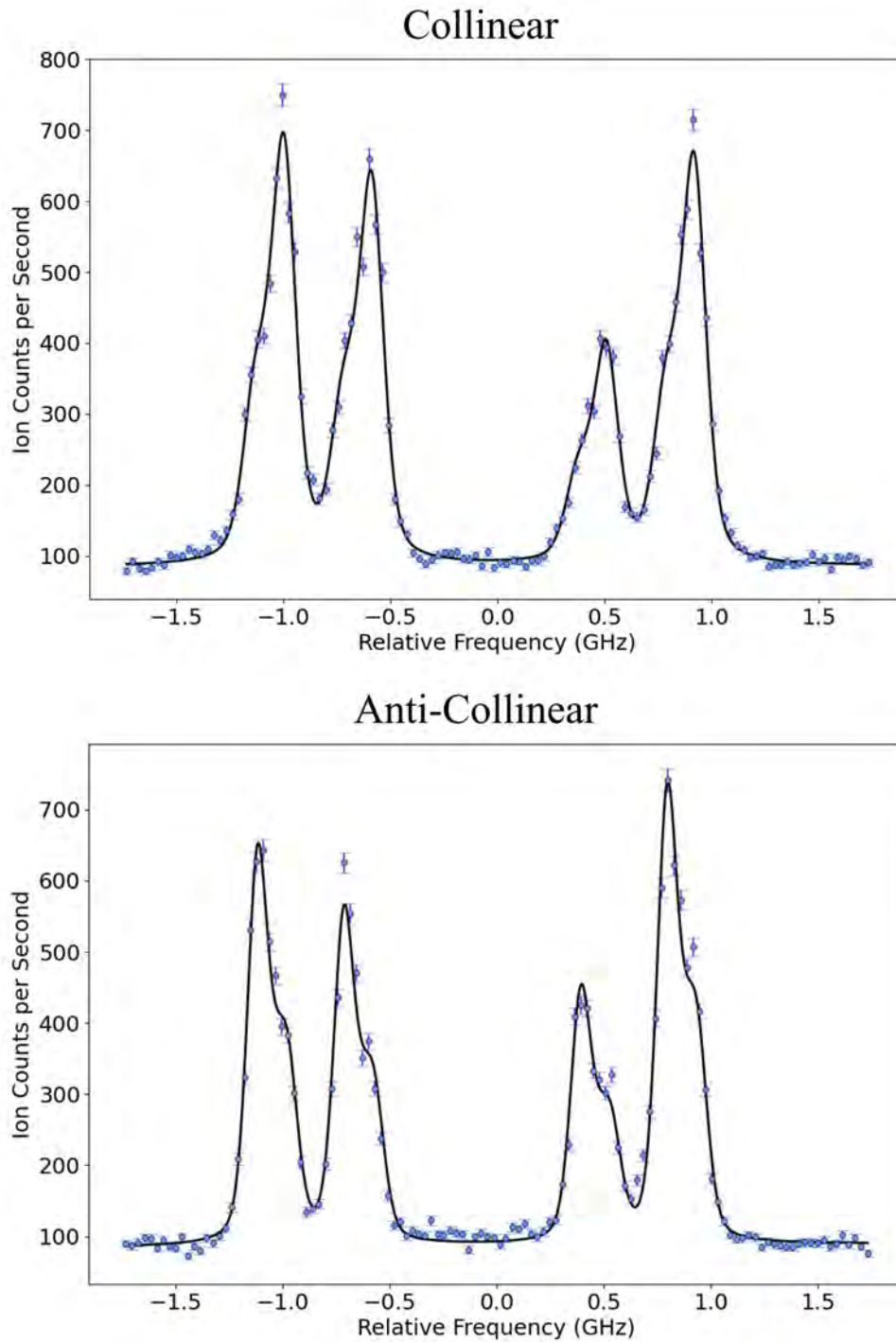


Figure 5.3 Collinear and anti-collinear ^{27}Al spectra. The figure shows a collinear and anti-collinear spectra for ^{27}Al . The upper spectra is collinear and the lower spectra is anti-collinear. The side peak appears at a lower frequency for the collinear spectra and at a higher frequency for the anti-collinear spectra due to the laser propagation direction change.

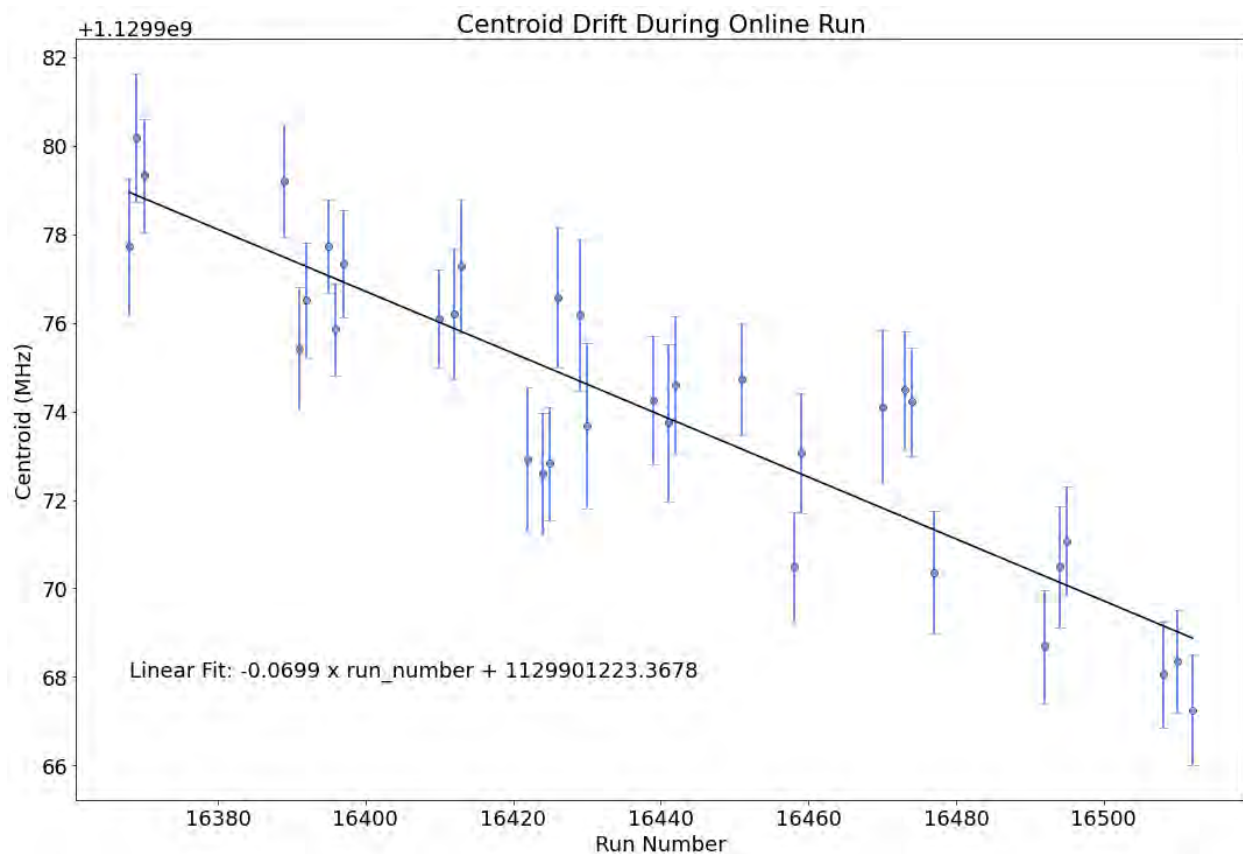


Figure 5.4 Centroid drift plotted as a function of run number. A plot of the centroid value drift versus the run number during the online run. The centroid value of each calibration run is plotted in light blue and a linear fit to the values is plotted as a solid black line.

5.4 Calibration Runs

Throughout the online run the offline ion source was used to measure sets of data for ^{27}Al . This allowed for monitoring of the system for any inconsistencies throughout the day or any drift in the beam energy. Three sets of three scans were taken before and after every isotope measured as well as every six to eight hours during long isotope run times. Fitting the calibration run data a linear drift of the centroids was observed as shown in Figure 5.4. The centroid value for each calibration run are plotted in light blue. A linear line was fit to the centroid values resulting in the solid black line, emphasizing the linearity. To account for the linear drift of the centroids the beam energy needed to be corrected for each isotope run. The applied beam energy correction was found from the differences in the ^{27}Al calibration

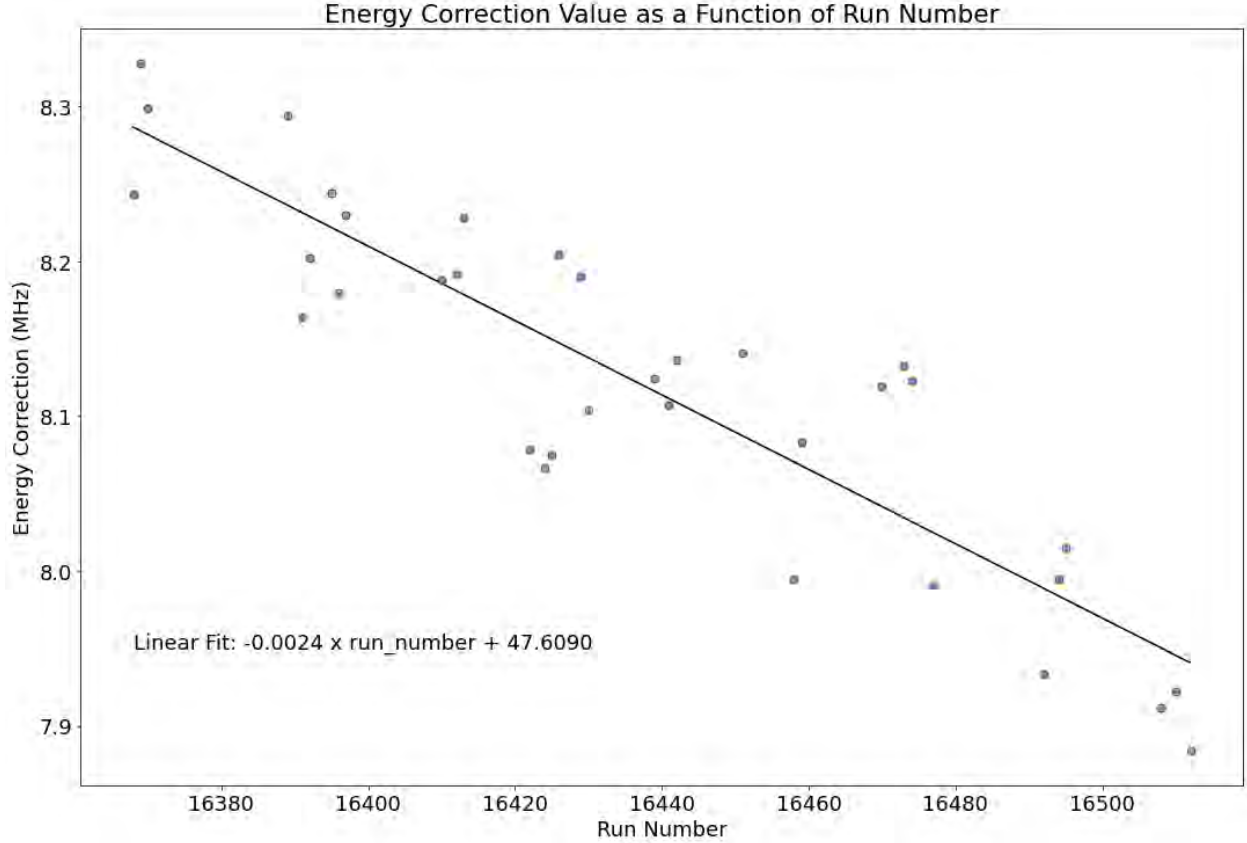


Figure 5.5 Energy correction values as a function of run number. A plot of the energy correction value drift versus the run number during the online run. Energy correction values are plotted in light blue and a linear fit to the values is plotted as a solid black line.

run centroids and the previously found v_0 . Using Equation 5.13 the energy correction values were found for each calibration run. Where v_0 is previously found, fr_0 is the fitted centroid from the run the energy correction is being calculated for, mc^2 is the mass of ^{27}Al in $\frac{eV}{c^2}$, and v_c is the laser frequency.

$$\Delta E = (v_0 - fr_0) \frac{mc^2(v_c^2 - v_0^2)}{2v_0v_c^2} \quad (5.13)$$

The resulting energy correction values plotted as a function of calibration run number are shown in Figure 5.5. The energy correction values are plotted in light blue and a linear fit to the values is shown as a solid black line. As a check the found energy correction values were applied to each calibration run. The resulting centroid values are shown in Figure 5.6. The plot shows that all of the resulting centroid values are well within uncertainty of each other. The energy correction brought all of the calibration run centroids to v_0 , confirming

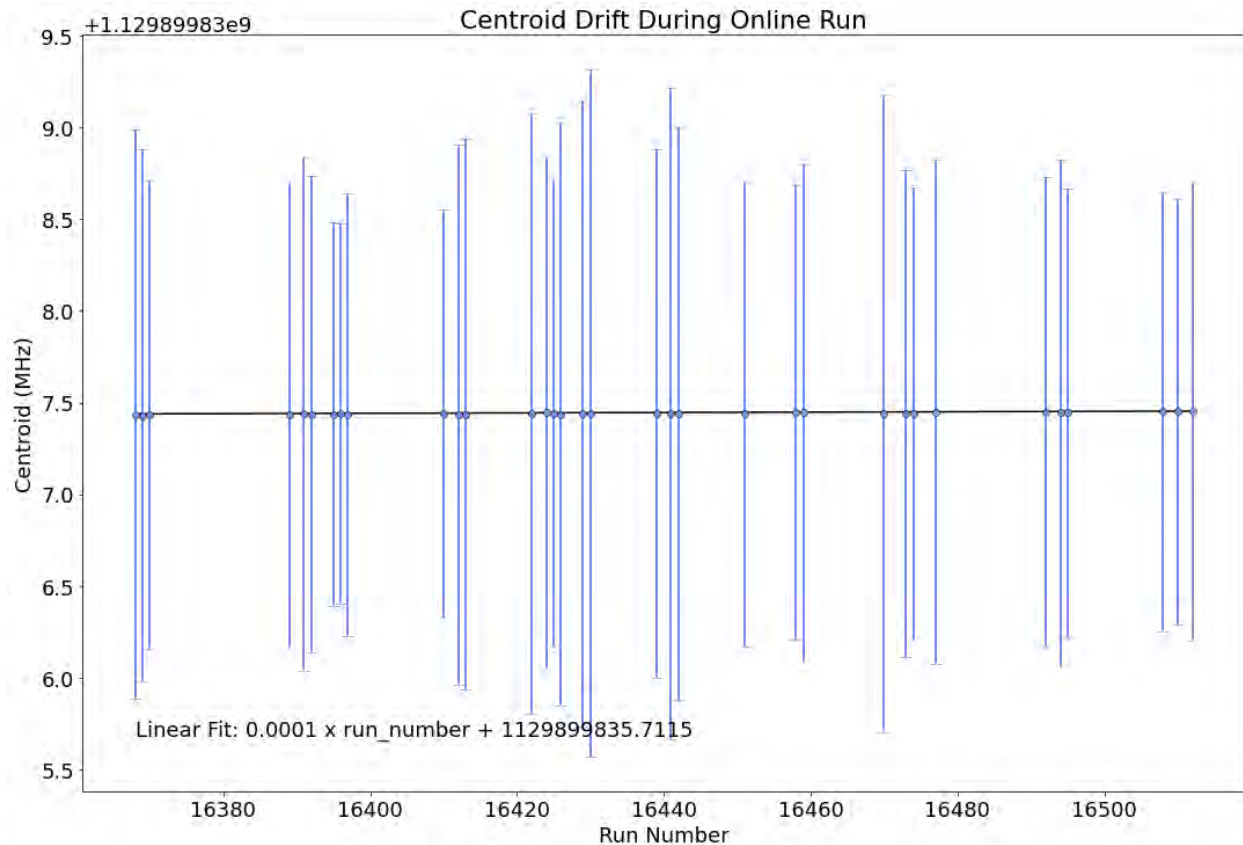


Figure 5.6 Centroid drift as a function of run number after an applied energy correction. A plot of the centroid value drift versus the run number during the online run with an applied energy correction is shown. Applying the energy correction results in the centroid values to be equivalent within error. A linear fit to the data is shown as a black solid line, showing the slope is very close to zero.

the energy corrections were properly calculated.

5.4.1 Energy Correction for Each Isotope

To find the energy correction that needed to be applied for each isotope run, the time the run occurred is compared to the fitted linear line of energy corrections. Figure 5.5 shows the energy correction needed to be applied to each calibration run as a function of run number. For one run of a rare isotope the run number was plugged into the resulting linear equation from the calibration run linear fit to determine what energy correction should be applied. For example, run number 16406 for ^{23}Al was plugged in to find an energy correction of 8.1954 eV needed to be applied. However the length of each run and the time between runs was not consistent. Calibration runs were only 6 minutes long, isotope runs were as long as an

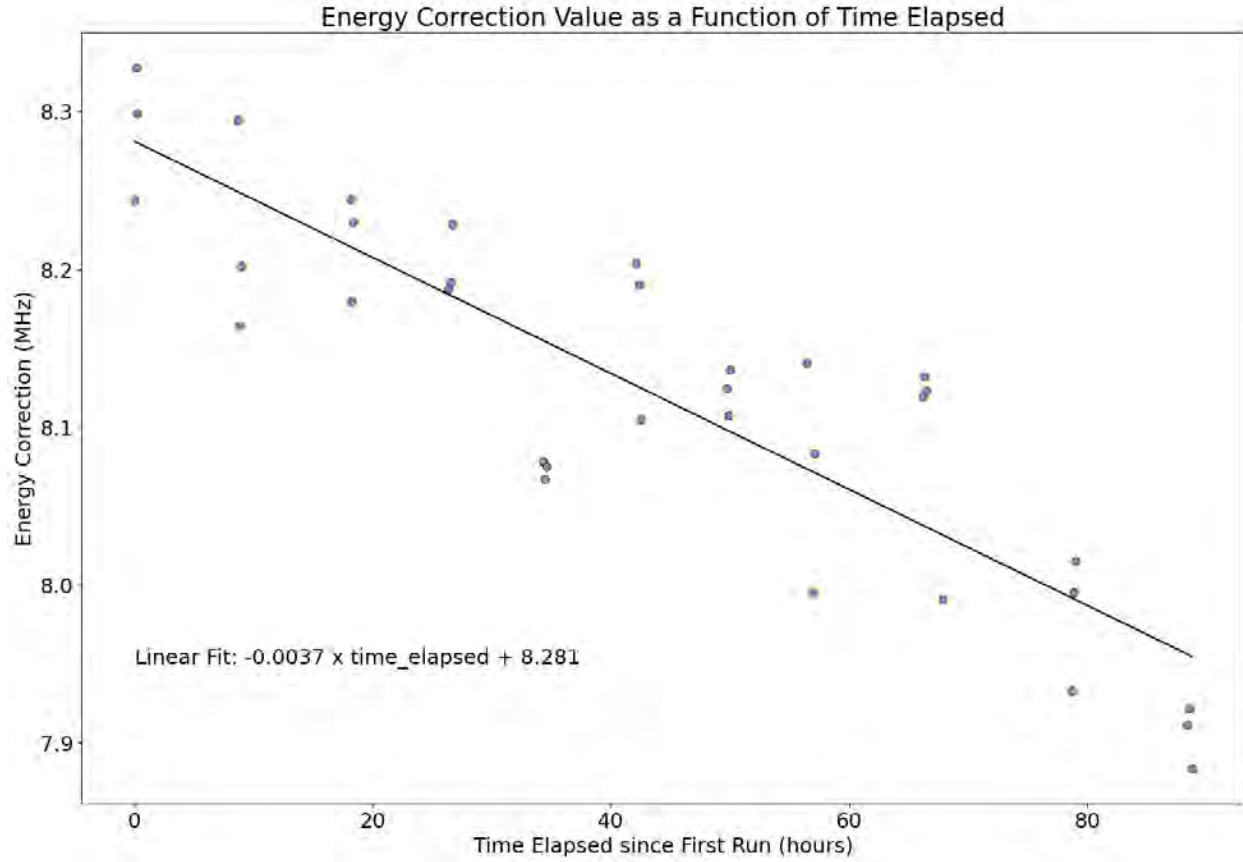


Figure 5.7 Energy corrections as a function of run time. A plot of the energy correction value drift versus the start time of each run during the online run. Energy correction values are plotted in light blue and a linear fit to the values is plotted as a solid black line.

hour. Sometimes a run was started and immediately ended due to pressing start before the experiment was ready. Between back to back runs of the same isotope there was less than a minute to renew the run. When the isotope was being switched and the beam was being aligned through the gas cell, there were up to multiple hours between runs. To ensure the run number was an accurate representation of the centroid drift over the day, the absolute time of each run needed to be considered. The energy correction of each run was plotted as a function of absolute run start time in Figure 5.7. The very first calibration run of the experiment was taken as time zero, every subsequent run during the experiment's time was the time elapsed since the first calibration run start time. The start time of each isotope run was then plugged into the linear fit of the corrections as a function of time to find the corresponding energy correction. For example, using the same run number 16406 for ^{23}Al

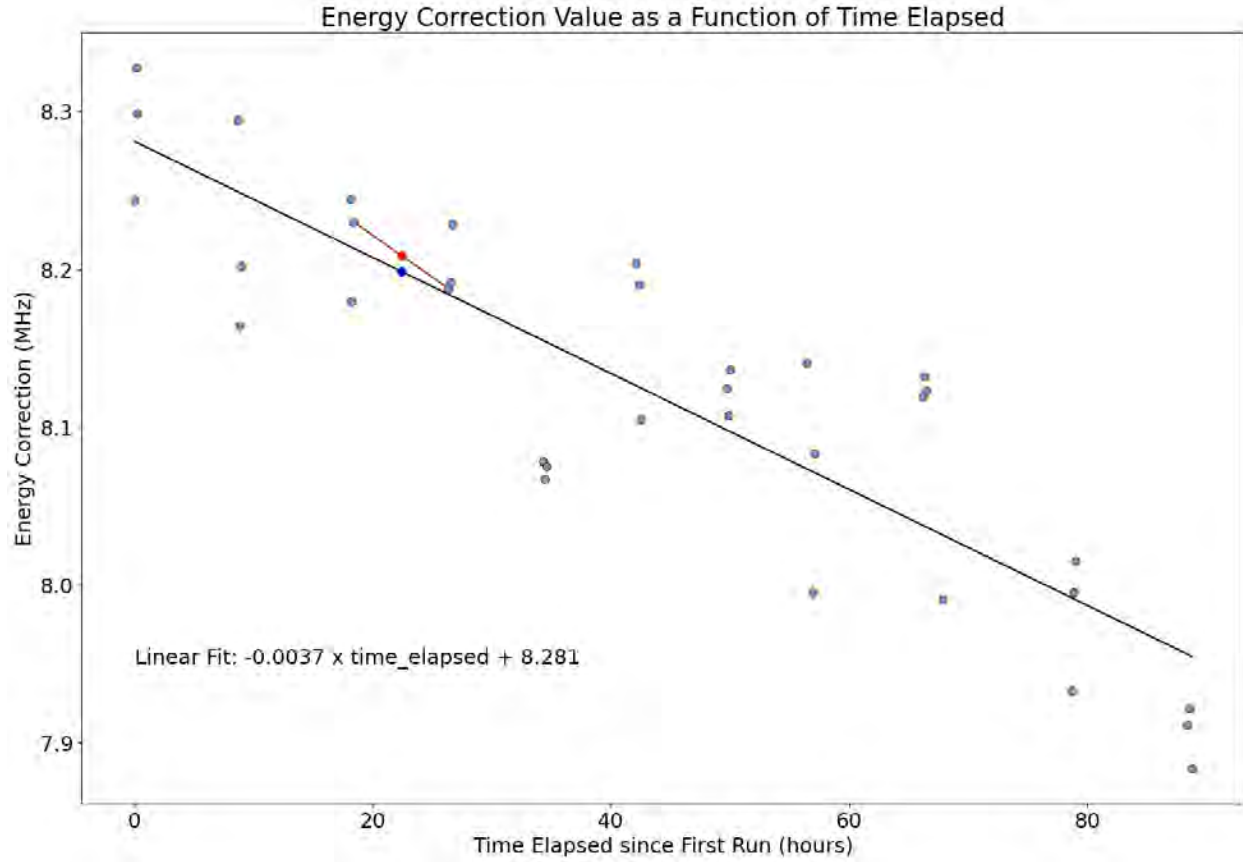


Figure 5.8 Energy corrections found using a linear fit and closest calibration runs. A plot of the energy correction value drift versus the start time of each run during the online run. Energy correction values are plotted in light blue and a linear fit to the values is plotted as a solid black line. The closest calibration run before and after the online run are connected with a red line. The linear fit correction value is shown as a blue point and the closest calibration run correction value is shown in red.

as before, the start time of the run relative to the start time of the first calibration run was found to be 80,841 seconds or 22.46 hours. Plugging that time into the linearly fit equation resulted in an energy correction of 8.1985 eV. Using time rather than run number results in a 0.0031 eV difference. 0.0031 eV is equivalent to a 0.09 MHz difference for the applied correction. Although this value is small relative to the uncertainty on the centroid values, it was accounted for in this analysis.

Rather than using a linear fit, the closest calibration run before and after the online run can be used. Figure 5.8 shows both the linear fit and closest calibration run correction values. In the figure the black line shows the linear fit to all of the calibration run energy correction

values. Using the same run number 16406 for ^{23}Al as before, the time the online run took place is plotted on the linear line in blue. The linear fit energy correction value found was 8.1985 eV. Taking the closest calibration run before and after the online run and making a linear line between them resulted in the red line shown in the figure. Plugging the online run time into the linear equation between the two points resulted in an energy correction of 8.2085 eV and is shown as a red point. The difference between the two methods is 0.01 eV equivalent to 0.2916 MHz. The difference is within the uncertainty of the fitted linear line which was included in the final charge radius value uncertainty. Although the difference in methods is larger for some runs, the resulting centroid value of each method is consistently within one sigma uncertainty.

In addition to accounting for time rather than using run number, one energy correction could be applied to all of the runs for an isotope, to each run, or to each scan within the runs. To use one energy correction for all runs of a given isotope, the correction for the center point in time was used. For example, the first run of ^{25}Al was at 4.60 hours and the final run at 7.74 hours. The halfway point through the runs was at 6.17 hours. That time was plugged into the linearly fit equation and resulted in a 8.2583 MHz correction that was used for all runs for ^{25}Al . To use one correction for each run, each run start time was plugged into the linear equation. For ^{25}Al this was five runs with resulting energy corrections ranging from 8.2641 eV to 8.2525 eV. Within each run were a number of scans, for example the first run of ^{25}Al had 24 scans with each scan taking 2 minutes to complete. Resulting in the final scan of the run to have started 0.77 hours after the initial run start time. Plugging in each scan start time into the linear equation resulted in a 0.0028 eV difference in the applied energy correction from the first to last scan. A full analysis was completed with each method and the resulting centroids all agreed within one sigma uncertainty.

Applying the energy corrections accounted for any drift that occurred throughout the day. The uncertainty of the fitted linear line was included in the systematic error of the measurement.

5.5 Each Isotope Fit

Table 5.1 Experimental isotope shift values. The resulting isotope shift values from the CEC simulation fitting method, CEC , and the one side peak fitting method, $1\ SP$, are shown for each Al isotope measured. In addition to the statistical uncertainty shown in parenthesis, there is an additional 3.14 MHz systematic uncertainty shown in square brackets.

Isotope	Isotope Shift $_{CEC}$ (MHz)	Isotope Shift $_{1\ SP}$ (MHz)
22	8.09(4.74)[3.14]	9.79(5.10)[3.14]
23	10.44(1.82)[3.14]	11.14(1.82)[3.14]
24	3.83(1.78)[3.14]	4.00(2.24)[3.14]
24m	9.67(2.24)[3.14]	9.95(2.31)[3.14]
25	0.97(1.17)[3.14]	1.00(1.12)[3.14]

Table 5.2 Experimental hyperfine coefficients. The resulting A hyperfine coefficient values for the atomic ground $3p\ ^2P_{1/2}$, Grd, and excited $5s\ ^2S_{1/2}$ state, Exc, are shown from the CEC simulation fitting method, CEC , and from the one side peak fitting method, $1\ SP$, for each Al isotope measured. In addition to the statistical uncertainty shown in parenthesis, there is an additional 0.18 MHz systematic uncertainty on the ground state A hyperfine coefficient and 0.05 MHz systematic uncertainty on the excited state A hyperfine coefficient shown in square brackets.

Isotope	$A\ Grd_{CEC}$ (MHz)	$A\ Exc_{CEC}$ (MHz)	$A\ Grd_{1\ SP}$ (MHz)	$A\ Exc_{1\ SP}$ (MHz)
22	168.36(2.09)[0.18]	43.88(1.63)[0.05]	168.51(2.21)[0.18]	43.90(1.75)[0.05]
23	537.72(0.94)[0.18]	145.18(0.94)[0.05]	537.52(0.97)[0.18]	145.20(0.94)[0.05]
24	243.52(0.68)[0.18]	65.74(0.64)[0.05]	242.68(0.93)[0.18]	67.49(0.83)[0.05]
24m	1032.36(0.87)[0.18]	278.96(1.42)[0.05]	1030.04(2.68)[0.18]	279.88(0.64)[0.05]
25	501.91(0.61)[0.18]	135.84(0.59)[0.05]	501.90(0.64)[0.18]	135.96(0.59)[0.05]

5.5.1 ^{25}Al

^{25}Al had the highest rates of all of the isotopes measured resulting in high statistics similar to stable ^{27}Al measurements. No changes or unique features needed to be applied to the fitting function. The isotope shift was found using Equation 2.15, the reference centroid used was the v_0 found from the offline collinear anti-collinear measurements shown in Equation 5.12. The resulting isotope shift was found to be 0.97 MHz with a 1.17 MHz uncertainty for the CEC fitting method and 1.00 MHz with a 1.12 MHz uncertainty for the one side peak fitting method. The hyperfine coefficients were measured to be 501.91 MHz with 0.61 MHz uncertainty for the ground state and 135.84 MHz with 0.59 MHz uncertainty for the excited

state for the CEC fitting method, 501.90 MHz with 0.64 MHz uncertainty for the ground state and 135.96 MHz with 0.59 MHz uncertainty for the excited state for the one side peak fitting method. The results from the fits are included in Table 5.1 and 5.2.

5.5.2 ^{24}Al

^{24}Al had high statistics, comparable to ^{25}Al , however the ^{24}Al spectra contained both a ground nuclear state and an isomeric nuclear state, referred to as 24m. The isomeric state has spin 1+ and four allowed hyperfine transitions. The ^{24}Al spectrum contains eight peaks in total, four from the ground state and four from the isomeric state. To properly fit the spectrum the fitting function needed to be altered to account for the two states. This was accomplished by adding in pseudo-Voigt profiles for each isomeric peak and corresponding side peaks. The isomeric peak profiles share a sigma and fraction with the ground state peaks but have their own centroid and hyperfine coefficients.

There was concern of ensuring the fit was assigning each peak to the proper nuclear state. To ensure the peaks were being assigned properly the spectra containing different amounts of ions in the isomeric state were used. During the online run multiple spectra were measured with a varying amount of ions in the isomeric state, which has a 130 ms half-life, relative to the amount of ions in the ground state, which has a 2.053 s half-life, see experimental data chapter for details. Fitting these spectra, the location of the isomeric peaks could be compared. As the amount of ions in the isomeric state decreases the isomeric peaks should decrease in amplitude but their peak centers should not change. These spectra were fit and consistency was found among the spectra. An example spectra with an increased bunching time and less ions in the isomeric state is shown in Figure 5.9 relative to a spectra with the shortest bunching time possible and largest amount of ions in the isomeric state. The spectra with less ions in the isomeric state has poorer statistics since only a few runs were taken with the different buncher settings. In the figure it can be seen that the fit assigned the isomeric peaks in the same location and the relative amplitude scaled as expected with less ions in the isomeric state. For example, the furthest isomeric state peak to the left is

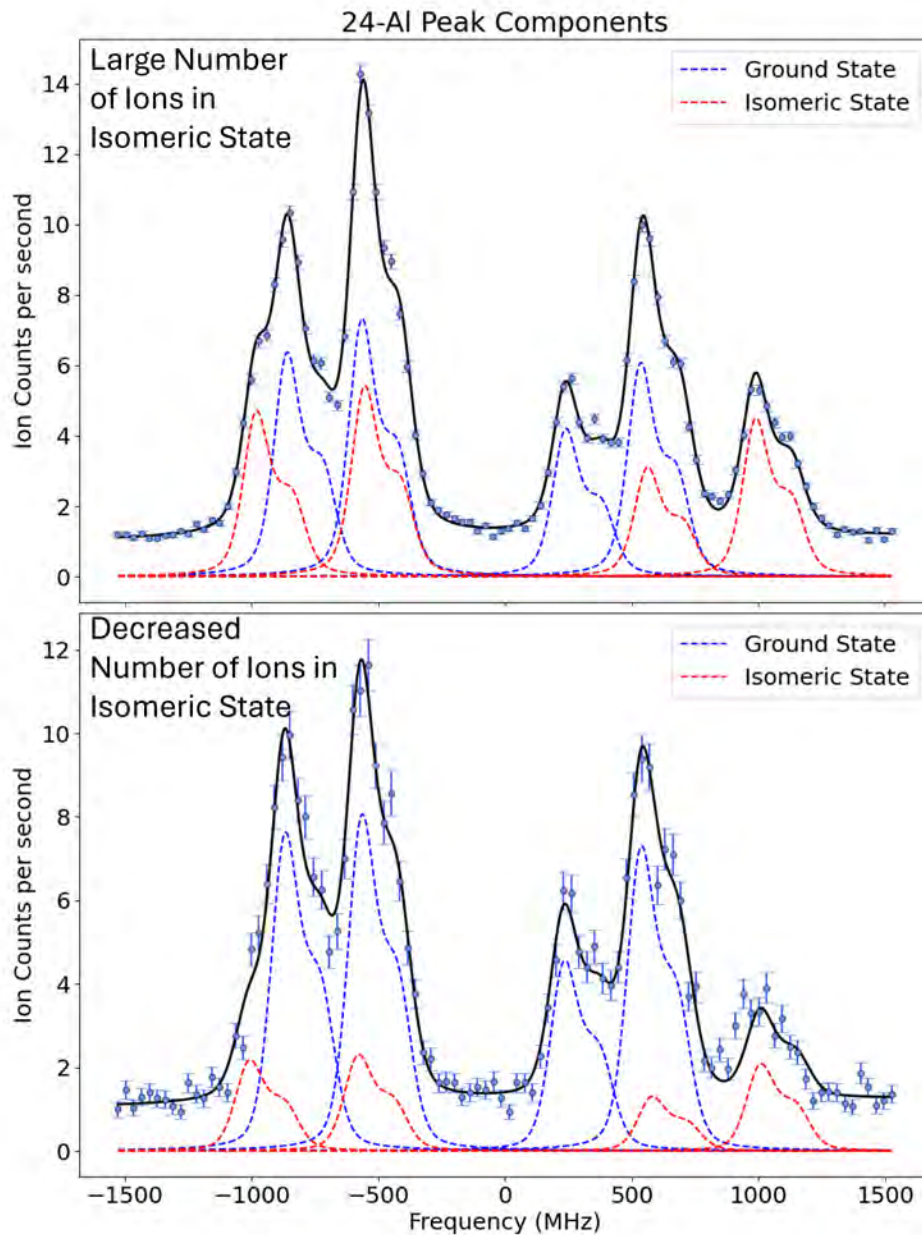


Figure 5.9 Variation of the amount of isomeric state in the ^{24}Al spectra. Two spectra for ^{24}Al are shown. The light blue points are the data taken, the black line is the line of best fit using the CEC simulation fitting method, the blue dashed line is the nuclear ground state peak components, and the red dashed line is the nuclear isomeric state peak components. The peak components do not include the background to be offset below the data for visual clarity. The bottom spectra has less ions in the isomeric state than the top spectra. The peak components have the same center location in both spectra, but the amplitude of the isomeric peaks are smaller when less ions are in the isomeric state.

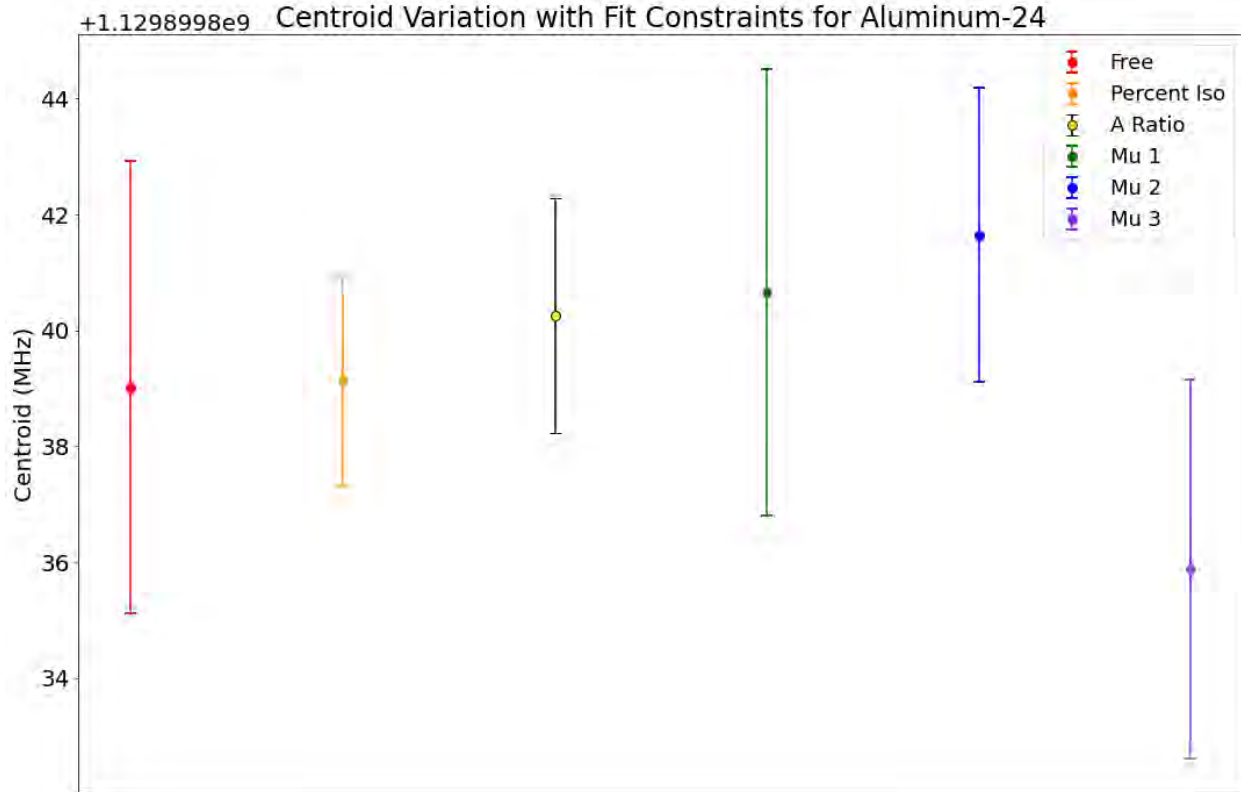


Figure 5.10 Parameter variation for ^{24}Al . A plot of the centroid values for a variety of fitting methods for ^{24}Al is shown. The results shown were found using the CEC simulation fitting method, the same analysis was completed using the one side peak fitting method and has consistent results, the one side peak fitting results are omitted from the plot for clarity. See text for details.

centered around -1000 MHz in both spectra. However, when there is a larger number of ions in the isomeric state the peak height is over 4 ions per second, compared to when less ions are in the isomeric state and the peak height is only about 2 ions per second. The resulting frequency values for each of the eight peak centers agree within error.

In addition to confirming the proper peak placement between the nuclear states, a variety of fit parameters were tested to test the fit. Fixing fit parameters to stable ^{27}Al or theoretical values and comparing the resulting centroids can confirm agreement and consistency. Figure 5.10 shows the resulting centroid values for a variety of fit parameter settings.

One thing that could be fixed was the magnetic dipole moment of the isomeric nuclear state. Multiple theory values and one literature value are available to be used to fix the A hyperfine coefficients for the isomeric state. In Figure 5.10 the resulting centroid values from

fixing μ for the isomeric state are shown in green, blue, and purple as "Mu 1", "Mu 2", and "Mu 3" respectively. The value of Mu 1 is 2.99(9) μ_N found in literature in Reference [107], Mu 2 is 2.98 μ_N from USDB free and Mu 3 is 3.07 μ_N from USDB eff. both theoretically calculated by Alex Brown, details of his calculations can be found in the Results chapter. Looking at the three points in the figure, the different μ values vary the centroid value, however given the uncertainty they agree within one or two sigma. In addition to fixing μ , the A hyperfine coefficients could be tied together using the ratio between A values found in ^{27}Al . The resulting centroid value from fixing the A ratio is shown in Figure 5.10 as a yellow circle with a black error bar labeled "A Ratio". Fixing to the A ratio is explained more in the ^{22}Al sub-section. The resulting centroid agrees with the free parameter fit centroid result within one sigma and has a smaller uncertainty due to reducing the fit parameters.

In addition to fixing to stable ^{27}Al or theoretical values, having knowledge of the beam composition could be used to constrain the fit and reduce free parameters. The beam delivered to the BECOLA facility for the experiment had a given fraction of ions in the isomeric state versus the ground state. The height of each peak in the spectrum varied based on the number of ions available to ionize. Since there was a given fraction of the incoming beam that was in the isomeric state, then the hyperfine spectra isomeric state peaks would be a given fraction of the height of the ground state peaks. Assuming none of the peaks are saturated, each isomeric peak height was the same fraction of the height of the corresponding ground state peak. To reduce free parameters in the fit, the isomeric peak heights could be tied to the ground state peak heights with a shared parameter across each pair of peaks. This one shared parameter which accounts for fitting the amount of isomeric state present replaced the four parameters that adjusted each individual isomeric state peak height. The resulting centroid is shown in Figure 5.10 in orange and is labeled "Percent Iso". The resulting centroid agrees well within uncertainty with the free parameter fit centroid result with a smaller uncertainty.

After confirming the isomeric state peak centers the isotope shift was found using Equa-

tion 2.15 for both the nuclear ground state, 3.83 MHz with a 1.78 MHz uncertainty, and nuclear isomeric state, 9.67 MHz with a 2.24 MHz uncertainty for the CEC fitting method. For the nuclear ground state, 4.00 MHz with a 2.24 MHz uncertainty, and nuclear isomeric state, 9.95 MHz with a 2.31 MHz uncertainty for the one side peak fitting method. In addition the hyperfine coefficients were measured for the nuclear ground state to be 243.52 MHz with 0.68 MHz uncertainty for the atomic ground state and 65.74 MHz with a 0.64 MHz uncertainty for the atomic excited state using the CEC simulation fitting method. For the nuclear ground state to be 242.68 MHz with 0.93 MHz uncertainty for the atomic ground state and 67.49 MHz with a 0.83 MHz uncertainty for the atomic excited state using the one side peak fitting method. For the nuclear isomeric state the atomic ground state hyperfine coefficient was 1032.36 MHz with 0.87 MHz uncertainty and 278.96 MHz with 1.42 MHz uncertainty for the atomic excited state using the CEC simulation fitting method. For the nuclear isomeric state the atomic ground state hyperfine coefficient was 1030.04 MHz with 2.68 MHz uncertainty and 279.88 MHz with 0.64 MHz uncertainty for the atomic excited state using the one side peak fitting method. The results from the fits are included in Table 5.1 and 5.2.

5.5.3 ^{23}Al

^{23}Al required a longer run time to have good statistics, but with no isomeric state all peaks were well resolved. Although statistics were not as good as ^{25}Al , no adjustments needed to be made to the fit. Using Equation 2.15, the resulting isotope shift was found to be 10.44 MHz with a 1.82 MHz uncertainty using the CEC simulation fitting method and 11.14 MHz with a 1.82 MHz uncertainty using the one side peak fitting method. The hyperfine coefficients were measured to be 537.72 MHz with 0.94 MHz uncertainty for the ground state and 145.18 MHz with 0.94 MHz uncertainty for the excited state using the CEC simulation fitting method, 537.52 MHz with 0.97 MHz uncertainty for the ground state and 145.20 MHz with 0.94 MHz uncertainty for the excited state using the one side peak fitting method. The results from the fits are included in Table 5.1 and 5.2.

5.5.4 ^{22}Al

With ^{22}Al having the lowest rates, it also had the worst statistics. In addition to poor statistics, the peak centers were much closer together than the other isotopes, making the peaks less resolved. The Aluminum experiment had a finite time to run, an infinite amount of time could not be spent taking data on ^{22}Al to slowly gain statistics. Combining the poor statistics with the poorly resolved peak, ^{22}Al had the highest statistical uncertainty on the parameters. The fit was still able to be done using all free parameters and the resulting centroid value is referred to in this sub-section as the free centroid. To ensure the fit was giving the correct parameters, the fit condition was varied to verify consistency. Many different parameters could be fixed to theoretical or stable Aluminum values.

The ratio between the ground and excited states hyperfine coefficients is the same across all isotopes. The ratio found in analyzing the stable Aluminum data could be used to fix the ratio of ^{22}Al . Many runs of the transition used in the online experiment were performed with ^{27}Al in preparation for the online experiment. The A ratio was found by dividing the ground state A hyperfine coefficient by the excited state A hyperfine coefficient. The ratio can be inverted to take the excited state A divided by the ground state A , the parameter the ratio is multiplied with to fix the ratio for ^{22}Al just needs to be changed as well. The weighted average of all offline ^{27}Al runs A ratios resulted in a ratio of 3.706(0.020), which was used to fix the ratio for ^{22}Al . Fixing the A ratio was done by tying one coefficient to the other, for example the ground state coefficient was set equal to the excited state coefficient times the ratio. This eliminated one free parameter, the result of this fit agrees with the free fit within error. The difference in centroid values is 0.49 MHz, the free centroid has an uncertainty of 4.67 MHz and the fixed A ratio centroid has an uncertainty of 4.53 MHz from the fit. The difference in values is well within the fit uncertainty. In addition to the statistical uncertainty on the centroid from the fit, the uncertainty of the A ratio needs to be included. Equation 5.1 related the centroid to the A hyperfine coefficients. Setting B

equal to zero and solving for the centroid results in Equation 5.14.

$$centroid = peak\ center + F_{A_{ground}}A_{ground} - F_{A_{excited}}A_{excited} \quad (5.14)$$

Plugging in the excited state A coefficient times the A ratio for the ground state A hyperfine coefficient results in Equation 5.15.

$$centroid = peak\ center + F_{A_{ground}}A_{excited}A_{ratio} - F_{A_{excited}}A_{excited} \quad (5.15)$$

To find the uncertainty on the centroid due to the A ratio uncertainty, the partial derivative of Equation 5.15 with respect to the A ratio was taken, shown in Equation 5.16.

$$\frac{\partial centroid}{\partial A_{ratio}} = F_{A_{ground}}A_{excited} \quad (5.16)$$

The partial derivative was then be multiplied by the uncertainty of the A ratio as shown in Equation 5.17 where Δ represents error.

$$\Delta centroid = \Delta A_{ratio} \frac{\partial centroid}{\partial A_{ratio}} \quad (5.17)$$

Plugging in the values, an uncertainty of 1.86 MHz on the centroid due to the uncertainty of the A ratio was found. Adding this uncertainty in quadrature with the 4.53 MHz uncertainty from the fit resulted in a total uncertainty of 4.90 MHz. The difference in centroid values is still well within the total uncertainty, but the total uncertainty of the fixed A ratio centroid is larger than the uncertainty of the centroid value of the fit with all parameters free with the A ratio uncertainty included.

The magnetic dipole moment for all the isotopes were found theoretically prior to the data analysis. The theoretical moment values and how they were calculated can be found in the Results chapter. Using the magnetic dipole moment, the hyperfine coefficients could be fixed to a theoretical guess to fit the data. The resulting centroid is 18.44 MHz less than the free parameter fit centroid result. The fixed-to-theory centroid result has a 42.37 MHz uncertainty, while the values are within the uncertainty of the fixed-to-theory centroid result, the fixed-to-theory centroid result is only within 5 sigma of the free centroid result uncertainty.

Fixing to theory is dependent on the theoretical model used to find the magnetic dipole moment. This value cannot be used as a result, but can be a good check for consistency. In this case it is known that the theory used to find the magnetic dipole moment is less reliable moving to dripline nuclei such as ^{22}Al so a deviation from the theoretical result was expected.

Another parameter that could be assumed was the Racah coefficients. The Racah coefficients are a theoretical combination of the quantum numbers for each allowed transition to predict the probability of each transition, which is correlated to the relative height of each peak. The details of the Racah coefficients are explained in the Simulation sub-section of the Experimental Data chapter. With unresolved peaks these Racah coefficients could be used to fix the relative height between all of the peaks. RISE laser spectroscopy results vary from this theoretical prediction. One reason for the disagreement is some allowed transitions in the hyperfine structure saturate at a lower laser power than others. If the laser power is set very high to maximize efficiency, then all transitions are saturated and the line shape is broadened. If the laser power is set very low to prioritize a very narrow line shape, then the transitions are not all saturated but the efficiency is reduced. In these measurements the line shape and efficiency are both important and were considered in choosing the laser power. In the maximization of both factors the laser power was set to a value where some peaks are saturated while others are not, causing the peak heights to vary from the predicted relative heights. An assumption could be made that the relative peak amplitudes vary from theory the same for each isotope, allowing the relative amplitudes for stable Aluminum to be used for ^{22}Al . However, with different rates, spins, and conditions of the measurements, this may not be a fair assumption. The ^{22}Al spectra was fit both fixed to theoretical Racah coefficients and ^{27}Al relative peak amplitudes. Starting with the Racah coefficient values, each set of two peaks were tied together using the relative heights predicted by the Racah coefficients. The centroid value obtained by fixing peak amplitudes to the Racah coefficients varied from the centroid obtained with all fitting parameters free by 1.28 MHz, well within the free centroid

error, however the Racah fit had large error, having an uncertainty on the centroid of 46.64 MHz. This large uncertainty is due to the actual peak heights variation from the Racah coefficients. The centroid value obtained by fixing the peak heights to the ^{27}Al relative peak amplitudes results in a centroid value that is 4.44 MHz different than the centroid value obtained with all fitting parameters free with a 4.37 MHz uncertainty. Although the spin and conditions of the measurements were different, the centroid value obtained by fixing the peak heights to the ^{27}Al relative peak amplitudes better reproduced the centroid value obtained with all fitting parameters free. The value is within the uncertainty of the centroid value obtained with all fitting parameters free but slightly outside of the uncertainty of the centroid value obtained by fixing the peak heights to the ^{27}Al relative peak amplitudes.

A plot with the centroid values for each parameter variation is shown in Figure 5.11. Fitting with all parameters free is shown in red and labeled "Free". The two fit variations in best agreement, fixing to the A ratio of ^{27}Al and the relative peak heights of ^{27}Al , are shown in orange and green labeled "A Ratio" and "27 Peak Height". The two fit variations with large uncertainty, fixing to a theoretical μ value and theoretical Racah coefficients, are shown in blue and purple, labeled "Mu" and "Racah". In addition to the centroid value, other fit parameter results were compared to verify agreement. The parameter variation showed good agreement when fixing to values from ^{27}Al and some variation when fixing to theory. This result supported the free parameter fit result, resulting in the free fit result to be used as a final result.

The spin of ^{22}Al is not known, it is highly indicated in literature to be 4+ [108], but has not been definitively determined. Laser spectroscopy is sensitive to the spin and can determine the spin of rare isotopes, for example Zirconium isotopes [109]. However, the transition used for this Al experiment was not sensitive to the spin. A statement regarding the spin assignment could still be made, but with the low rates and hence low statistics of the ^{22}Al spectra, the ability to make a statement was much more challenging. Despite the difficulties, it was attempted to provide insight for the spin of ^{22}Al . The possible spins for

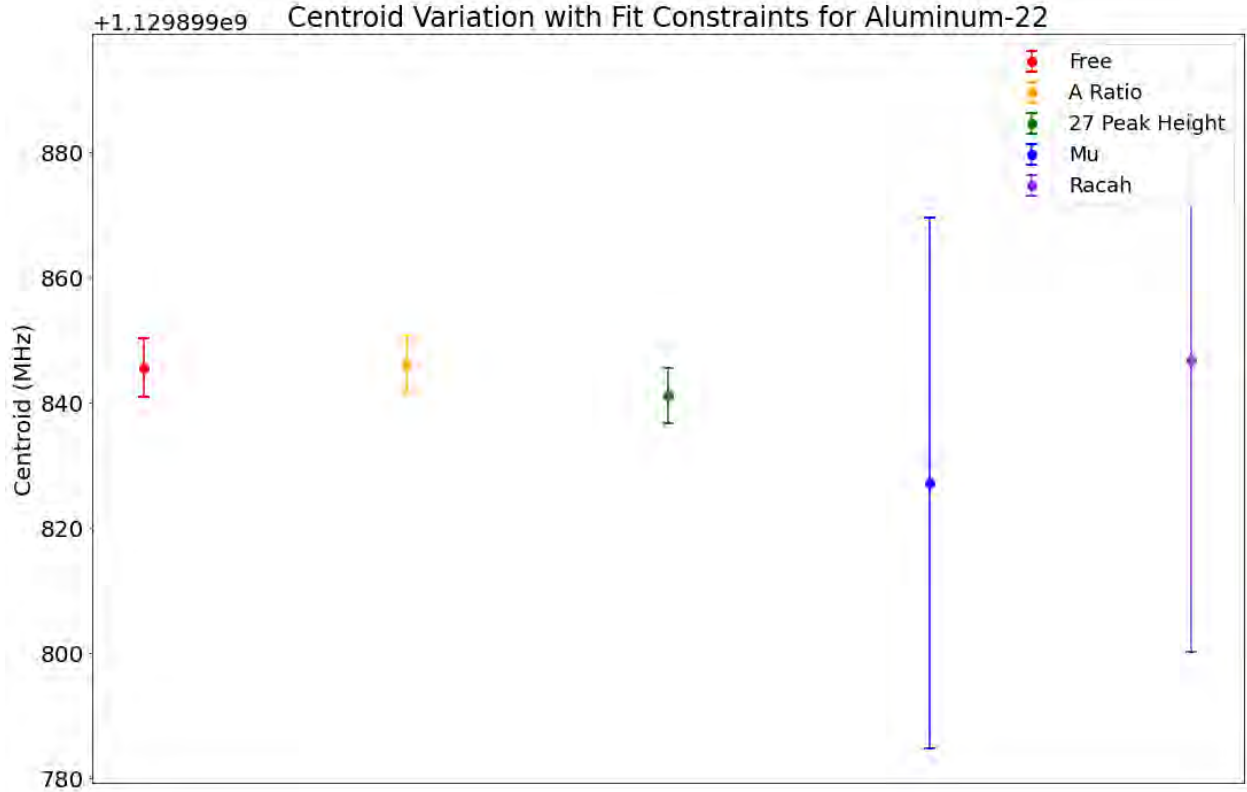


Figure 5.11 Parameter variation for ^{22}Al . A plot of the centroid values for a variety of parameter sets for ^{22}Al is shown. The results shown were found using the CEC simulation fitting method, the same analysis was completed using the one side peak fitting method and has consistent results, the one side peak fitting results are omitted from the plot for clarity. See text for details.

^{22}Al are 1, 2, 3, 4, and 5 assuming the last unpaired proton and neutron occupy the $d_{5/2}$ orbital. To start, the spectra was fit with each of these spins and the result was used to determine the charge radius, which was plotted with the isotopic chain. The results are shown in Figure 5.12. Looking at the results, spin 1, shown as a blue diamond, and 2, shown as an orange x, give physically unrealistic results and can be ruled out. A figure showing the charge radii trend without spin 1 and 2 plotted is shown in Figure 5.13. Narrowing down to spin 3, 4, and 5 the A ratios were found and compared to the A ratio of ^{27}Al . The results are shown in Figure 5.14. In the figure the size of the uncertainty is evident. While all of the ratios are larger than that of ^{27}Al , the error bars for both spin 4 and 5 touch the band of ratios for ^{27}Al . Although with such large overlapping uncertainty for spin 3, no spin can be ruled out at this level. To try and get a better insight into the spin assignment, fixing the

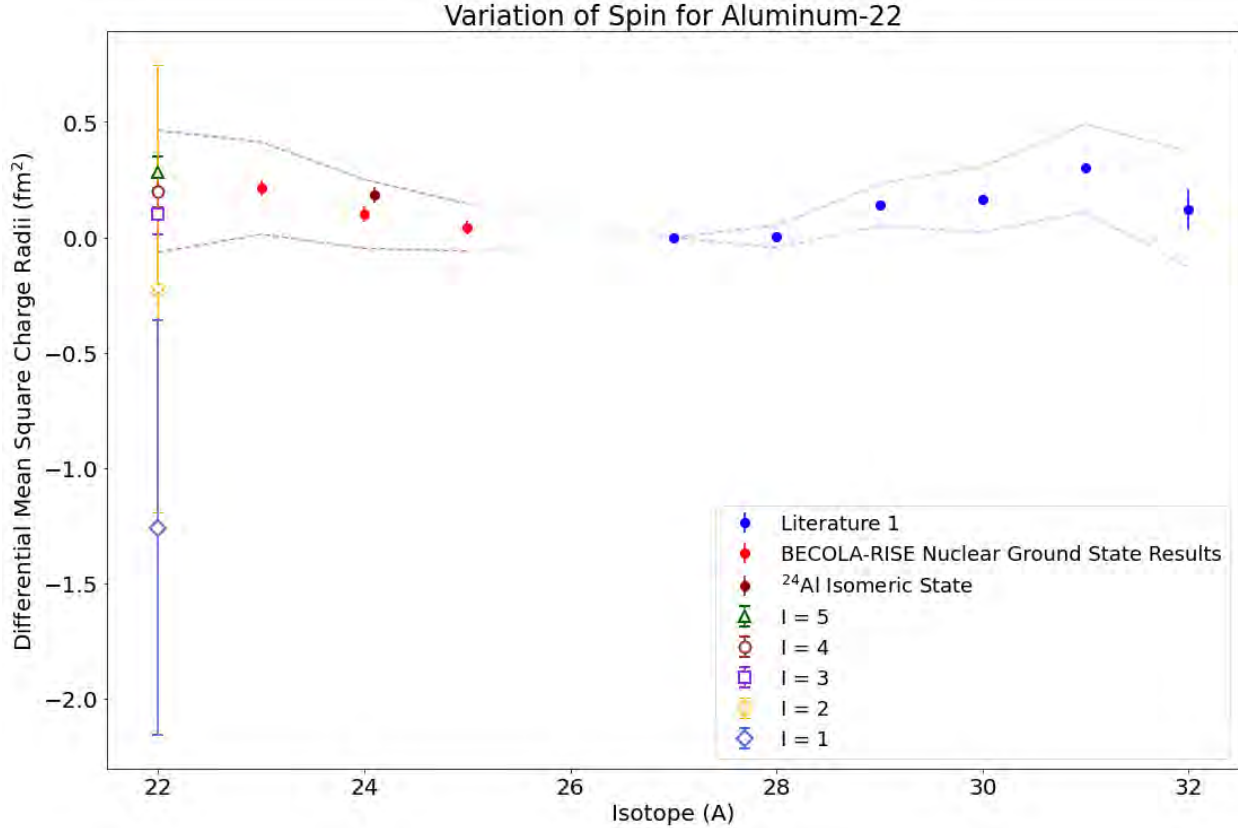


Figure 5.12 Charge radii trend with ^{22}Al results for spins 1, 2, 3, 4, and 5. The charge radii trend for the Al isotopic chain is shown. A variety of charge radii results for ^{22}Al are included for different spin values. The results shown were found using the CEC simulation fitting method, the same analysis was completed using the one side peak fitting method and has consistent results, the one side peak fitting results are omitted from the plot for clarity.

centroid to the other spin values centroids was tried. For example fitting with the spin set to 4, the fit centroid was fixed to the resulting value from the spin 3 fit. The hope was that a large divergence would be seen for a given spin when fixing the centroid to different spins results. However, as seen in Figure 5.15, the resulting A ratio was very consistent within the error bars. With the magnitude of this error, it was concluded that the data collected for ^{22}Al was not high enough statistics to determine or make a definitive statement about the spin. However, looking at the varying spins resulting charge radius in the radii trend, a spin 4 or 5 would be most likely. This is also consistent with the A ratio analysis, that spin 4 and 5 are the most overlapped and closest to the A ratio of ^{27}Al although the error is large. With most previous literature having strong arguments supporting a spin 4+ and the shell model

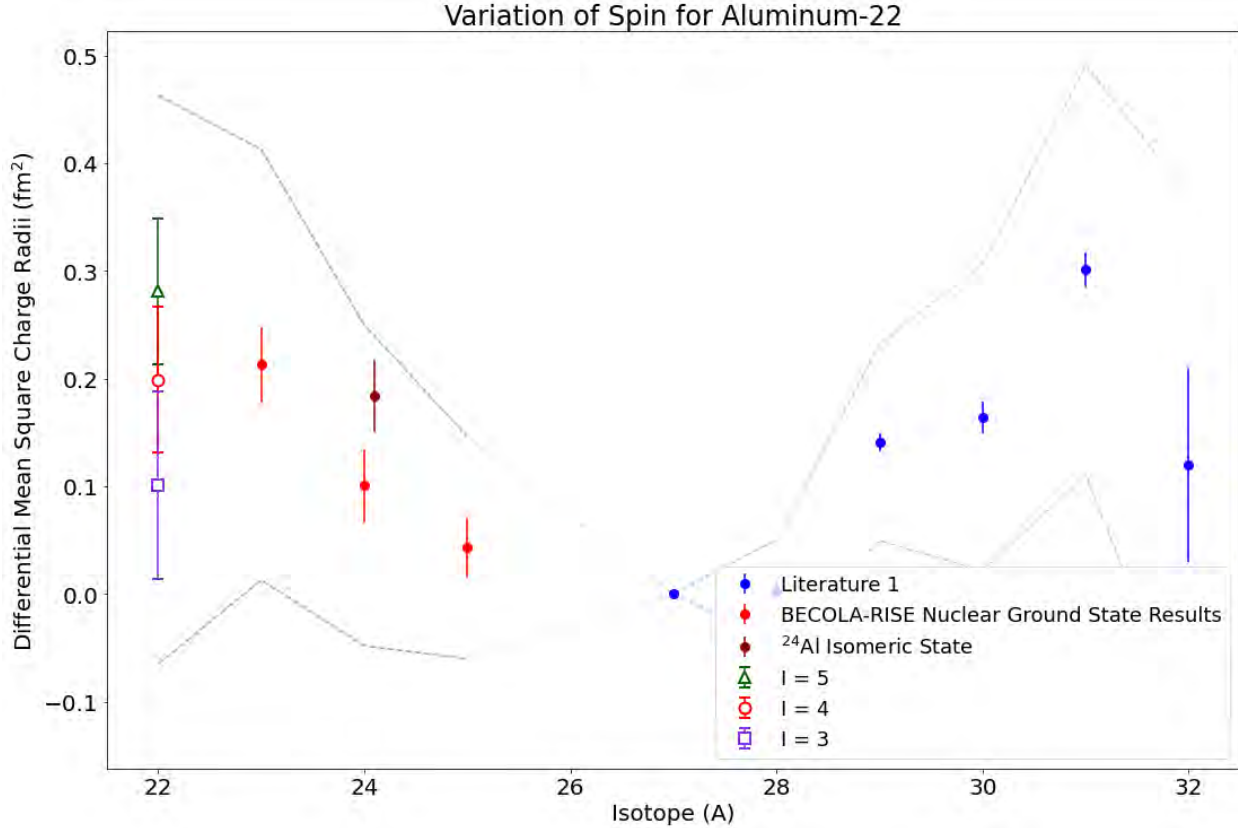


Figure 5.13 Charge radii trend with ^{22}Al results for spins 3, 4, and 5. The charge radii trend for the Al isotopic chain is shown. A few charge radii results for ^{22}Al are included for different spin values. The results shown were found using the CEC simulation fitting method, the same analysis was completed using the one side peak fitting method and has consistent results, the one side peak fitting results are omitted from the plot for clarity.

predicting a spin 4+ ground state, the analysis for this experiment was continued with spin 4+.

Using Equation 2.15, the resulting isotope shift was found to be 8.09 MHz with a 4.74 MHz uncertainty using the CEC simulation fitting method and 9.79 MHz with a 5.10 MHz uncertainty using the one side peak analysis method. The hyperfine coefficients were measured to be 168.36 MHz with 2.09 MHz uncertainty for the ground state and 43.88 MHz with 1.63 MHz uncertainty for the excited state using the CEC simulation fitting method, 168.51 MHz with 2.21 MHz uncertainty for the ground state and 43.90 MHz with 1.75 MHz uncertainty for the excited state using the one side peak fitting method. The results from the fits are included in Table 5.1 and 5.2.

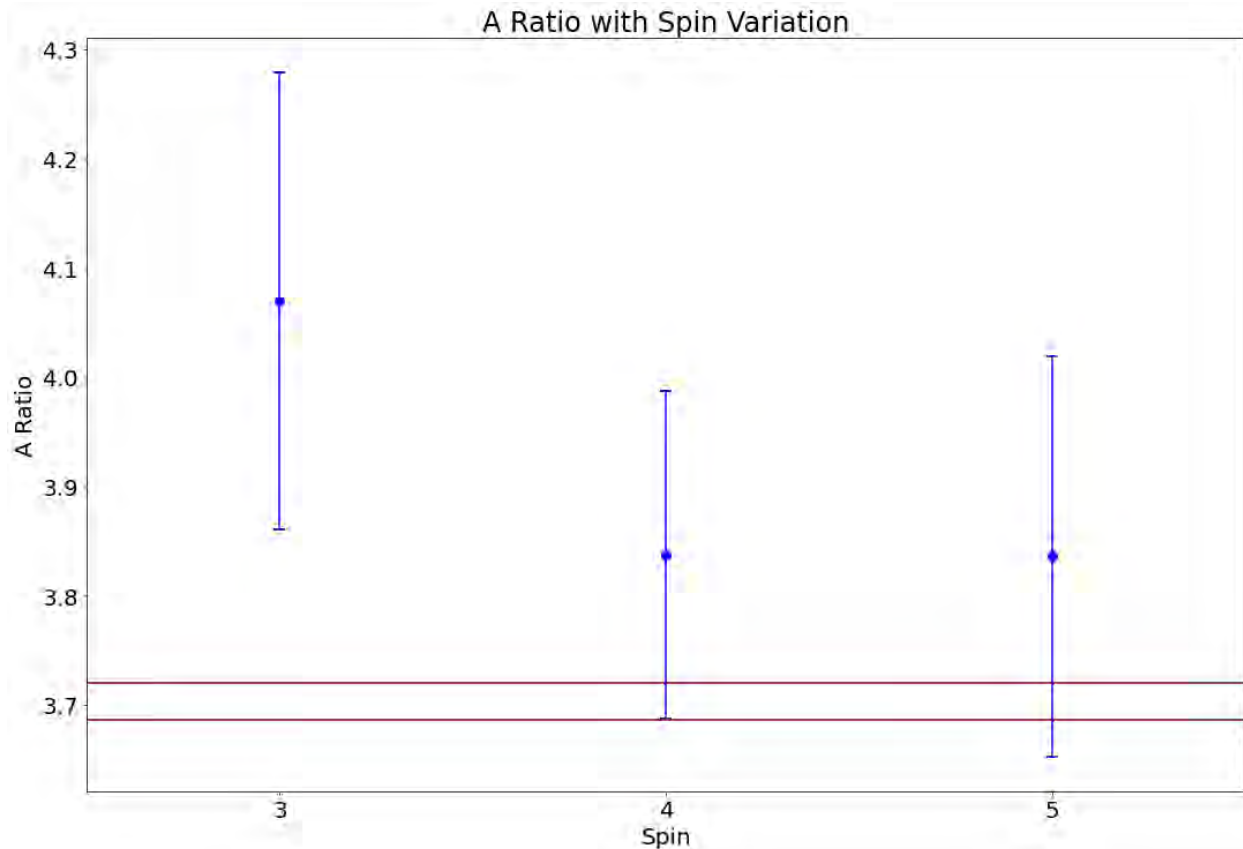


Figure 5.14 *A* ratio results for spins 3, 4, and 5 for ^{22}Al . The *A* ratio results for ^{22}Al with different spin values are shown, plotted in blue. The red horizontal lines indicate the band of *A* ratio results for ^{27}Al . The results shown were found using the CEC simulation fitting method, the same analysis was completed using the one side peak fitting method and has consistent results, the one side peak fitting results are omitted from the plot for clarity.

5.6 Systematic Error Analysis

In addition to the statistical uncertainties coming from the fit of the spectra, an analysis of systematic uncertainty must be considered. This section outlines the factors included in the systematic uncertainty determination.

5.6.1 Beam Energy

The beam energy correction applied to the data for the online experiment rely on comparing the collinear and anticollinear measurements made to determine v_0 . Although switching between the two measurement was relatively fast and there was a high voltage stabilization system maintaining the voltage in the beam line, there could still be a drift of beam energy between the collinear and anticollinear measurements. Through a test of the high voltage

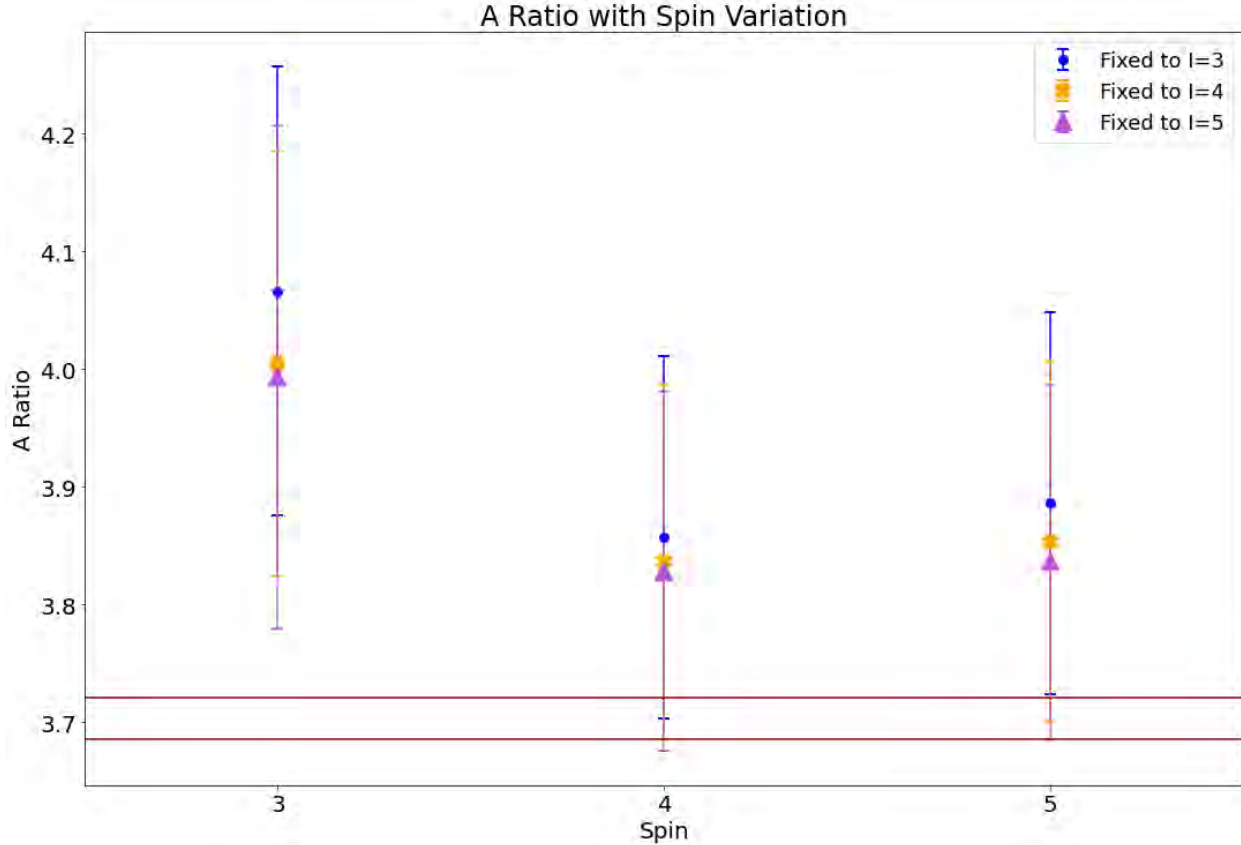


Figure 5.15 The A ratio results for spins 3, 4, and 5 for ^{22}Al fixing to different centroid values. The A ratio results for ^{22}Al with different spin values fixing to different centroid values is shown, plotted in blue. The red horizontal lines show the band of A ratio results for ^{27}Al . The results shown were found using the CEC simulation fitting method, the same analysis was completed using the one side peak fitting method and has consistent results, the one side peak fitting results are omitted from the plot for clarity.

stabilization system it was found that the voltage can change up to 6.49×10^{-7} volts per second. The longest switching between a collinear and anticollinear measurement could take was one hour. Over that one hour the voltage could change up to 2.34×10^{-3} volts. Converting to MHz, the beam energy maximum change would contribute a 6.80×10^{-2} MHz uncertainty to the resulting isotope shift.

5.6.2 Beam Energy Drift

The drift in centroids for the calibration runs show the beam energy was drifting throughout the online run. Although the calibration runs could be linearly fit to account for the drift throughout the isotope runs, there was an uncertainty to the linear fit and picking points

along it. The uncertainty of the linear fit and standard deviation from the fit contribute a 2.23 MHz uncertainty to the isotope shift. Any drift in the laser wavelength or drift in the high voltage would be accounted for in the drift of the calibration run centroids.

5.6.3 Laser Wavelength

The wavemeter used to set the wavelength for the ν_0 determination has uncertainty in coming back to the exact wavelength for each measurement. This uncertainty in wavelength variation is known to be 1 MHz. The laser wavelength fed into the wavemeter for this experiment was then tripled to use for spectroscopy resulting in a 3 MHz uncertainty for the wavelength used. Measuring the ν_0 twice reduces this uncertainty by a root two. The equation for determining the resulting ν_0 variation is $\Delta\nu_0 = \frac{1}{\sqrt{2}}\Delta\nu_{\text{wavemeter variation}}$ [106]. Inserting the 3 MHz wavemeter variation into this equation a 2.12 MHz uncertainty on ν_0 was found, contributing a 2.12 MHz uncertainty to the isotope shift.

5.6.4 Scanning Voltage

The same scanning voltage range was scanned over for each measurement. The Matsusada used to scan this voltage does not have a systematic error for repeating the same voltage scan for each measurement. No uncertainty was added for the isotope shift determination from the scanning voltage. The hyperfine coefficients however depend on the location of the peaks for each isotope, which would vary isotope to isotope. The Matsusada has an uncertainty of 50 ppm which was included for the hyperfine coefficients.

5.6.5 MagneToF

The MagneToF detector used to count the ions in the experiment is a high precision detector with nanosecond precision, able to count single ions. For the rates of this experiment sent to the detector, the company specifications quote error less than this measurements sensitivity. Any error would come from an issue observed in running the detector or over-saturating the detector. The rates of this experiment were not close to the quoted rates able to saturate this detector. Saturating the detector would be visible in the spectra as a "flat top". The detector would only be saturating at the peaks and not in the background. This

causes a visible flat line at the top of the peak where we would no longer be sensitive to the line shape. This phenomena was never observed in running the Aluminum experiment, confirming no saturation of the detector occurred. Since no issues were observed with the detector throughout the run and no saturation, the MagneToF detector did not contribute any significant error.

5.6.6 Beam Alignment

Laser spectroscopy relies on the overlap of the lasers and ion beam within the beamline. If the lasers are fully misaligned with the ion beam, no resonance will be seen. However, if the lasers are partially overlapped with the ion beam a resonance can still be seen. The irises in the beamline used to overlap the laser and ion beam were five millimeter in diameter, while the beams were all one centimeter in diameter. During alignment the two may seem fully overlapped but it can only be confirmed by eye that five millimeters of each beam were overlapped, this leaves room for error on the actual alignment of the beams. There are two beamline irises five millimeter in diameter, about 84 inches apart. Assuming a one millimeter uncertainty on the visual overlap, geometry can be used to determine it corresponds to a 0.1 radian angle of uncertainty. A 0.1 radian angle of uncertainty corresponds to 0.015 MHz uncertainty on the isotope shift.

Adding all sources of systematic uncertainty in quadrature resulted in a 3.14 MHz uncertainty on the isotope shift values, which corresponds to a 0.045 fm^2 uncertainty on the differential mean square charge radius.

CHAPTER 6

RESULTS

6.1 Magnetic Dipole Moment Determination

The measured hyperfine coefficients in Table 5.2 can be used with values from stable ^{27}Al to determine the magnetic dipole moment of each isotope. The relationship used is shown in Equation 2.12 in the Hyperfine Interaction chapter. The μ used for ^{27}Al was $(3.6415069 \pm 0.0000007)\mu_N$ with a spin of $5/2+$ [110]. The measured A hyperfine coupling constants for ^{27}Al are listed in 4.1. The resulting magnetic dipole moments for each isotope are listed in Table 6.1 for the CEC simulation analysis and Table 6.2 for the one side peak analysis. The

Table 6.1 CEC Analysis Magnetic Dipole Moment Results. The resulting magnetic moments using the CEC simulation analysis method for each isotope are listed. Calculated from the atomic ground state, μ_g , excited state, μ_e , and a weighted average of the two, μ_{avg} . The spin used to find the values are listed. In addition to the listed statistical uncertainty in parenthesis, there is a 0.003 systematic uncertainty listed in square brackets.

Isotope	Spin	μ_g	μ_e	μ_{avg}
22	(4)+	1.951(25)[3]	1.885(19)[3]	1.923(15)[3]
23	$\frac{5}{2}+$	3.895(8)[3]	3.898(7)[3]	3.897(5)[3]
24	4+	2.823(9)[3]	2.824(8)[3]	2.823(6)[3]
24m	1+	2.991(4)[3]	2.996(4)[3]	2.994(3)[3]
25	$\frac{5}{2}+$	3.636(6)[3]	3.647(5)[3]	3.641(4)[3]

Table 6.2 1 Side Peak Analysis Magnetic Dipole Moment Results. The resulting magnetic moments using the one side peak analysis method for each isotope are listed. Calculated from the atomic ground state, μ_g , excited state, μ_e , and a weighted average of the two, μ_{avg} . The spin used to find the values are listed. In addition to the listed statistical uncertainty in parenthesis, there is a 0.003 systematic uncertainty listed in square brackets.

Isotope	Spin	μ_g	μ_e	μ_{avg}
22	(4)+	1.953(26)[3]	1.886(20)[3]	1.924(16)[3]
23	$\frac{5}{2}+$	3.894(8)[3]	3.899(7)[3]	3.896(5)[3]
24	4+	2.813(12)[3]	2.899(10)[3]	2.852(8)[3]
24m	1+	2.985(9)[3]	3.006(2)[3]	2.989(2)[3]
25	$\frac{5}{2}+$	3.636(6)[3]	3.651(5)[3]	3.642(4)[3]

moments were calculated from the A hyperfine coefficients of the atomic ground, $3p\ ^2P_{1/2}$, and excited, $5s\ ^2S_{1/2}$, state probed in this experiment. The weighted average of these values are taken for the final result. Equation 6.1 was used to find the weighted average where x is the value and w is the uncertainty on each quantity, i , being averaged for all quantities, n .

$$\text{weighted average} = \frac{\sum_i^n w_i x_i}{\sum_i^n w_i} \quad (6.1)$$

The uncertainty on the weighted average was found using Equation 6.2 where w , i , and n are defined the same as in Equation 6.1.

$$\text{weighted average uncertainty} = \frac{1}{\sqrt{\sum_i^n \frac{1}{w_i^2}}} \quad (6.2)$$

6.2 Magnetic Dipole Moment Theory Results

Following the experimental determination of the magnetic dipole moments, theorists independently calculated the nuclear moments. Three different theory methods were used and compared with the experimental results. Nuclear Lattice Effective Field Theory (NLEFT) calculations were performed by Dean Lee and his group at FRIB at MSU [111]. From his group, Teng Wang performed the magnetic dipole moment calculations with help from Bing-Nan Lu, Yuanzhuo Ma, and Shuang Zhang. Shell Model calculations were performed by Alex Brown at FRIB at MSU [45]. Valence-Space In-Medium Similarity Renormalization Group (VS-IMSRG) calculations were performed by Antoine Belley from the Massachusetts Institute of Technology (MIT) [44]. The details of each theory are outlined below and all results are listed in Table 6.3 and are plotted in Figure 6.1. To better visualize the comparison between theoretical and experimental results, the magnetic dipole moment values are plotted in Figure 6.2 with the experimental result as the zero.

6.2.1 NLEFT

NLEFT calculations are performed with Monte Carlo lattice simulations at several different values of Euclidean time [111] [112]. The protons and neutrons are placed on a lattice. The lattice is produced using Chiral Effective Field theory to construct the effective poten-

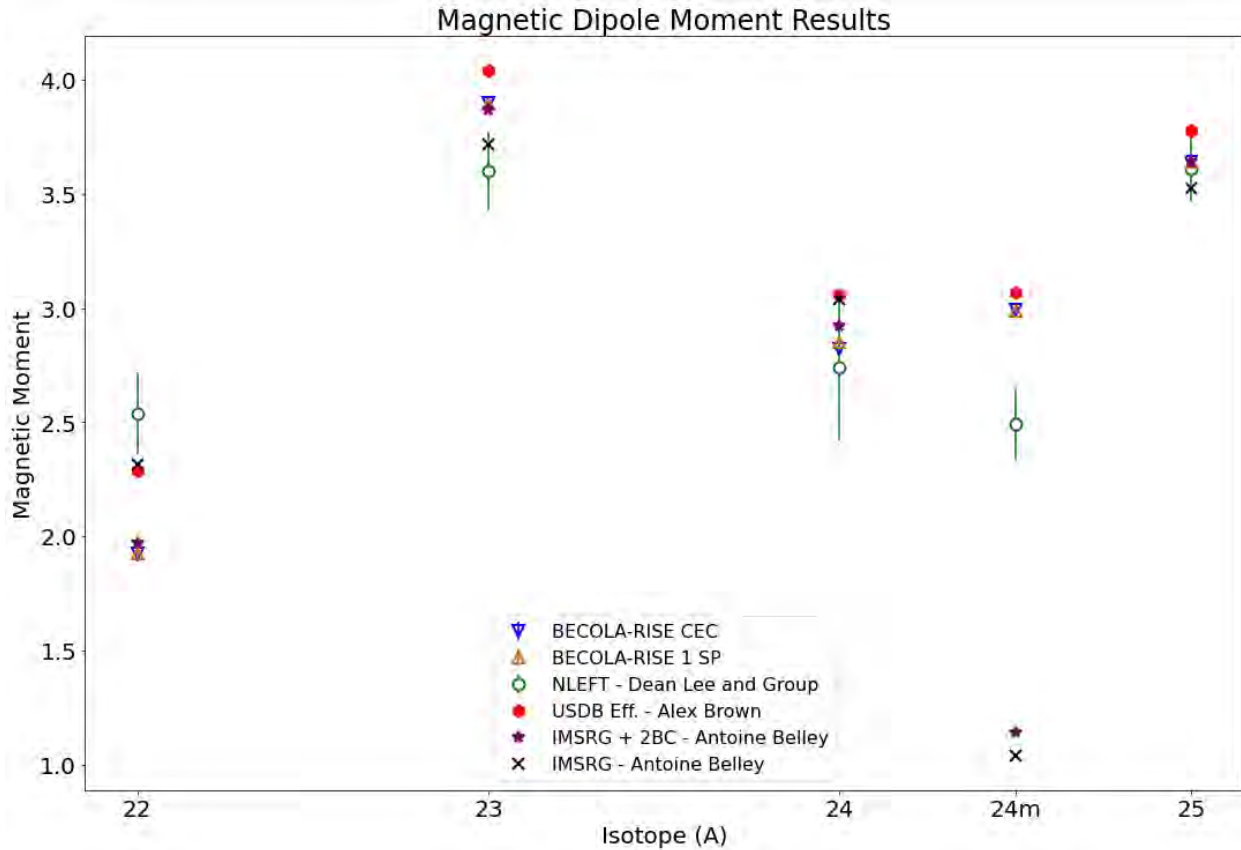


Figure 6.1 Magnetic Dipole Moment Results. The magnetic dipole moment experimental and theoretical results are plotted for $^{22-25}\text{Al}$. BECOLA-RISE CEC indicates experimental results found using the CEC simulation analysis method. BECOLA-RISE 1 SP indicates experimental results found using the one side peak analysis method. NLEFT indicates theoretical results found using NLEFT calculations. USDB Eff. indicates theoretical results found using shell model calculations. IMSRG indicates theoretical results found using VS-IMSRG calculations. IMSRG+2BC indicates theoretical results found using VS-IMSRG calculations that included two body currents. Individual comparison plots are separately shown in Figures 6.3, 6.4, and 6.6.

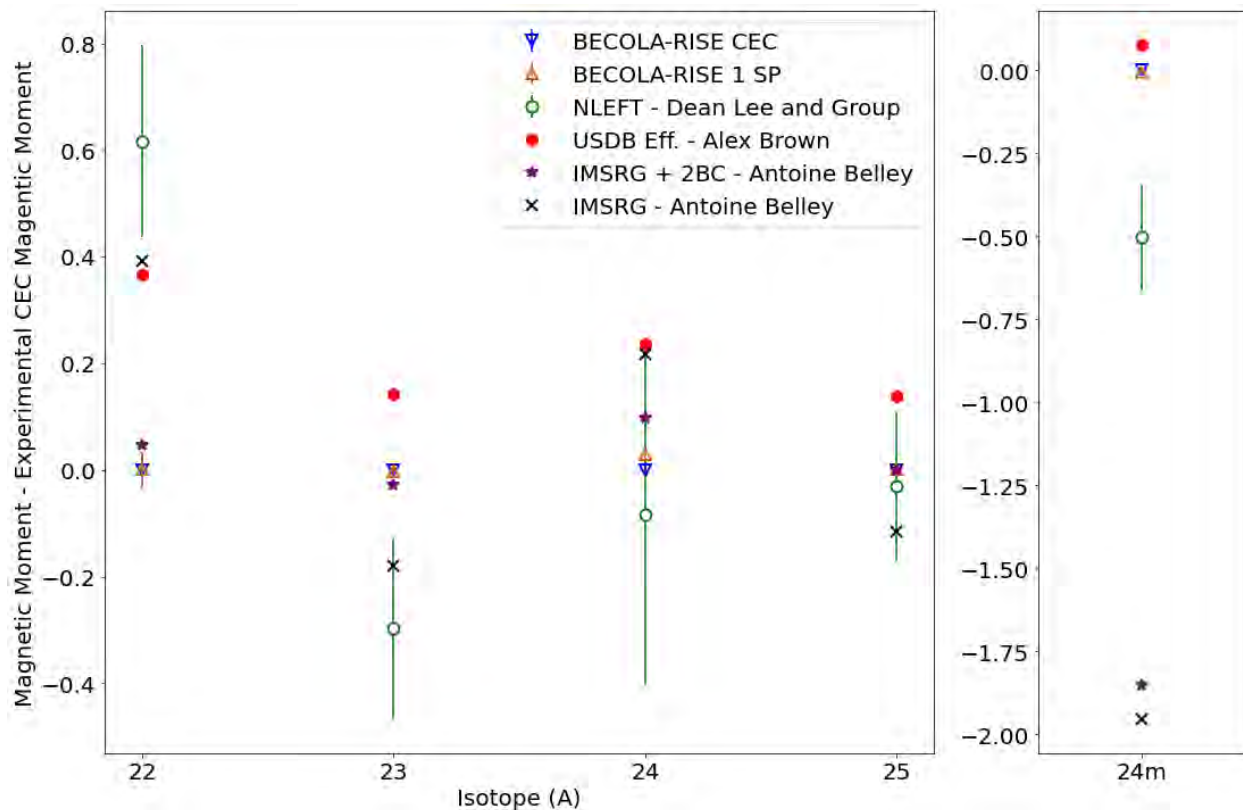


Figure 6.2 Magnetic Dipole Moment Results Relative to Experimental Value.

The magnetic dipole moment experimental and theoretical results are plotted for $^{22-25}\text{Al}$ with the experimental CEC result as the zero. The experimental result plotted is the weighted average of the ground state and excited state result. BECOLA-RISE CEC indicates experimental results found using the CEC simulation analysis method. BECOLA-RISE 1 SP indicates experimental results found using the one side peak analysis method. NLEFT indicates theoretical results found using NLEFT calculations. USDB Eff. indicates theoretical results found using shell model calculations. IMSRG indicates theoretical results found using VS-IMSRG calculations. IMSRG+2BC indicates theoretical results found using VS-IMSRG calculations that included two body currents.

Table 6.3 Magnetic Dipole Moment Results. The magnetic moment values from experiment and theory results. The spin used to find the values are listed. Square brackets, [], indicate systematic uncertainty.

Isotope	Spin	$\mu_{exp\ CEC}$	$\mu_{exp\ 1sp}$	μ_{NLEFT}	$\mu_{Shell\ Model}$	μ_{ISMGR}
22	(4)+	1.923(15)[3]	1.924(16)[3]	2.54(18)	2.299	1.969
23	$\frac{5}{2}+$	3.897(5)[3]	3.896(5)[3]	3.60(17)	4.047	3.874
24	4+	2.823(6)[3]	2.852(8)[3]	2.49(16)	3.065	2.915
24m	1+	2.994(3)[3]	2.989(2)[3]	2.74(32)	–	–
25	$\frac{5}{2}+$	3.641(4)[3]	3.642(4)[3]	3.61(14)	3.791	3.643

tial order by order, it can be improved by tuning the interaction coefficients to reproduce experimental results. Monte Carlo simulations are used to compute a ratio using the Hamiltonian, H , the initial state which determines the nucleus being studied, Ψ_{init} , the Euclidean time, t , and the operator to compute the charge radius or magnetic dipole moment, O . To solve many body problems efficiently a Euclidean time projection, e^{-Ht} , is performed to extrapolate the data at finite Euclidean time to infinite Euclidean time. The ratio is shown in Equation 6.3 [111].

$$f(t) = \frac{\langle \Psi_{init} | e^{-Ht} O e^{-Ht} | \Psi_{init} \rangle}{\langle \Psi_{init} | e^{-Ht} e^{-Ht} | \Psi_{init} \rangle} \quad (6.3)$$

The Hamiltonian contains a kinetic energy term which models the nucleons doing a random walk in space as a function of euclidean time. There are interactions between nucleons as they progress in Euclidean time such as pion exchange and other short range interactions that can be written as exponentials of the interaction using Gaussian integral identity. These interactions between nucleons can be replaced by interactions of each nucleon with the background. A minimum of four parameters are required to model the interaction when A is greater than three. Three of the four parameters are tuned with an $A = 2, 3$ nucleus; the strength of the 2-nucleon s -wave interaction, range of the 2-nucleon s -wave interaction, and the strength of the 3-nucleon contact interaction. The final parameter is tuned using nuclei with A greater than three; the range of the local part of the 2-nucleon interaction [111].

Taking the limit of the ratio, Equation 6.3, as t goes to infinity gives the ground state charge radius or magnetic dipole moment, depending on which operator is used. For each

nucleus about six to eight different values of t are computed. For each nucleus and each value of t , millions of configurations for the numerator and denominator of the ratio are computed. The numerator and denominator resulting values are summed, shown mathematically in Equation 6.4.

$$\begin{aligned} \langle \Psi_{init} | e^{-Ht} O e^{-Ht} | \Psi_{init} \rangle &= \text{numerator}(1) + \text{numerator}(2) + \dots \\ \langle \Psi_{init} | e^{-Ht} e^{-Ht} | \Psi_{init} \rangle &= \text{denominator}(1) + \text{denominator}(2) + \dots \end{aligned} \quad (6.4)$$

With the resulting values the original ratio can then be computed as shown in Equation 6.5.

$$f(t) = \frac{\text{numerator}(1) + \text{numerator}(2) + \dots}{\text{denominator}(1) + \text{denominator}(2) + \dots} \quad (6.5)$$

Using the operator to compute the magnetic dipole moment, the magnetic dipole moments were calculated by Teng Wang from the group of Dean Lee for the Aluminum isotopes [111]. The results are included in Table 6.3 and shown in Figure 6.3 with experimental results, Figure 6.1 and Figure 6.2 with experimental and all theoretical results.

6.2.2 Shell Model

Shell model calculations using the USDB [113] interaction and effective operators were performed by Alex Brown to find the magnetic dipole moments of the Aluminum isotopes. The magnetic moment is found using Equation 6.6 [45], where $(M1)^{op}$ is the $M1$ operator.

$$\mu = \sqrt{\frac{4\pi}{3}} \langle \Psi | (M1)^{op} | \Psi \rangle_{M=J} \quad (6.6)$$

The $M1$ operator is shown in Equation 6.7 [45]. The sum is taken over the number of protons, Z , and neutrons, N , in the equation $\tau_z = p$ or n for the respective proton or neutron sum. The $M1$ operator term $\sqrt{8\pi} [Y^2(r_i, \tau_z) \otimes \vec{s}_i, \tau_z]^{(1)}$ [46] represents the corrections for given observables. The $M1$ operator term is the same for all nuclei, making it an universal operator. The g variables are the effective g -factors; dimensionless values which characterize properties of the nucleus. $g_{s\tau_z}$ characterizes the spin of the nucleons, $g_{l\tau_z}$ characterizes the orbital of the nucleons, and $g_{t\tau_z}$ characterizes the total angular momentum of the nucleons. \vec{s}_{i,τ_z} is the spin of the nucleons and \vec{l}_{i,τ_z} is the orbital angular momentum of the nucleons.

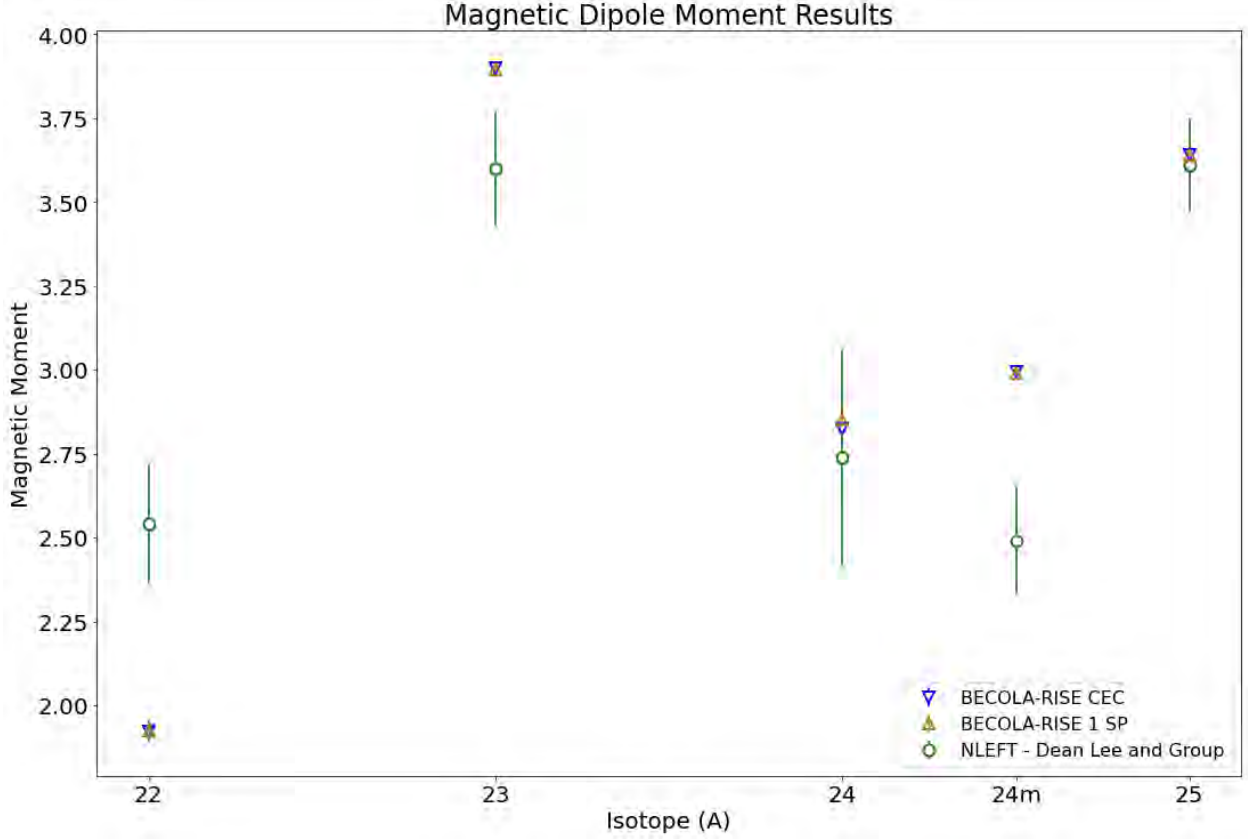


Figure 6.3 NLEFT and Experimental Magnetic Dipole Moment Results. The magnetic dipole moment experimental and NLEFT theoretical results are plotted for $^{22-25}\text{Al}$. BECOLA-RISE CEC indicates experimental results found using the CEC simulation analysis method. BECOLA-RISE 1 SP indicates experimental results found using the one side peak analysis method. NLEFT indicates theoretical results found using NLEFT calculations.

Using a free-nucleon operator for the g -factors results in $g_{sp} = 5.586$ $g_{sn} = -3.826$ $g_{lp} = 1$ $g_{ln} = 0$ $g_{tp} = 0$ and $g_{tn} = 0$ [45]. An effective or fitted operator can be used to find the six g -factors from a least-square fit to the existing $M1$ data [45].

$$(M1)^{op} = \sqrt{\frac{4\pi}{3}} \sum_{i,\tau_z} \left\{ g_{s\tau_z} \vec{s}_{i,\tau_z} + g_{l\tau_z} \vec{l}_{i,\tau_z} + g_{t\tau_z} \sqrt{8\pi} [Y^2(r_i, \tau_z) \otimes \vec{s}_{i,\tau_z}]^{(1)} \right\} \mu_N \quad (6.7)$$

The USDB calculations were performed using the free and fitted g -factors. The results are compared to experimental results in Figure 6.4 along with other nuclei results using this theoretical approach. The results show that all theoretical μ values for the Aluminum isotopes are within expected deviation, with ^{22}Al having the largest deviation. Since ^{22}Al is very neutron-deficient and far from $N = Z$ the effective g -factors, which are obtained by fitting properties of nuclei close to $N = Z$, are no longer accurate compared to nuclei

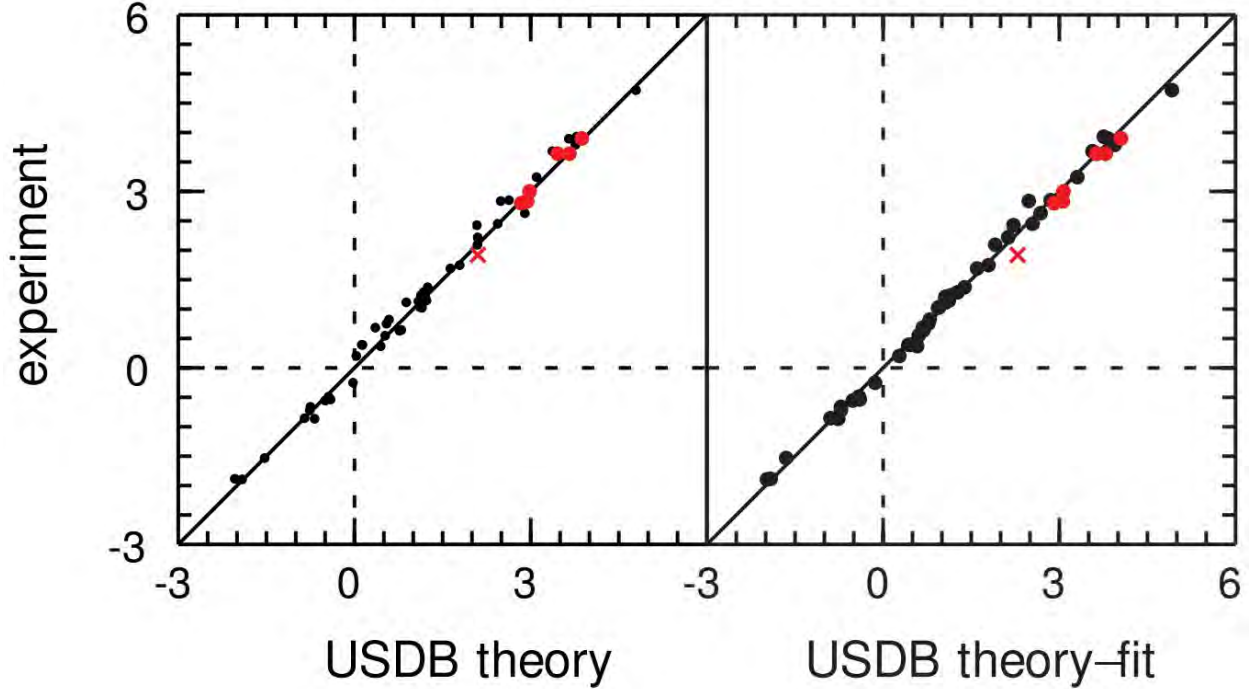


Figure 6.4 Experimental vs USDB Magnetic Dipole Moment Results. The left hand side of the figure plots experimental results versus the USDB theoretical results with free-nucleon g -factors. The right hand side of the figure plots experimental results versus the USDB theoretical results with fitted effective g -factors. The Aluminum results are plotted in red, with ^{22}Al plotted as a red x . This figure was made by Alex Brown from his figure in Reference [45].

close to $N = Z$. It is interesting that the magnetic moment of ^{22}Al is better reproduced by free nucleon g -factors. Nucleus dependent g -factors would be necessary to improve these calculation results. The results are included in Table 6.3 and shown in Figure 6.5 with experimental results, Figure 6.1 and Figure 6.2 with experimental and all theoretical results.

6.2.3 VS-IMSRG

VS-IMSRG calculation results were calculated with and without a two body correction. VS-IMSRG calculations find μ from the magnetic dipole operator shown in Equation 6.8, where $j(q)$ is the EM spatial current and q is the momentum transfer carried by photon [44].

$$\mu = -i \lim_{q \rightarrow 0} \nabla_q \times \frac{j(q)}{2} \quad (6.8)$$

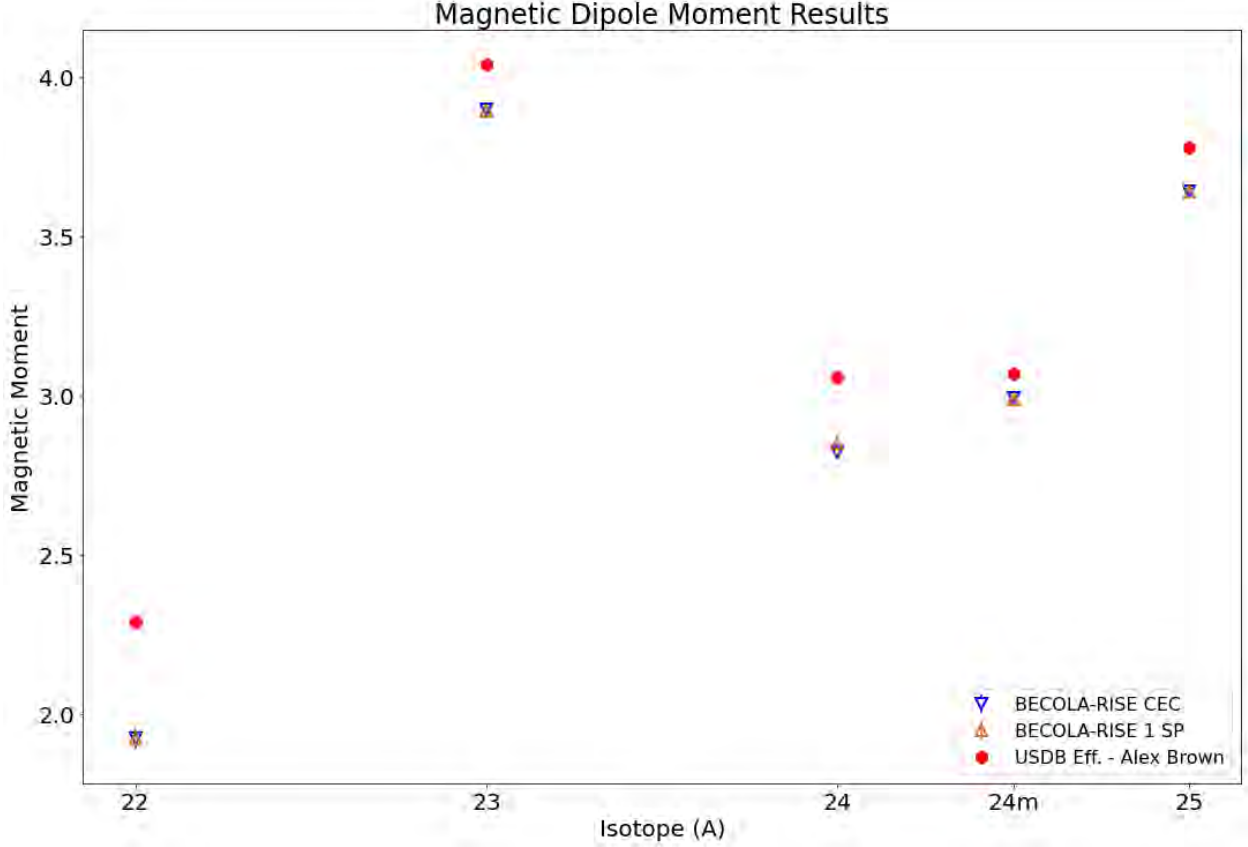


Figure 6.5 USDB and Experimental Magnetic Dipole Moment Results. The magnetic dipole moment experimental and theoretical results are plotted for $^{22-25}\text{Al}$. BECOLA-RISE CEC indicates experimental results found using the CEC simulation analysis method. BECOLA-RISE 1 SP indicates experimental results found using the one side peak analysis method. USDB Eff. indicates theoretical results found using shell model calculations.

For the one-body level, μ_{1B} , in the z direction the magnetic moment operator is calculated as shown in Equation 6.9. The sum is taken over the number of nucleons, g_i^l is the orbital g -factor, g_i^s is the spin g -factor, $l_{i,z}$ is the z component of the orbital angular momentum operator, and $\sigma_{i,z}$ is the z component of the spin operator [44]. Calculations used $g_{proton}^l = 1$, $g_{neutron}^l = 0$, $g_{proton}^s = 2.792$, and $g_{neutron}^s = -1.913$ [44].

$$\mu_{1B} = \mu_N \sum_i (g_i^l l_{i,z} + g_i^s \sigma_{i,z}) \quad (6.9)$$

Including the leading two body correction, 2BC, accounts for the parameter free pion exchange contributions. The magnetic moment calculation including the 2BC, μ_{2B} , is calculated by two terms; the intrinsic, μ_{ij}^{intr} , and Sachs, μ_{ij}^{Sachs} , terms as shown in Equation 6.10

summed over the nucleons i and j [44].

$$\mu_{2B} = \sum_{i < j} \mu_{ij}^{int} + \mu_{ij}^{Sachs} \quad (6.10)$$

The intrinsic term only depends on the intrinsic coordinates of the nucleons and is shown in Equation 6.11. τ_i is the isospin operator of the subscripted nucleon, $r_{ij} \equiv r_i - r_j$ with r_i being the relative coordinate of the subscripted nucleon, and $V_{int,z}(r_{ij})$ is the potential from the next to leading order contribution of the "seagull" and "pion-in-flight terms" [114].

$$\mu_{ij}^{int} = \mu_N (\tau_i \times \tau_j)_z V_{int,z}(r_{ij}) \quad (6.11)$$

The Sachs term depends on the center of mass of the nucleons and is shown in Equation 6.12. $R_{ij} \equiv \frac{(r_i + r_j)}{2}$ is the center of mass coordinates of the nucleons, $V_{Sachs}(r_{ij})$ is the coordinate-space one-pion-exchange potential without isospin dependence, τ_i , and r_{ij} are defined the same as in μ_{ij}^{int} [114].

$$\mu_{ij}^{Sachs} = \mu_N (\tau_i \times \tau_j)_z (R_{ij} \times r_{ij})_z V_{Sachs}(r_{ij}) \quad (6.12)$$

The results are listed in Table 6.3 and shown in Figure 6.6 with experimental results, Figure 6.1 and 6.2 with experimental and all theoretical results. The plot shows that including a two body correction improves the agreement of the theoretical result with the experimental.

6.2.4 μ Comparison

The difference between the two experiment analysis methods is well within uncertainty for all isotopes except ^{24}Al . For ^{22}Al , ^{23}Al , and ^{25}Al the difference is 0.001, which is a third of the systematic uncertainty and well within the total given uncertainty. For ^{24}Al the isomeric state result is within one sigma and the ground state result is just outside of one sigma statistical uncertainty, within two sigma. Due to the complexity of the ^{24}Al spectrum with two nuclear state peak sets to identify, different fitting methods result in a variation of the fitted peak centers. For example, the two methods fit the width of overlapping peaks differently. For a wide set of two overlapping peaks, the one side peak fitting method can increase the distance to the side peak to widen each peak that is overlapped. For the CEC

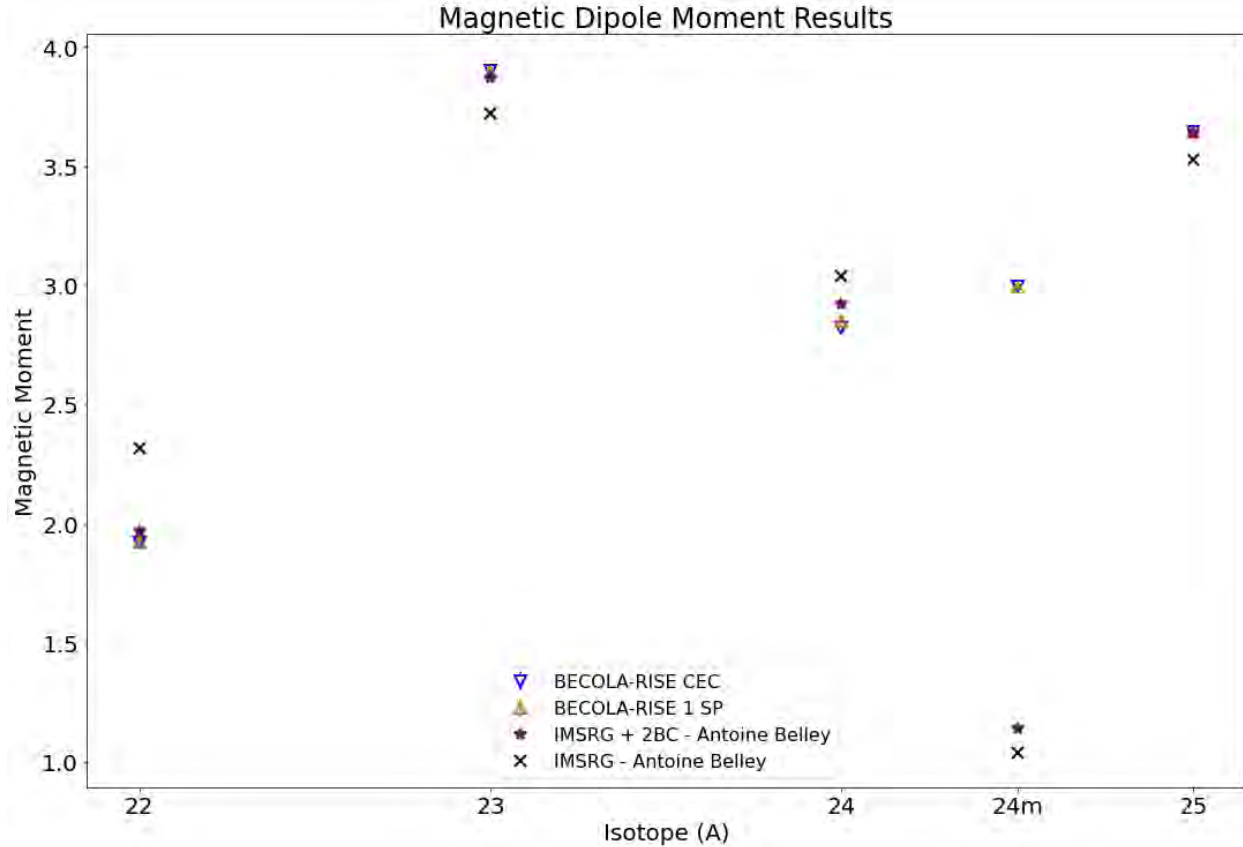


Figure 6.6 IMSRG and Experimental Magnetic Dipole Moment Results. The magnetic dipole moment experimental and theoretical results are plotted for $^{22-25}\text{Al}$. BECOLA-RISE CEC indicates experimental results found using the CEC simulation analysis method. BECOLA-RISE 1 SP indicates experimental results found using the one side peak analysis method. IMSRG indicates theoretical results found using VS-IMSRG calculations. IMSRG+2BC indicates theoretical results found using VS-IMSRG calculations that included two body currents.

simulation method, the distances to the side peaks are fixed and the fit must account for the width by increasing the distance between the two overlapped peaks. The differences in the fits results in a different μ value that is within two sigma uncertainty for ^{24}Al and one sigma for the remaining isotopes, considering the complexity of the ^{24}Al fit the two analysis methods are in good agreement.

The NLEFT μ results have better agreement for isotopes closer to stability. ^{25}Al and the nuclear ground state of ^{24}Al experimental values are within one sigma of the NLEFT results with the difference increasing for each isotope out to ^{22}Al . The largest difference between experimental values and NLEFT results is for the isomeric state of ^{24}Al . This is most likely

due to the complexity of the excited state. These are the first magnetic moments calculated using NLEFT and show the theory produces good results, especially close to stability.

The shell model μ results are consistently larger than the experimental values. The largest difference is seen for ^{22}Al due to the isotope being far from $N = Z$, where the effective g -factors are not as accurate. ^{22}Al is better reproduced by free nucleon g -factors than fitted. The universal effective $M1$ operator has been used for more than twenty years in the sd -shell theory, it has been and is still successful in predicting magnetic moments. To improve the results, nucleus dependent g -factors would need to be used.

The VS-IMSRG μ results show that including a two body correction improves the agreement between the theoretical and experimental results. Meaning the two body currents are important to include in the calculations and have a large effect. Among the IMSRG results the isomeric state result varies the most from the experimental value. This may be because the transition density for states in the $s_{5/2}$ orbit is much weaker for the isomeric state than they are in the ground state. The transition density for the isomeric state is about a factor of five times less than the ground state. The transition density changes in the μ calculation for the different states. The reduction of transition density for the isomeric state would cause a reduction in the μ value. The results including the two body currents reproduce the experimental results the best of the three theories compared.

6.3 Determining Charge Radii Trend

The calculated atomic factors and measured isotope shifts, listed in Table 5.1, can be combined in Equation 2.26 to determine the differential mean square charge radius for each isotope. The total uncertainty of the differential mean square charge radius is found by taking a quadrature sum of the statistical, theoretical, and systematic uncertainties. Experimental results are listed in Table 6.4 for the CEC simulation analysis and Table 6.5 for the one side peak analysis. The experimental results for $^{22-25}\text{Al}$ are plotted with literature values for $^{28-32}\text{Al}$ in Figure 6.7.

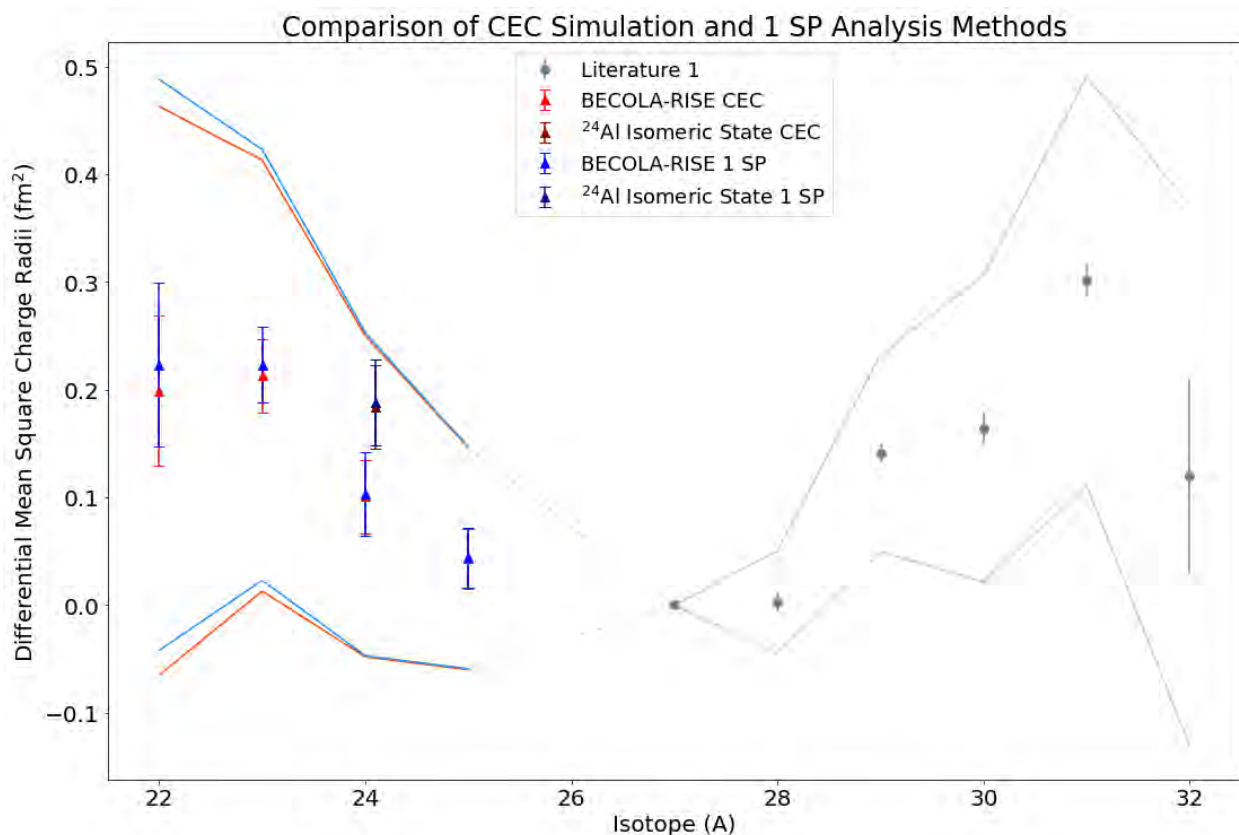


Figure 6.7 Experimental CEC and 1 SP Differential Mean Square Charge Radii Results. The experimental results for $^{22-25}\text{Al}$ are plotted with literature values for $^{28-32}\text{Al}$. The error bars on each point show the statistical uncertainty. The solid lines show the uncertainty of the differential mean square charge radius due to the uncertainty on the atomic factor calculations. Literature 1 indicates the literature results from Reference [37]. BECOLA-RISE CEC indicates experimental results found using the CEC simulation analysis method. BECOLA-RISE 1 SP indicates experimental results found using the one side peak analysis method. The isomeric state is plotted slightly offset from ^{24}Al and the theoretical uncertainty of the isomeric state is not included in the plot to better visualize the ground state charge radii trend.

Table 6.4 CEC Analysis Differential Mean Square Charge Radius Results. The experimental differential mean square charge radius results for the CEC simulation analysis are listed. The total uncertainty is found by adding the statistical, theoretical, and systematic uncertainties in quadrature.

Isotope	$\delta\langle r^2 \rangle$ (fm ²)	Total Error	Statistical Error	Theoretical Error	Systematic Error
22	0.199	0.264	0.070	0.250	0.045
23	0.213	0.200	0.034	0.192	0.045
24	0.101	0.149	0.034	0.138	0.045
24m	0.184	0.150	0.043	0.138	0.045
25	0.043	0.103	0.028	0.088	0.045

Table 6.5 1 Side Peak Analysis Differential Mean Square Charge Radius Results. The experimental differential mean square charge radius results for the one side peak analysis are listed. The total uncertainty is found by adding the statistical, theoretical, and systematic uncertainties in quadrature.

Isotope	$\delta\langle r^2 \rangle$ (fm ²)	Total Error	Statistical Error	Theoretical Error	Systematic Error
22	0.223	0.265	0.076	0.250	0.045
23	0.223	0.200	0.035	0.192	0.045
24	0.103	0.150	0.039	0.138	0.045
24m	0.188	0.150	0.040	0.138	0.045
25	0.044	0.103	0.028	0.088	0.045

6.3.1 Analysis Method Comparison

The difference between the two experiment analysis methods is within one sigma statistical uncertainty for all isotopes. The differential mean square charge radius results for the CEC simulation and one side peak analysis methods are plotted in Figure 6.7. The difference in analysis methods increases moving towards the dripline nucleus, ²²Al. This is most likely due to a combination of decrease in statistics and that the simulated peaks used in the fitting function were simulated for ²⁷Al. As the mass changes, the velocity of the ion beam changes, which is an important input for calculating the cross section. The CEC simulation that produces the relative peak heights and energy contributions for the side peaks was run and tested with ²⁷Al. The same side peak parameters were then used for each isotope. To improve the simulated lineshape for each isotope, the CEC simulation can

be run for each isotope. This was first done for ^{22}Al to check if there was an effect on the resulting fitted centroid. Running the CEC simulation to find the simulated peaks specific to ^{22}Al and refitting results in an increase of the isotope shift by 1.59 MHz. This brings the isotope shift from 8.09 MHz to 9.68 MHz for the CEC analysis method which is closer in agreement to the 9.79 MHz isotope shift found using the one side peak analysis method. Plugging the new isotope shift value into Equation 2.26 results in a differential mean square charge radius value of 0.221 which is in better agreement with the one side peak analysis result. The same was done for ^{23}Al and an increase of 0.33 MHz was seen resulting in a 10.77 MHz isotope shift compared to the previous 10.44 MHz. Although the effect is much smaller, it does bring the value closer to the one side peak analysis result of 11.14 MHz. The analysis was completed for the remaining isotopes and the results are listed in Table 6.6. Comparing

Table 6.6 CEC Isotope Specific Analysis Differential Mean Square Charge Radius Results. The experimental differential mean square charge radius results for the updated CEC simulation analysis. The total uncertainty is found by adding the statistical, theoretical, and systematic uncertainties in quadrature.

Isotope	$\delta\langle r^2 \rangle$ (fm ²)	Total Error	Statistical Error	Theoretical Error	Systematic Error
22	0.222	0.265	0.074	0.250	0.045
23	0.218	0.200	0.034	0.192	0.045
24	0.095	0.149	0.035	0.138	0.045
24m	0.205	0.151	0.041	0.138	0.045
25	0.045	0.103	0.028	0.088	0.045

the results with the previous CEC simulation analysis shows there is a mass dependence in the simulated peaks and the line shape. The results of all three analysis methods, one side peak, CEC simulation, and isotope specific CEC simulation, are listed in Table 6.7 and shown in Figure 6.8. The largest difference between the one side peak analysis and CEC isotope specific analysis is for ^{24}Al . This is most likely due to the complexity of fitting the overlapping ground and isomeric state peaks in the spectrum. Overall, the isotope specific CEC simulation results are within one sigma of the one side peak analysis results. This analysis comparison confirmed there is a mass dependence of the lineshape and the isotope

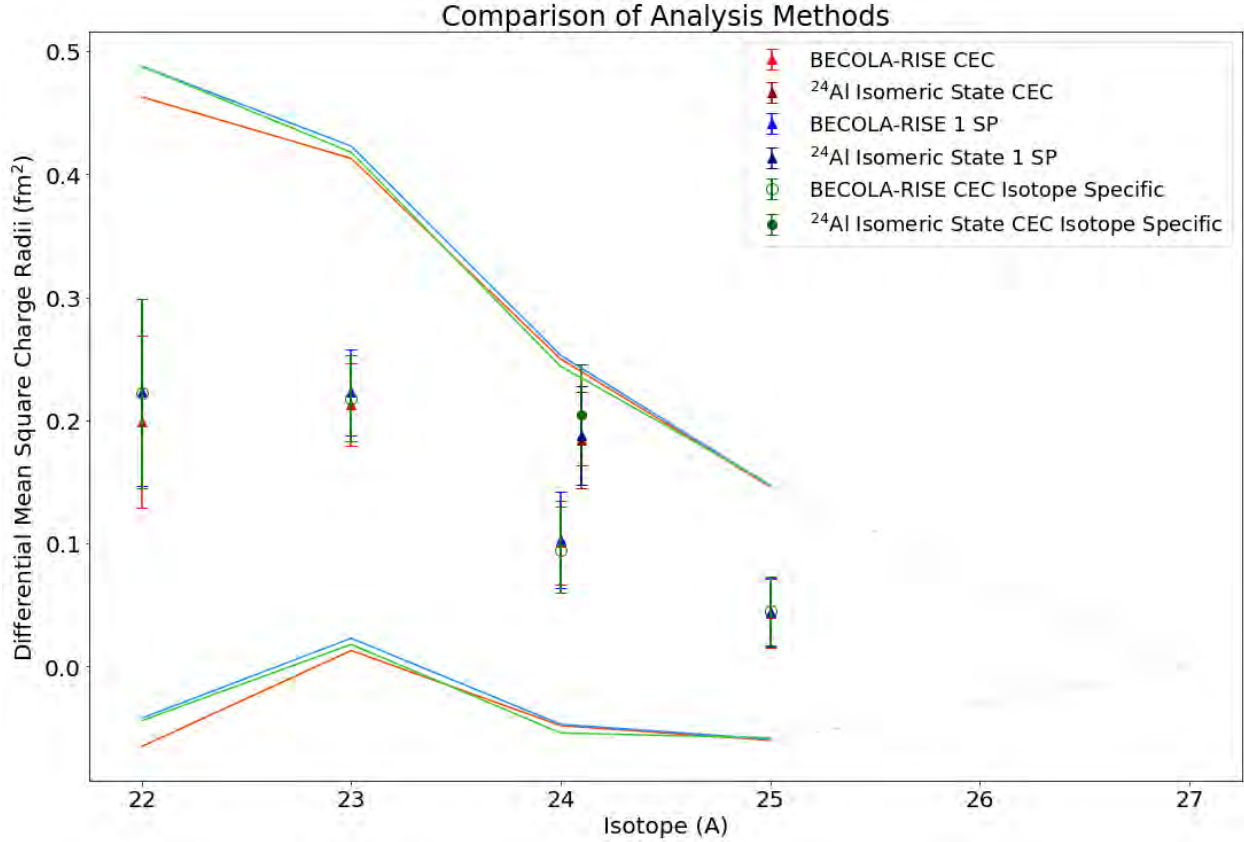


Figure 6.8 Three Analysis Method Comparison for Experimental Differential Mean Square Charge Radius Results. The experimental results for $^{22-25}\text{Al}$ are plotted to compare three analysis methods. The error bars on each point show the statistical uncertainty. The solid lines show the uncertainty of the differential mean square charge radius due to the uncertainty on the atomic factor calculations. BECOLA-RISE CEC indicates experimental results found using the CEC simulation analysis method that shares the lineshape of ^{27}Al for each isotope. BECOLA-RISE 1 SP indicates experimental results found using the one side peak analysis method. BECOLA-RISE CEC Isotope Specific indicates experimental results found using the CEC simulation analysis method where the lineshape of each isotope is independently simulated. The isomeric state is plotted slightly offset from ^{24}Al and the theoretical uncertainty of the isomeric state is not included in the plot to better visualize the ground state charge radii trend.

Table 6.7 Three Experiment Analysis Differential Mean Square Charge Radius Results. () indicates statistical uncertainty [] indicates theoretical uncertainty {} indicates systematic uncertainty.

Isotope	$\delta\langle r^2 \rangle_{exp\ CEC}$	$\delta\langle r^2 \rangle_{exp\ 1SP}$	$\delta\langle r^2 \rangle_{exp\ CEC_{specific}}$
22	0.199(70)[250]{45}	0.223(76)[250]{45}	0.222(74)[250]{45}
23	0.213(34)[192]{45}	0.223(35)[192]{45}	0.218(34)[250]{45}
24	0.101(34)[138]{45}	0.103(39)[138]{45}	0.0.095(35)[250]{45}
24m	0.184(39)[138]{45}	0.188(40)[138]{45}	0.205(41)[250]{45}
25	0.043(28)[88]{45}	0.044(28)[88]{45}	0.045(28)[250]{45}

specific analysis is the more accurate representation of the lineshape. The isotope specific analysis is the method that should be used. For comparison with theory the isotope specific CEC simulation, $CEC_{specific}$, and one side peak, 1 SP, analysis results are used.

6.4 Charge Radii Theory Results

Following the experimental determination of the differential mean square charge radius, theorists independently calculated the charge radius. Three different theory methods were used and compared with the experimental results. NLEFT calculations were performed by Dean Lee and his group at FRIB at MSU [111]. From his group, Shuang Zhang performed the nuclear ground state charge radius calculations with help from Yuanzhuo Ma and Yuanzhuo Ma performed the simulations for the charge radius of the 1+ isomer of ^{24}Al . VS-IMSRG calculations were performed by Takayuki Miyagi from the Center for Computational Sciences, University of Tsukuba, Tsukuba in Ibaraki Japan [115]. Skyrme Energy Density Functional (SKX-EDF) calculations were performed by Alex Brown at FRIB at MSU [116]. The details of each theory are outlined below and all differential mean square charge radius results are included in Table 6.8 and shown in Figure 6.9. To determine the experimental absolute charge radius from the differential mean square charge radius, the absolute charge radius of ^{27}Al , 3.061(6) determined using electron scattering in Reference [51], was used. The absolute charge radius was found using Equation 6.13.

$$\sqrt{\langle r^2 \rangle} = \sqrt{(3.061)^2 + \delta\langle r^2 \rangle} \quad (6.13)$$

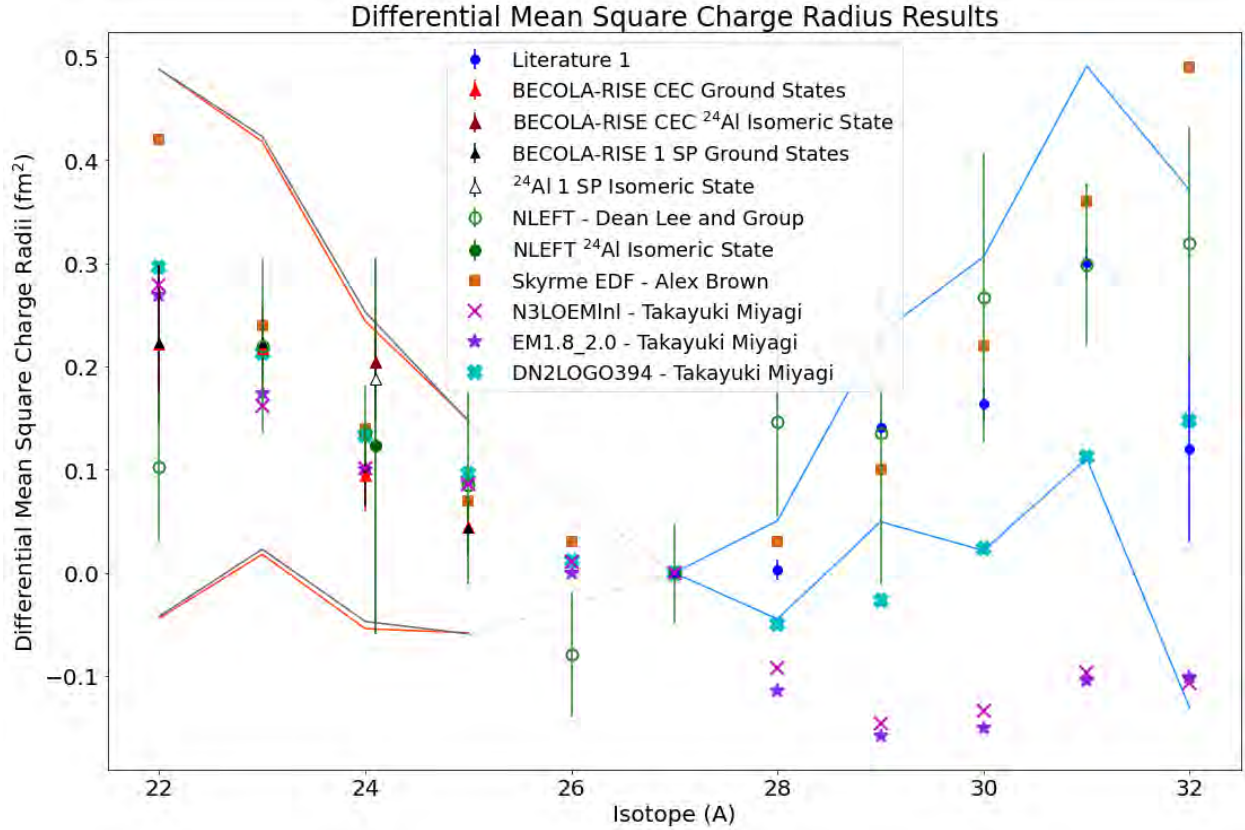


Figure 6.9 Differential Mean Square Charge Radius Results. The differential mean square charge radii results are plotted for experiment, literature, and theory. Literature 1 indicates the literature results from Reference [37]. BECOLA-RISE CEC indicates experimental results found using the CEC simulation analysis method where the lineshape of each isotope is independently simulated. BECOLA-RISE 1 SP indicates experimental results found using the one side peak analysis method. The isomeric state is plotted slightly offset from ²⁴Al and the theoretical uncertainty of the isomeric state is not included in the plot to better visualize the ground state charge radii trend. NLEFT indicates theoretical results found using NLEFT calculations. Skyrme EDF indicates theoretical results found using SKX-EDF calculations. N3LOEMnl indicates theoretical results found using VS-IMSRG calculations with N³LO_{EMnl} interactions. EM1.8_2.0 indicates theoretical results found using VS-IMSRG calculations with EM_{1.8-2.0} interactions. DN2LOGO394 indicates theoretical results found using VS-IMSRG calculations with DN²LO_{GO394} interactions. Individual comparison plots are shown in Figures 6.11, 6.13, and 6.15.

Table 6.8 Differential Mean Square Charge Radius Results. Experimental and theoretical differential mean square charge radius results are listed. For experimental results, () is statistical uncertainty [] is theoretical uncertainty { } is systematic uncertainty. For theoretical results total error is shown in () brackets when available.

Isotope	$\delta\langle r^2 \rangle_{exp\ CEC_{specific}}$	$\delta\langle r^2 \rangle_{exp\ 1SP}$	$\delta\langle r^2 \rangle_{NLEFT}$	$\delta\langle r^2 \rangle_{N^3LO:EM:DN^2LO}$	$\delta\langle r^2 \rangle_{SKX}$
22	0.222(74)[250]{45}	0.223(76)[250]{45}	0.103(72)	0.279 : 0.269 : 0.297	0.42
23	0.218(34)[192]{45}	0.223(35)[192]{45}	0.220(84)	0.162 : 0.174 : 0.213	0.24
24	0.095(35)[138]{45}	0.103(39)[138]{45}	0.135(47)	0.102 : 0.100 : 0.133	0.14
24m	0.205(41)[138]{45}	0.188(40)[138]{45}	0.123(182)	–	–
25	0.045(28)[88]{45}	0.044(28)[88]{45}	0.085(96)	0.086 : 0.087 : 0.096	0.07

The uncertainty of the absolute charge radius was found using partial derivatives of Equation 6.13 with respect to each variable. The equation used to find the total uncertainty is shown in Equation 6.14 where Δ represents uncertainty.

$$\Delta\sqrt{\langle r^2 \rangle} = \frac{\partial}{\partial\sqrt{\langle r^2 \rangle_{27}}} \Delta\sqrt{\langle r^2 \rangle_{27}} + \frac{\partial}{\partial\delta\langle r^2 \rangle} \Delta\delta\langle r^2 \rangle \quad (6.14)$$

All absolute square charge radius results are included in Table 6.9 and shown in Figure 6.10.

Table 6.9 Absolute Charge Radius Results. Experimental and theoretical absolute charge radius results are listed. Experimental results for the absolute charge radius are found using the absolute charge radius of ^{27}Al , 3.061(6). determined using electron scattering in Reference [51]. For experimental results, () is the total uncertainty, $\langle \rangle$ is statistical uncertainty [] is theoretical uncertainty { } is systematic uncertainty. For theoretical results total error is shown in () brackets when available.

Isotope	$\sqrt{\langle r^2 \rangle}_{exp\ CEC_{specific}}$	$\sqrt{\langle r^2 \rangle}_{exp\ 1sp}$	$\sqrt{\langle r^2 \rangle}_{NLEFT}$	$\sqrt{\langle r^2 \rangle}_{N^3LO:EM:DN^2LO}$
22	3.097(43)(12)[40]{7}	3.097(43)(12)[40]{7}	3.081(10)	2.947 : 2.965 : 3.017
23	3.096(33)(5)[31]{7}	3.097(33)(6)[31]{7}	3.100(12)	2.927 : 2.949 : 3.004
24	3.076(25)(6)[22]{7}	3.078(25)(6)[22]{7}	3.086(5)	2.917 : 2.936 : 2.990
24m	3.094(25)(7)[22]{7}	3.092(25)(6)[22]{7}	3.084(29)	–
25	3.068(18)(5)[14]{7}	3.068(18)(5)[14]{7}	3.078(15)	2.914 : 2.934 : 2.984

6.4.1 NLEFT

The NLEFT calculations use the same process as outlined in the NLEFT sub-section in the Magnetic Dipole Moment section, changing the operator to the operator for the charge

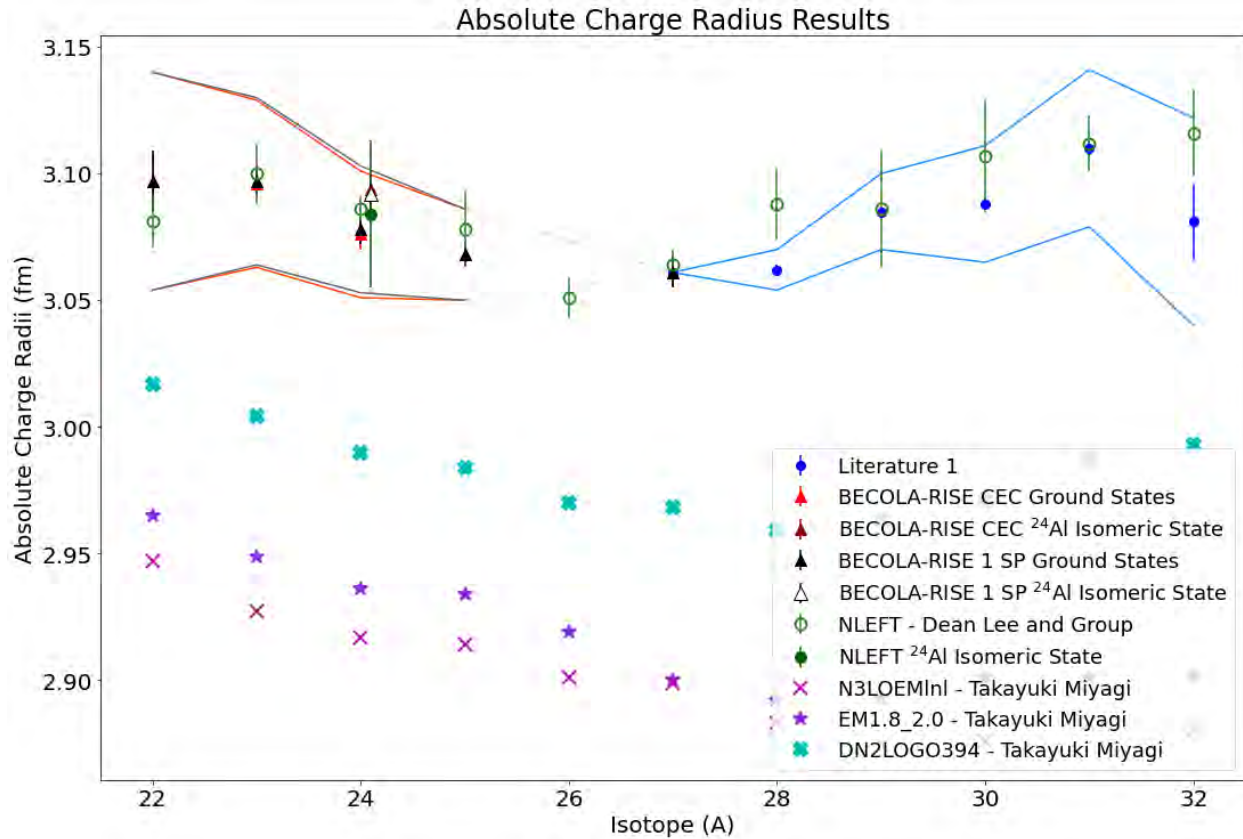


Figure 6.10 Absolute charge radius results. The absolute charge radii results are plotted for experiment, literature, and theory. Literature 1 indicates the literature results from Reference [37]. BECOLA-RISE CEC indicates experimental results found using the CEC simulation analysis method where the lineshape of each isotope is independently simulated. BECOLA-RISE 1 SP indicates experimental results found using the one side peak analysis method. The isomeric state is plotted slightly offset from ^{24}Al and the theoretical uncertainty of the isomeric state is not included in the plot to better visualize the ground state charge radii trend. NLEFT indicates theoretical results found using NLEFT calculations. Skyrme EDF indicates theoretical results found using SKX-EDF calculations. N3LOEMlnl indicates theoretical results found using VS-IMSRG calculations with $\text{N}^3\text{LO}_{EMlnl}$ interactions. EM1.8.2.0 indicates theoretical results found using VS-IMSRG calculations with $\text{EM}_{1.8-2.0}$ interactions. DN2LOGO394 indicates theoretical results found using VS-IMSRG calculations with $\text{DN}^2\text{LO}_{GO394}$ interactions. Individual comparison plots are shown in Figures 6.12 and 6.14.

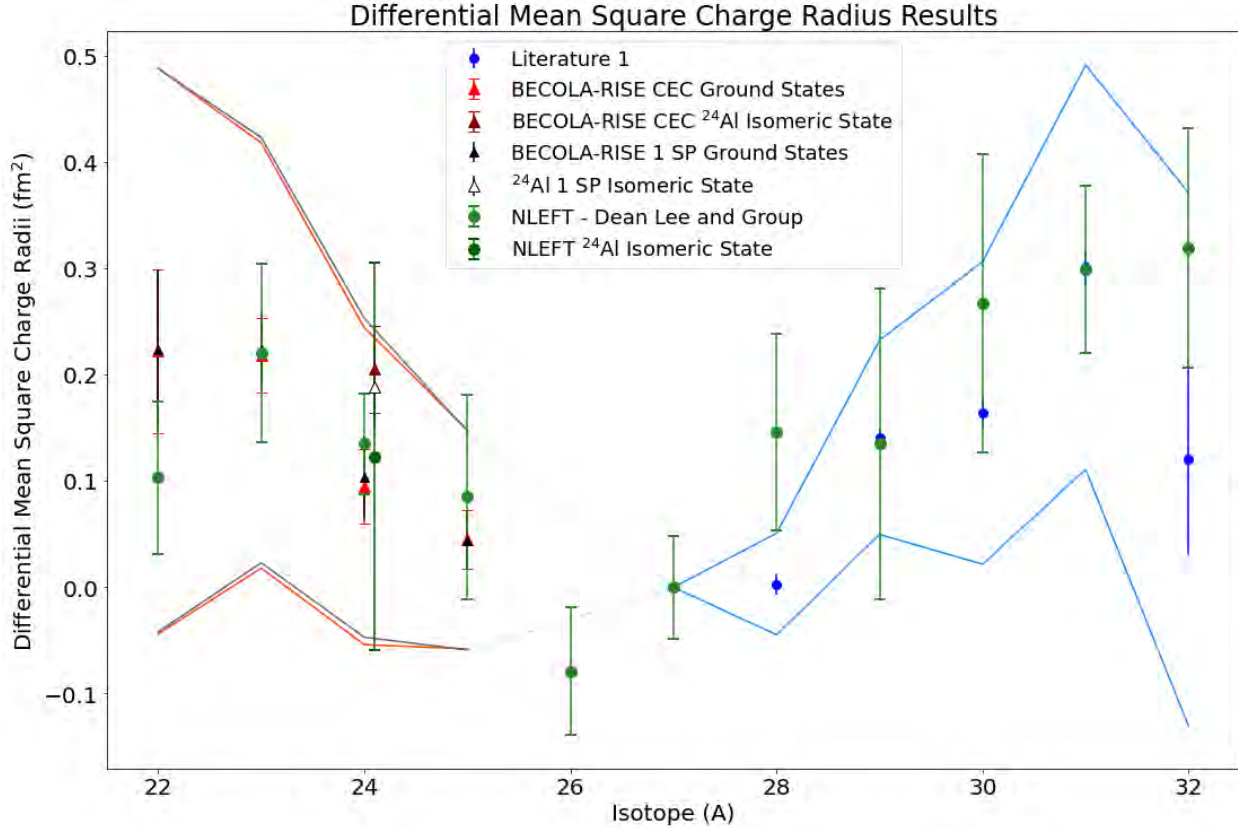


Figure 6.11 NLEFT and experimental differential mean square charge radius results. The experimental results for $^{22-25}\text{Al}$ are plotted with literature values for $^{28-32}\text{Al}$ and NLEFT theoretical results. Literature 1 indicates the literature results from Reference [37]. BECOLA-RISE CEC indicates experimental results found using the CEC simulation analysis method where the lineshape of each isotope is independently simulated. BECOLA-RISE 1 SP indicates experimental results found using the one side peak analysis method. The isomeric state is plotted slightly offset from ^{24}Al and the theoretical uncertainty of the isomeric state is not included in the plot to better visualize the ground state charge radii trend. NLEFT indicates theoretical results found using NLEFT calculations.

radius. The NLEFT results are plotted with the experimental results in Figure 6.11. Experimental results for $^{22-25}\text{Al}$ are within a one sigma error of the NLEFT theoretical results, indicating the theory reproduces experimental values well. Converting from differential mean square charge radius to absolute charge radius, the results are plotted in Figure 6.12 Moving to the absolute charge radius the experimental results are within one sigma uncertainty of the NLEFT theoretical results. The NLEFT theory approach is able to reproduce experimental values remarkably well.

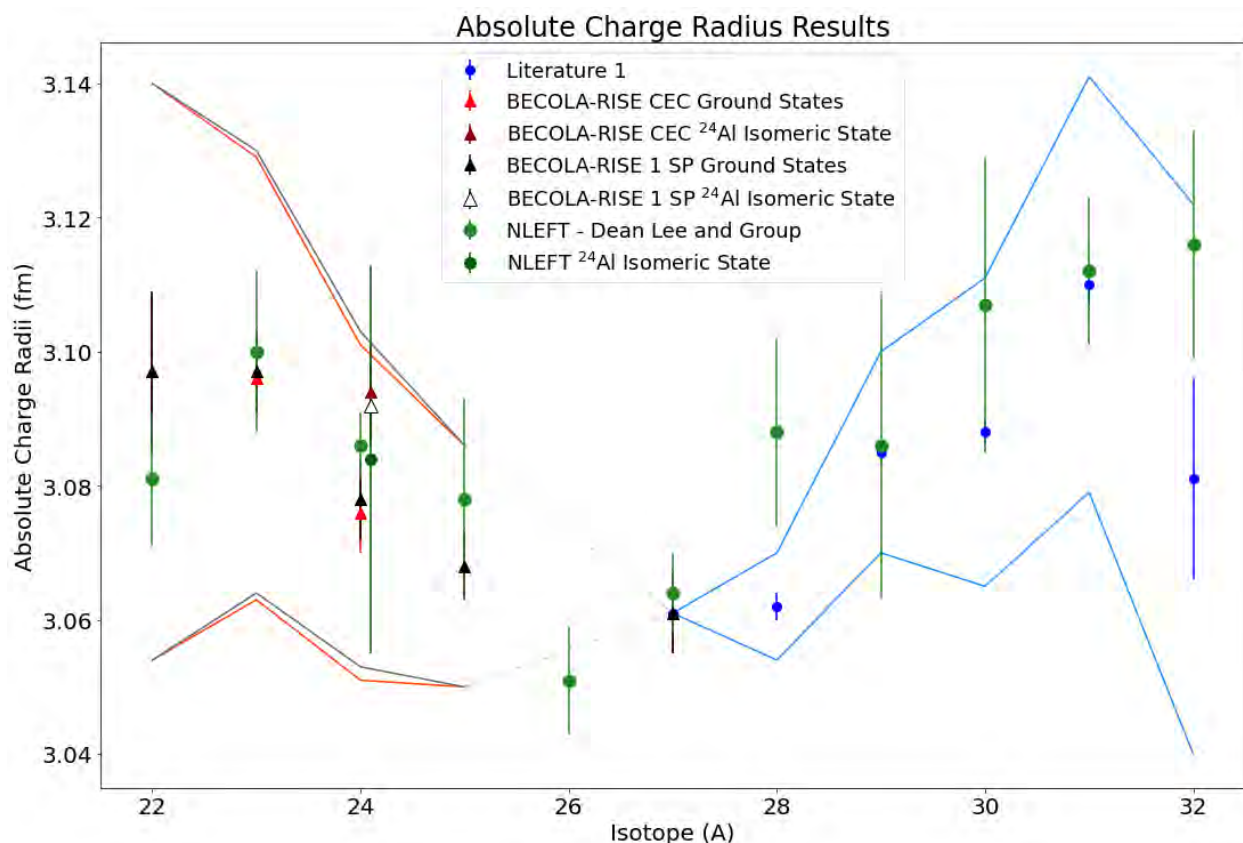


Figure 6.12 NLEFT and experimental absolute charge radius results. The experimental results for $^{22-25}\text{Al}$ are plotted with literature values for $^{28-32}\text{Al}$ and NLEFT theoretical results. Literature 1 indicates the literature results from Reference [37]. BECOLA-RISE CEC indicates experimental results found using the CEC simulation analysis method where the lineshape of each isotope is independently simulated. BECOLA-RISE 1 SP indicates experimental results found using the one side peak analysis method. The isomeric state is plotted slightly offset from ^{24}Al and the theoretical uncertainty of the isomeric state is not included in the plot to better visualize the ground state charge radii trend. NLEFT indicates theoretical results found using NLEFT calculations.

6.4.2 VS-IMSRG

VS-IMSRG calculations were performed with three different interactions; N^3LO_{EMlnl} , $EM_{1.8-2.0}$, and DN^2LO_{GO394} . All three interactions are derived from chiral effective field theory and have subtle differences. The N^3LO_{EMlnl} interaction includes up to third order expansions, next to next to next leading order, indicated by N^3LO [117]. *lnl* indicates that the interaction employs local and nonlocal regulators of the 3N interaction [118]. *EM* indicates the interaction uses the Entem Machleidt potential. The $EM_{1.8-2.0}$ interaction uses the Entem Machleidt potential [119] with a momentum cutoff of 1.8 and 2.0 fm^{-1} [120]. The DN^2LO_{GO394} interaction includes up to second order expansions, next to next leading order, indicated by N^2LO . *GO394* indicates the interaction uses the Gothenburg-Oak Ridge potential with a 394 MeV momentum cutoff [121]. *D* indicates the interaction accounts for all intermediate delta interactions [122] [121]. The three interaction results are included in Table 6.8 and 6.9 as well as shown in Figure 6.13 and 6.14 with experimental results and Figure 6.9 and 6.10 with experimental and all theory results. The resulting difference in charge radius results for the different interactions is evident, however for $^{22-25}Al$ the resulting trend is consistent for each interaction. All three predicated a close to linear increase in charge radius moving towards ^{22}Al , which varies from experimental results.

6.4.3 SKX-EDF

Mean field calculations with SKX-EDF were performed to find the charge radius of the Aluminum isotopes using Equation 6.15 [116]. $\langle r^2 \rangle_0$ is the charge radius of the equivalent spherical nucleus obtained with canonical mean field calculations with SKX parameters and β accounts for deformation that causes deviation from a spherical nucleus.

$$\langle r^2 \rangle = \langle r^2 \rangle_0 \left(1 + \frac{5\beta^2}{4\pi} \right) \quad (6.15)$$

The results are listed in Table 6.8 and shown in Figure 6.15 with experimental results and Figure 6.9 with experimental and all theory results. The SKX-EDF results are within one sigma for ^{23}Al and ^{24}Al and two sigma for ^{25}Al . The largest deviation is seen between the experimental and theoretical result for ^{22}Al .

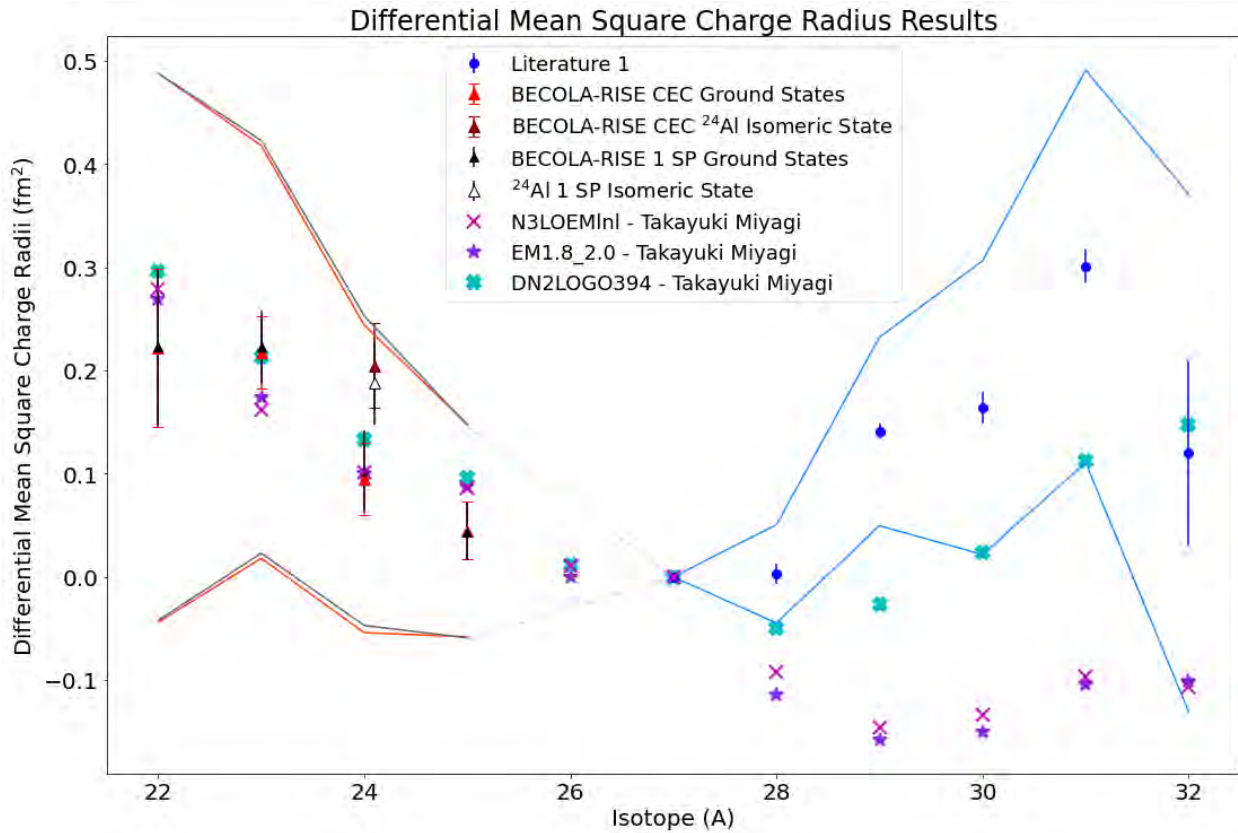


Figure 6.13 IMSRG and experimental differential mean square charge radius results. The differential mean square charge radii results are plotted for experiment, literature, and theory. Literature 1 indicates the literature results from Reference [37]. BECOLA-RISE CEC indicates experimental results found using the CEC simulation analysis method where the lineshape of each isotope is independently simulated. BECOLA-RISE 1 SP indicates experimental results found using the one side peak analysis method. The isomeric state is plotted slightly offset from ^{24}Al and the theoretical uncertainty of the isomeric state is not included in the plot to better visualize the ground state charge radii trend. N3LOEMlnl indicates theoretical results found using VS-IMSRG calculations with $\text{N}^3\text{LO}_{EMlnl}$ interactions. EM1.8.2.0 indicates theoretical results found using VS-IMSRG calculations with $\text{EM}_{1.8-2.0}$ interactions. DN2LOGO394 indicates theoretical results found using VS-IMSRG calculations with $\text{DN}^2\text{LO}_{GO394}$ interactions.

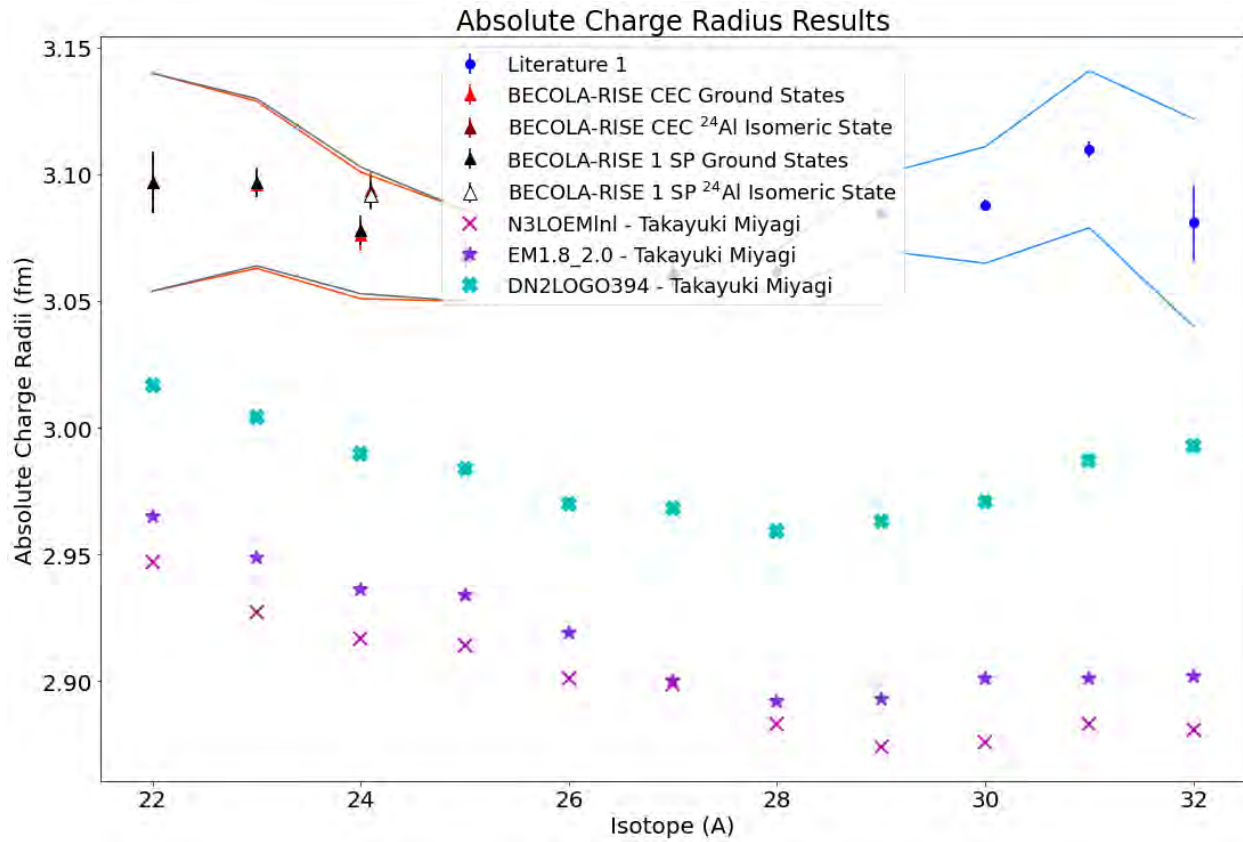


Figure 6.14 IMSRG and experimental absolute charge radius results. The absolute charge radii results are plotted for experiment, literature, and theory. Literature 1 indicates the literature results from Reference [37]. BECOLA-RISE CEC indicates experimental results found using the CEC simulation analysis method where the lineshape of each isotope is independently simulated. BECOLA-RISE 1 SP indicates experimental results found using the one side peak analysis method. The isomeric state is plotted slightly offset from ²⁴Al and the theoretical uncertainty of the isomeric state is not included in the plot to better visualize the ground state charge radii trend. N3LOEMlnl indicates theoretical results found using VS-IMSRG calculations with N³LO_{EMlnl} interactions. EM1.8_2.0 indicates theoretical results found using VS-IMSRG calculations with EM_{1.8-2.0} interactions. DN2LOGO394 indicates theoretical results found using VS-IMSRG calculations with DN²LO_{GO394} interactions.

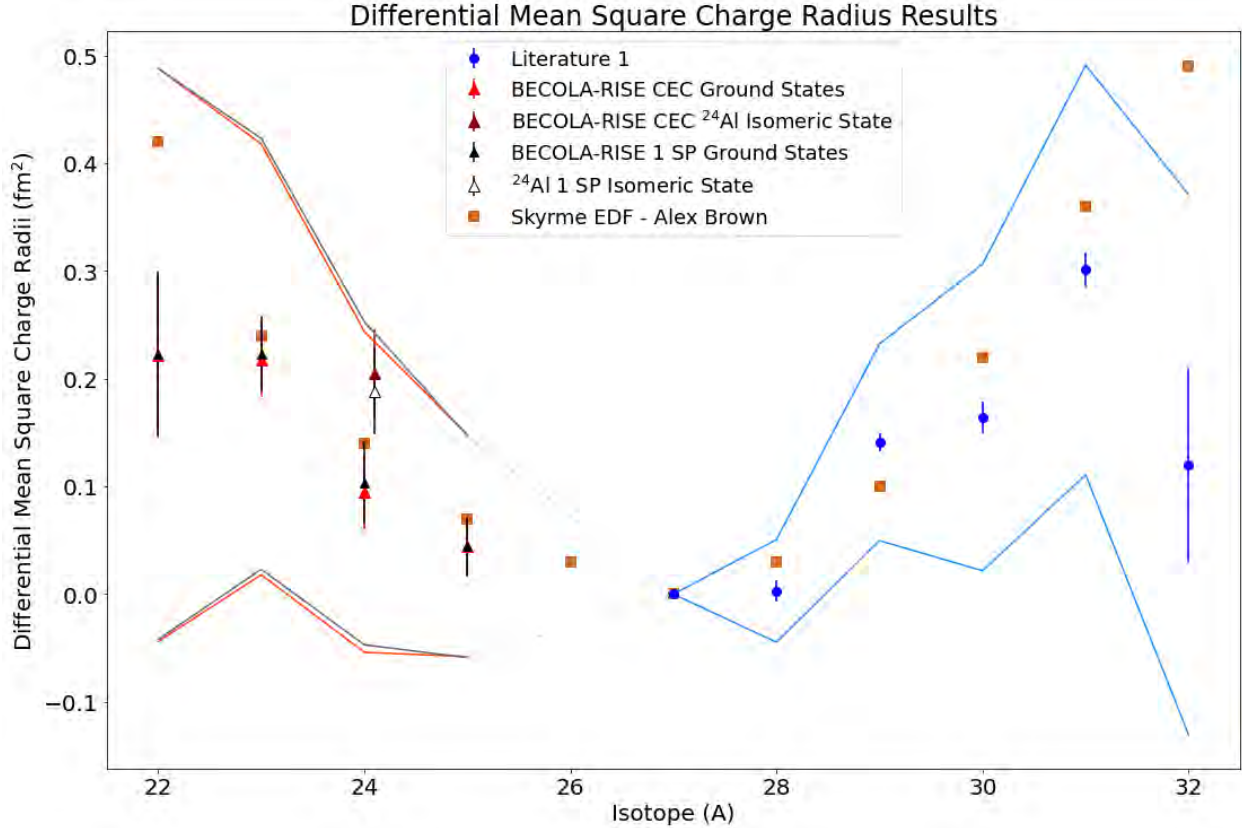


Figure 6.15 SKX-EDF and experimental differential mean square charge radii results. The differential mean square charge radii results are plotted for experiment, literature, and theory. Literature 1 indicates the literature results from Reference [37]. BECOLA-RISE CEC indicates experimental results found using the CEC simulation analysis method where the lineshape of each isotope is independently simulated. BECOLA-RISE 1 SP indicates experimental results found using the one side peak analysis method. The isomeric state is plotted slightly offset from ^{24}Al and the theoretical uncertainty of the isomeric state is not included in the plot to better visualize the ground state charge radii trend. Skyrme EDF indicates theoretical results found using SKX-EDF calculations.

6.4.4 Charge Radii Comparison

The NLEFT $\delta\langle r^2 \rangle$ and $\sqrt{\langle r^2 \rangle}$ results have very good agreement with experimental results. For $\delta\langle r^2 \rangle$ the experimental results for all isotopes except ^{22}Al are within one sigma uncertainty of the NLEFT values. The experimental statistical uncertainty and NLEFT uncertainty for the result of ^{22}Al are overlapping. When converting from $\delta\langle r^2 \rangle$ to $\sqrt{\langle r^2 \rangle}$ the experimental results for ^{23}Al , ^{24m}Al , and ^{25}Al are within one sigma of the NLEFT results, ^{22}Al and ^{24}Al are within two sigma. NLEFT calculations are in very good agreement with the experimental results. NLEFT calculations do a better job at reproducing radius results

compared to magnetic moments. NLEFT is the only theory compared here that does not predict an increase in radius moving towards ^{22}Al .

The IMSRG $\delta\langle r^2 \rangle$ and $\sqrt{\langle r^2 \rangle}$ results do not reproduce the experimental results as well as the NLEFT calculations. IMSRG calculations predict a more linear increase moving towards the dripline nucleus and predict a larger increase from ^{23}Al to ^{22}Al . The overall radii trend is not in agreement with experimental results and the $\sqrt{\langle r^2 \rangle}$ results for all isotopes are smaller than the experimental results.

The SKX-EDF $\delta\langle r^2 \rangle$ results do a good job in reproducing the overall radii trend, excluding ^{22}Al and ^{23}Al . The SKX-EDF results for $^{23-25}\text{Al}$ are within one sigma of the experimental statistical uncertainty. The SKX-EDF radii trend disagree for ^{22}Al , SKX-EDF predicts a large increase for ^{22}Al .

6.5 Structure of ^{22}Al and ^{23}Al

A driving goal of this experiment was to address the possible halo structure in ^{22}Al and ^{23}Al through the differential mean square charge radius. To confirm a halo structure or an enlarged proton distribution, a large increase in the charge radius trend would need to be observed. Focusing on the results for the charge radii of ^{22}Al and ^{23}Al , there is not an observed large increase. The charge radius trend slowly increases moving from ^{27}Al to ^{23}Al , however there is not an abnormally large increase in radius for ^{23}Al . Moving from ^{23}Al to ^{22}Al there is no large increase seen. ^{22}Al is the same size or smaller than ^{23}Al . Within error ^{22}Al could be larger than ^{23}Al , however it is not a large increase that is associated with an enlarged proton distribution. Overall, our experimental results do not support an extended proton distribution or halo structure in the nuclear ground state of ^{22}Al or ^{23}Al .

CHAPTER 7

CONCLUSION

^{22}Al and ^{23}Al were thought to have a proton halo structure in their nuclear ground state due to their small proton separation energy, enhancement of their reaction cross section, large quadrupole deformation, and theoretically predicted increase in charge radius. However, the possible halo structure was doubted due to the large centrifugal barrier for the protons to penetrate due to the large spin of the isotopes and large uncertainty of measured quantities such as the reaction cross section. The existing arguments were not strong enough alone to make a definitive statement regarding the structure of ^{22}Al or ^{23}Al . A measurement that directly addressed the proton distribution was necessary to directly address the structure of ^{22}Al and ^{23}Al .

The differential mean square charge radius directly addresses the proton distribution of a nucleus. To determine if ^{22}Al and ^{23}Al have an extended proton distribution or halo structure the differential mean square charge radii were determined using laser spectroscopy. At the BECOLA facility at FRIB at MSU the hyperfine spectra of $^{22-25}\text{Al}$ and ^{27}Al were determined. Stable ^{27}Al was produced using an offline ion source at the BECOLA facility. $^{22-25}\text{Al}$ were produced at the FRIB facility using the LINAC and separated using the ARIS fragment separator. Once the isotopes were produced and separated, they were sent into a gas cell to deliver a 30 keV ion beam to the stopped beam experimental area which contains the BECOLA facility. Whether the ions came from the offline ion source or from the gas cell, the ions were injected into a cooler buncher to convert the incoming DC beam into a bunched ion beam. The bunched ion beam was then neutralized in a charge exchange cell to create a bunched neutral atom beam. The neutral beam then interacted with two lasers. The first resonantly excited an electron from the lower state, $3p\ ^2P_{1/2}$, to the upper state, $5s\ ^2S_{1/2}$. The second laser non-resonantly excited the electron to the continuum to ionize the neutral atom beam. The resonant ion was then steered to a MagneToF detector to be counted and measure the hyperfine spectra as a function of the first step laser light frequency.

The measured hyperfine spectra was fit using a psuedo-Voigt profile for each hyperfine transition peak and corresponding side peaks. The fit results included a centroid value for each isotope. The difference between the isotope's centroid value and stable ^{27}Al 's centroid value is the isotope shift of the isotope. The isotope shift value was then combined with atomic factors determined by atomic theory and quantities from literature such as mass to determine the differential mean square charge radius for each isotope. The fit results also included A hyperfine coupling constants for each isotope. The coupling constants were combined with properties of the isotopes and the magnetic dipole moment of ^{27}Al to determine the magnetic dipole moment of each isotope.

The determined differential mean square charge radii are compared to determine the relative size of the Al isotopic chain. Although an increase in size was seen from ^{24}Al to ^{23}Al , the increase was not abnormally large or large enough to indicate an extended proton distribution. From ^{23}Al to ^{22}Al there was very little to no increase in size. Within statistical uncertainty ^{22}Al may be larger than ^{23}Al , however the difference is very small and not large enough to indicate an extended proton distribution. Neither isotopes differential mean square charge radius indicates an extended proton distribution or halo structure.

Theoretical calculations were independently performed to compare to the experimental results. VS-IMSRG and SKX-EDF charge radii calculations predicted an increase in charge radius for ^{22}Al , NLEFT charge radii calculations predicted a decrease in charge radius for ^{22}Al . Comparing with experimental results, NLEFT calculations do a good job in reproducing experimental results, SKX-EDF calculations do a good job in reproducing the overall differential mean square charge radius trend excluding ^{22}Al and ^{23}Al , and IMSRG calculations are the least in agreement with experimental results. NLEFT magnetic dipole moment calculations were not as accurate in reproducing experimental magnetic dipole moment results as the NLEFT charge radii calculations were in reproducing experimental charge radii results. NLEFT magnetic dipole moment calculations deviate further from experimental results moving towards ^{22}Al . Shell model USDB magnetic dipole moment calculations are

consistently larger than experimental results but are within expected deviation. The largest disagreement between shell model USDB magnetic dipole moment calculations and experimental results is for ^{22}Al due to its distance from $N = Z$. IMSRG magnetic dipole moment calculations including a two body correction have the best agreement with experimental values for $^{22-23}\text{Al}$ and ^{25}Al , tied for the best agreement for ^{24}Al , and see the largest deviation for the isomeric state of ^{24}Al .

Although there was not a proton halo structure found in Aluminum, it does not rule out the general existence of proton halos. To help benchmark nuclear theory, other nuclei in the region of Al and other possible halo candidates can be measured using laser spectroscopy. Possible halo candidates such as ^8B are planned to be measured using laser spectroscopy in the near future to search for an enlarged proton distribution [30]. The debate still remains if a nucleus can overcome the Coulomb barrier to create a proton halo structure, however we have determined ^{22}Al and ^{23}Al do not.

BIBLIOGRAPHY

- [1] K. Riisager, A.S. Jensen, and P. Møller. “Two-body halos”.
In: *Nuclear Physics A* 548.3 (1992), pp. 393–413. ISSN: 0375-9474.
DOI: [https://doi.org/10.1016/0375-9474\(92\)90691-C](https://doi.org/10.1016/0375-9474(92)90691-C). URL:
<https://www.sciencedirect.com/science/article/pii/037594749290691C>.
- [2] X. Z. Cali. “Existence of a proton halo in ^{23}Al and its significance”.
In: *Phys. Rev. C* 65 (2002), p. 024610.
- [3] W. J. Huang et al. “The AME2020 atomic mass evaluation”.
In: *Chinese Physics C* 45 (2021), p. 030002. DOI: 10.1088/1674-1137/abddaf.
- [4] S. E. Campbell et al.
“Precision Mass Measurement of the Proton Dripline Halo Candidate ^{22}Al ”.
In: *Phys. Rev. Lett.* 132 (2024), p. 152501.
- [5] R. N. Panda et al. “Evidence of a Proton Halo in ^{23}Al : A Mean Field Analysis”.
In: *Physics of Atomic Nuclei* 81 (2018), pp. 417–428.
- [6] Isao Tanihata, Herve Savajols, and Rituparna Kanungo.
“Recent experimental progress in nuclear halo structure studies”.
In: *Progress in Particle and Nuclear Physics* 68 (2013), pp. 215–313.
- [7] I. Tanihata et al. “Measurements of Interaction Cross Sections and Nuclear Radii in the Light p -Shell Region”. In: *Phys. Rev. Lett.* 55 (1985), p. 2676.
DOI: <https://doi.org/10.1103/PhysRevLett.55.2676>.
- [8] W. Nörtershäuser et al. “Charge radii and ground state structure of lithium isotopes: Experiment and theory reexamined”.
In: *Phys. Rev. C* 84 (2011), p. 024307.
- [9] T. Moriguchi et al.
“Density distributions of ^{11}Li deduced from reaction cross-section measurements”.
In: *Phys. Rev. C* 88 (2 2013), p. 024610. DOI: 10.1103/PhysRevC.88.024610.
- [10] I. Tanihata. “Neutron halo nuclei”.
In: *J. Phys. G: Nucl. Part. Phys.* 22 (1996), p. 157.
DOI: 10.1088/0954-3899/22/2/004.
- [11] Jim Al-Khalili. “An introduction to halo nuclei”.
In: *The Euroschool Lectures on Physics with Exotic Beams, Vol. I*. Springer, 2004,
pp. 77–112.
- [12] Wilfried Nörtershäuser et al.

- “Nuclear Charge Radii of Be 7, 9, 10 and the One-Neutron Halo Nucleus Be 11”.
In: *Physical review letters* 102.6 (2009), p. 062503.
- [13] D. Q. Fang et al. “One-neutron halo structure in ^{15}C ”.
In: *Phys. Rev. C* 69 (3 2004), p. 034613. DOI: 10.1103/PhysRevC.69.034613.
URL: <https://link.aps.org/doi/10.1103/PhysRevC.69.034613>.
- [14] D. Bazin et al. “One-Neutron Halo of ^{19}C ”.
in: *Phys. Rev. Lett.* 74 (18 1995), pp. 3569–3572.
DOI: 10.1103/PhysRevLett.74.3569.
URL: <https://link.aps.org/doi/10.1103/PhysRevLett.74.3569>.
- [15] Rituparna Kanungo, I. Tanihata, and A. Ozawa.
“Possibility of enlarged core structure of N=15 neutron-rich nuclei”.
In: *Physics Letters B* 512.3 (2001), pp. 261–267. ISSN: 0370-2693.
DOI: [https://doi.org/10.1016/S0370-2693\(01\)00719-5](https://doi.org/10.1016/S0370-2693(01)00719-5). URL:
<https://www.sciencedirect.com/science/article/pii/S0370269301007195>.
- [16] C. Ji, Ch. Elster, and D. R. Phillips. “ ^6He nucleus in halo effective field theory”.
In: *Phys. Rev. C* 90 (4 2014), p. 044004. DOI: 10.1103/PhysRevC.90.044004.
URL: <https://link.aps.org/doi/10.1103/PhysRevC.90.044004>.
- [17] M. Labiche et al. “Halo Structure of ^{14}Be ”.
In: *Phys. Rev. Lett.* 86 (4 2001), pp. 600–603. DOI: 10.1103/PhysRevLett.86.600.
URL: <https://link.aps.org/doi/10.1103/PhysRevLett.86.600>.
- [18] ZhengGuo Hu et al. “The properties of halo structure for ^{17}B ”. in: *Science in China Series G: Physics, Mechanics and Astronomy* 51.7 (2008), pp. 781–787.
- [19] K. J. Cook et al. “Halo Structure of the Neutron-Dripline Nucleus ^{19}B ”.
In: *Phys. Rev. Lett.* 124 (21 2020), p. 212503.
DOI: 10.1103/PhysRevLett.124.212503.
URL: <https://link.aps.org/doi/10.1103/PhysRevLett.124.212503>.
- [20] Manjari Sharma et al. “Neutron density distribution and the halo structure of ^{22}C ”.
In: *Phys. Rev. C* 83 (3 2011), p. 031601. DOI: 10.1103/PhysRevC.83.031601.
URL: <https://link.aps.org/doi/10.1103/PhysRevC.83.031601>.
- [21] W. Geithner et al.
“Masses and Charge Radii of $^{17-22}\text{Ne}$ and the Two-Proton-Halo Candidate ^{17}Ne ”.
In: *Phys. Rev. Lett.* 101 (2008), p. 252502.
DOI: <https://doi.org/10.1103/PhysRevLett.101.252502>.
- [22] Zhongzhou Ren et al. “One-proton halo in ^{26}P and two-proton halo in ^{27}S ”.
In: *Phys. Rev. C* 53 (2 1996), R572–R575. DOI: 10.1103/PhysRevC.53.R572.

URL: <https://link.aps.org/doi/10.1103/PhysRevC.53.R572>.

- [23] B.A. Brown, A. Arima, and J.B. McGrory.
“E2 core-polarization charge for nuclei near 16O and 40Ca”.
In: *Nuclear Physics A* 277.1 (1977), pp. 77–108. ISSN: 0375-9474.
DOI: [https://doi.org/10.1016/0375-9474\(77\)90263-9](https://doi.org/10.1016/0375-9474(77)90263-9).
- [24] A. S. Demyanova et al. “Proton Halo in the ^{13}N Nucleus”.
In: *JETP Letters* 104 (2016), pp. 526–530. DOI: 10.1134/S0021364016200108.
- [25] BA Brown and PG Hansen. “Proton halos in the 1s0d shell”.
In: *Physics Letters B* 381.4 (1996), pp. 391–396.
- [26] T. Minamisono et al.
“Proton Halo of ^8B Disclosed by Its Giant Quadrupole Moment”.
In: *Phys. Rev. Lett.* 69 (1992), p. 14.
- [27] M. Lewitowicz et al.
“ ^8B proton halo via reaction and breakup cross section measurements”.
In: *Phys. Rev. C* 54 (1996), p. 4.
- [28] M.H. Smedberg et al. “New results on the halo structure of ^8B ”.
in: *Physics Letters B* 452.1 (1999), pp. 1–7. ISSN: 0370-2693.
DOI: [https://doi.org/10.1016/S0370-2693\(99\)00245-2](https://doi.org/10.1016/S0370-2693(99)00245-2). URL:
<https://www.sciencedirect.com/science/article/pii/S0370269399002452>.
- [29] H. Nakada and T. Otsuka.
“E2 properties of nuclei far from stability and the proton-halo problem of ^8B ”.
In: *Phys. Rev. C* 49 (2 1994), pp. 886–894. DOI: 10.1103/PhysRevC.49.886.
- [30] Bernhard Maaß et al.
“Towards laser spectroscopy of the proton-halo candidate boron-8”.
In: *Hyperfine Interactions* 238 (2017), pp. 1–9.
- [31] W. Geithner et al.
“Masses and Charge Radii of $^{17-22}\text{Ne}$ and the Two-Proton-Halo Candidate ^{17}Ne ”.
In: *Phys. Rev. Lett.* 101 (25 2008), p. 252502.
DOI: 10.1103/PhysRevLett.101.252502.
- [32] C. Lehr et al. “Unveiling the two-proton halo character of ^{17}Ne : Exclusive measurement of quasi-free proton-knockout reactions”.
In: *Physics Letters B* 827 (2022), p. 136957. ISSN: 0370-2693.
DOI: <https://doi.org/10.1016/j.physletb.2022.136957>. URL:
<https://www.sciencedirect.com/science/article/pii/S0370269322000910>.

- [33] B.A Brown and P.G Hansen. “Proton halos in the 1s0d shell”.
In: *Physics Letters B* 381.4 (1996), pp. 391–396. ISSN: 0370-2693.
DOI: [https://doi.org/10.1016/0370-2693\(96\)00634-X](https://doi.org/10.1016/0370-2693(96)00634-X). URL:
<https://www.sciencedirect.com/science/article/pii/037026939600634X>.
- [34] Cai Xiang-Zhou et al.
“One-Proton Halo in ^{31}Cl with Relativistic Mean-Field Theory”.
In: *Chinese Physics Letters* 19.8 (2002), p. 1068.
DOI: 10.1088/0256-307X/19/8/312.
URL: <https://dx.doi.org/10.1088/0256-307X/19/8/312>.
- [35] C.R. Bingham et al.
“Nuclear structure studies at the proton drip line via proton radioactivity studies”.
In: *Nuclear Instruments and Methods in Physics Research Section B: Beam Interactions with Materials and Atoms* 241.1 (2005). The Application of Accelerators in Research and Industry, pp. 185–189. ISSN: 0168-583X.
DOI: <https://doi.org/10.1016/j.nimb.2005.07.082>.
- [36] G. A. Lalazissis et al.
“New parametrization for the Lagrangian density of relativistic mean field theory”.
In: *Phys. Rev. C* 55 (1997), p. 540.
DOI: <https://doi.org/10.1103/PhysRevC.55.540>.
- [37] H. Heylen et al. “High-resolution laser spectroscopy of $^{27-32}\text{Al}$ ”.
In: *Phys. Rev. C* 103 (2021), p. 014318.
- [38] F. G. Kondev et al. “The NUBASE2020 evaluation of nuclear physics properties”.
In: *Chinese Phys. C* 45 (2021), p. 030001.
- [39] C. G. Wu et al. “ β -decay spectroscopy of the proton drip-line nucleus ^{22}Al ”.
In: *Phys. Rev. C* 104 (2021), p. 044311.
DOI: <https://doi.org/10.1103/PhysRevC.104.044311>.
- [40] K. Y. Zhang et al. “Examination of the evidence for a proton halo in ^{22}Al ”.
In: *Phys. Rev. C* 110 (2024), p. 014320.
DOI: <https://doi.org/10.1103/PhysRevC.110.014320>.
- [41] Z. H. Yang et al. “Quasifree Neutron Knockout Reaction Reveals a Small s -Orbital Component in the Borromean Nucleus ^{17}B ”.
in: *Phys. Rev. Lett.* 126 (2021), p. 082501.
DOI: <https://doi.org/10.1103/PhysRevLett.126.082501>.
- [42] J. Lee et al. “Large Isospin Asymmetry in $^{22}\text{Si}/^{22}\text{O}$ Mirror Gamow-Teller Transitions Reveals the Halo Structure of ^{22}Al ”.
In: *Phys. Rev. Lett.* 125 (2020), p. 192503.

- [43] P. Campbell et al. “Laser spectroscopy for nuclear structure physics”.
In: *Progress in Particle and Nuclear Physics* 86 (2016), pp. 127–180.
DOI: <https://doi.org/10.1016/j.ppnp.2015.09.003>.
- [44] T. Miyagi et al.
“Impact of Two-Body Currents on Magnetic Dipole Moments of Nuclei”.
In: *Phys. Rev. Lett.* 132 (23 2024), p. 232503.
DOI: 10.1103/PhysRevLett.132.232503.
- [45] W. A. Richter, S. Mkhize, and B. Alex Brown.
“*sd*-shell observables for the USDA and USDB Hamiltonians”.
In: *Phys. Rev. C* 78 (6 2008), p. 064302. DOI: 10.1103/PhysRevC.78.064302.
- [46] B. A. Brown and B. H. Wildenthal. “Corrections to the free-nucleon values of the single-particle matrix elements of the *M1* and Gamow-Teller operators, from a comparison of shell-model predictions with *sd*-shell data”.
In: *Phys. Rev. C* 28 (6 1983), pp. 2397–2413. DOI: 10.1103/PhysRevC.28.2397.
- [47] J.R. Persson. “Table of hyperfine anomaly in atomic systems — 2023”.
In: *Atomic Data and Nuclear Data Tables* 154 (2023), p. 101589. ISSN: 0092-640X.
DOI: <https://doi.org/10.1016/j.adt.2023.101589>.
- [48] S Büttgenbach. “Magnetic hyperfine anomalies”.
In: *Hyperfine Interactions* 20.1 (1984), pp. 1–64.
- [49] K. König et al.
“Isotope-shift measurements and King-fit analysis in nickel isotopes”.
In: *PRC* 103 (2021), p. 054305.
DOI: <https://doi.org/10.1103/PhysRevC.103.054305>.
- [50] Ingo Sick. “Proton charge radius from electron scattering”.
In: *Atoms* 6.1 (2017), p. 2.
- [51] R.M. Lombard and G.R. Bishop. “The scattering of high-energy electrons by ^{27}Al ”.
In: *Nuclear Physics A* 101.3 (1967), pp. 601–624. ISSN: 0375-9474.
DOI: [https://doi.org/10.1016/0375-9474\(67\)90655-0](https://doi.org/10.1016/0375-9474(67)90655-0). URL:
<https://www.sciencedirect.com/science/article/pii/0375947467906550>.
- [52] Hans Alfred Bentz, Michael Loewenhaupt, and Horst Theissen. “Nuclear charge radii of Al and Si from elastic electron scattering between 25 and 60 MeV”.
in: *Zeitschrift für Physik A Hadrons and nuclei* 231 (1970), pp. 484–490.
- [53] E. C. SELTZER. “*K* X-Ray Isotope Shifts”.
In: *Phys. Rev.* 188 (4 1969), pp. 1916–1919. DOI: 10.1103/PhysRev.188.1916.
URL: <https://link.aps.org/doi/10.1103/PhysRev.188.1916>.

- [54] Leonid V Skripnikov et al. “Isotope-shift factors with quantum electrodynamics effects for many-electron systems: A study of the nuclear charge radius of Al 26 m”. In: *Physical Review A* 110.1 (2024), p. 012807.
- [55] G Fricke et al. “Nuclear ground state charge radii from electromagnetic interactions”. In: *Atomic Data and Nuclear Data Tables* 60.2 (1995), pp. 177–285.
- [56] Klaus Blaum, Jens Dilling, and Wilfried Nörtershäuser. “Precision atomic physics techniques for nuclear physics with radioactive beams”. In: *Physica Scripta* 2013.T152 (2013), p. 014017.
- [57] K. König et al. “Nuclear Charge Radii of Silicon Isotopes”. In: *PRL* 132 (2024), p. 162502.
DOI: <https://doi.org/10.1103/PhysRevLett.132.162502>.
- [58] Kristian König et al. “Surprising Charge-Radius Kink in the Sc Isotopes at $N = 20$ ”. In: *Phys. Rev. Lett.* 131 (10 2023), p. 102501.
DOI: [10.1103/PhysRevLett.131.102501](https://doi.org/10.1103/PhysRevLett.131.102501).
URL: <https://link.aps.org/doi/10.1103/PhysRevLett.131.102501>.
- [59] Felix Sommer et al. “Charge Radii of $^{55,56}\text{Ni}$ Reveal a Surprisingly Similar Behavior at $N = 28$ in Ca and Ni Isotopes”. In: *Phys. Rev. Lett.* 129 (13 2022), p. 132501.
DOI: [10.1103/PhysRevLett.129.132501](https://doi.org/10.1103/PhysRevLett.129.132501).
URL: <https://link.aps.org/doi/10.1103/PhysRevLett.129.132501>.
- [60] H. J. Andrä, A. Gaupp, and W. Wittmann. “New Method for Precision Lifetime Measurements by Laser Excitation of Fast-Moving Atoms”. In: *Phys. Rev. Lett.* 31 (8 1973), pp. 501–504. DOI: [10.1103/PhysRevLett.31.501](https://doi.org/10.1103/PhysRevLett.31.501).
URL: <https://link.aps.org/doi/10.1103/PhysRevLett.31.501>.
- [61] William H. Wing et al. “Observation of the Infrared Spectrum of the Hydrogen Molecular Ion HD^+ ”. In: *Phys. Rev. Lett.* 36 (25 1976), pp. 1488–1491.
DOI: [10.1103/PhysRevLett.36.1488](https://doi.org/10.1103/PhysRevLett.36.1488).
URL: <https://link.aps.org/doi/10.1103/PhysRevLett.36.1488>.
- [62] K. R. Anton et al. “Collinear Laser Spectroscopy on Fast Atomic Beams”. In: *Phys. Rev. Lett.* 40 (10 1978), pp. 642–645.
DOI: [10.1103/PhysRevLett.40.642](https://doi.org/10.1103/PhysRevLett.40.642).
URL: <https://link.aps.org/doi/10.1103/PhysRevLett.40.642>.
- [63] B. Schinzler et al. “Collinear laser spectroscopy of neutron-rich Cs isotopes at an on-line mass separator”. In: *Physics Letters B* 79.3 (1978), pp. 209–212.

ISSN: 0370-2693. DOI: [https://doi.org/10.1016/0370-2693\(78\)90224-1](https://doi.org/10.1016/0370-2693(78)90224-1). URL: <https://www.sciencedirect.com/science/article/pii/0370269378902241>.

- [64] Ernst W Otten. “Nuclear radii and moments of unstable isotopes”. In: *Treatise on Heavy Ion Science: Volume 8: Nuclei Far From Stability* (1989), pp. 517–638.
- [65] W. Nörtershäuser. *MS Windows NT Kernel Description*. 1999. URL: www.ikp.tu-darmstadt.de/laser_nuclear_chart (visited on 03/04/2025).
- [66] Kristian König et al. “Surprising charge-radius kink in the Sc isotopes at N= 20”. In: *Physical Review Letters* 131.10 (2023), p. 102501.
- [67] A Nieminen et al. “On-line ion cooling and bunching for collinear laser spectroscopy”. In: *Physical review letters* 88.9 (2002), p. 094801.
- [68] B. A. Brown et al. “Implications of the $^{36}\text{Ca} - ^{36}\text{S}$ and $^{38}\text{Ca} - ^{38}\text{Ar}$ difference in mirror charge radii on the neutron matter equation of state”. In: *Phys. Rev. Res.* 2 (2 2020), p. 022035. DOI: 10.1103/PhysRevResearch.2.022035.
- [69] Sirah Lasertechnik GmbH. *Fully Automated Ti:Sa CW Ring Laser*. 2024. URL: <https://www.sirah.com/lasers/cw/matisse-c/> (visited on 03/19/2025).
- [70] mks Spectra-Physics Newport Corporation. *WaveTrain® 2 CW Frequency Doublers*. 2024. URL: <https://www.spectra-physics.com/en/f/wavetrain-2-cw-frequency-doubler> (visited on 03/19/2025).
- [71] M Reponen et al. “Towards in-jet resonance ionization spectroscopy: An injection-locked Titanium: Sapphire laser system for the PALIS-facility”. In: *Nuclear Instruments and Methods in Physics Research Section A: Accelerators, Spectrometers, Detectors and Associated Equipment* 908 (2018), pp. 236–243.
- [72] Photonics Industries International. Inc. *TU Series*. 2025. URL: <https://www.photonix.com/product/tu-series/> (visited on 03/19/2025).
- [73] HighFinesse. *WX6-600 Series*. 2024. URL: <https://www.highfinesse.com/en/wavelengthmeter/wavelengthmeter-ws-6-600.html> (visited on 03/19/2025).
- [74] SIOS Meßtechnik GmbH. *Frequency stabilized HeNe lasers*. 2024. URL: <https://www.sios-precision.com/en/products/stabilized-hene-lasers> (visited on 03/19/2025).

- [75] TEM-Messtechnik GmbH. *LaseLock – Universal laser stabilization electronics*. 2025. URL: <https://tem-messtechnik.de/en/products/laselock-universal-laser-stabilization-electronics/> (visited on 05/27/2025).
- [76] Dr. Arlee Smith AS-Photonics. *SNLO classic (free version)*. 2025. URL: <https://as-photonics.com/products/snlo/> (visited on 05/27/2025).
- [77] Yushi Kaneda. *iPhasematch*. 2011-2025.
- [78] Quantel laser by Lumibird. *Merion MW*. 2024. URL: <https://www.quantel-laser.com/en/products/item/merion-mw-752.html> (visited on 03/19/2025).
- [79] Quantum Composers Inc. *9520 Series Pulse Generators for Timing and Synchronization*. 2024. URL: <https://www.quantumcomposers.com/pulse-delay-generator-9520> (visited on 03/13/2025).
- [80] MRC Systems GmbH. *Active Laser Beam Stabilization*. 2025. URL: <https://www.mrc-systems.de/en/products/laser-beam-stabilization> (visited on 03/19/2025).
- [81] Michigan State University. *Facility for Rare Isotope Beams at Michigan State University*. 2025. URL: <https://frib.msu.edu/> (visited on 03/19/2025).
- [82] J Wei et al. “Accelerator commissioning and rare isotope identification at the Facility for Rare Isotope Beams”. In: *Modern Physics Letters A* 37.09 (2022), p. 2230006.
- [83] M. Hausmann et al. “Design of the Advanced Rare Isotope Separator ARIS at FRIB”. in: *Nuclear Instruments and Methods in Physics Research Section B: Beam Interactions with Materials and Atoms* 317 (2013). XVIth International Conference on ElectroMagnetic Isotope Separators and Techniques Related to their Applications, December 2–7, 2012 at Matsue, Japan, pp. 349–353. ISSN: 0168-583X. DOI: <https://doi.org/10.1016/j.nimb.2013.06.042>. URL: <https://www.sciencedirect.com/science/article/pii/S0168583X13007210>.
- [84] K. Cooper et al. “Extraction of thermalized projectile fragments from a large volume gas cell”. In: *NIMA* 763 (2014), pp. 543–546. DOI: <https://doi.org/10.1016/j.nima.2014.06.075>.

- [85] K.R. Lund et al. “Online tests of the Advanced Cryogenic Gas Stopper at NSCL”.
in: *Nuclear Instruments and Methods in Physics Research Section B: Beam Interactions with Materials and Atoms* 463 (2020), pp. 378–381. ISSN: 0168-583X.
DOI: <https://doi.org/10.1016/j.nimb.2019.04.053>. URL:
<https://www.sciencedirect.com/science/article/pii/S0168583X1930237X>.
- [86] Ting Xu et al.
“Completion of FRIB superconducting linac and phased beam commissioning”.
In: *Proc. SRF’21* (2021), pp. 197–202.
- [87] C.S. Sumithrarachchi et al. “Beam thermalization in a large gas catcher”.
In: *Nuclear Instruments and Methods in Physics Research Section B: Beam Interactions with Materials and Atoms* 463 (2020), pp. 305–309. ISSN: 0168-583X.
DOI: <https://doi.org/10.1016/j.nimb.2019.04.077>. URL:
<https://www.sciencedirect.com/science/article/pii/S0168583X19302617>.
- [88] C.S. Sumithrarachchi et al. “The new Batch Mode Ion Source for stand-alone operation at the Facility for Rare Isotope Beams (FRIB)”.
in: *Nuclear Instruments and Methods in Physics Research Section B: Beam Interactions with Materials and Atoms* 541 (2023), pp. 301–304. ISSN: 0168-583X.
DOI: <https://doi.org/10.1016/j.nimb.2023.05.061>. URL:
<https://www.sciencedirect.com/science/article/pii/S0168583X23002665>.
- [89] R. Ringle et al. “Penning trap mass spectrometry of rare isotopes produced via projectile fragmentation at the LEBIT facility”.
In: *International Journal of Mass Spectrometry* 349-350 (2013), pp. 87–93.
DOI: <https://doi.org/10.1016/j.ijms.2013.04.001>.
- [90] Z. Nouri et al. “A Penning sputter ion source with very low energy spread”.
In: *Nuclear Instruments and Methods in Physics Research Section A: Accelerators, Spectrometers, Detectors and Associated Equipment* 614.2 (2010), pp. 174–178.
ISSN: 0168-9002. DOI: <https://doi.org/10.1016/j.nima.2009.12.060>. URL:
<https://www.sciencedirect.com/science/article/pii/S0168900209023973>.
- [91] CA Ryder et al. “Population distribution subsequent to charge exchange of 29.85 keV Ni⁺ on sodium vapor”.
In: *Spectrochimica Acta Part B: Atomic Spectroscopy* 113 (2015), pp. 16–21.
- [92] B. R. Barquest et al.
“RFQ beam cooler and buncher for collinear laser spectroscopy of rare isotopes”.
In: *NIMA* 866 (2017), pp. 18–28.
DOI: <https://doi.org/10.1016/j.nima.2017.05.036>.
- [93] A. Klose et al.
“Tests of atomic charge-exchange cells for collinear laser spectroscopy”.

- In: *NIMA* 678 (2012), pp. 114–121.
DOI: <http://dx.doi.org/10.1016/j.nima.2012.03.006>.
- [94] K Minamisono et al. “Commissioning of the collinear laser spectroscopy system in the BECOLA facility at NSCL”.
in: *Nuclear instruments and methods in physics research section a: accelerators, spectrometers, detectors and associated equipment* 709 (2013), pp. 85–94.
- [95] ETP-MS Electron Multipliers. *MagneToFTM: A New Class of Robust Sub-nanosecond TOF Detectors with Exceptional Dynamic Range*. 2013.
URL: <https://www.etp-ms.com/file-repository/8> (visited on 09/16/2024).
- [96] K. Minamisono et al. “Commissioning of the collinear laser spectroscopy system in the BECOLA facility at NSCL”. in: *NIMA* 709 (2013), pp. 85–94.
DOI: <https://doi.org/10.1016/j.nima.2013.01.038>.
- [97] E. S. Chang. “Energy Levels of Atomic Aluminum with Hyperfine Structure”.
In: *Journal of Physical and Chemical Reference Data* 19 (1990), p. 119.
- [98] Hiroki Nakai et al.
“Hyperfine Structure of ²⁷Al by High-Resolution Ultraviolet Laser Spectroscopy”.
In: *Jpn. J. Appl. Phys.* 46 (2007), p. 815.
- [99] H. Heylen et al. “High-resolution laser spectroscopy of ^{27–32}Al”.
In: *Physical Review C* 103 (2021), p. 014318.
- [100] B. K. Sahoo et al.
“Application of relativistic coupled-cluster theory to heavy atomic systems with strongly interacting configurations: Hyperfine interactions in ²⁰⁷Pb⁺”.
In: *Physical Review A* 72 (2005), p. 032507.
- [101] S. Majumder et al. “Many-body effects in hyperfine interactions in ²⁰⁵Pb⁺”.
In: *Euro. J. Phys. D* 41 (2007), pp. 441–445.
- [102] Paul Siddons et al. “Absolute absorption on rubidium D lines: comparison between theory and experiment”. In: *Journal of Physics B: Atomic, Molecular and Optical Physics* 41.15 (2008), p. 155004.
- [103] FG Kondev et al. “The NUBASE2020 evaluation of nuclear physics properties”.
In: *Chinese Physics C* 45.3 (2021), p. 030001.
- [104] M. Newville et al. In: *LMFIT: Non-linear Least-Squares Minimization and Curve-Fitting for Python* (2024), Built-in Fitting Models in the models module.
DOI: https://lmfit.github.io/lmfit-py/builtin_models.html.

- [105] A. Dockery et al. “Charge Exchange Simulations”. In: (2025).
- [106] Kristian König et al. “Beam energy determination via collinear laser spectroscopy”. In: *Phys. Rev. A* 103 (3 2021), p. 032806. DOI: 10.1103/PhysRevA.103.032806.
- [107] NJ Stone. “Table of nuclear magnetic dipole and electric quadrupole moments”. In: *Atomic Data and Nuclear Data Tables* 90.1 (2005), pp. 75–176.
- [108] NL Achouri et al. “The β -decay of ^{22}Al ”. In: *The European Physical Journal A-Hadrons and Nuclei* 27 (2006), pp. 287–300.
- [109] P. Campbell et al. “Laser Spectroscopy of Cooled Zirconium Fission Fragments”. In: *Phys. Rev. Lett.* 89 (8 2002), p. 082501. DOI: 10.1103/PhysRevLett.89.082501. URL: <https://link.aps.org/doi/10.1103/PhysRevLett.89.082501>.
- [110] NJ Stone. “Table of nuclear magnetic dipole and electric quadrupole moments”. In: *Atomic Data and Nuclear Data Tables* 90.1 (2005), pp. 75–176.
- [111] Dean Lee. “Lattice Effective Field Theory Simulations of Nuclei”. In: *arXiv preprint arXiv:2501.03303* (2025).
- [112] Dean Lee. “Lattice simulations for few- and many-body systems”. In: *Progress in Particle and Nuclear Physics* 63.1 (2009), pp. 117–154. ISSN: 0146-6410. DOI: <https://doi.org/10.1016/j.ppnp.2008.12.001>.
- [113] B Alex Brown and WA Richter. “New “USD” Hamiltonians for the sd shell”. In: *Physical Review C—Nuclear Physics* 74.3 (2006), p. 034315.
- [114] R. Seutin et al. “Magnetic dipole operator from chiral effective field theory for many-body expansion methods”. In: *Phys. Rev. C* 108 (5 2023), p. 054005. DOI: 10.1103/PhysRevC.108.054005.
- [115] S. R. Stroberg et al. “Ab Initio Limits of Atomic Nuclei”. In: *Phys. Rev. Lett.* 126 (2 2021), p. 022501. DOI: 10.1103/PhysRevLett.126.022501. URL: <https://link.aps.org/doi/10.1103/PhysRevLett.126.022501>.
- [116] B. Alex Brown. “New Skyrme interaction for normal and exotic nuclei”. In: *Phys. Rev. C* 58 (1 1998), pp. 220–231. DOI: 10.1103/PhysRevC.58.220. URL: <https://link.aps.org/doi/10.1103/PhysRevC.58.220>.
- [117] Gaute Hagen et al. “Coupled-cluster computations of atomic nuclei”. In: *Reports on Progress in Physics* 77.9 (2014), p. 096302.

- [118] V. Somà et al. “Novel chiral Hamiltonian and observables in light and medium-mass nuclei”. In: *Phys. Rev. C* 101 (1 2020), p. 014318. DOI: 10.1103/PhysRevC.101.014318. URL: <https://link.aps.org/doi/10.1103/PhysRevC.101.014318>.
- [119] K Hebeler et al. “Improved nuclear matter calculations from chiral low-momentum interactions”. In: *Physical Review C—Nuclear Physics* 83.3 (2011), p. 031301.
- [120] K. Hebeler and A. Schwenk. “Chiral three-nucleon forces and neutron matter”. In: *Phys. Rev. C* 82 (1 2010), p. 014314. DOI: 10.1103/PhysRevC.82.014314. URL: <https://link.aps.org/doi/10.1103/PhysRevC.82.014314>.
- [121] W. G. Jiang et al. “Accurate bulk properties of nuclei from $A = 2$ to ∞ from potentials with Δ isobars”. In: *Phys. Rev. C* 102 (5 2020), p. 054301. DOI: 10.1103/PhysRevC.102.054301. URL: <https://link.aps.org/doi/10.1103/PhysRevC.102.054301>.
- [122] A Ekström et al. “ Δ isobars and nuclear saturation”. In: *Physical Review C* 97.2 (2018), p. 024332.
- [123] A. W. Weiss. “Series perturbations in atomic spectra: Superposition-of-configurations calculations on Al I and Al II”. in: *PRA* 9 (1974), p. 4.
- [124] V. Kaufman and W. C. Martin. “Wavelengths and Energy Level Classifications for the Spectra of Aluminum (Al I through Al XIII)”. In: *Journal of Physical and Chemical Reference Data* 20 (1991), p. 775. DOI: <https://doi.org/10.1063/1.555895>.

APPENDIX

OFFLINE TRANSITIONS

.1 Stable ^{27}Al Offline Transitions

In preparation for the online Aluminum experiment, a transition had to be chosen that would obtain the best results; highest statistics with a large efficiency. Seven different transitions, involving six different states, were measured to both commission the new RISE beamline extension and pick a transition for the online experiment. The transitions studied are summarized below.

.1.1 $3p\ ^2P_{3/2}$ to $yd\ ^2D_{5/2}$

The $3p\ ^2P_{3/2}$ to $yd\ ^2D_{5/2}$ transition contains 12 hyperfine transitions, resulting in a complex structure. A sample spectrum of the transition is shown in Figure .1. As shown in Figure .2 not all 12 peaks are fully resolved. Due to the small splitting between peaks, two overlapped peaks are visible as one single peak. When analyzing and fitting this spectrum any overlapping peaks must be tied together. The fitting function has no way of determining the relative size of two fully overlapped peaks. To most accurately fit the two overlapped peaks, each have their own peak parameters but share a parameter to tie their peak heights together. Using the theoretical Racah coefficients, a theoretical ratio of peak heights can be obtained. Any overlapping peaks contain the shared parameter for relative height times their Racah coefficient. This makes the peaks relative height ratio theoretically correct and allows the fit to vary the height of the fixed pairs of peaks. Previous experiments have shown that laser spectroscopy results vary from the Racah coefficient values. One example of a cause for this is saturating one peak's transition before another. Since it is a known characteristic to vary from the Racah coefficients, using their values to fix peak ratios is not ideal. Moving from offline stable work to the online run, transitions with overlapping peaks that require fixing to the Racah coefficients were avoided.

The excited state for this transition, $yd\ ^2D_{5/2}$, is a mixed state. At the time of running and studying this transition until after the conclusion of the online Aluminum experiment

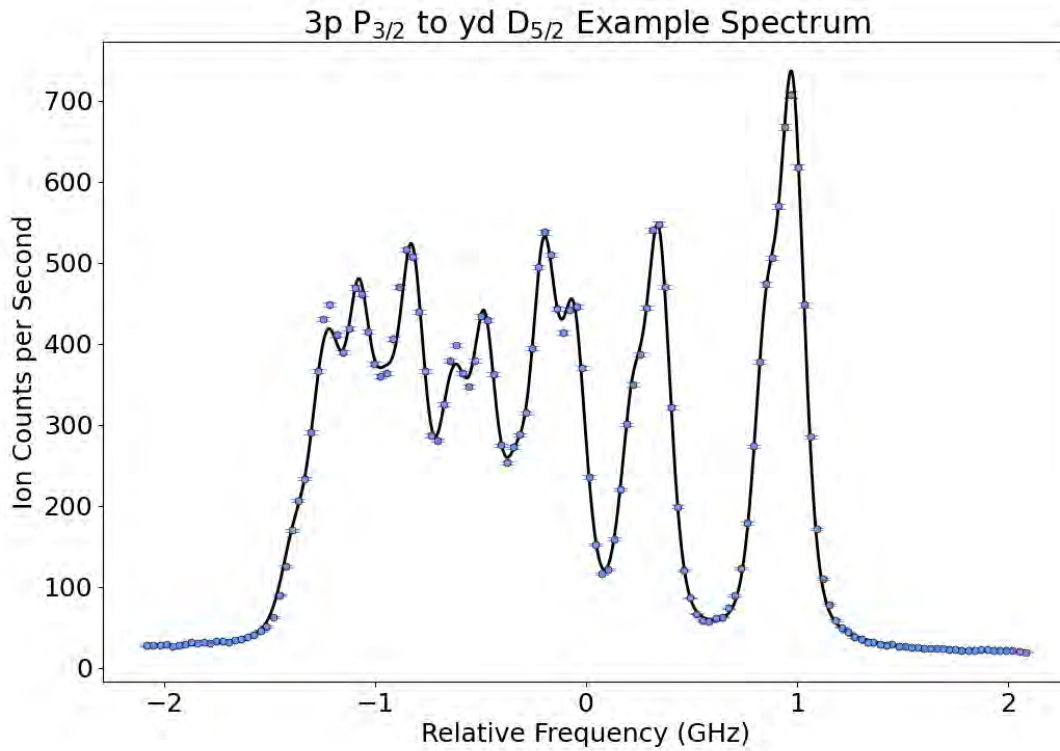


Figure .1 $3p \ ^2P_{3/2}$ to $yd \ ^2D_{5/2}$ transition spectrum. A sample spectrum of the $3p \ ^2P_{3/2}$ to $yd \ ^2D_{5/2}$ transition for ^{27}Al is shown.

there were no theoretical calculations for A or B hyperfine coupling constants for the $yd \ D_{3/2}$ and $yd \ D_{5/2}$ states, since they are mixed states. The $3s3p^2 \ ^2D$ state is distributed among the $3s^2nd \ ^2D$ series which makes the state hard to define [123]. Due to the mixing, the $3s^24d \ ^2D$ state was relabeled as $3s^2nd \ ^2D$ referring to it as the $y \ ^2D$ state [124].

Due to the mixed state and overlapping, unresolved, peaks the $3p \ ^2P_{3/2}$ to $yd \ ^2D_{5/2}$ transition would not be a good choice for the online experiment. Despite the difficulties with this transition the hyperfine coefficients were successfully measured. Through discussion with many theorists, theoretical values for the mixed state were recently obtained. Experimental and theoretical results are listed in Table 4.1 and 4.2.

.1.2 $3p \ ^2P_{3/2}$ to $yd \ ^2D_{3/2}$

The $3p \ ^2P_{3/2}$ to $yd \ ^2D_{3/2}$ transition contains 10 hyperfine transitions and is similar in characteristics to the previous $3p \ ^2P_{3/2}$ to $yd \ ^2D_{5/2}$ transition. The hyperfine spectra for

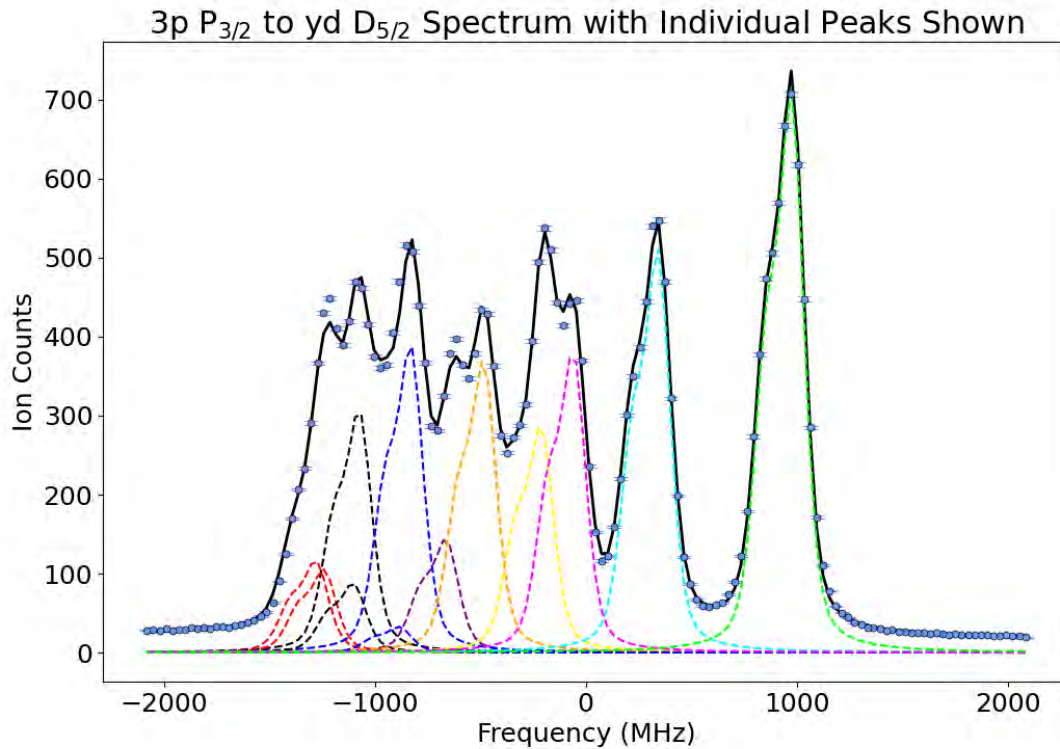


Figure .2 $3p \ ^2P_{3/2}$ to $yd \ ^2D_{5/2}$ transition peak components. The individual peaks of the $^2P_{3/2}$ to $yd \ ^2D_{5/2}$ transition for ^{27}Al are shown. The peaks are offset below the data for clarity. Peaks of the same color indicate peaks that have their amplitudes tied together by their Racah coefficients, due to the individual peaks not being fully resolved.

this transition is shown in Figure .3. This transition has multiple overlapping peaks, shown in Figure .4, and has a mixed excited state. Hyperfine coefficients were measured for this transition and are included in Table 4.1 and 4.2. Due to the overlapping peaks and mixed excited state, this transition was not used for the online run.

.1.3 $3p \ ^2P_{1/2}$ to $yd \ ^2D_{3/2}$

The $3p \ ^2P_{1/2}$ to $yd \ ^2D_{3/2}$ transition contains 6 hyperfine transitions. The hyperfine structure for this transition is shown in Figure .6. All 6 peaks for this transition are resolved, shown in Figure .6, making it a more promising transition to use for the online experiment. However, the excited state is a mixed state. In addition the ground state spin is $1/2$ meaning the ground state is not sensitive to the quadrupole moment and we would be dependent on the mixed state to determine the quadrupole moment. The hyperfine coupling constants

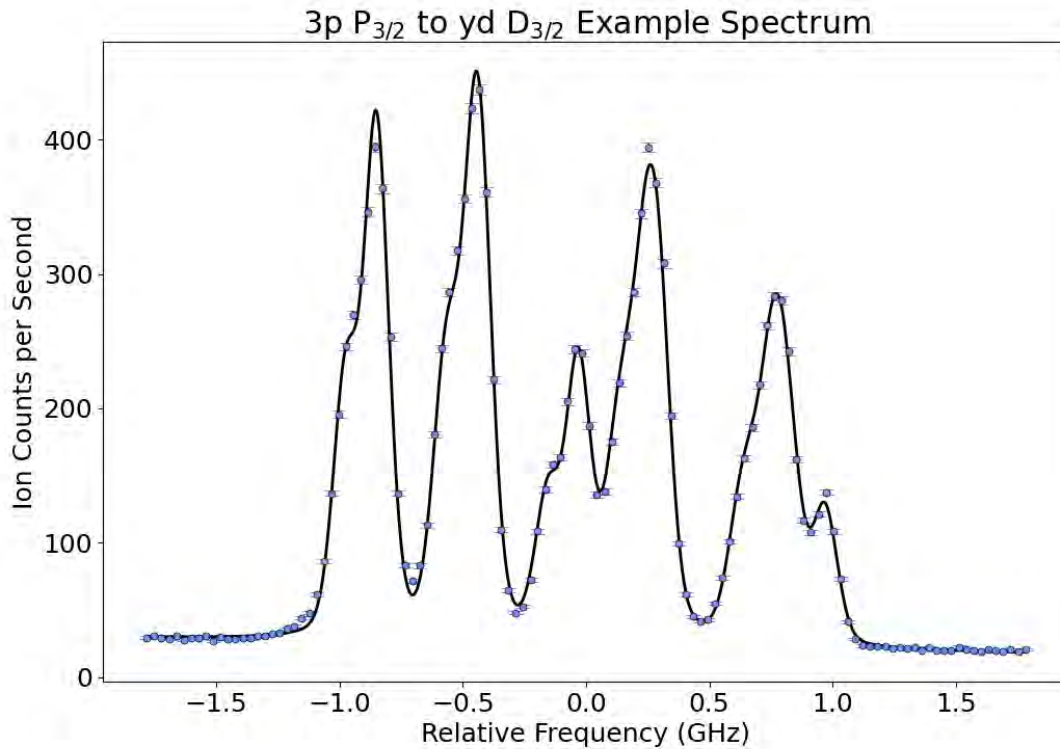


Figure .3 3p $^2P_{3/2}$ to yd $^2D_{3/2}$ transition spectrum. A sample spectrum of the 3p $^2P_{3/2}$ to yd $^2D_{3/2}$ transition for ^{27}Al is shown.

were successfully measured and are included in Table 4.1 and 4.2.

.1.4 3p $^2P_{3/2}$ to 4s $^2S_{1/2}$

In addition to the resonant ionization transitions mentioned above, two fluorescence transitions to obtain the hyperfine coefficients of the 4s $^2S_{1/2}$ state were measured. The 3p $^2P_{3/2}$ to 4s $^2S_{1/2}$ transition contains six hyperfine transitions which are all resolved, the hyperfine structure is shown in Figure .7. The peak components are shown in Figure .8. The hyperfine coefficients were measured and are included in Table 4.1 and 4.2.

This transition could be measured using resonant ionization rather than fluorescence as a three step ionization scheme. However, the lasers required to measure this transition using resonant ionization were not available at the time of the Aluminum experiment. This fluorescence transition has a smaller signal to noise ratio compared to the previously discussed resonant ionization transitions in low ion beam rate measurements, therefore these fluo-

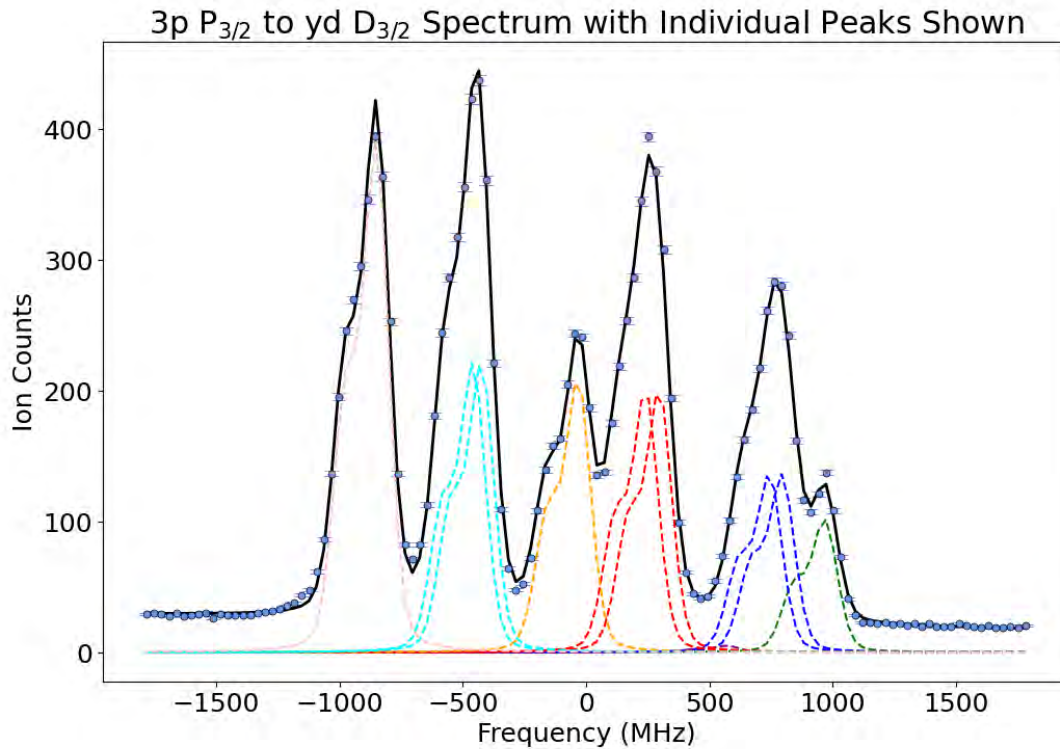


Figure .4 $3p \ ^2P_{3/2}$ to $yd \ ^2D_{3/2}$ transition peak components. The individual peaks of the $3p \ ^2P_{3/2}$ to $yd \ ^2D_{3/2}$ transition for ^{27}Al are shown. Peaks of the same color indicate peaks that have their amplitudes tied together by their rakar coefficients, due to the individual peaks not being fully resolved.

cence transitions could not be used to measure the dripline nucleus ^{22}Al without a very long run time. The biggest drop in signal to noise for the fluorescence measurements compared to the resonant ionization transitions for Aluminum is the background for fluorescence measurements does not scale with the number of ions coming in. The resonant ionization technique does scale the background with a decrease in the ion counts coming in. In addition for the Aluminum resonant ionization techniques studied there was no large background produced by the non-resonant laser step, creating very low background measurements. The smaller efficiency and need for a longer run time ruled out using any fluorescence transitions for the online run.

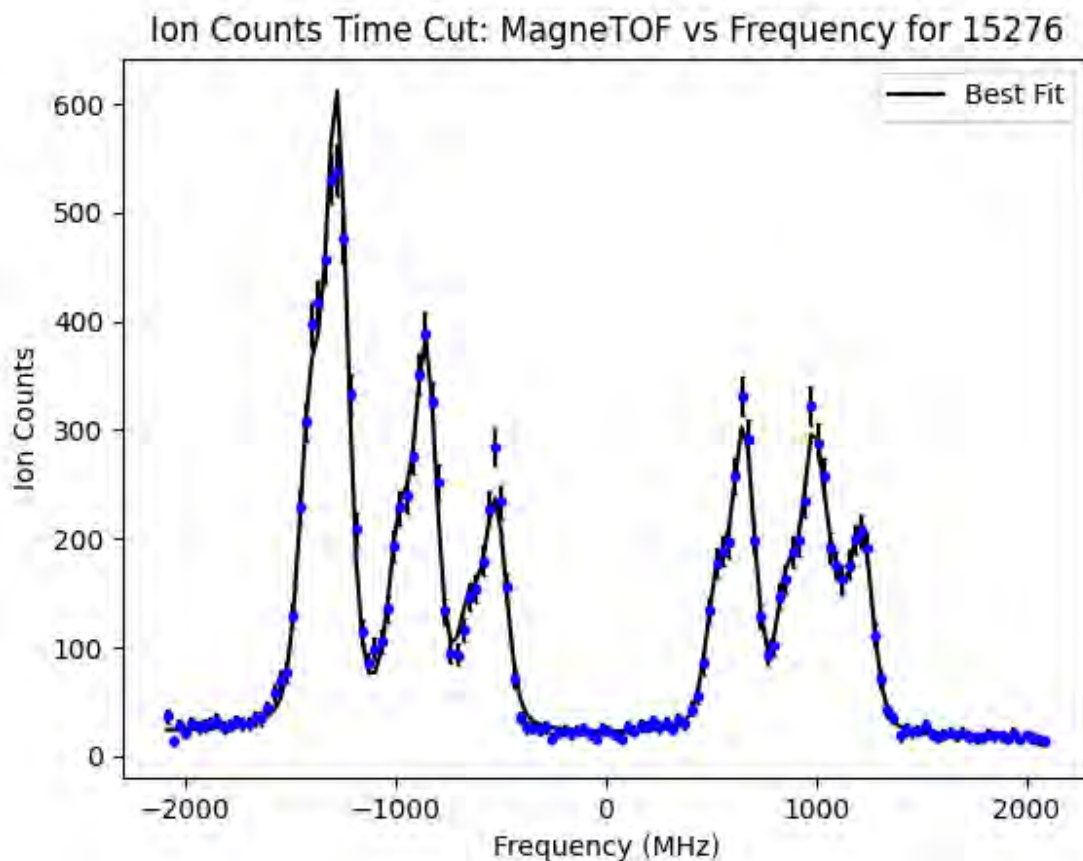


Figure .5 $3p\ ^2P_{1/2}$ to $4d\ ^2D_{3/2}$ transition spectrum. *Place Holder Figure* A sample spectrum of the $3p\ ^2P_{1/2}$ to $4d\ ^2D_{3/2}$ transition for ^{27}Al is shown.

.1.5 $3p\ ^2P_{1/2}$ to $4s\ ^2S_{1/2}$

To finish all the transitions the $3p\ ^2P_{1/2}$ to $4s\ ^2S_{1/2}$ transition was measured using fluorescence. This transition contains 4 well resolved peaks, the hyperfine structure is shown in Figure .9 and components in Figure .10. The hyperfine coefficients for this transition were measured and are included in Table 4.1.

.1.6 $3p\ ^2P_{3/2}$ to $5s\ ^2S_{1/2}$ and $3p\ ^2P_{1/2}$ to $5s\ ^2S_{1/2}$

The $3p\ ^2P_{3/2}$ to $5s\ ^2S_{1/2}$ and $3p\ ^2P_{1/2}$ to $5s\ ^2S_{1/2}$ transitions were the most promising to be used for the online experiment. The $3p\ ^2P_{1/2}$ to $5s\ ^2S_{1/2}$ was used for the online experiment. Both transitions are discussed in the main text in detail, including simulations for each transition for the online experiment.

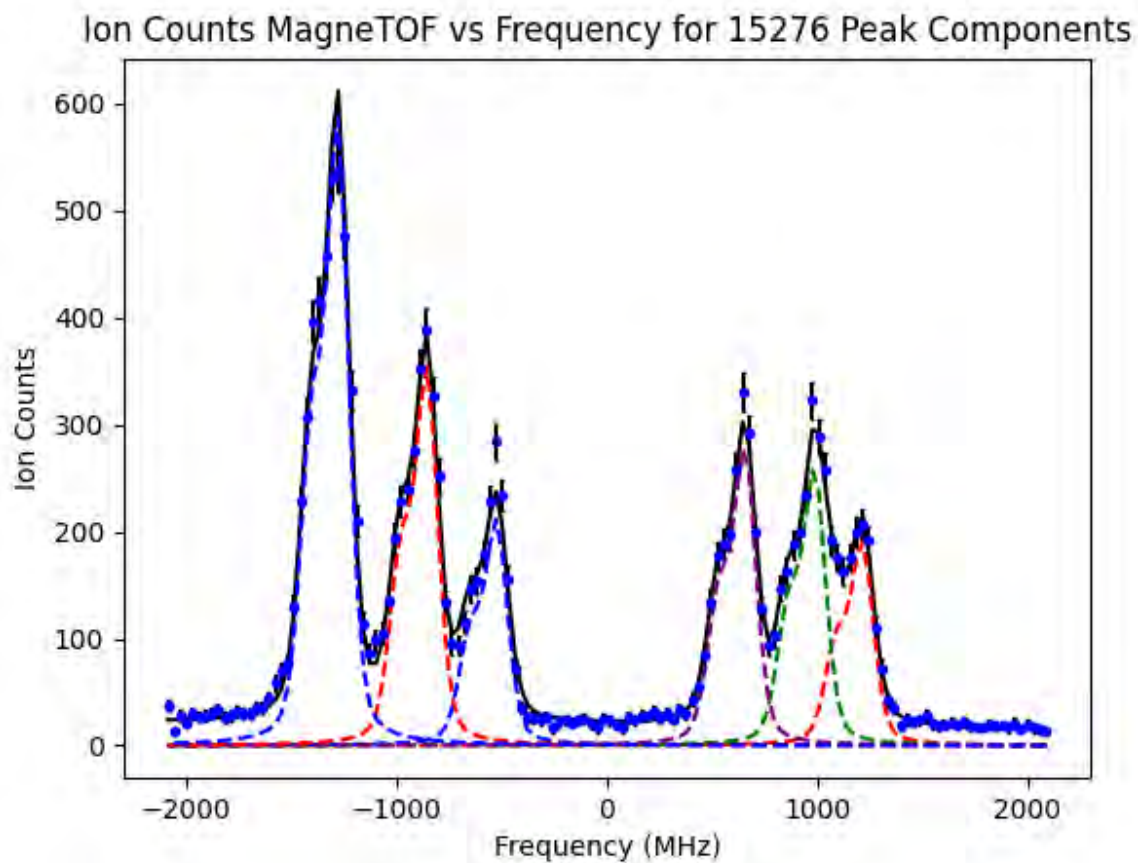


Figure .6 $3p\ ^2P_{1/2}$ to $yd\ ^2D_{3/2}$ transition peak components. *Place Holder Figure*
 The individual peaks of the $3p\ ^2P_{1/2}$ to $yd\ ^2D_{3/2}$ transition for ^{27}Al are shown.

The efficiency of each offline transition measured is listed in Table .1.

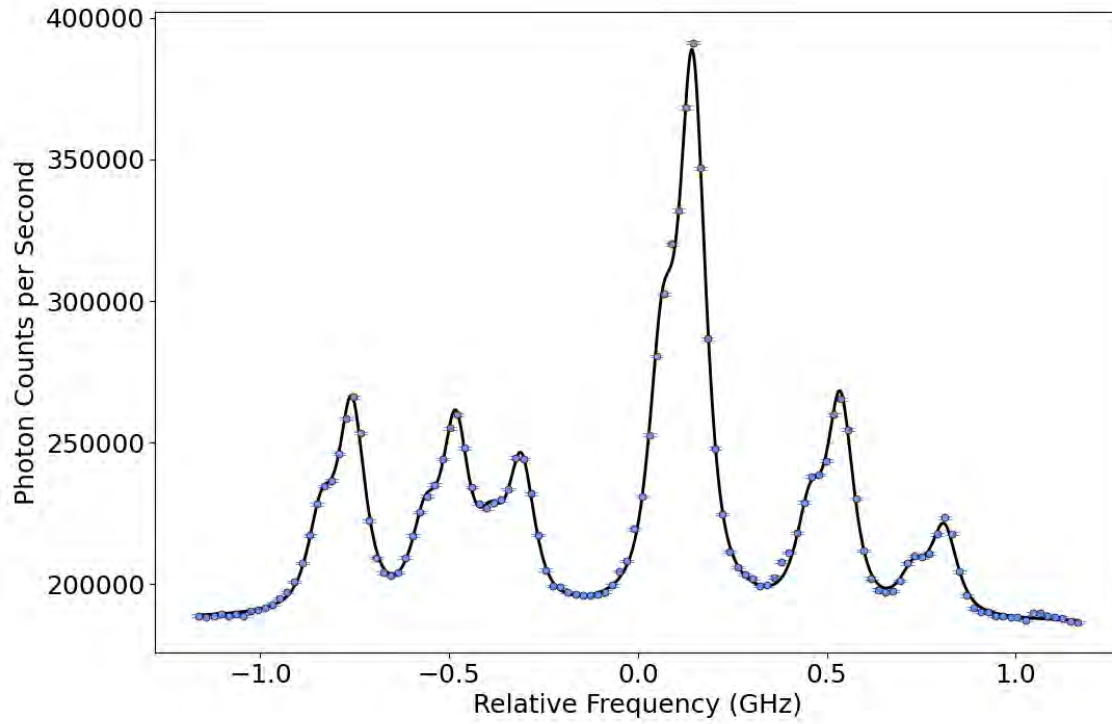


Figure .7 $3p\ ^2P_{3/2}$ to $4s\ ^2S_{1/2}$ transition spectrum. *Needs Title* A sample spectrum of the $3p\ ^2P_{3/2}$ to $4s\ ^2S_{1/2}$ transition for ^{27}Al is shown.

Table .1 Efficiency of each transition run comparing number of ions in the highest peak of a transition to the number of ions in a bunch leaving the cooler buncher.

Transition	Efficiency
$3p\ ^2P_{1/2}$ to $4s\ ^2S_{1/2}$	2.45×10^{-5}
$3p\ ^2P_{3/2}$ to $4s\ ^2S_{1/2}$	3.10×10^{-5}
$3p\ ^2P_{1/2}$ to $5s\ ^2S_{1/2}$	2.96×10^{-5}
$3p\ ^2P_{3/2}$ to $5s\ ^2S_{1/2}$	3.11×10^{-5}
$3p\ ^2P_{1/2}$ to $yd\ ^2D_{3/2}$	5.11×10^{-5}
$3p\ ^2P_{3/2}$ to $yd\ ^2D_{3/2}$	2.89×10^{-5}
$3p\ ^2P_{3/2}$ to $yd\ ^2D_{5/2}$	6.08×10^{-5}

Counts PMT vs Frequency for summ Peak Co

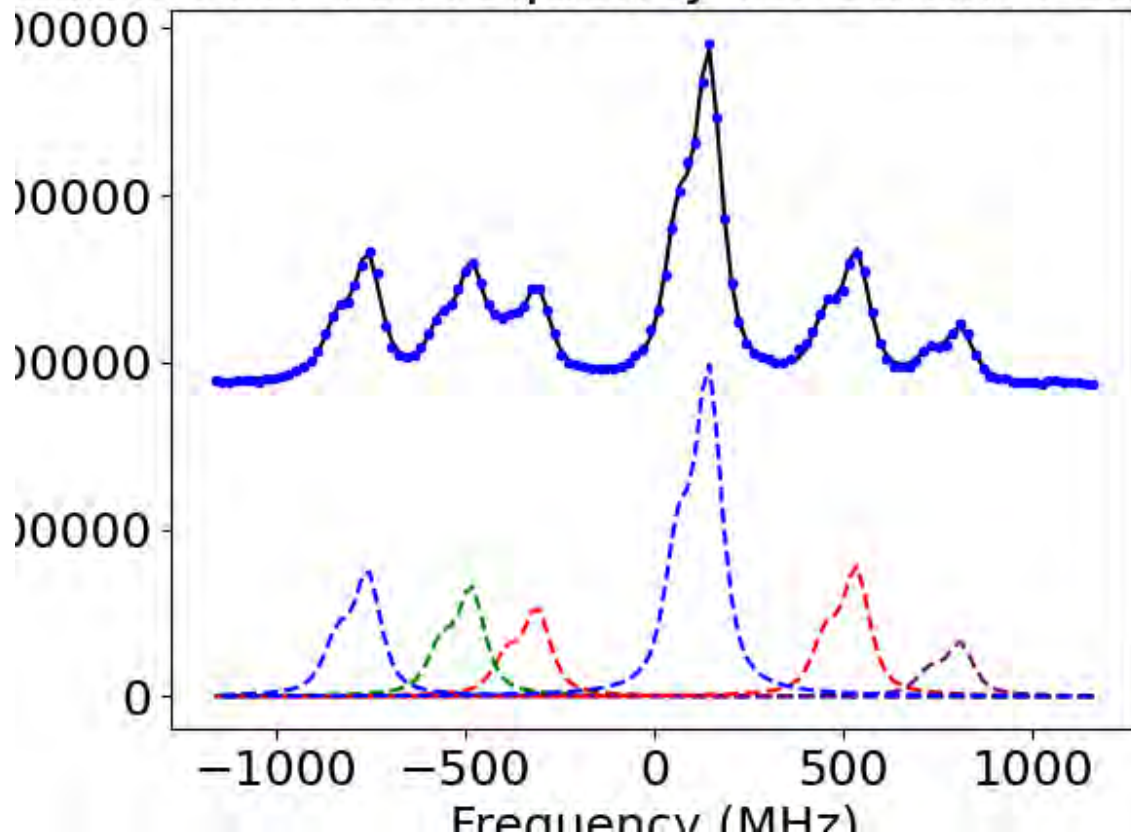


Figure .8 $3p \ ^2P_{3/2}$ to $4s \ ^2S_{1/2}$ transition peak components. *Place Holder Figure*
 The individual peaks of the $3p \ ^2P_{3/2}$ to $4s \ ^2S_{1/2}$ transition for ^{27}Al are shown.

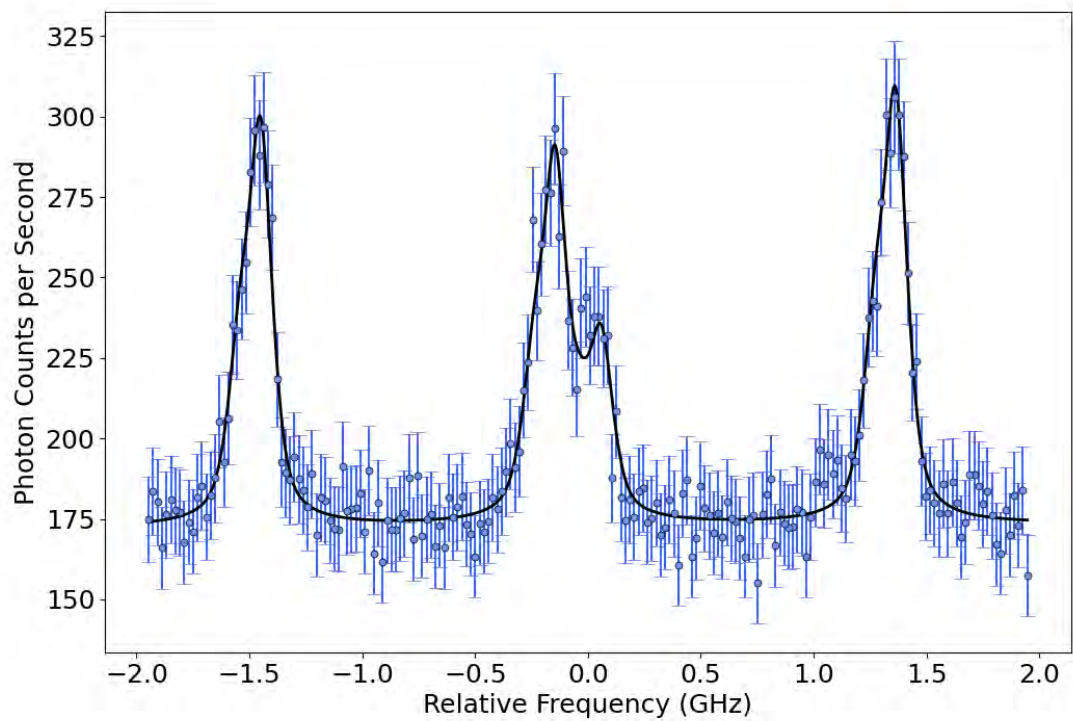


Figure .9 $3p\ ^2P_{1/2}$ to $4s\ ^2S_{1/2}$ transition spectrum. *Needs Title* A sample spectrum of the $3p\ ^2P_{1/2}$ to $4s\ ^2S_{1/2}$ transition for ^{27}Al is shown.

ounts PMT vs Frequency for summ Peak Co

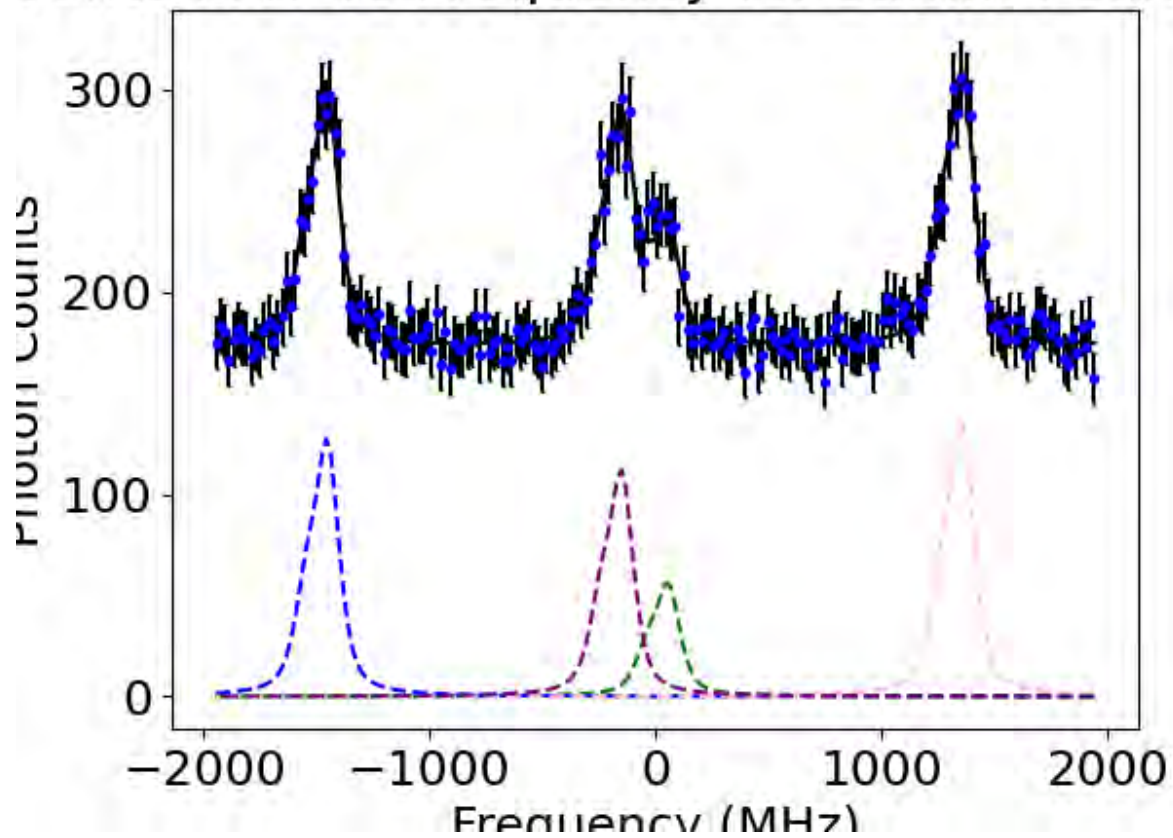


Figure .10 $3p \ ^2P_{1/2}$ to $4s \ ^2S_{1/2}$ transition peak components. *Place Holder Figure*
The individual peaks of the $3p \ ^2P_{1/2}$ to $4s \ ^2S_{1/2}$ transition for ^{27}Al are shown.